CHARACTERIZATION OF THE WATER TRANSPORT PROPERTIES OF THE ACTIVE LAYERS OF POLYAMIDE REVERSE OSMOSIS AND NANOFILTRATION MEMBRANES

Lin Lin

A dissertation submitted to the faculty at the University of North Carolina at Chapel Hill in partial fulfillment of the requirements for the degree of Doctor of Philosophy in the Department of Environmental Sciences and Engineering in the Gillings School of Global Public Health.

Chapel Hill
2015

Approved by:

Orlando Coronell

Michael Aitken

Gregory Characklis

Thomas Clegg

Prasun Dewan

Rene Lopez

ABSTRACT

Lin Lin: Characterization of the Water Transport Properties of the Active Layers of Polyamide Reverse Osmosis and Nanofiltration Membranes
(Under the direction of Orlando Coronell)

The overall objective of this study was to elucidate which parameter among water partitioning, water diffusion and active layer thickness accounts for the differences in water permeability among polyamide reverse osmosis (RO) and nanofiltration (NF) membranes. To achieve this overall objective, the following specific objectives were pursued: (i) to identify appropriate methods (facile and accurate) for measuring active layer thickness in RO/NF membranes; (ii) to ascertain the existence of voids within the polyamide active layers of RO/NF membranes and develop methods to quantify void volume fraction in active layers; (iii) to measure the partition coefficient of water into membrane active layers, and calculate the diffusion coefficient of water in active layers based on measurements of membrane water permeability (A), active layer thickness (δ), and water partition coefficient (K); and (iv) to correlate membrane water permeability (A) to active layer thickness (δ), water partition coefficient (K) and water diffusion coefficient (D) for a group of polyamide RO/NF membranes with a broad range of performance levels.

The following major conclusions were drawn through this dissertation: (i) atomic force microscopy (AFM), Rutherford backscattering spectrometry (RBS), quartz crystal microbalance (QCM), profilometry and ellipsometry produce consistent active layer thickness results among each other and likely provide the most accurate results of active layer thickness of RO/NF

membranes; (ii) scanning electron microscopy (SEM) and transmission electron microscopy (TEM) likely overestimate active layer thickness; (iii) voids with sizes in the ≈10-100 nm range commonly exist in the active layers of RO/NF membranes, occupy a significant volume fraction of the active layers, and are filled with water when the membranes are in contact with water (e.g., when they are being used for water purification); (iii) among active layer thickness, water partition coefficient and water diffusion coefficient, the differences in water permeabilities among RO/NF membranes were mostly accounted for by the differences in the water diffusion coefficients in their active layers; (iv) the presence of the voids in the active layer increases the membrane water permeance; and (v) there was not a clear correlation between void volume fraction and water permeance, water partition coefficient or water diffusion coefficient.

ACKNOWLEDGEMENTS

I would like to express my deepest gratitude to my advisor, Dr. Orlando Coronell. In the past five years, Orlando has always been very supportive and helpful to me. He has provided me with so much guidance, expertise and assistance during the course of my doctoral studies. I simply cannot imagine a better advisor.

I would also like to give special thanks to Dr. Thomas Clegg, who has not only been very supportive but also has educated me so much about the Rutherford backscattering spectrometry which is a very important technique in my research, since the very first week of my Ph.D. studies.

I am also very grateful to Dr. Rene Lopez for teaching me about and helping me with ellipsometry. Rene has provided me with many valuable suggestions during our discussion about applying ellipsometry in membrane research.

I would also like to express my great appreciation to Dr. Michael Aitken, Dr. Gregory Characklis and Dr. Prasun Dewan for being part of my Ph.D. committee and for providing insightful feedback that have helped me improve my research and my dissertation. Their expertise in chemical and biological processes in the environment, management of water resource, treatment and supply, and computer science has enriched my doctoral studies.

I would also like to thank Chengcheng Feng, Lamar Perry, Jingbo Wang, Eliot Meyer, Pete Attayek and Joshua Powell for their help on experiments of and discussion on ellipsometry, quartz crystal microbalance and Rutherford backscattering spectrometry. And I appreciate all

the help from Chuan Wang, Panitan Jutaporn, Ariel Atkinson, Kasia Grzebyk, Alex Gorzalski, John Gilles, Mikayla Armstrong in the Coronell research group.

Special thanks to Dr. Carrie Donley, Wallace Ambrose, Dr. Hugon Karwowski, John Dunham, Grayson Rich, Amar Kumbhar, Dr. Yang Liu, Dr. Yingchi Liu, Dr. Robert Geil for all their generous help on the characterization techniques used in this dissertation.

The work in this dissertation was supported by the National Science Foundation (NSF) Grants Opportunities for Academic Liason with Industry (GOALI) and Chemical and Biological Separations programs under Award#1264690, the NSF Environmental Engineering program under Award#1336532, the University of North Carolina IBM Junior Faculty Award and the Okun Scholarship. The financial support provided by the funding agencies is gratefully acknowledged.

TABLE OF CONTENTS

LIST OF TABLES

LIST OF FIGURES

LIST OF ABBREVIATIONS

AFM	Atomic force microscopy
NF	Nanofiltration
QCM	Quartz crystal microbalance
RBS	Rutherford backscattering spectrometry
RH	Relative humidity
RO	Reverse osmosis
SEM	Scanning electron microscopy
STEM-EDS	Scanning transmission electron microscopy-energy dispersive X-ray spectroscopy
STEM-EELS	Scanning transmission electron microscopy-electron energy loss spectroscopy
TEM	Transmission electron microscopy
TFC	Thin-film composite

LIST OF SYMBOLS

A	Water permeability coefficient
B	Solute permeability coefficient
C	Water concentration
C_{feed}	Solute concentration in feed
$C_{permeate}$	Solute concentration in permeate
D_{AL}	Water diffusion coefficient of active layer
D_P	Water diffusion coefficient of active layer polymer
D_P'	Water diffusion coefficient of active layer polymer ignoring voids
δ_{AL}	Active layer thickness
δ_P	Thickness of active layer polymer
Δp	Applied trans-membrane pressure
$\Delta \pi$	Trans-membrane osmotic pressure
f_{void}	Volume fraction of voids
J_{solute}	Solute flux
J_{water}	Water flux
K_{AL}	Water partition coefficient of active layer
K_P	Water partition coefficient of active layer polymer
K_P'	Water partition coefficient of active layer polymer ignoring voids
m_{AL}	Areal mass of active layer
m_l	Water uptake in liquid water
m_v	Water uptake in humidified nitrogen
n_{AL}	Refractive index of active layer
$n_{polymer}$	Refractive index of active layer polymer
n_{void}	Refractive index of void

P_{AL}	Water permeance of active layer
P_P	Water permeance of active layer polymer
R	Ideal gas constant
σ	Surface roughness of membrane
T	Temperature
v	Molar volume of liquid water

CHAPTER 1: INTRODUCTION

1.1 BACKGROUND AND MOTIVATION

1.1.1 The importance and structure of polyamide reverse osmosis and nanofiltration membranes

Reverse osmosis (RO) and nanofiltration (NF) are pressure-driven permeation processes which remove unwanted substances (i.e., solutes) from feed solutions. The removal of the solutes is achieved with the semi-permeability of RO/NF membranes that allows preferential permeation of solvent (i.e., water for RO/NF processes) over solutes. The preferential permeation of solvent leads to dilution of the solutes on the permeate side and effectively constitutes solute removal.[1] RO and NF membranes are widely used to produce drinking water from various source waters, including seawater, groundwater and recycled water.[2–4] RO/NF membranes are among the most important technologies to address the rising fresh water scarcity problems around the world because they are very effective in removing a very broad range of solutes in water.[1,2,5] Besides producing drinking water, RO and NF membranes have also been used for a variety of other applications including energy production, food processing, biotechnology, beverage industry, etc.[1,6]

In RO and NF processes, two important aspects of membrane performance are solute rejection and solvent flux (i.e., water flux for water purification applications).[5] Solute rejection is an indicator of the quality of the water produced, since higher solute rejection corresponds to lower solute concentration in the water produced. Water flux, characterized through the membrane water permeability coefficient (A) as discussed in Section 1.1.2, has a significant impact on the costs of RO/NF processes, especially on energy consumption. Since 1978,

increased water permeability of membranes has reduced the costs of RO/NF processes by more than 10 times.[7] However, even after more than 50 years of membrane research since Loeb and Sourirajan developed the first successful RO membrane, and even with the widespread use of RO/NF membranes around the world, energy consumption still remains as a major disadvantage of RO/NF processes. [1,7–9] Therefore, comprehensive research about the factors that determine water permeability in RO/NF membranes is needed to further reduce the associated energy costs. The market of RO and NF membranes for water purification has been dominated by thin-film composite (TFC) membranes since the development of the Loeb-Sourirajan membrane in 1960.[8,9] TFC membranes usually have a three-layer structure, with an ultrathin active layer (~20 – 200 nm) on top of an intermediate porous support layer (~20-50 μm) and a backing fabric layer (~300 μm).[5,7] The active layer, support layer and backing layer are commonly made of polyamide, polysulfone and polyester, respectively. The polyamide active layer controls the permeation of water and solutes through the membrane,[5,10] while the other two layers mainly provide physical support to the active layer.

1.1.2. Mechanisms of water and solute permeation through TFC membranes

The transport of water and solutes through the membrane active layers is commonly described by the solution-diffusion model,[11] which is depicted in Figure 1.1. In the solution-diffusion model, the active layer is assumed to be a dense uniform layer of polyamide and the permeation of water and solutes through the active layer is achieved in three steps: (1) at the interface between the feed water (e.g., seawater, recycled water) and the membrane active layer, water and solutes dissolve into the active layer, then (2) the dissolved water and solutes move through the active layer (from the feed side to the permeate side) by diffusion, and finally (3) at the interface between the active layer and the permeate (e.g., purified water), the water and solutes which have reached the permeate side in the active layer dissolve into the permeate.

In RO and NF processes, the performance of the membrane in terms of water production is described by the flux of water that permeates the membrane. According to the solution-diffusion model, the water flux (J_{water}) is described by [11]

$$J_{water} = A\ (\Delta p - \Delta\pi)\ , \qquad (1.1)$$

where A (m s^{-1} Pa^{-1}) is the water permeability coefficient of the membrane (i.e., of the active layer), Δp (Pa) is the applied trans-membrane pressure, and $\Delta\pi$ (Pa) is the trans-membrane osmotic pressure. According to Equation 1.1, a high water permeability coefficient is a desired active layer property, because a higher water permeability coefficient (A) allows for achieving a higher water flux at a reduced applied pressure (Δp), and thus at reduced energy costs.

The performance of the membrane in terms of solute removal is described by the solute rejection (R) as calculated by

$$R = 1 - \frac{c_{permeate}}{c_{feed}}\ , \qquad (1.2)$$

where c_{feed} (mol m^{-3}) and $c_{permeate}$ (mol m^{-3}) are the solute concentrations in the feed and permeate water, respectively. The solute concentration in the permeate water is both a function of and determines the solute flux as given by[11]

$$J_{solute} = B\ (c_{feed} - c_{permeate}\ ), \qquad (1.3)$$

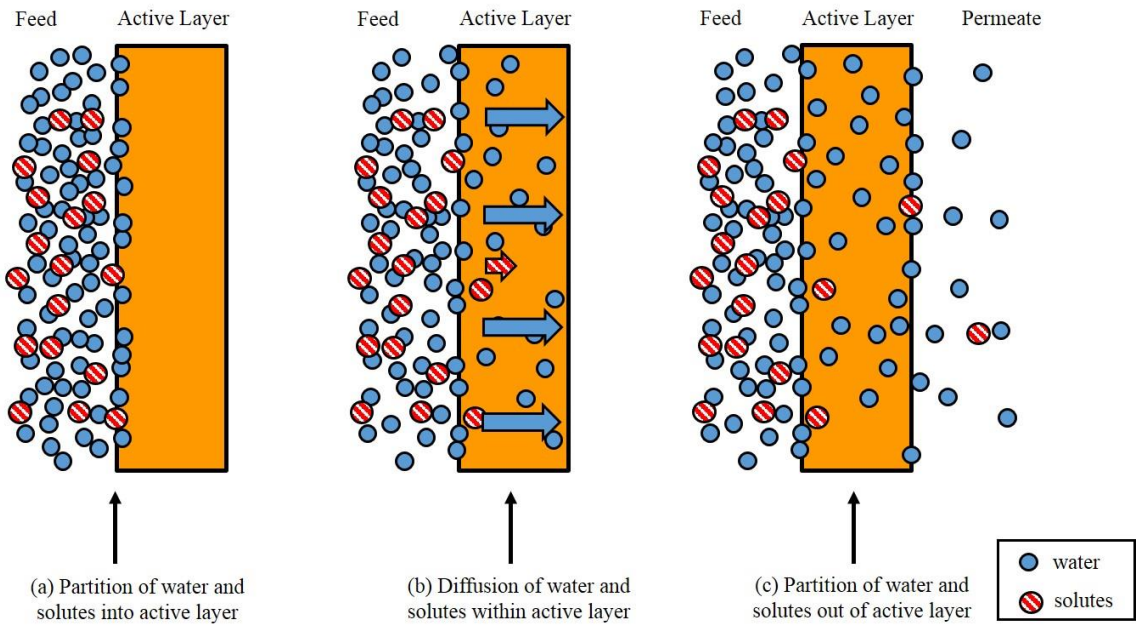

Figure 1.1. Permeation of water and solutes through membrane active layers as described by the solution-diffusion model. The permeation process consists of three steps: water and solute molecules (a) dissolve into the active layer at the feed-membrane interface, then (b) diffuse through the active layer, and finally (c) partition out of the active layer into the permeate.

where B (m s^{-1}) is the solute permeability coefficient. From Equations 1.1-1.3, solute rejection can also be expressed as

$$R = \frac{A\,(\Delta p - \Delta \pi)}{A\,(\Delta p - \Delta \pi) + B}\,. \tag{1.4}$$

Equation 1.4 shows that the water permeability coefficient not only determines the rate of water production, but also strongly affects the quality of the water produced. Therefore, it is very important to understand the water permeability of membrane active layers for improvement of membrane performance in terms of both quality and rate of permeate water production. According to the solution-diffusion model, the water permeability coefficient is given by[11]

$$A = \frac{DK}{\delta}\frac{C_{H_2O}v}{RT}\,, \tag{1.5}$$

where K (-) is the partition coefficient of water into the active layer, D (m^2 s^{-1}) is the diffusion coefficient of water within the active layer, δ (nm) is the thickness of the active layer, C_{H_2O} (mol m^{-3}) is the molar concentration of bulk water, v (m^3 mol^{-1}) is the molar volume of liquid water, R (m^3 Pa K^{-1} mol^{-1}) is the ideal gas constant, and T (K) is the absolute temperature. While C_{H_2O}, v, R and T are either constants or operational parameters, the properties of the membranes that affect the water permeability are the partition coefficient, the diffusion coefficient and the thickness of the active layer. Thus, to understand which membrane properties (K, D and/or δ) should be targeted in membrane development towards the production of improved membranes, one must understand the relative importance of K, D and/or δ in the overall water permeability of existing membranes.

1.1.3 State of the art of measurements of partition and diffusion coefficients in active layers

Despite the importance of water partition and diffusion coefficients in active layers in understanding what makes any two membranes perform differently, neither property has been thoroughly characterized in the peer-reviewed literature. Only two studies[12,13] (both for RO

membranes) have characterized water partitioning into active layers by measuring water uptake by polyamide active layers of commercial RO/NF membranes. Zhang *et al.*[12] obtained water uptake values of 11.2 wt% and 12.8 wt% for the FT30 RO and LF10 RO membranes, respectively, and Lee *et al.*[13] obtained water uptake of 20.1 wt% for the SW30 RO membrane, which was approximately 57-80% higher than the water uptake obtained by Zhang *et al.* Both studies have focused only on RO membranes.

Zhang *et al.* and Lee *et al.* also calculated the diffusion coefficients of water within membrane active layers using Equation 1.5, and their corresponding water permeability, water uptake and active layer thickness results.[12,13] While Zhang *et al.* reported calculated diffusion coefficients of 0.8×10^{-9} m^2 s^{-1} and 1.2×10^{-9} m^2 s^{-1} for the FT30 RO and LF10 RO membranes, respectively,[12] Lee et al obtained a significantly lower diffusion coefficient value of 0.43×10^{-9} m^2 s^{-1} for the SW30 RO membrane.[13] The diffusion coefficient of water in polyamide active layer has also been studied through atomistic simulations mimicking the active layer of the FT30 RO membrane with values of 0.71-0.85 $\times10^{-9}$ m^2/s being reported.[14] The diffusion coefficient values calculated with atomistic simulations[14] were comparable to the values obtained by Zhang et al,[12] but 98% higher than the value obtained by Lee *et al.*[13] No direct measurement of the diffusion coefficient of water within polyamide active layers of RO/NF membrane has been reported in the peer-reviewed literature. All three studies discussed above focused only on RO membranes.

Thus, the peer-reviewed literature lacks a thorough study of water partitioning and diffusion in polyamide active layers of membranes with a broad range of performance levels (i.e., seawater RO, brackish water RO, NF). Also, the existing experimental studies[12,13] reported significantly different water partition and diffusion coefficients in polyamide active layers for

similarly performing membranes. Thus, there is a need for further characterization studies of water partitioning and diffusion in active layers to fully understand the range of partition and diffusion coefficients values throughout the whole spectrum of RO/NF membranes (i.e., seawater RO, brackish water RO, NF).

It is important to note that a major reason why there are so few studies of partitioning and diffusion in active layers in the peer-reviewed literature is the experimental difficulties in characterizing material properties and phenomena occurring in the bulk region of active layers. Given that the active layers of TFC membranes have thicknesses on the nanometer scale and account for less than 0.1% of the total thickness of the membranes, nanoscale spatial resolution is required in any experimental procedure intended to probe the bulk region of the active layer. The extreme thinness of the active layers also results in an exceptionally small time scale of diffusion of water in the active layer (~10^{-5} s) (i.e., the average time that it takes a water molecule to diffuse through the active layer), which makes measuring water diffusion coefficients experimentally extremely difficult, and so far not possible.

1.1.4. State of the art of measurements of active layer thickness

Unfortunately, there is also a need to verify that the methods that are being used in the literature to measure active layer thickness (δ) provide accurate measurements. Several techniques that have been used in the literature include scanning electron microscope (SEM),[15–18] transmission electron microscopy (TEM),[15,19,20] atomic force microscopy (AFM)[21,22] and Rutherford backscattering spectrometry (RBS).[12,15,23–26]

Thickness measurements with SEM and TEM for RO/NF membranes are based on image analysis of cross-sectional electron micrographs of the active layers.[15–18] Thickness measurements with AFM are achieved through analysis of the topography profiles of thin strips of active layer isolated on a hard solid substrate, such as a silicon wafer.[21,22] More recently, RBS

has been used to quantify active layer thickness based on the measured atomic areal density (atoms $\cdot m^{-2}$) and elemental composition of the active layer, which can be used to calculate the mass areal density (g $\cdot m^{-2}$) of the active layer. The active layer thickness is then calculated as the ratio between the areal mass density and the volumetric mass density (g $\cdot m^{-3}$) of the polyamide material.[12,15,23–26] One important drawback of quantifying thickness of active layers using SEM, TEM or AFM is that the small size (a few micrometers for SEM and TEM, and around 30×30 μm^2 for AFM) of sample analysis could potentially result in thickness results unrepresentative of the active layer being studied. One important drawback of RBS analysis is the need to use an active layer volumetric mass density value in the calculation of active layer thickness. This is because the volumetric mass density of active layers in RO/NF membranes has not been measured experimentally and only corresponding educated estimates are available. Thus, the accuracy of RBS estimates of active layer thickness is limited to the accuracy of the assumption about the volumetric mass density of the active layer.

While all four methods described above have important drawbacks in measuring active layer thickness, no study in the peer-reviewed literature has compared thickness values measured with these different techniques to conclude whether there is agreement, or not, among the different measurements. In addition to the need to determine whether active layer thickness measurements are accurate or not for their own importance as a physical property of the active layer, one must remember that accurate measurements of active layer thickness are needed for the calculation of accurate diffusion coefficients (D) in active layers (see Equation 1.5). Therefore, there is a need to compare the currently available methods to measure active layer thickness and, if possible, to introduce new methods as the existing methods all have significant drawbacks.

1.1.5. Void and nodular structures within active layers

A new important development has recently arisen in the study of water and solute transport phenomena through active layers. Contrary to the conceptualization of the solution-diffusion model that the active layer is a continuous, dense polymer phase, recent experimental studies based on TEM imaging[27–32] suggest that voids (i.e., regions without polymer) with tens of nanometers in diameter exist within the polyamide layer. Pacheco *et al.*[33] provided a different interpretation of the features in active layers identified as voids in TEM images by other researchers[27–32] proposing that they are nodules and indicating that polyamide active layers are composed of a dense 'nodular' base from which the ridge-and-valley structure extends outwards (see Figure 1.2(c)). Similar features as those interpreted as nodules by Pacheco *et al.* and voids by others[27–32] are visible in TEM images reported by other authors,[34–36] although these authors did not identify them as nodules or voids. The presence of voids or nodules in the active layer disagrees with the assumption that the active layer is dense and uniform.

While it is not settled in the literature whether the features in TEM images are voids or nodules,[28] it can be observed in the TEM images reported in the literature[29–36] that these features are significantly lighter in shade than the rest of the active layer in bright-field TEM images. Based on the principles of TEM imaging, darker and lighter regions in bright-field TEM images are associated with higher and lower electron density regions, respectively, in the sample described above, current models do not take into account the existence of voids. Moreover, if the voids are important in the mechanisms of permeation of water and solutes, membrane developers could target manipulation of volume fraction, size and size distribution of

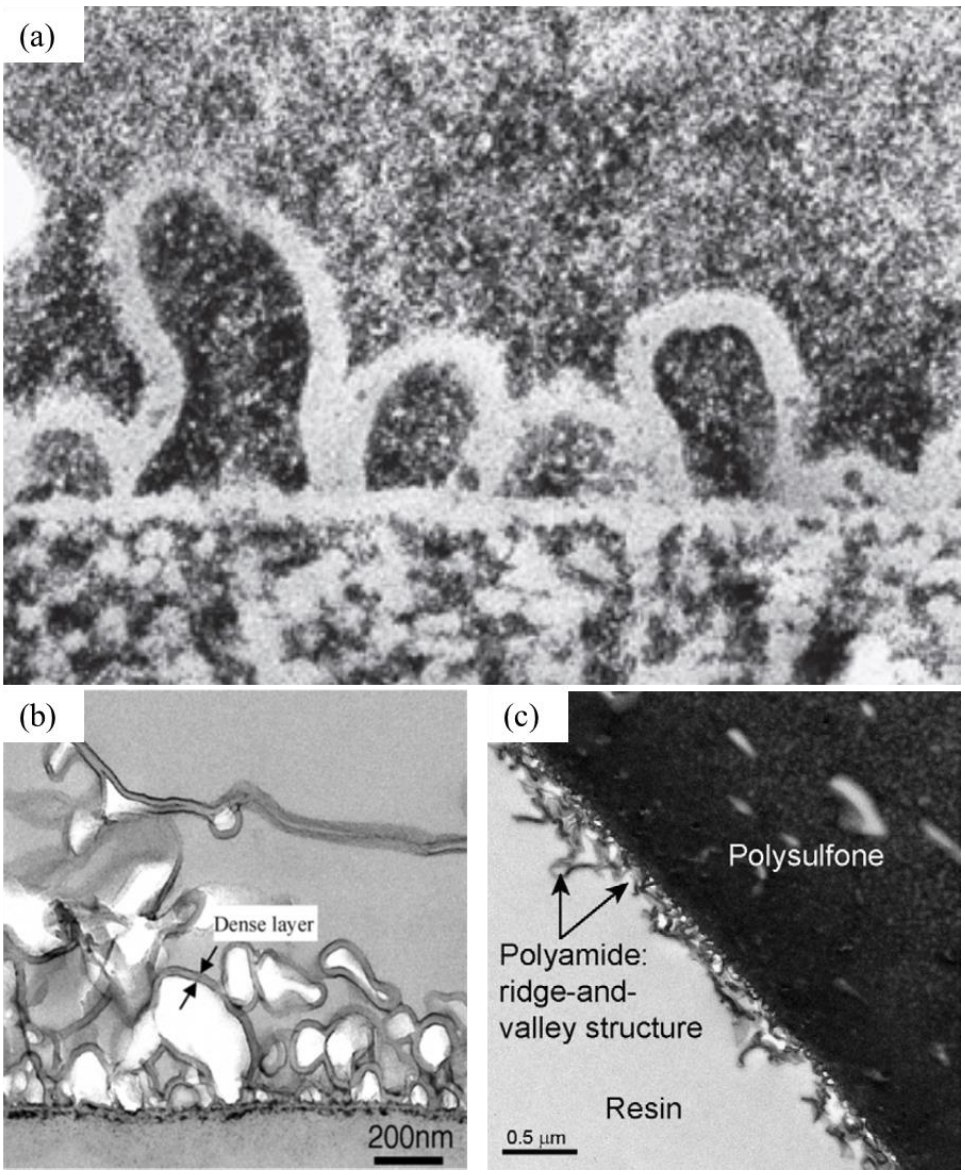

Figure 1.2. (a) A dark-field TEM image of a membrane cross-section that shows the protuberances of the ridge-and-valley structure and apparent voids within it.[27] (b) A bright-field TEM image of the cross-section of a membrane prepared by interfacial polymerization that shows the apparent voids. (c) A bright-field TEM image of the cross-section of an ESPA3 membrane sample which shows the proposed nodular base of the active layer and the ridge-and-valley structure.[33]

the voids to develop improved membranes. As a result, there is a need to evaluate whether these features are in fact voids, whether they are permeable to water, and estimate how important they are in terms the volume fraction of the active layer that they account for.

1.1.6 Gaps in the literature regarding the mechanisms of water transport through active layers

Based on the background discussed in Sections 1.1.1-1.1.5, the following gaps exist in the literature that must be overcome to achieve a full understanding about the mechanisms of water transport through the active layers of TFC membranes: (1) there is no comparison available of the different methods that exist to measure active layer thickness to determine whether one or more of the methods provide thickness values unrepresentative of the active layer that one tries to characterize and the advantages and disadvantages of each of the methods; (2) it remains to be settled whether the bright features identified in cross-sectional bright-field TEM images of polyamide active layers are voids or nodules; (3) it is unknown whether these features are common in polyamide active layers of a broad range of performance levels, comprise a significant volume fraction of active layers when present in them, or are permeable to water; (4) there are only two studies that have measured experimentally water partition coefficients in polyamide active layers, and have calculated corresponding water diffusion coefficients from such measurements, and the results from these studies were limited to a few RO membranes and did not agree with each other; (5) it is unknown which among the water partition coefficient (K), water diffusion coefficient (D) and active layer thickness (δ) is/are the factor(s) that typically account for most of the difference in water permeabilities between any two polyamide RO/NF membranes.

1.2. OBJECTIVES

1.2.1. Overall Research Goal

Addressing the gaps in the literature identified above, the overall goal of my research is to elucidate which parameter among water partitioning, water diffusion and active layer thickness accounts for the differences in water permeability among polyamide reverse osmosis (RO) and nanofiltration (NF) membranes.

1.2.2. Specific Objectives

To achieve my overall research goal, the following specific objectives were pursued:

1. To identify appropriate methods (facile and accurate) for measuring active layer thickness in RO/NF membranes;
2. To ascertain the existence of voids within the polyamide active layers of RO/NF membranes and develop methods to quantify void volume fraction in active layers;
3. To measure the partition coefficient of water into membrane active layers, and calculate the diffusion coefficient of water in active layers based on measurements of membrane water permeability (A), active layer thickness (δ), and water partition coefficient (K);
4. To correlate membrane water permeability (A) to active layer thickness (δ), water partition coefficient (K) and water diffusion coefficient (D) for a group of polyamide RO/NF membranes with a broad range of performance levels.

1.3 Dissertation Organization

This dissertation is composed of six chapters and three appendices. Chapters 1, 5 and 6 correspond to the introduction, conclusions and future work, respectively, and Chapters 2-4 are individual comprehensive chapters addressing the specific research objectives listed above with

their own introductions, materials and methods, results and discussion, conclusions, acknowledgements and references sections. Chapters 2-4 are briefly described below:

- Chapter 2: The work reported in this chapter compared seven thickness measurement techniques for active layers of TFC membranes. The seven techniques are scanning electron microscopy, transmission electron microscopy, atomic force microscopy, Rutherford backscattering spectrometry, quartz crystal microbalance, profilometry and ellipsometry. The six TFC membranes studied were NF270, NF90, XLE, ESPA3, SWC4+ and SW30HR membranes. For each membrane, active layer thickness was measured with all seven techniques and the results were compared using statistical analyses. Advantages and disadvantages of each technique were discussed. Through comparison of thickness results and discussion of advantages and disadvantages of each technique, conclusions were drawn regarding the accuracy of the techniques and preferred techniques under specific circumstances.
- Chapter 3: Studies reported in this chapter were on the features identified as voids by some, and as nodules by others, in cross-sectional TEM images of polyamide active layers of TFC membranes. The features were studied with image analysis of TEM images of membrane cross sections supported by SEM images of membrane cross sections, water uptake tests using quartz crystal microbalance, and effective refractive indices of active layers using spectroscopic ellipsometry. The five membranes studied were NF90, XLE, ESPA3, SWC4+ and SW30HR membranes. The NF270 membrane that was included in the work reported in Chapter 2 was not studied because the features were not clearly observed in the corresponding SEM cross-sectional images obtained. Through comparison of the volume fraction that the features occupy in active layers

obtained through various experimental approaches, conclusions were drawn regarding the void nature of the features and the permeability of the voids to water when membranes are immersed in water.

- Chapter 4: In this chapter, I reported investigation on the reasons why TFC membranes having active layers with the same chemistry (fully aromatic polyamide) have very different water permeabilities. The research approach consisted of measuring water permeability and the three main parameters that determine it (i.e., active layer thickness, water partition coefficient, and water diffusion coefficient) for five commercial fully aromatic polyamide TFC membranes (NF90, XLE, ESPA3, SWC4+ and SW30HR membranes). Through statistical analyses, conclusions were drawn regarding which of the three parameter accounted for the differences in water permeabilities among TFC membranes. Data analysis was performed taking into account the presence of voids in the active layers.

The appendices follow Chapter 6. The appendices include experimental data obtained for Chapter 2, Chapter 3 and Chapter 4, and the "Supporting Information" referenced in the main text of Chapter 3.

REFERENCES

(1) Malaeb, L.; Ayoub, G. M. Reverse osmosis technology for water treatment: State of the art review. *Desalination* **2011**, *267*, 1–8.

(2) Greenlee, L. F.; Lawler, D. F.; Freeman, B. D.; Marrot, B.; Moulin, P. Reverse osmosis desalination: water sources, technology, and today's challenges. *Water Res.* **2009**, *43*, 2317–2348.

(3) Jacangelo, J. G.; Trussell, R. R.; Watson, M. Role of membrane technology in drinking water treatment in the United States. *Desalination* **1997**, *113*, 119–127.

(4) Van der Bruggen, B.; Everaert, K.; Wilms, D.; Vandecasteele, C. Application of nanofiltration for removal of pesticides, nitrate and hardness from ground water: rejection properties and economic evaluation. *J. Membr. Sci.* **2001**, *193*, 239–248.

(5) Petersen, R. J. Composite reverse osmosis and nanofiltration membranes. *J. Membr. Sci.* **1993**, *83*, 81–150.

(6) Yip, N. Y.; Tiraferri, A.; Phillip, W. A.; Schiffman, J. D.; Hoover, L. A.; Kim, Y. C.; Elimelech, M. Thin-film composite pressure retarded osmosis membranes for sustainable power generation from salinity gradients. *Environ. Sci. Technol.* **2011**, *45*, 4360–4369.

(7) Lee, K. P.; Arnot, T. C.; Mattia, D. A review of reverse osmosis membrane materials for desalination—Development to date and future potential. *J. Membr. Sci.* **2011**, *370*, 1–22.

(8) Matsuura, T. Progress in membrane science and technology for seawater desalination - a review. *Desalination* **2001**, *134*, 47–54.

(9) Loeb, S. The Loeb-Sourirajan Membrane: How It Came About. *ACS Symp. Ser.* **1981**, *153-154*, 1–9.

(10) Bellona, C.; Drewes, J. E.; Xu, P.; Amy, G. Factors affecting the rejection of organic solutes during NF/RO treatment—A literature review. *Water Res.* **2004**, *38*, 2795–2809.

(11) Wijmans, J. G.; Baker, R. W. The solution-diffusion model: a review. *J. Membr. Sci.* **1995**, *107*, 1–21.

(12) Zhang, X.; Cahill, D. G.; Coronell, O.; Mariñas, B. J. Absorption of water in the active layer of reverse osmosis membranes. *J. Membr. Sci.* **2009**, *331*, 143–151.

(13) Lee, J.; Doherty, C. M.; Hill, A. J.; Kentish, S. E. Water vapor sorption and free volume in the aromatic polyamide layer of reverse osmosis membranes. *J. Membr. Sci.* **2013**, *425-426*, 217–226.

(14) Kotelyanskii, M. J.; Wagner, N. J.; Paulaitis, M. E. Atomistic simulation of water and salt transport in the reverse osmosis membrane FT-30. *J. Membr. Sci.* **1998**, *139*, 1–16.

(15) Mi, B.; Coronell, O.; Mariñas, B. J.; Watanabe, F.; Cahill, D. G.; Petrov, I. Physico-chemical characterization of NF/RO membrane active layers by Rutherford backscattering spectrometry. *J. Membr. Sci.* **2006**, *282*, 71–81.

(16) Singh, P. S.; Rao, A. P.; Ray, P.; Bhattacharya, A.; Singh, K.; Saha, N. K.; Reddy, A. V. R. Techniques for characterization of polyamide thin film composite membranes. *Desalination* **2011**, *282*, 78–86.

(17) La, Y.-H.; Sooriyakumaran, R.; Miller, D. C.; Fujiwara, M.; Terui, Y.; Yamanaka, K.; McCloskey, B. D.; Freeman, B. D.; Allen, R. D. Novel thin film composite membrane containing ionizable hydrophobes: pH-dependent reverse osmosis behavior and improved chlorine resistance. *J. Mater. Chem.* **2010**, *20*, 4615–4620.

(18) Boussu, K.; De Baerdemaeker, J.; Dauwe, C.; Weber, M.; Lynn, K. G.; Depla, D.; Aldea, S.; Vankelecom, I. F. J.; Vandecasteele, C.; Van der Bruggen, B. Physico-chemical characterization of nanofiltration membranes. *ChemPhysChem* **2007**, *8*, 370–379.

(19) Freger, V.; Gilron, J.; Belfer, S. TFC polyamide membranes modified by grafting of hydrophilic polymers: an FT-IR/AFM/TEM study. *J. Membr. Sci.* **2002**, *209*, 283–292.

(20) Ghosh, A. K.; Jeong, B.-H.; Huang, X.; Hoek, E. M. V. Impacts of reaction and curing conditions on polyamide composite reverse osmosis membrane properties. *J. Membr. Sci.* **2008**, *311*, 34–45.

(21) Freger, V. Swelling and morphology of the skin layer of polyamide composite membranes: an atomic force microscopy study. *Environ. Sci. Technol.* **2004**, *38*, 3168–3175.

(22) Dražević, E.; Košutić, K.; Freger, V. Permeability and selectivity of reverse osmosis membranes: Correlation to swelling revisited. *Water Res.* **2014**, *49*, 444–452.

(23) Coronell, O.; González, M. I.; Mariñas, B. J.; Cahill, D. G. Ionization behavior, stoichiometry of association, and accessibility of functional groups in the active layers of reverse osmosis and nanofiltration membranes. *Environ. Sci. Technol.* **2010**, *44*, 6808–6814.

(24) Coronell, O.; Mariñas, B. J.; Zhang, X.; Cahill, D. G. Quantification of functional groups and modeling of their ionization behavior in the active layer of FT30 reverse osmosis membrane. *Environ. Sci. Technol.* **2008**, *42*, 5260–5266.

(25) Jubera, A. M. S. de; Gao, Y.; Moore, J. S.; Cahill, D. G.; Mariñas, B. J. Enhancing the Performance of Nanofiltration Membranes by Modifying the Active Layer with Aramide Dendrimers. *Environ. Sci. Technol. Technol.* **2012**, *46*, 9592–9599.

(26) Matthews, T. D.; Yan, H.; Cahill, D. G.; Coronell, O.; Mariñas, B. J. Growth dynamics of interfacially polymerized polyamide layers by diffuse reflectance spectroscopy and Rutherford backscattering spectrometry. *J. Membr. Sci.* **2013**, *429*, 71–80.

(27) Kurihara, M.; Hanakawa, M. Mega-ton water system: Japanese national research and development project on seawater desalination and wastewater reclamation. *Desalination* **2013**, *308*, 131–137.

(28) Ridgway, H. F.; Gale, J. D.; Hughes, Z. E.; Stewart, M. B.; Orbell, J. D.; Gray, S. R. Molecular scale modeling of membrane water treatment processes. In *Functional Nanostructured Materials and Membranes for Water Treatment*; Duke, M.; Zhao, D.; Semiat, R.; Lu, M., Eds.; John Wiley & Sons, 2013; pp. 249–300.

(29) An, Q.; Hung, W.; Lo, S.; Li, Y.; Guzman, M. De; Hu, C.-C.; Lee, K.-R.; Jean, Y.-C.; Lai, J.-Y. Comparison between Free Volume Characteristics of Composite Membranes Fabricated through Static and Dynamic Interfacial Polymerization Processes. *Macromolecules* **2012**, *45*, 3248–3435.

(30) Kong, C.; Shintani, T.; Kamada, T.; Freger, V.; Tsuru, T. Co-solvent-mediated synthesis of thin polyamide membranes. *J. Membr. Sci.* **2011**, *384*, 10–16.

(31) Kong, C.; Koushima, A.; Kamada, T.; Shintani, T.; Kanezashi, M.; Yoshioka, T.; Tsuru, T. Enhanced performance of inorganic-polyamide nanocomposite membranes prepared by metal-alkoxide-assisted interfacial polymerization. *J. Membr. Sci.* **2011**, *366*, 382–388.

(32) Kong, C.; Kanezashi, M.; Yamomoto, T.; Shintani, T.; Tsuru, T. Controlled synthesis of high performance polyamide membrane with thin dense layer for water desalination. *J. Membr. Sci.* **2010**, *362*, 76–80.

(33) Pacheco, F. A.; Pinnau, I.; Reinhard, M.; Leckie, J. O. Characterization of isolated polyamide thin films of RO and NF membranes using novel TEM techniques. *J. Membr. Sci.* **2010**, *358*, 51–59.

(34) Tang, C. Y.; Kwon, Y.-N.; Leckie, J. O. Probing the nano- and micro-scales of reverse osmosis membranes—A comprehensive characterization of physiochemical properties of uncoated and coated membranes by XPS, TEM, ATR-FTIR, and streaming potential measurements. *J. Membr. Sci.* **2007**, *287*, 146–156.

(35) Tang, C. Y.; Fu, Q. S.; Robertson, A. P.; Criddle, C. S.; Leckie, J. O. Use of reverse osmosis membranes to remove perfluorooctane sulfonate (PFOS) from semiconductor wastewater. *Environ. Sci. Technol.* **2006**, *40*, 7343–7349.

(36) Yin, J.; Kim, E.-S.; Yang, J.; Deng, B. Fabrication of a novel thin-film nanocomposite (TFN) membrane containing MCM-41 silica nanoparticles (NPs) for water purification. *J. Membr. Sci.* **2012**, *423-424*, 238–246.

(37) Bozzola, J. J.; Russell, L. D. *Electron Microscopy: Principles and Techniques for Biologist*; 2nd ed.; Jones and Bartlett, 1999.

CHAPTER 2: IDENTIFYING FACILE AND ACCURATE METHODS TO MEASURE THE THICKNESS OF THE ACTIVE LAYERS OF THIN-FILM COMPOSITE MEMBRANES – A COMPARISON OF SEVEN CHARACTERIZATION TECHNIQUES

2.1 Introduction

Reverse osmosis (RO) and nanofiltration (NF) membranes are widely used for water purification in a broad range of applications, including desalination, hardness removal and water reuse.[1–3] The market of RO and NF membranes is dominated by thin-film composite (TFC) membranes which consist of a polyamide active layer (~20-200 nm), a porous polysulfone support (~20-50 μm) and a polyester backing fabric (~300 μm).[4,5] The polyamide active layer serves the role of selective barrier determining the permeation of water and solutes through the membrane.[4,6]

The solution-diffusion model[7] is commonly used to describe water and solute permeation through membrane active layers. The model describes the water flux (J_{water}) as

$$J_{water} = A(\Delta p - \Delta \pi), \tag{2.1}$$

where A (m s^{-1} Pa^{-1}) is the water permeability coefficient of the membrane, Δp (Pa) is the applied trans-membrane pressure and $\Delta \pi$ (Pa) is the trans-membrane osmotic pressure. The water permeability coefficient A is given by

$$A = \frac{DK}{\delta}\frac{C_{H_2O}v}{RT}, \tag{2.2}$$

where D (m^2 s^{-1}) is the diffusion coefficient of water within the active layer, K (-) is the partition coefficient of water into the active layer, δ (m) is the thickness of the active layer, C_{H_2O} (mol m^{-3}) is the molar concentration of bulk water, v (m^3 mol^{-1}) is the molar volume of liquid water, R

(m^3 Pa K^{-1} mol^{-1}) is the ideal gas constant, and T (K) is the absolute temperature. Similarly, the solution-diffusion model describes solute flux (J_{solute}) as

$$J_{solute} = B(c_{feed} - c_{permeate}), \quad (2.3)$$

where B (m s^{-1}) is the solute permeability coefficient, c_{feed} (mol m^{-3}) is the solute concentration in the feed water, and $c_{permeate}$ (mol m^{-3}) is the solute concentration in the permeate water. The solute permeability coefficient B is given by

$$B = \frac{D_i K_i}{\delta}, \quad (2.4)$$

where D_i (m^2 s^{-1}) is the diffusion coefficient of solute *i* within the active layer, K_i (-) is the partition coefficient of solute *i* into the active layer and δ(m) is the thickness of the active layer. Equations 2.1-2.4 show that the active layer thickness is a strong determinant of membrane performance (i.e., water flux and solute flux) through its effects on the water and solute permeability coefficients.

Current quantification methods of K and D require the value of the active layer thickness.[8,9] For example, to obtain the water partition coefficient in RO active layers, Zhang *et al.*[8] and Lee *et al.*[9] calculated the concentration of water in the active layer (C_m, mol·m^{-3}) as the ratio between measurements of the areal mass of water sorbed by the active layer (C_{H_2O}, g·cm^{-2}) and measurements of active layer thickness (δ, m). To obtain the corresponding water diffusion coefficients, Zhang *et al.* and Lee *et al.* calculated the values of D using Equation 2.2[8,9] which requires the active layer thickness as well. In fact, in the peer-reviewed literature, the diffusion coefficient of water within polyamide active layers has been obtained only through calculations based on Equation 2.2 and knowledge of the other variables in the equation, including thickness. This is due to the extreme difficulty in experimentally measuring the diffusion coefficient of water in the active layers as a result of the corresponding exceptionally small time scale of

diffusion (~10^{-5} s). Therefore, accurate measurements of active layer thickness are important not just in understanding the effect of thickness on membrane performance, but also in characterizing the partitioning and diffusion coefficients of water and solutes in the active layers and their effects on performance.

The active layer thickness of RO/NF membranes has been typically measured using several microscopy techniques, including scanning electron microscopy (SEM),[10] transmission electron microscopy (TEM)[10–13] and atomic force microscopy (AFM).[14,15] Thickness measurements with SEM and TEM are based on image analysis (typically eyeball estimates) of cross-section images of membrane active layers, with the scale of the images being no larger than a few micrometers.[10–13] AFM thickness measurements, which are much less common than SEM and TEM measurements, are obtained by analyzing topography profiles of thin strips of a membrane active layer isolated on a hard solid substrate, such as a silicon wafer.[14,15] The typical size of such polyamide thin strips is on the order of 30×30 μm^2.[14,15] One important drawback of thickness measurements using SEM, TEM or AFM is that the small size of active layers measured with the techniques could potentially result in thickness measurements unrepresentative of the membranes being studied, since studies in the literature have shown significant variability of physico-chemical properties (e.g, concentration of carboxylic group) at different locations on a membrane active layer even though the values measured for the properties were averaged on areas with size of a few square centimeters.[16] Also, measuring active layer thickness with SEM or TEM typically requires subjective judgment about the location of the interface between the active layer and the support layer, as the active layer cannot always be easily distinguished from the support layer shown in the cross-section images.

More recently, Rutherford backscattering spectrometry (RBS) has also been used to estimate active layer thickness.[8,10,17–20] The typical size of samples under study in RBS analyses is on the scale of several square centimeters,[8,10,17–20] which represents an improvement of several orders of magnitude over the area of analysis for SEM , TEM and AFM. In RBS, however, active layer thickness is calculated as the ratio between the active layer areal mass density (g cm^{-2}) obtained experimentally and literature values of active layer volumetric mass density.[10,17,20] Thus, an important drawback of RBS measurements of active layer thickness is that it does not directly measure thickness, but rather uses an assumption of the active layer volumetric mass density to calculate it. Unfortunately, experimental measurement of the volumetric mass density of polyamide active layers of RO/NF membranes has not been reported in the peer-reviewed literature, so researchers have relied on corresponding educated estimates.[8,21] This approach limits the accuracy of RBS estimates of active layer thickness to the accuracy of the assumption about the active layer volumetric mass density.

While these four techniques are the ones commonly found in the literature to measure thickness of the active layers of TFC membranes, and they all have significant drawbacks of different nature, no study reported in the peer-reviewed literature has compared thickness values measured with these techniques to conclude whether their measurements are in agreement or not. Therefore, there exists a need to compare thickness measurements for TFC membrane active layers with these four techniques and, if possible, to introduce new techniques as the existing methods have important drawbacks.

Three techniques that are reasonable candidates to measure active layer thickness are profilometry, ellipsometry and quartz crystal microbalance (QCM). Profilometry and ellipsometry are well-established techniques to measure the thickness of thin films[22–25]; however,

there has not been a study in the peer-reviewed literature that has used profilometry to estimate thickness of active layers for commercial RO and NF membranes. Similarly, I could find only one study[26] where ellipsometry was used to measure the active layer thickness of an NF membrane, but the same study indicated that ellipsometry could not be used with RO membranes because of their high surface roughness. While QCM has not been used to estimate active layer thickness, QCM provides the same information about the active layer (polymer areal mass, $g \cdot cm^{-2}$) that is extracted from RBS analyses to calculate active layer thickness, and therefore it should be possible to use QCM analyses to estimate active layer thickness.

Accordingly, the objectives of the work reported in this chapter were to: (i) compare various methods for measurement of active layer thickness of RO/NF membranes to identify which methods provide consistent thickness measurements, and (ii) evaluate the use of QCM, profilometry and ellipsometry as analytical techniques for measurement of the thickness of active layers of RO/NF membranes. The measurements were performed under the premise that consistent results among different techniques working under different physical principles would suggest that the techniques provide accurate thickness measurements. Six commercially available membranes, including NF, brackish water RO and seawater RO membranes, from two major manufacturers were studied, and seven analytical techniques, including SEM, TEM, AFM, RBS, QCM, profilometry and ellipsometry, were used. I present and compare the active layer thickness results obtained for each membrane with each analytical technique, identify which techniques provide consistent (and inconsistent) results among each other, and discuss the advantages and limitations of each method. I also present a thorough description of the experimental methods and data analysis used with each analytical technique, in particular for the

QCM, profilometry and ellipsometry methods which have not been commonly used for determining the thickness of the active layers of RO/NF membranes.

2.2. Materials and Methods

2.2.1. Target membranes

Six TFC membranes were used in this study: NF90, XLE, NF270 and SW30HR (DOW FILMTEC, Minneapolis, MN) and ESPA3 and SWC4+ (Hydranautics, Oceanside, CA). The membranes cover a broad range of performance, with NF90 and NF270 being NF membranes, XLE and ESPA3 being brackish water RO membranes, and SW30HR and SWC4+ being seawater RO membranes. Attenuated total reflectance Fourier transform infrared spectroscopy (ATR-FTIR) analyses in earlier studies[27,28] indicated that the NF270 membrane has a semi-aromatic poly(piperazine amide) active layer, and the other five membranes all have fully-aromatic polyamide active layers. The active layer of the SW30HR membrane also has a coating likely consisting of poly(vinyl alcohol).[27,28] Because the membranes studied are used for a wide range of applications and contain three commonly used materials for TFC membrane active layers (i.e., fully-aromatic polyamide, semi-aromatic poly(piperazine amide), and poly(vinyl alcohol)), conclusions drawn in this study can be applied to most commercial TFC membranes.

2.2.2. Membrane sample preparation for active layer thickness measurements

Membrane coupons having a size of 2.5 ×5 cm^2 were cut from flat sheets obtained from the manufacturers and were thoroughly rinsed with and stored in ultrapure water (>18 MΩ·cm) before further sample preparation. For SEM analyses, membrane coupons were cracked in air after immersion in liquid nitrogen and coated with a thin film (<5 nm) of Au (60%):Pd (40%). For TEM analyses, membrane coupons were dried between two filter papers by applying fingertip pressure, further dehydrated with ethanol (Fisher Scientific, Pittsburgh, PA), embedded with LR White resin (London Resin Co, Reading, UK) and cut into thin slices (~90-100 nm)

with a Sorvall MT 6000 Ultramicrotome (RMC Co., Tucson, AR). For RBS analyses, membrane coupons were dried between two filter papers by applying fingertip pressure. For AFM and profilometry analyses, active layers were isolated onto silicon wafers and then gently scratched to obtain thin strips of the active layer polymer. For QCM and ellipsometry analyses, active layers were isolated onto QCM crystal sensors and silicon wafers, respectively. The active layer isolation procedure is similar to that described by Perry and Coronell.[29] with slight modifications. In this study, after peeling off the polyester backing layer by hand and placing the polyamide-polysulfone composite on a silicon wafer substrate (with the active layer facing the wafer), the composite and the substrate were secured to each other using a customized stainless steel frame with an open window that allowed access to the polysulfone support. Then, Dimethylformamide (DMF) was gently added through the open window in a dropwise manner onto the sample, the DMF-polysulfone solution was discarded after 1 min, and the cycle of addition and discarding of DMF was repeated 15 times. By then, the sample showed a smooth surface by visual inspection. To further remove any polysulfone that might have not been dissolved by that time, the sample was air dried overnight and then dipped in fresh DMF for 4 h and air dried overnight again. At last, the sample was rinsed with ultrapure water and gently dried with nitrogen gas. This active layer isolation procedure has been proven not to alter the membrane active layer physico-chemical properties and provide isolated active layers free of polysulfone.[29]

2.2.3. SEM analyses

An FEI Helios 600 Nanolab Dual Beam System (FEI, Hillsboro, OR) was used to obtain SEM images of membrane cross-sections. Three images were taken for each membrane at magnifications of 40,000×, 60,000× or 80,000× depending on the active layer thickness. Each

SEM image was analyzed with the software ImageJ 1.47v[30] to obtain the area and length of the active layer in the corresponding cross section. The typical length of active layer observed in the images obtained was in the 1.5-3 μm range. The thickness was then calculated as the ratio between the area and length of the active layer cross section.

2.2.4. TEM analyses

A JEOL 100CX II TEM (JEOL USA, Peabody, MA) was used to obtain dark-field TEM images of membrane cross sections at an acceleration voltage of 80 kV. Three images were taken for each membrane at magnifications of 29,000× or 72,000× depending on the active layer thickness. Each TEM image was analyzed in the same manner as the SEM images with the software ImageJ 1.47v[30] to determine the thickness of the active layer in the corresponding cross section. The typical length of active layer observed in the images obtained was in the 1.5-4 μm range.

2.2.5. AFM analyses

AFM imaging was performed with an Asylum Research MFP-3D AFM (Santa Barbara, CA) equipped with Tap300Al tips from BudgetSensors (Sofia, Bulgaria). For measuring active layer thickness, a procedure similar to that described by Freger[14] was used. Briefly, topography profiles of thin strips of active layers were measured by scanning the AFM tip in tapping mode across the sample surface, and the average thickness was calculated as the difference in the average height of the polyamide surface and the average height of the silicon wafer surface. Three samples were analyzed for each membrane, and three locations on each sample were analyzed with a scanning size of 30×30 μm^2 for each location. AFM analyses was also used to characterize membrane surface roughness using samples prepared in the same manner as samples for RBS analyses (i.e., membrane coupons dried between two filter papers). For measuring

surface roughness, membrane surface topography of each sample was obtained by scanning the AFM tip in tapping mode over the sample surface, and the root-mean-square roughness was calculated from the surface topography profile as described by Kwak *et al.*[31] Three samples were analyzed for each membrane with a scanning size of 10×10 μm^2 for each sample.

2.2.6. RBS analyses

RBS spectra were acquired with a tandem Van de Graaff accelerator (High Voltage Engineering Corporation, Burlington, MA) and the semi-automatic target system described by Attayek *et al.*[32] A 2-MeV He^{2+} beam at incident, exit and scattering angles of 22.5 °, 42.5 ° and 160 °, respectively, was used. To avoid possible damage of the membranes by the helium beam, the fluence of helium ions was kept below 1×10^{14} He^{2+} cm^{-2}.[33] The commercial software SIMNRA 6.06v[34] was used to simulate RBS spectra and obtain the elemental composition and atomic areal density (atoms cm^{-2}) of membrane active layers, which were used to calculate the thickness of the membrane active layers as described in Section 2.3.3. Two samples of each membrane, with each sample having an analysis area of 2.5×5.0 cm^2, were analyzed by RBS.

2.2.7. QCM analyses

Areal mass (g cm^{-2}) of isolated active layers was measured with a Q-Sense E4 QCM (Biolin Scientific, Lithicum Heights, MD) in the manner described by Perry *et al.*[29] In brief, for each sample of isolated active layer, a blank QCM sensor was tested for its vibration frequency, then coated with the isolated active layer, and tested again in QCM for its new vibration frequency. The areal mass of the isolated active layer was then obtained from the change in the vibration frequency of the sensor as described by the Sauerbrey equation (see Section 2.3.3). During each QCM test, a control sensor (a blank QCM sensor) was also tested in parallel to account for experimental uncertainties caused by minor differences in the placement of sensors in the microbalance chamber between runs, and the change in frequency of the control sensor

was subtracted from the frequency change of the sample in the calculation of the areal mass of the active layer. The thickness of active layers was calculated as the ratio between the measured areal mass and an estimate of the volumetric mass density (1.24 g cm^{-3}) of the active layers obtained from the literature.[8] Two samples, each having 1.54 cm^2 in area, were tested for each membrane at a temperature of 22 $\pm$0.02 ℃.

2.2.8. Profilometry analyses

A P-6 Stylus Profiler (KLA Tencor, Milpitas, CA) was used for profilometry analyses of active layers isolated on silicon wafers. The tip of the profiler had a radius of 5 μm and a cone angle of 60 °. Topography profiles of thin strips of active layers were obtained at a scanning speed of 20 μm s and a force of 2 mg, and were used for the calculation of active layer thickness as the difference in the average height of the polyamide surface and the average height of the silicon wafer surface. Three samples were analyzed for each membrane, and three locations on each sample were analyzed. The typical length of active layer scanned during the experiments was in the 100-300 μm range.

2.2.9. Ellipsometry analyses

Ellipsometry spectra were obtained with a J.A. Woollam variable angle spectroscopic ellipsometer (J.A. Woollam Co., Lincoln, NE) at incidence angles of 65 °, 70 °and 75 °and wavelength range of 380-1000 nm using the AutoRetarder feature. Ellipsometry measures the phase change (Δ) and the amplitude change (Ψ) of a light beam upon reflection off the sample under study as a function of light wavelength and incidence angle. Such information is then used for fitting simulations from a model of the samples with adjustable parameters. The model used to simulate the samples consists of a base layer of silicon with 1 mm thickness to represent the silicon substrate of the sample, an intermediate layer of silicon dioxide with a thickness of 2

nm[35] and a top thin polymer layer that represents the isolated active layers of RO/NF membranes. The Cauchy dispersion formula[36] was used to describe the optical properties of the active layers. Optical constants of the silicon layer and silicon dioxide layer are available in the database of the WVASE® software (J.A. Woollam Co.) used for ellipsometry data analyses. The adjustable parameters in this study were the refractive index and the thickness[37] of the Cauchy layer (active layer). The parameter values were changed until the mean squared error between simulated and experimental Δ and Ψ values was less than 20. Three samples were analyzed for each membrane with three locations (0.3 cm^2 each location) analyzed for each sample.

2.3. Results and Discussion

2.3.1. Thickness measurements with SEM and TEM

Both SEM and TEM measurements of active layer thickness are based on microscopy imaging of the cross sections of membrane active layers. Figure 2.1 shows representative SEM and TEM images of active layer cross sections of the SWC4+ membrane (polyester backing was not in the imaging field). From both images in Figure 2.1, the ridge-and-valley structure that is commonly reported[4] for RO/NF membrane active layers can be observed, and was outlined in red. The images also show that the surface of the active layer has relatively high roughness, which is consistent with the roughness measurements obtained by AFM discussed later in this section and the relatively high roughness reported for polyamide active layers in the literature.[38–40] The SEM and TEM images of all other membranes showed similar ridge-and-valley structures and high roughness of active layer surface.

From the SEM image in Figure 2.1(a), the active layer can be distinguished from the support layer by subjective judgment based on the visual difference in the appearance of the two layers. For the case of the image in Figure 2.1(a), the boundary between active and support layer

was determined to be the region where there seems to be a change in the morphology of the polymer layers. Similarly, from the TEM image in Figure 2.1(b), the active layer can be distinguished by a subjective judgment based on the slightly different colors of the active layer and the support layer, as the active layer appears darker than the support layer.

The software ImageJ 1.47v[30] was used to obtain the area and the length of the active layer cross section in each image obtained for each membrane. The active layer thickness was then calculated as the ratio between the area and the length of the active layer. The thickness values for the active layers of NF270, NF90, XLE, ESPA3, SWC4+ and SW30HR membranes obtained from SEM analyses were 56.5 ±1.8 nm, 183.6 ±22.9 nm, 185.8 ±27.0 nm, 155.4 ±24.2 nm, 199.9 ±43.5 nm and 165.4 ±22.2 nm, respectively, and the thickness values obtained from TEM analyses were 103.9 ±22.6 nm, 229.9 ±30.8 nm, 238.3 ±31.1 nm, 155.4 ±22.9 nm, 340.0 ±55.4 nm and 168.9 ±14.3 nm, respectively. The relative standard deviations of the SEM thickness results are in the 3.2-21.8% range with an average of 13.5%, and the relative standard deviation of the TEM thickness results are in the 8.5-21.8% range with an average of 14.6%.

Using SEM or TEM as analytical techniques for measuring thickness of active layers of RO/NF membranes have several advantages and disadvantages that have been summarized in Table 2.1. As described in Section 2.2.2, neither SEM nor TEM requires active layer isolation

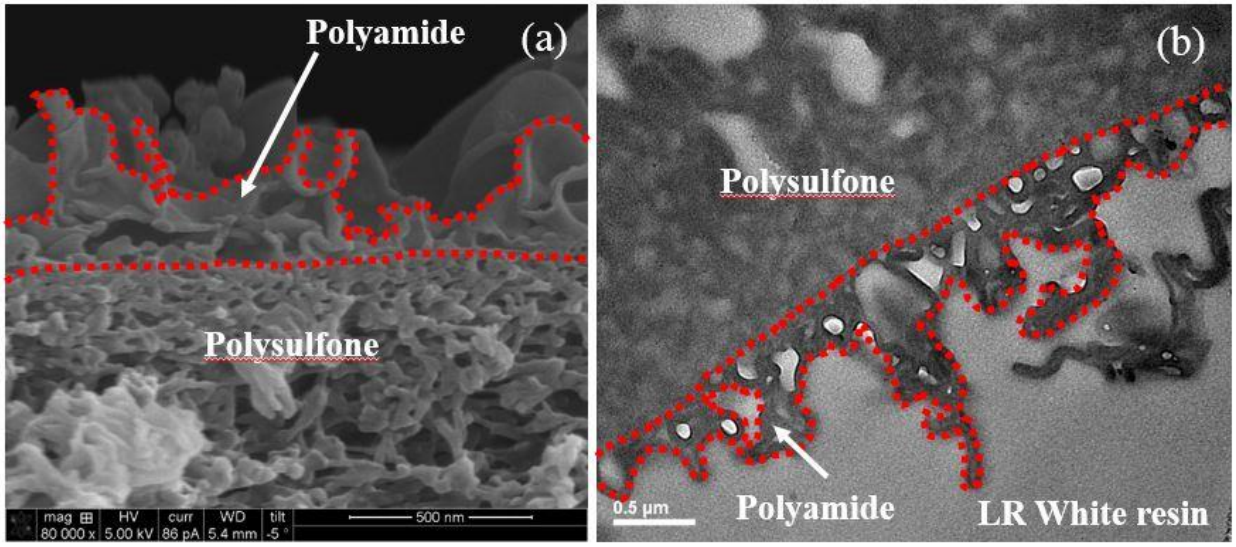

Figure 2.1. Representative (a) SEM and (b) bright-field TEM images of the cross section of a SWC4+ membrane sample. In both images, the active layers are outlined in red. The SEM and TEM images do not correspond to the same cross section.

for sample preparation, i.e., both techniques use full membrane samples instead of isolated active layer samples for analyses. Using full membrane samples avoids any potential deterioration of the active layer that can possibly be caused by the active layer isolation process. Also, preparing the samples for SEM or TEM is a much easier procedure compared to active layer isolation, and thus, requires much less overall effort to obtain the active layer thickness. Additionally, analyzing membrane samples in SEM or TEM is not very time consuming (≈1 min per sample for SEM and ≈0.5 min per sample for TEM) compared to other methods. Other advantages of using SEM and TEM for measuring active layer thickness include that instruments for both techniques are readily available in many research facilities due to their wide use in other research fields, that the measurement of thickness is a direct measurement and does not require any important assumptions about the property of active layer, and that both techniques provide visual images of the active layers that show the structure of the active layer and such provide more information about the active layer than other methods that do not provide visual observations.

A major disadvantage of measuring active layer thickness using SEM or TEM is that the size of samples being analyzed is only on the micrometer scale (see Figure 2.1). This small characterization scale could potentially result in unrepresentative values of active layer thickness, especially given the rough nature of polyamide active layers. For example, the surface roughness measured using AFM and active layer roughness-to-thickness ratio calculated using the thickness measured with TEM were 7.5 ±0.6 nm and 7.2 ±1.7% for NF270, 103.7 ±38.1 nm and 45.1 ±17.6% for NF90, 63.5 ±11.4 nm and 26.6 ±5.9% for XLE, 102.4 ±5.5 nm and 65.9 ±10.4% for ESPA3, 125.3 ±6.6 nm and 36.8 ±6.3% for SWC4+ and 79.8 ±1.6 nm and 47.2 ±4.1% for SW30HR. These values indicate that surface roughness can be as large as more than 60% of the active layer thickness, or in other words, as observed in Figure 2.1, that acti

Table 2.1. Advantages and disadvantages of SEM, TEM, AFM, profilometry, RBS, QCM and ellipsometry as analytical techniques for the measurement of active layer thickness of RO/NF membranes.

Techniques	SEM	TEM	AFM	Profilometry	RBS	QCM	Ellipsometry
Size of samples	µm	µm	hundred μm^2	hundred µm	cm^2	cm^2	cm^2
Assumption required	None	None	None	None	Yes[a]	Yes[a]	None
Subjective judgment required	Yes[b]	Yes[b]	No	No	No	No	No
Relative standard deviation	High	High	High	High	Low	Low	Low
Direct measurement	Yes	Yes	Yes	Yes	No[c]	No[d]	No[e]
Active layer isolation required	No	No	Yes	Yes	No	Yes	Yes
Sample preparation	Medium	Medium	Very hard	Very hard	Easy	Hard	Hard
Sample analysis	Easy	Easy	Hard	Easy	Hard	Medium	Easy
Availability of equipment	Easy	Easy	Easy	Easy	Hard	Medium	Medium
Visual Method	Yes	Yes	Yes	No	No	No	No

[a] Volumetric mass density of active layer

[b] Location of boundary between active layer and support layer

[c] Measures atomic areal density

[d] Measures mass areal density

[e] Measures phase change and amplitude change of light beam

layer thickness can vary by as much as 60% in the span of fractions of a micron. Another significant disadvantage of the SEM and TEM techniques for measuring thickness of membrane active layers is the requirement of subjective judgment in data analysis. As previously described in this section, distinguishing the active layer from the support layer in SEM or TEM images requires subjective judgment of the location of the interface between active layer and support layer based on visual observation of the images. Such subjective judgment could easily introduce error to the data analysis results, as well as lead to low consistency of results among different measurements or different researchers for the same membrane. In fact, the high relative standard deviations of SEM and TEM results shown earlier in this section provide evidence for the low consistency among measurements by both techniques.

2.3.2. Thickness measurements with AFM and profilometry

Both AFM and profilometry measurements of active layer thickness of RO/NF membranes are based on obtaining height profiles of the isolated active layer surface, therefore they share many similarities in terms of sample preparation, data analysis, advantages and disadvantages. Figure 2.2(a) shows a representative AFM image of the surface of a thin strip of the active layer of the NF90 membrane, and Figure 2.2(b) shows the corresponding topography profile of the active layer surface and the silicon substrate surface. The AFM image in Figure 2.2(a) shows the typical ridge-and-valley structure of RO/NF membrane active layers,[4] with brighter areas indicating the ridges (i.e., protrusions) and darker areas indicating the valleys (i.e., depressions). Each average height value at a specific *x*-axis location in Figure 2.2(b) was calculated as the average *z*-axis (height) value in Figure 2.2(a) for all corresponding *y*-axis locations within the data analysis region. The data analysis region along the *y*-axis direction is delimited by the two white dashed lines in Figure 2.2(a) and was chosen as an area without imaging imperfections as determined by visual observation of the image. Imaging imperfections

are observable discontinuities on the images caused by the high roughness of the active layer surface. This high roughness sometimes leads to sudden changes of the AFM tip movement when scanning the sample surface and is observed in the AFM image as the imperfections indicated by arrows in Figure 2.2(a).

Figure 2.3 shows a representative height profile of a thin strip of the active layer of the SW30HR membrane obtained by profilometry. The height profile was obtained along a single line on the sample surface (as opposed to over an area as it was the case with AFM analyses). Even though the height profiles in Figure 2.3 (profilometry) and Figure 2.2(b) (AFM) look similar, they are very different in nature. While in Figure 2.3 (profilometry), the height value for a given *x*-axis location corresponds to the height at a single *y*-axis location (i.e., where the active layer surface corresponds to the *x*-*y* plane), in Figure 2.2(b) (AFM) the average height value for a given *x*-axis location corresponds to the average of the height values for a range of y-axis locations.

The height profiles in Figure 2.2(b) and Figure 2.3 were used to obtain the active layer thickness, which was calculated as the difference in the average height of the active layer surface and the average height of the silicon substrate. For each calculation, the portions of the height profile that were very close (within 3 μm) to the edge of the thin strip of the active layer were not included in the calculation of the thickness to avoid any possible artifacts related to damage of the active layer caused by the scratching step in sample preparation (see Section 2.2.2). For NF270, NF90, XLE, ESPA3, SWC4+ and SW30HR membranes, the active layer thickness results obtained by AFM analyses were 20.5 ±8.1 nm, 119.9 ±12.9 nm, 136.1 ±22.8 nm, 76.1 ±12.0 nm, 113.0 ±14.2 nm and 176.3 ±24.5 nm, respectively, and the corresponding results obtained by

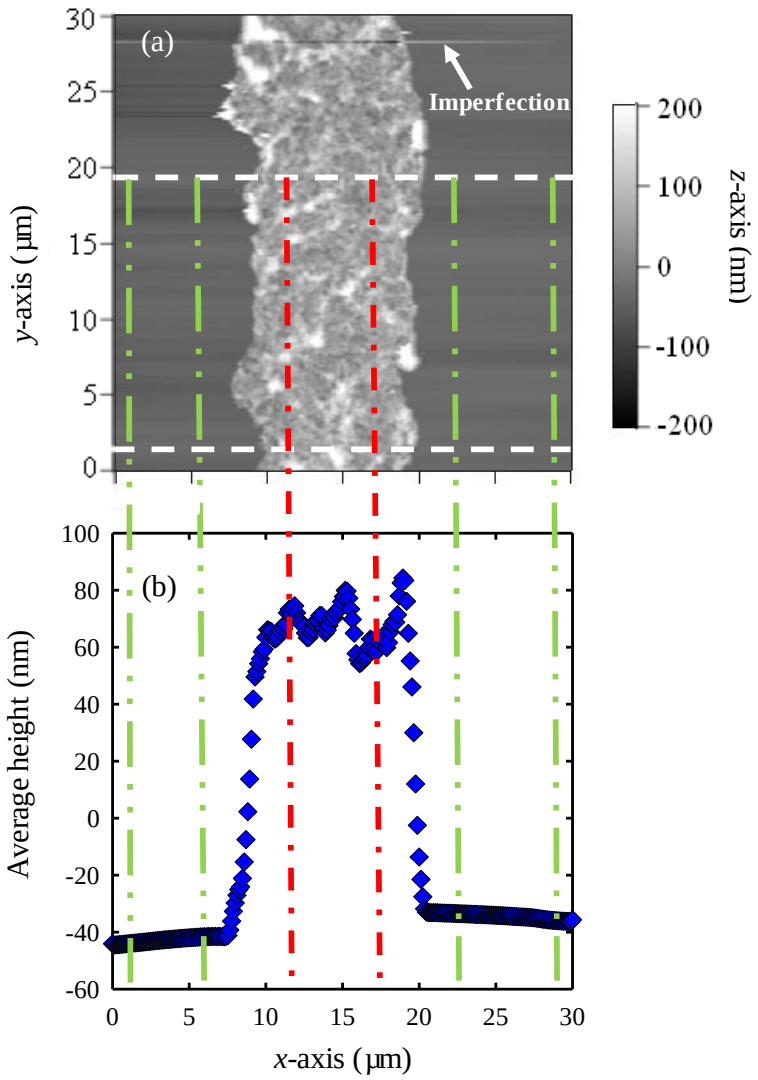

Figure 2.2. (a) An AFM image and (b) the corresponding average height profile of an NF90 membrane. At each specific *x*-axis location, the average height data in (b) was calculated as the average of height for all locations in (a) with the same *x*-axis value and different *y*-axis values between the two white dashed lines. The average height of the active layer was calculated as the mean of the height values in (b) between the two red dash-dotted lines. The average height of the silicon substrate was calculated as the mean of the height values in (b) between the two (green) long-dashed lines on the left and on the right. The active layer thickness was calculated as the difference between the average height of the active layer and the average height of the silicon substrate. The average thickness of the active layer for this sample was 110.3±16.3 nm. Imaging imperfections are observable discontinuities on the images caused by the high roughness of the active layer surface.

profilometry analyses were 14.4±4.7 nm, 124.4±7.6 nm, 129.3±10.9 nm, 88.5±5.0 nm, 112.1±14.9 nm and 175.8±23.3 nm, respectively. The relative standard deviations of the AFM thickness results were in the 10.8-39.5% range with an average of 18.2%, and the relative standard deviations of the profilometry thickness results were in the 5.7-32.7% range with an average of 13.2%.

Table 2.1 summarizes several advantages that AFM and profilometry have as analytical techniques for the measurement of active layer thickness. Like SEM and TEM, AFM and profilometry are analytical techniques that are used in a broad range of applications, and therefore the instruments are readily available to many researchers. Also, both AFM and profilometry provide direct measurement of active layer thickness without the requirement of any assumptions. Also, in contrast to SEM and TEM, measuring thickness with AFM or profilometry has the advantage of not requiring subjective judgment of the location of the interface between the active layer and the support layer. In addition to these advantages shared by both AFM and profilometry, AFM analysis also has the advantage that its analysis region corresponds to a surface area (as opposed to a cross section or line as for SEM, TEM and profilometry), and profilometry has the advantage of easy and fast data collection for each measurement (≈1 min per sample).

The disadvantages of thickness measurement with AFM and profilometry are summarized in Table 2.1. As described in Section 2.2.2, the sample preparation procedure for both techniques requires active layer isolation and scratching the isolated active layer into thin strips. This sample preparation procedure is both complex and time consuming, and could potentially result in damage of the active layer in the scratching step, which could introduce error to the thickness results. It is also possible that the polysulfone support may not be fully

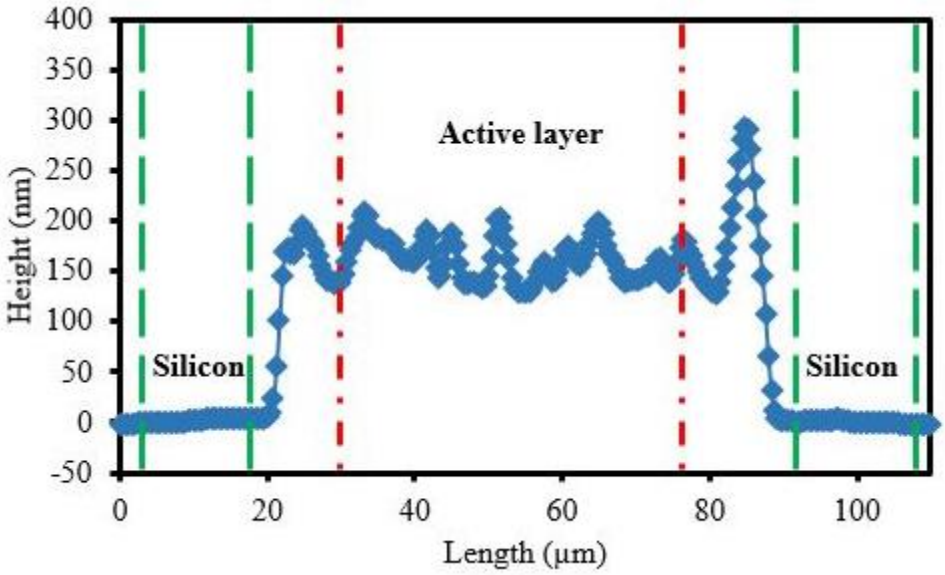

Figure 2.3. Representative profilometry height profile of an SW30HR active layer strip on a silicon wafer. The average height of the active layer (162.2±20.5 nm) was calculated as the mean height in the 30-76 µm range on the *x*-axis as indicated by the red dash-dotted lines. The average height of the silicon wafer (1.3±1.9 nm) was calculated as the mean height in the 3-17 µm and 92-108 µm ranges on the *x*-axis as indicated by the green dashed lines. Data near the edge of the active layer strip (17-30 µm and 76-92 µm) were not used to avoid any potential confounding edge effects. Active layer thickness (161.0±20.6 nm) was calculated as the difference between the polymer height and the substrate height.

dissolved and removed during the sample preparation process which could result in an overestimation of active layer thickness with AFM and profilometry. AFM and profilometry also share a disadvantage that SEM and TEM measurements have, which is that the sizes of the samples under analyses are very small ($< 30 \times 30\ \mu m^2$ for AFM and ~200 μm for profilometry). As discussed in Section 2.1, the small measurement scale could lead to thickness results that are unrepresentative of the membrane active layers. The small measurement scale is one possible cause of the relatively high relative standard deviations from AFM and profilometry thickness measurements which indicate low consistency of thickness measurements for each of these two techniques.

An additional disadvantage of AFM analysis for active layer measurements is that it is time consuming as it is often not an easy task to find a strip of active layer that is thin enough to be analyzed within the small measurement scale and big enough for data analysis after discarding the portions that are very close to the edge of the strip. Also, as mentioned above, imaging imperfections exist in AFM analyses due to the high roughness of the active layer surface, and therefore, the experimenter needs to scan multiple regions of the sample under study in order to obtain an image without excessive imaging imperfections. A disadvantage mostly associated with profilometry analysis is that there are intrinsic limitations to the accuracy of the data collected related to the dimensions of the tips used on the profiler. In this study, while the tip used for AFM analyses had a radius of less than 10 nm which is likely capable of accurately following the sample topography, the tip for profilometry analyses had a radius of 5 μm which may not be able to do so (the typical radius of tips available for the profiler is in the range of 2-25 μm, but the 5 μm tip was found to provide results consistent with AFM analysis). One must note, however, that the topography profiles obtained with AFM and profilometry for active layer

measurements are those of the backside of the active layer which has been reported to be much flatter than the active layer surface,[41] and therefore, the tip size may not be a problem. For cases in which the tip of the profiler does not reach the bottom of depressions in the sample surface, the active layer thickness would be overestimated. Countering this potential artifact, in this study, the tip of the profiler pressed the active layer surface of the samples under study at a force of 2 mg, which could potentially result in underestimation of the active layer thickness. Given that AFM and profilometry thickness results were within 0.2-30.1% of each other, it appears that these two potential disadvantages of profilometry measurements (i.e., over estimation of thickness due to large tip radius and underestimation due to force applied on sample) approximately canceled each other out.

2.3.3. Thickness measurements with RBS and QCM

Active layer thickness estimates with RBS and QCM are based on measurements of the areal mass of the active layers. Figure 2.4 shows representative experimental and simulated RBS spectra of the XLE membrane and its polysulfone support. RBS has a depth of analysis of a few micrometers and therefore the RBS spectra of TFC membranes is generated by signals from the polyamide active layer and from its polysulfone support only (not from the polyester backing). As Figure 2.4 shows, the RBS spectra of the TFC membrane and polysulfone support differ by the presence of a nitrogen peak and shift to lower energies of the onset of the sulfur plateau in the TFC membrane spectrum; these two features are caused by the presence of the active layer and are used during data analysis to determine the active layer thickness. The nitrogen peak appears only in the spectrum of the TFC membrane because the nitrogen element only exists in the polyamide active layer but not in the polysulfone support; therefore, the width of the nitrogen peak is directly related to the thickness of the active layer. The onset of the sulfur plateau recedes to lower energies in the spectrum of the TFC membrane because the analysis beam (i.e.,

He^{2+} particles) loses energy traversing the active layer on its way to and from the polysulfone layer (where sulfur exists); therefore, the degree of recession of the onset of the sulfur plateau shift is directly related to the thickness of the active layer. To analyze the RBS spectra, the elemental composition of the polysulfone support ($C_{0.500}H_{0.409}O_{0.072}S_{0.019}$) was obtained by fitting the RBS simulation of the polysulfone support to its experimental spectrum. The polysulfone support composition was then used as the substrate layer in the simulation of the spectrum of the TFC membranes (featuring the nitrogen peak and receded sulfur plateau). For the case of the XLE membrane in Figure 2.4, an elemental composition of $C_{0.500}H_{0.334}O_{0.083}N_{0.083}$ and atomic areal density of 1.15×10^{18} atoms cm^{-2} were obtained for its polyamide active layer.

In the analyses of the elemental composition, RBS spectra do not have a hydrogen signal because RBS cannot detect elements in the sample under study that are lighter than the He^{2+} particles of the analysis beam. Therefore, to obtain the elemental compositions of the polysulfone support and active layers of membrane samples, H:C ratios were assumed to be consistent with the theoretical compositions of the polymers involved as given by: 0.82 for the polysulfone support, consistent with the theoretical composition of polysulfone ($C_{27}H_{22}O_4S$);[18] 1.0 for the active layer of NF270 membrane, consistent with the theoretical composition of poly(piperazine amide) (C_5H_5ON);[28] 0.67 for the active layers of the NF90, XLE, ESPA3, SWC4+ and SW30HR membranes, consistent with the theoretical composition of fully aromatic polyamide ($C_{36}H_{24}O_6N_6$);[10] and 2.0 for the coating layer of the SW30HR membrane, consistent with a theoretical composition C_2H_4O.

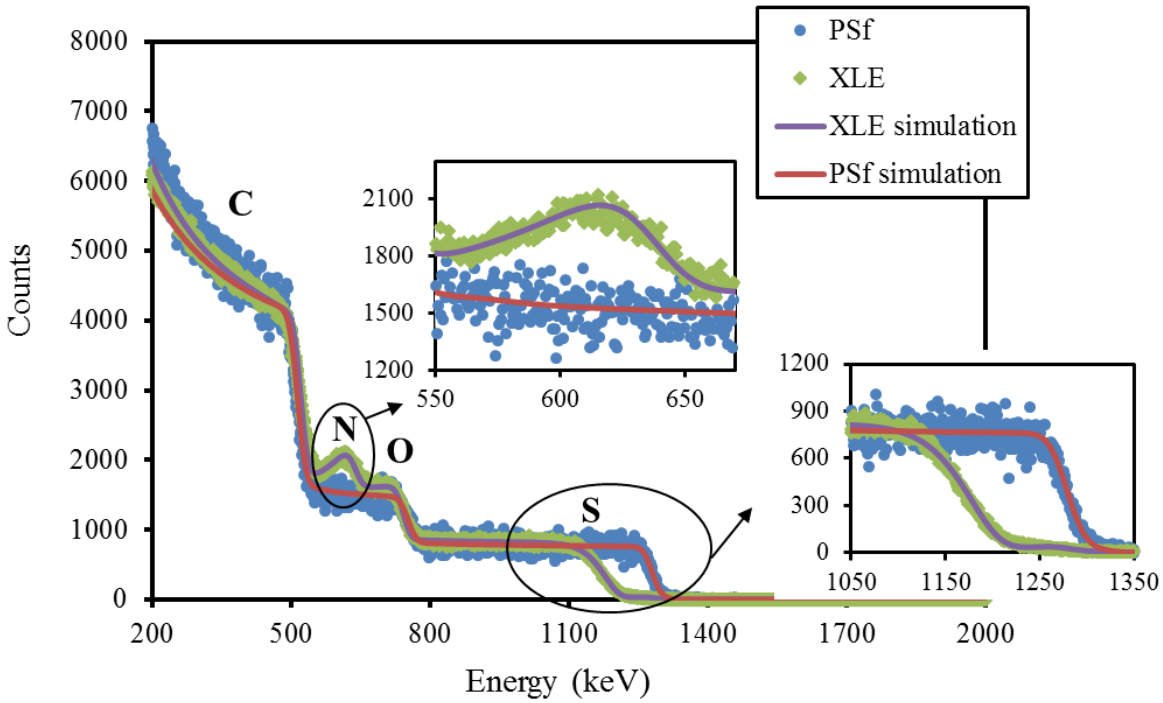

Figure 2.4. Representative RBS experimental data (symbols) and corresponding simulations (lines) for the polysulfone support (blue circles) and the XLE membrane (green diamonds). The polysulfone support contains H, C, O and S and the active layer contains H, C, N and O. The N and S signals are enlarged to show the differences between the spectrum of the support layer and the spectrum of the full polyamide membrane. The atomic areal density of the polyamide active layer obtained from the XLE spectrum in the figure is 1.15×10^{18} atoms cm^{-2} and the corresponding thickness is 135.9 nm.

For any given membrane, the atomic areal density and elemental composition of the active layer were used to obtain the areal mass density (g cm^{-2}) of the active layer as given by

$$m_{AL-RBS} = \frac{MW_{AL} N_{areal}}{L_A}, \quad (2.5)$$

where m_{AL-RBS} is the areal mass density (g cm^{-2}) and N_{areal} is the atomic areal density (atoms cm^{-2}) of membrane active layer obtained by RBS analysis, L_A=6.022 ×10^{23} atoms mol^{-1} is the Avogadro's number and MW_{AL} (g mol^{-1}) is the average molecular weight of the active layer calculated using

$$MW_{AL} = \sum MW_i \, x_i, \quad (2.6)$$

where MW_i is the molecular weight of element i in the active layer and x_i is the elemental ratio of element i in the active layer obtained by RBS analysis. The thickness of active layers was then calculated as the ratio between the mass areal density and the volumetric mass density (1.24 g cm^{-3})[8] of the active layer. The thickness values obtained by RBS analyses for the NF270, NF90, XLE, ESPA3, SWC4+ and SW30HR membranes were 15.7 ±1.5 nm, 142.4 ±1.7 nm, 130.0 ±8.4 nm, 94.5 ±3.3 nm, 106.5 ±2.0 nm and 166.3 ±4.2 nm, respectively, and their relative standard deviations were in the range of 1.2-9.6% with an average of 4.2%.

Representative results of QCM tests are shown in Figure 2.5 for a QCM sensor with isolated active layer of the XLE membrane and a corresponding control sensor. In a complete QCM analysis in this study, a control QCM sensor and a test bare QCM sensor were first tested three times for their vibration frequencies, $f_{control-before}$ and $f_{test-before}$, respectively. The bare test sensor was then used as the substrate onto which to isolate a membrane active layer as described in Section 4.2.2. Finally, the control sensor and the active layer loaded test sensor were tested in the QCM three times for their vibration frequencies, $f_{control-after}$ and $f_{test-after}$, respectively. The difference between $f_{control-before}$ and $f_{control-after}$ was experimental

uncertainty caused by minor difference in the placement of sensors in the microbalance chamber between runs, and the difference between $f_{test-before}$ and $f_{test-after}$ was caused by minor difference in the placement of sensors between runs and the isolated active layer. Therefore, the net change in vibration frequency of the test sensor due to only the isolated active layer was calculated as

$$\Delta f = \left(f_{test-after} - f_{test-before}\right) - \left(f_{control-after} - f_{control-before}\right). \quad (2.7)$$

The areal mass of the active layer (m_{AL-QCM}, g·cm^{-2}) isolated on the test sensor was related to Δf using the Sauerbrey equation[42] as given by

$$m_{AL-QCM} = -\frac{C}{n}\Delta f, \quad (2.8)$$

where C (ng·cm^{-2}·Hz^{-1}) is the mass sensitivity constant of the QCM, n (-) is the overtone number. In this study, C=17.7 ng·cm^{-2}·Hz^{-1}, and n=3.

The thickness of the active layer isolated on the test sensor was then calculated as the ratio between m_{AL-QCM} and the volumetric mass density (1.24 g·cm^{-3})[8] of the active layer. The active layer thickness values obtained with QCM analyses for the NF270, NF90, XLE, ESPA3, SWC4+ and SW30HR membranes were 17.2±4.5 nm, 139.2±1.0 nm, 113.4±8.6 nm, 111.0±7.4 nm, 108.2±12.8 nm and 149.7±6.8 nm, respectively, and their relative standard deviations were in the range of 0.7-26.1% with an average of 9.6%.

Table 2.1 summarizes the advantages and disadvantages of RBS and QCM as analytical techniques to measure active layer thickness. Regarding measuring the active layer thickness of RO/NF membranes, RBS and QCM have a significant advantage over the four methods discussed above in Sections 2.3.1 and 2.3.2, in that the size of the active layer analysis region is on the square centimeter scale (2.5×5.0 cm^2 for RBS as shown in Section 2.2.6 and 1.54 cm^2 for

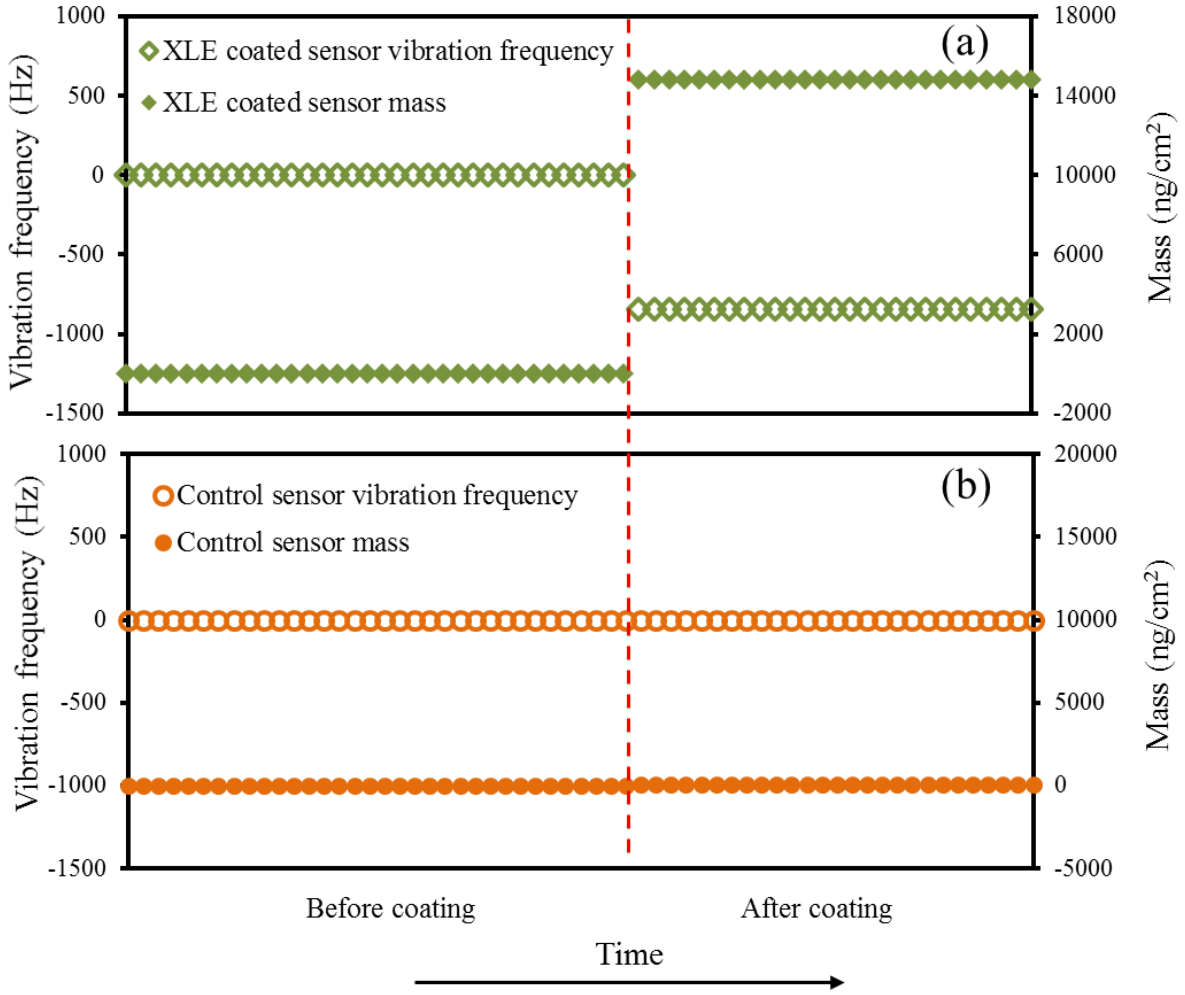

Figure 2.5. Representative vibration frequency and calculated areal mass change of (a) a QCM test sensor before and after coating with the active layer of a XLE membrane sample, and (a) a QCM control sensor. The vibration frequency of the test sensor declined 843.9 Hz after coating with the XLE active layer, which indicates an addition of 14,801 ng cm^{-2} to the areal mass of the sensor. The vibration frequency of the control sensor decreased 3.9 Hz in the second run compared to in the first run, which corresponds to an estimated uncertainty of 68 ng cm^{-2} (<0.5%) in the areal mass measurements. This areal mass variability is likely to be caused by minor differences in the placement of the sensor in the microbalance chamber between runs.

QCM as shown in Section 2.2.7, with RBS being able to analyze even larger samples of up to tens of square centimeters). Since the scale of analysis of RBS and QCM are about 3-5 orders of magnitude larger than the scale of analysis of SEM, TEM, AFM and profilometry, the thickness results obtained from RBS and QCM are more likely to be representative values of the actual active layer thickness of RO/NF membranes (see also discussion in Section 2.3.1). The low relative standard deviations of the thickness values obtained with each RBS and QCM also support that their large measurement scales provide more representative results. Another advantage that RBS and QCM analyses share is that no subjective judgment is required in calculating active layer thickness from RBS or QCM experimental data. Besides these advantages shared with QCM, RBS analyses also have the advantage of using full membrane samples instead of isolated active layers for thickness measurement and very easy sample preparation.

A major disadvantage of RBS and QCM analyses is that they both provide information about the areal mass of membrane active layers instead of the thickness of membrane active layers. To calculate the active layer thickness, one then requires an assumption about the value of the volumetric mass density of the active layer. However, the volumetric mass density of the active layers of commercial RO/NF membranes has not been experimentally quantified in the peer-reviewed literature. A wet density value of 1.38 g $\cdot$cm^{-3} with 23 wt% water absorption[21] has been used in the literature when active layer densities were needed for RO/NF membranes with polyamide active layers; however, this value was claimed to have been obtained through private communication with Dow Filmtec for the FT-30 membrane without details provided on the experiments that were used to acquire it. More recently, Zhang *et al.*[8] calculated the dry active layer density for RO membranes as 1.24 g $\cdot$cm^{-3} using the 1.38 g $\cdot$cm^{-3} value available in the

literature for the wet active layer density and a measured water absorption value of 11.2 wt% by the active layer. The accuracy of the assumption about active layer density is a significant constraint on the accuracy of the active layer thickness obtained with RBS or QCM analyses, since the uncertainty in the volumetric mass density value directly propagates as an uncertainty in the calculated active layer thickness value. Another disadvantage that RBS and QCM analyses share is that the data collection process for both tests are very time consuming and require significant amount of training (particularly for RBS analyses). Besides the above discussed shared disadvantages, RBS experiments require a Van de Graaff accelerator to which access may be limited and expensive, and QCM analyses requires isolating active layers on a QCM crystal sensor which is a very time consuming procedure that requires extreme care. As for the samples used for AFM and profilometry, if the polysulfone support is not dissolved away completely, it could result in overestimation of the active layer thickness. Therefore, it is important to apply enough DMF for a long enough period of time to dissolve all polysulfone in the active layer isolation procedure described in Section 2.2.2.

2.3.4. Thickness measurements with ellipsometry

While ellipsometry is commonly used to measure thickness of thin films,[24,25] only one study reported in the peer-reviewed literature has used ellipsometry to measure the thickness of the active layers of RO/NF membranes.[26] Ben-David *et al.*[26] used ellipsometry to measure the active layer thickness of an NF membrane, and pointed out in their study that ellipsometry could not be used to estimate the active layer thickness of RO membranes because of the relatively high roughness of the active layers of RO membranes. Several studies have used ellipsometry to measure thickness of active layers that were directly prepared on solid substrates via interfacial polymerization or graft polymerization,[43,44] but not for active layers isolated from TFC

membranes. Contrary to Ben David *et al.*'s observations, in this study, it is found that measuring active layer thickness for both RO and NF membranes is possible with ellipsometry.

In my experience, there are two important aspects in ellipsometry analysis to which one needs to pay special attention in order to successfully measure the thickness of active layers of RO/NF membranes. The first aspect relates to sample preparation. As discussed for active layer measurements with AFM and profilometry (Section 2.3.2) and QCM (Section 2.3.3), active layer thickness could be potentially overestimated with ellipsometry measurements if the polysulfone support is not fully dissolved during the active layer isolation step. . Incomplete removal of the polysulfone support during the active layer isolation step can also result in an artificially rougher isolated active layer which would also affect the measurements because ellipsometry analysis is more readily accomplished on samples with low surface roughness. Therefore, as for sample preparation for AFM, profilometry and QCM analysis, it is important to apply enough DMF for a long enough period of time to dissolve all polysulfone in the active layer isolation step.

The second important aspect needing special attention to measure active layer thickness successfully with ellipsometry is to use the AutoRetarder (or equivalent) feature of the ellipsometer. The AutoRetarder of the ellipsometer is automatically controlled by the instrument software to introduce adjusted retardance into the path of the incident beam.[45] The AutoRetarder modifies the polarization of the incident beam and produces optimum measurement conditions.[46] With the AutoRetarder feature, I was able to find good fits of simulated spectra to experimental spectra for both RO and NF membranes, as shown in Figure 2.6. The figure includes experimental ellipsometry spectra and corresponding simulations based on the Cauchy-SiO_2-Si model (as described in Section 2.2.9) of isolated polyamide active layer samples for the NF270 (a NF membrane), ESPA3 (a brackish water RO membrane) and SWC4+ (a seawater RO

membrane) membranes. Similar fits (not shown) were also obtained for the NF90, XLE and SW30HR membranes.

Active layer thickness was obtained from each ellipsometry spectrum by fitting the simulations to the experimental spectrum, with the thickness, constants of the first three terms of the refractive index in the Cauchy formula of the active layer (A, B and C in Equation 2.9), and the amplitude (α) and the exponent factor (β) of the extinction coefficient (k) as the fitting variables. Except for the active layer thickness, all the other five fitting (A, B, C, α and β) variables are related to the refractive index of the active layer by the Cauchy formula and the extinction coefficient as given by

$$n(\lambda) = A + \frac{B}{\lambda^2} + \frac{C}{\lambda^4}, \tag{2.9}$$

and

$$k(\lambda) = \alpha e^{\beta\left(12400\left(\frac{1}{\lambda}-\frac{1}{\gamma}\right)\right)}, \tag{2.10}$$

respectively. In Equations 2.9 and 2.10, $n(\lambda)$ is the real part of the complex refractive index of the active layer, $k(\lambda)$ is the extinction coefficient, λ is the wavelength of the analysis beam, and γ = 4000 is the band edge. In the data analysis process for ellipsometry spectra, values of the six fitting variables (thickness, A, B, C, α and β) are changed to fit the simulations to the experimental spectra using six sets of data (spectra from three different angles, 65 °, 70 ° and 75 °, for each phase change Δ and the amplitude change Ψ) with wavelength in the range of 380-1000 nm, based on the zero approximation electromagnetic Cauchy-SiO_2-Si model. For the spectra of each sample, a fit that reached a minimized mean square error of less than 20 was considered satisfactory and yielded the unknown thickness of the active layer in the corresponding sample. The results of active layer thickness obtained with ellipsometry for the

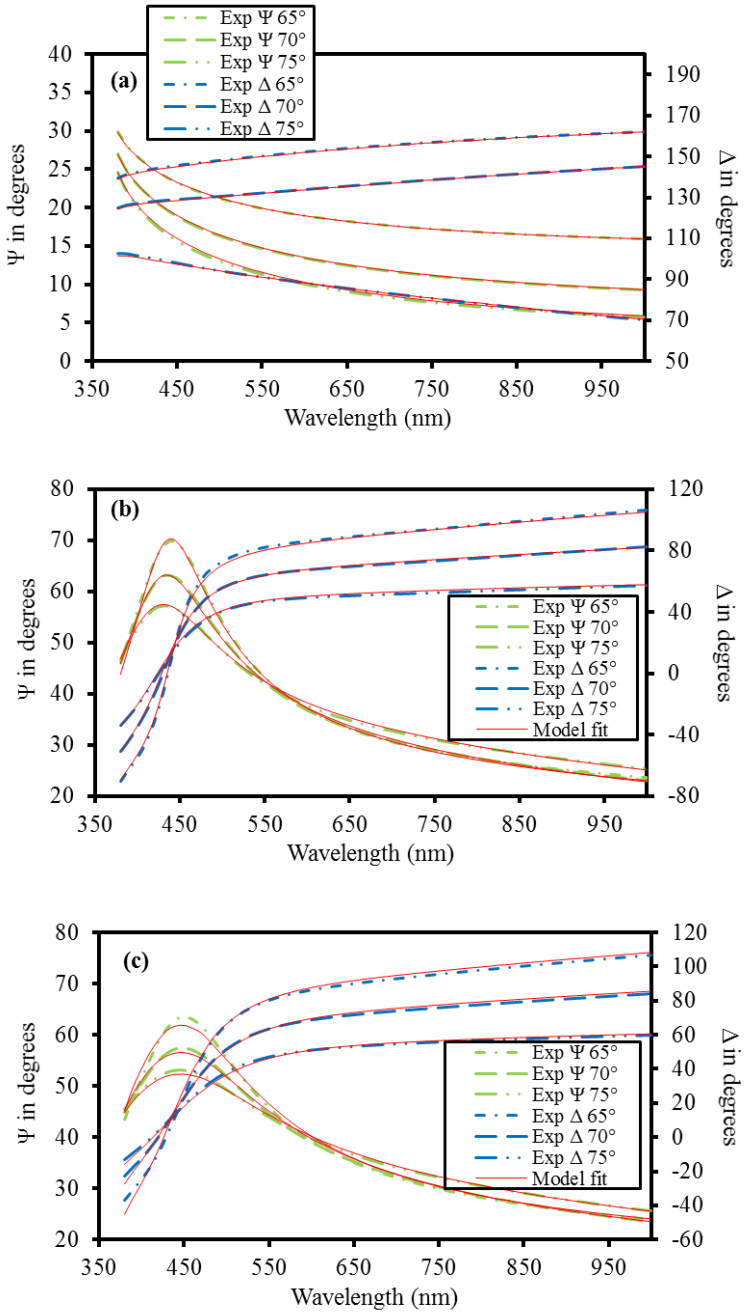

Figure 2.6. Representative experimental (interrupted lines) and simulated (red continuous lines) ellipsometry spectra of isolated active layers on silicon wafers for the (a) NF270, (b) ESPA3, and (c) SWC4+ membranes. Data acquisition was conducted at incidence angles of 65 °, 70 °and 75 °. The mean squared errors of the three fits shown are 0.91, 3.39 and 4.41, respectively. In ellipsometry analysis, mean squared errors lower than 20 are typically desired.

NF270, NF90, XLE, ESPA3, SWC4+ and SW30HR membranes were 21.7±0.5 nm, 131.3±11.8 nm, 135.5±3.7 nm, 90.2±2.5 nm, 115.6±16.6 nm and 157.2±5.4 nm, respectively. Their relative standard deviations were in the range of 2.5-14.3% with an average relative standard deviation of 5.8%.

Table 2.1 summarizes the advantages and disadvantages of ellipsometry analysis as an analytical techniques for measuring the thickness of the active layers of RO/NF membranes. Like RBS and QCM, ellipsometry measurements also have the advantage of being able to analyze square-centimeter-size samples (~0.3 cm^2 in this study), which is 3-5 orders of magnitude larger than the analysis scale of SEM, TEM, AFM and profilometry. Again, for measuring active layer thickness of RO/NF membranes, a technique with large measurement scale is likely to produce more representative thickness results for the RO/NF membranes. The small relative standard deviations of the thickness results suggest good consistency of ellipsometry analyses for active layer thickness, and therefore results representative of the membranes tested. The data collection process of ellipsometry measurement is not very complex and the ellipsometers are widely used instruments for measuring thin-film thickness which makes them readily available in research institutions.[24,25] Importantly, quantifying active layer thickness with ellipsometry does not require any subjective judgment or any assumption about other properties of the membrane active layer (e.g., volumetric mass density for RBS and QCM, location of the interface with the support layer for SEM and TEM).

Using ellipsometry for measuring the thickness of the active layers of RO/NF membrane also has disadvantages. Since the experiments require isolated active layer samples, the sample preparation process for ellipsometry is very time consuming and requires extreme care. Also, given that the thickness values obtained with ellipsometry are based on fitting model simulations

to experimental data, choosing an appropriate model that describes the sample under study is very important; however, as explained above, in this study, it was found that the Caucy+SiO2+Si model appropriately describes polyamide active layers isolated on silicon wafers. Additionally, while spectroscopic ellipsometers are instruments widely used in research institutions, they are not inexpensive and therefore lack of access to them may be a problem. Finally, ellipsometry measures the changes of phase and amplitude of the reflected light from the isolated active layer sample, so, like RBS and QCM, ellipsometry does not directly measure the thickness of the active layer. However, unlike RBS and QCM which require an assumption of active layer density, the indirect thickness measurement with ellipsometry is based on an electromagnetic zero approximation (i.e., no assumptions) model which makes it highly reliable (i.e., electromagnetic theory is more firmly established than gravitational theory).

2.3.5. Comparison of thickness values obtained with different analytical techniques

Figure 2.7 shows the thickness values of the active layers of the six commercial membranes studied, measured with the seven analytical techniques. The seven techniques operate on the basis of a broad range of physical principles. The SEM and TEM measurements are based on image analyses of electron micrographs of the cross sections of membrane samples; AFM and profilometry measurements are based on profiling the active layer height with respect to a solid substrate on which the active layer has been isolated; RBS and QCM estimates are based on the measurement of their areal mass (more specifically, RBS measures atomic areal density and QCM measures mass areal density); and ellipsometry measurements are based on fitting an electromagnetic zero approximation model to light reflection data. Therefore, consistent thickness results among several techniques serve as a strong indicator that the thickness values are accurate estimates of the true value of the active layer thickness. Similarly, substantial discrepancies between the values measured with one technique and consistent values

measured by several techniques likely indicate that the former technique does not provide accurate results. Accordingly, analysis of variance (ANOVA) was performed at 95% confidence level of the thickness values in Figure 2.7 to compare the results obtained with the different techniques for each of the membranes.

The ANOVA results indicate that for all six membranes studied, except for the SW30HR membrane, thickness values measured with SEM and TEM were significantly higher than thickness values measured with the non-electron microscopy techniques (AFM, RBS, QCM, profilometry and ellipsometry). For five membranes (NF270, NF90, XLE, SWC4+ and SW30HR) out of the six studied, the thickness values obtained for each membrane with the non-electron microscopy techniques were *not* statistically different from each other. While for the ESPA3 membrane, QCM gave an average thickness value that was statistically different from the ones obtained using the other non-electron microscopy techniques, the difference was of only 21% (compared to a difference of 44% for the value obtained with TEM) and could be the combined result of sample variability or level of error in the assumption of a polyamide density value of 1.24 g cm^{-3}.

Given that the six membranes studied cover a broad range of performance levels (including NF, brackish water RO and seawater RO) and three commonly used active layer materials (fully aromatic polyamide, semi-aromatic poly(piperazinamide) and poly(vinyl alcohol), it is concluded that: (1) AFM, RBS, QCM, profilometry and ellipsometry provide consistent thickness values for any given membrane studied, and thus they can be regarded as appropriate analytical techniques for the determination of active layer thickness of TFC membranes; and (2) SEM and TEM, in general, produce higher thickness values compared to non-electron microscopy methods, indicating that they should only be considered to provide

rough estimates of active layer thickness. A possible reason for the overestimations of active layer thickness using SEM and TEM is the subjective nature of the judgment of the location of the polyamide-polysulfone interface.

Based on the previous discussion, AFM, RBS, QCM, profilometry and ellipsometry all can be regarded as appropriate techniques to measure the thickness of the active layers of RO/NF membranes; however, each of these technique has several advantages and disadvantages as discussed in Sections 2.3.2-2.3.4 and shown in Table 2.1, and therefore, the preferred technique to use will depend on circumstances such as equipment availability, time available for sample preparation and analysis, etc. Among the various advantages and disadvantages listed in Table 2.1, the size of the sample, the need for major assumptions, and level of subjectivity needed to estimate the active layer thickness are three key features to evaluate the appropriateness of a technique, as these three aspects all directly affect the accuracy of the active layer thickness results. Based on the discussions in previous sections regarding advantages and disadvantages of each technique and corresponding summary in Table 2.1, ellipsometry is the only technique that has relatively large analysis scale, and does not require major assumptions and or subjective judgment to estimate active layer thickness. Therefore, ellipsometry is considered as the preferred technique to use to measure active layer thickness in RO/NF membranes. However, if an ellipsometer is not available, AFM and profilometry are the next preferred alternatives, since the ANOVA tests performed in this study showed that thickness results obtained by AFM and profilometry analyses were not significantly different from those obtained by ellipsometry analyses, and AFM and profilometry do not require major assumptions or subjective judgment to estimate active layer thickness.

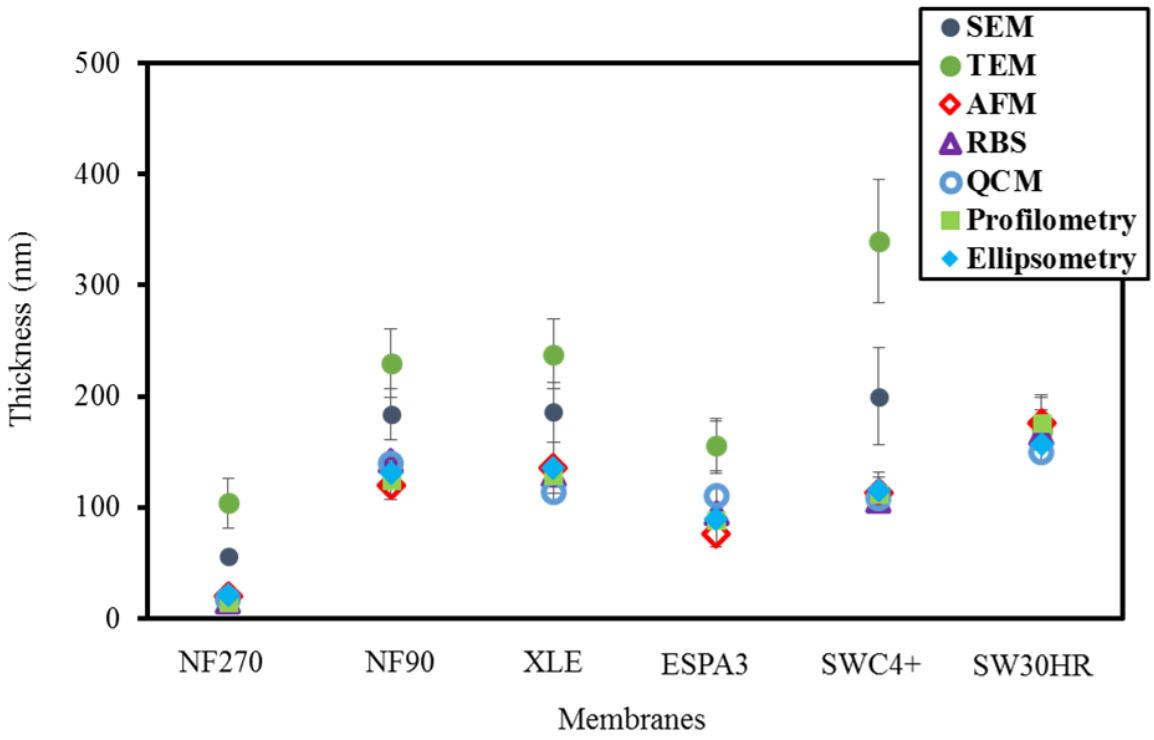

Figure 2.7. Measured thicknesses of the active layers of the NF270, NF90, XLE, ESPA3, SWC4+ and SW30HR membranes obtained by SEM, TEM, AFM, RBS, QCM, profilometry and ellipsometry analyses. For each membrane, the reported thickness value and corresponding error represent the average and standard deviation, respectively, for multiple samples. The thickness values obtained with the five techniques that produced consistent results among each other (i.e., AFM, RBS, QCM, profilometry and ellipsometry) ranged from 14.4±4.7 nm (NF270) to 176.3±24.5 nm (SW30HR).

In the case that the active layer density of the membrane of interest were known, RBS or QCM would be ideal techniques to measure active layer thickness, since they both perform analyses on samples with large areas, do not require subjective judgment to estimate active layer thickness, and ANOVA tests indicate that the thickness results obtained by RBS and QCM analyses are not significantly different from those obtained by ellipsometry analyses for five out of six membranes studied. To choose between RBS and QCM, one should evaluate the availability of RBS equipment and the time needed to prepare samples for QCM, since instruments needed to perform RBS tests are not widely available and are very expensive, and sample preparation for QCM tests (isolating active layers onto QCM sensors) is time consuming. Given that SEM and TEM in general overestimate the thickness of RO/NF membrane active layers, one should only use SEM or TEM for the characterization of active layer thickness when accurate thickness values are not required, but rather rough estimates of active layer thickness are acceptable.

2.3.6. Active layer density

As discussed in Section 2.3.3, the most significant drawback of RBS and QCM for characterizing active layer thickness is requiring an assumption about the value of the volumetric mass density of the active layer. This is a significant drawback because the accuracy of thickness results is limited by the accuracy of the assumption about active layer density, and active layer density has not been experimentally measured in the peer-reviewed literature. Therefore, given that in this study both the areal mass density (m_{AL}) and thickness (δ) of the active layers were obtained experimentally, the volumetric mass density of the active layers studied was calculated as the ratio between the former and the latter as given by

$$\rho = \frac{m_{AL}}{\delta}. \tag{2.11}$$

The results obtained serve as experimental estimates of active layer volumetric mass density for use in future studies where needed, e.g., where QCM or RBS are used to measure active layer thickness.

For the active layer thickness measurements in this study, five of the seven techniques (TEM, SEM, AFM, profilometry and ellipsometry) did not use an assumption of active layer density to obtain active layer thickness. Among these five techniques, AFM, profilometry and ellipsometry were found to provide accurate thickness measurements (see Section 2.3.5) and discussion about their advantages and disadvantages concluded that ellipsometry was the preferred technique to measure active layer thickness. Therefore, the thickness results obtained by ellipsometry analyses were used as the denominator in Equation 2.11 to calculate active layer volumetric mass density. Areal mass density was obtained in this study using both RBS and QCM analyses. Thickness analysis with RBS measured areal mass of active layer with full membrane samples while QCM experiments measured areal mass with isolated active layer samples. Since thickness results by ellipsometry analyses were used as denominator in Equation 2.11, areal mass values obtained by QCM analyses were used as numerator to maintain consistency in the sample preparation procedure used for samples that generated data for the calculation of volumetric mass density values.

The calculated values of active layer density for each of the six membranes studied are shown in Figure 2.8. Active layer densities ranged from 0.98±0.26 g cm^{-3} (NF270) to 1.53±0.11 g cm^{-3} (ESPA3), with an average of 1.20±0.20 g cm^{-3}. As described in Section 2.2.1, the NF270 membrane has a poly(piperazinamide) active layer, the SW30HR membrane has a fully aromatic polyamide active layer with a poly(vinyl alcohol) coating layer, and all the other membranes in this study have fully aromatic polyamide active layers without any coating. Therefore, besides

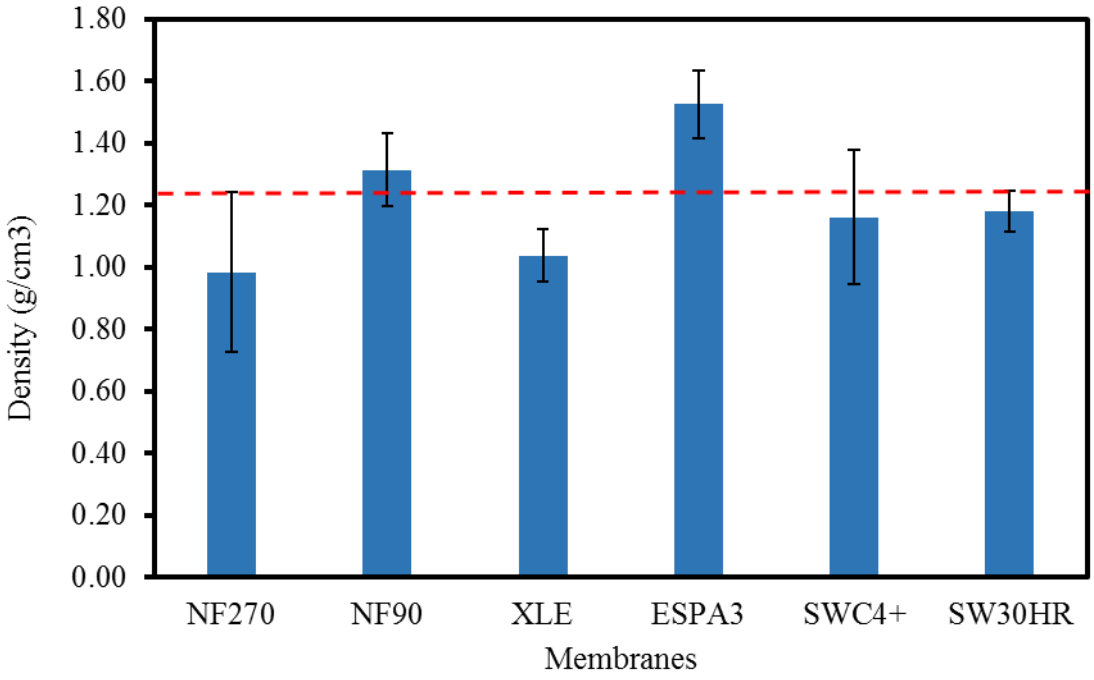

Figure 2.8. Mass densities of the six membranes studied calculated using the areal masses obtained from QCM analyses and thicknesses from ellipsometry analyses. The red dashed line represents the density estimate in the literature (1.24 g cm^{-3})[8] for polyamide active layers. The active layer density averaged 1.20±0.20 g $cm^{-3}$for the active layers of all six membranes and 1.26±0.21 g cm^{-3} for the uncoated fully aromatic active layers (NF90, XLE, ESPA3, and SWC4+).

the average active layer density of the six membranes, the average active layer density for membranes with uncoated fully aromatic active layers was calculated and the result was 1.26±0.21 g·cm^{-3}. Both values of average active layer density are not significantly different from the 1.24 g·cm^{-3} calculated by Zhang *et al.* Our ANOVA tests show that the average active layer density of all six membranes and the average active layer density of the membranes with uncoated fully aromatic polyamide active layers are not significantly different from each other. Similarly, ANOVA test shows that the active layer densities of the six membranes are not significantly different from each other. Therefore, if an assumption of active layer density is needed for future research of RO/NF membranes, a value between 1.20-1.26 g·cm^{-3} can be used as an adequate estimate of volumetric mass density of polyamide active layers.

2.4. Conclusions

The active layer thicknesses of the active layers of six commercial RO/NF membranes were measured with seven analytical techniques to study which techniques provide accurate thickness measurements for active layers of TFC membranes. The advantages and disadvantages of each techniques to measure active layer thickness were also discussed. A comparison of thickness values obtained with each technique and advantages and disadvantages that each technique offers led to the following conclusions:

- AFM, RBS, QCM, profilometry and ellipsometry produce consistent thickness results among each other, and therefore, given that they operate under completely different physical principles, they also likely provide the most accurate results of active layer thickness of TFC membranes.

- SEM and TEM produce, in general, significantly higher thickness values compared to the non-electron microscopy techniques, and therefore should only be used for rough estimates of active layer thickness.
- For RBS, QCM and ellipsometry analyses, thickness results for different samples of the same membrane obtained from the same technique have small relative standard deviations, which indicates good self-consistency of the technique. Such standard deviations are large for SEM, TEM, AFM and profilometry, which indicates that they do not provide as good self-consistency as RBS, QCM and ellipsometry.
- Ellipsometry is considered as the preferred technique to use to measure active layer thickness in TFC membranes because it uses a large area of analysis and does not require major assumptions or subjective judgment to determine active layer thickness.
- If an ellipsometer is not available, AFM and profilometry are the next preferred alternatives because they produce results that are not statistically significantly different from those obtained by ellipsometry, and do not require major assumptions or subjective judgment to estimate active layer thickness.
- RBS or QCM are ideal techniques to measure active layer thickness if the active layer density of the membrane of interest is known because they generally produce results that are not statistically significantly different from those obtained by ellipsometry, use the largest analysis areas, and do not require subjective judgment to estimate active layer thickness.
- For the six membrane studied, thickness values of their active layers ranged from 14 nm (NF270 membrane with a poly(piperazine amide) active layer) to 176 nm

(SW30HR membrane with a fully aromatic polyamide active layer coated with poly(vinyl alcohol)).

- The average volumetric mass density of the uncoated fully aromatic polyamide active layers studies was determined to be 1.26 ± 0.21 g cm^{-3}.
- The average volumetric mass density of all polyamide active layers studies was determined to be 1.20 ± 0.20 g cm^{-3}.
- A value between 1.20-1.26 g cm^{-3} was found to be an adequate estimate of polyamide active layer density.

The thickness of the active layers of RO/NF membranes not only directly affects membrane performance in terms of water and salt permeability. Knowledge of its magnitude is also essential to determine accurately water and solute transport properties that affect membrane performance (e.g., partition and diffusion coefficients in the active layers). Therefore, conclusions from this study provide membrane researchers with guidance on which analytical techniques to use to measure active layer thickness, including their advantages and disadvantages, and volumetric mass density values of polyamide active layers which are important for e.g. estimate active layer thickness with techniques that require such value (i.e., QCM, RBS).

2.5. Acknowledgments

The author would like to thank Dr. Rene Lopez for helpful discussion on ellipsometry and Yingchi Liu and Chengcheng Feng for their help on ellipsometry experiments. The author would also like to acknowledge Dr. Thomas Clegg for his help on RBS experiments, Dr. Carrie Donley for helping on SEM and Wallace Ambrose for taking TEM images. The RBS experiments were carried out at the Triangle Universities Nuclear Laboratory (TUNL) in Durham, NC. The SEM,

TEM, AFM, profilometry and ellipsometry experiments were conducted at the Chapel Hill Analytical and Nanofabrication Laboratory (CHANL) in Chapel Hill, NC. This work was supported by the National Science Foundation (NSF) Grants Opportunities for Academic Liason with Industry (GOALI) and Chemical and Biological Separations programs under Award#1264690, NSF Environmental Engineering program under Award#1336532 and the University of North Carolina IBM Junior Faculty Award. The author was partially supported by the Okun Scholarship.

REFERENCES

(1) Greenlee, L. F.; Lawler, D. F.; Freeman, B. D.; Marrot, B.; Moulin, P. Reverse osmosis desalination: water sources, technology, and today's challenges. *Water Res.* **2009**, *43*, 2317–2348.

(2) Jacangelo, J. G.; Trussell, R. R.; Watson, M. Role of membrane technology in drinking water treatment in the United States. *Desalination* **1997**, *113*, 119–127.

(3) Van der Bruggen, B.; Everaert, K.; Wilms, D.; Vandecasteele, C. Application of nanofiltration for removal of pesticides, nitrate and hardness from ground water: rejection properties and economic evaluation. *J. Membr. Sci.* **2001**, *193*, 239–248.

(4) Petersen, R. J. Composite reverse osmosis and nanofiltration membranes. *J. Membr. Sci.* **1993**, *83*, 81–150.

(5) Lee, K. P.; Arnot, T. C.; Mattia, D. A review of reverse osmosis membrane materials for desalination—Development to date and future potential. *J. Membr. Sci.* **2011**, *370*, 1–22.

(6) Bellona, C.; Drewes, J. E.; Xu, P.; Amy, G. Factors affecting the rejection of organic solutes during NF/RO treatment—A literature review. *Water Res.* **2004**, *38*, 2795–2809.

(7) Wijmans, J. G.; Baker, R. W. The solution-diffusion model: a review. *J. Membr. Sci.* **1995**, *107*, 1–21.

(8) Zhang, X.; Cahill, D. G.; Coronell, O.; Mariñas, B. J. Absorption of water in the active layer of reverse osmosis membranes. *J. Membr. Sci.* **2009**, *331*, 143–151.

(9) Lee, J.; Doherty, C. M.; Hill, A. J.; Kentish, S. E. Water vapor sorption and free volume in the aromatic polyamide layer of reverse osmosis membranes. *J. Membr. Sci.* **2013**, *425-426*, 217–226.

(10) Mi, B.; Coronell, O.; Mariñas, B. J.; Watanabe, F.; Cahill, D. G.; Petrov, I. Physico-chemical characterization of NF/RO membrane active layers by Rutherford backscattering spectrometry. *J. Membr. Sci.* **2006**, *282*, 71–81.

(11) Freger, V.; Gilron, J.; Belfer, S. TFC polyamide membranes modified by grafting of hydrophilic polymers: an FT-IR/AFM/TEM study. *J. Membr. Sci.* **2002**, *209*, 283–292.

(12) Freger, V. Nanoscale Heterogeneity of Polyamide Membranes Formed by Interfacial Polymerization. *Langmuir* **2003**, *19*, 4791–4797.

(13) Ghosh, A. K.; Jeong, B.-H.; Huang, X.; Hoek, E. M. V. Impacts of reaction and curing conditions on polyamide composite reverse osmosis membrane properties. *J. Membr. Sci.* **2008**, *311*, 34–45.

(14) Freger, V. Swelling and morphology of the skin layer of polyamide composite membranes: an atomic force microscopy study. *Environ. Sci. Technol.* **2004**, *38*, 3168–3175.

(15) Dražević, E.; Košutić, K.; Freger, V. Permeability and selectivity of reverse osmosis membranes: Correlation to swelling revisited. *Water Res.* **2014**, *49*, 444–452.

(16) Coronell, O.; Mariñas, B. I.; Cahill, D. G. Accessibility and ion exchange stoichiometry of ionized carboxylic groups in the active layer of FT30 reverse osmosis membrane. *Environ. Sci. Technol.* **2009**, *43*, 5042–5048.

(17) Coronell, O.; González, M. I.; Mariñas, B. J.; Cahill, D. G. Ionization behavior, stoichiometry of association, and accessibility of functional groups in the active layers of reverse osmosis and nanofiltration membranes. *Environ. Sci. Technol.* **2010**, *44*, 6808–6814.

(18) Coronell, O.; Mariñas, B. J.; Zhang, X.; Cahill, D. G. Quantification of functional groups and modeling of their ionization behavior in the active layer of FT30 reverse osmosis membrane. *Environ. Sci. Technol.* **2008**, *42*, 5260–5266.

(19) Jubera, A. M. S. de; Gao, Y.; Moore, J. S.; Cahill, D. G.; Mariñas, B. J. Enhancing the Performance of Nanofiltration Membranes by Modifying the Active Layer with Aramide Dendrimers. *Environ. Sci. Technol. Technol.* **2012**, *46*, 9592–9599.

(20) Matthews, T. D.; Yan, H.; Cahill, D. G.; Coronell, O.; Mariñas, B. J. Growth dynamics of interfacially polymerized polyamide layers by diffuse reflectance spectroscopy and Rutherford backscattering spectrometry. *J. Membr. Sci.* **2013**, *429*, 71–80.

(21) Kotelyanskii, M. J.; Wagner, N. J.; Paulaitis, M. E. Atomistic simulation of water and salt transport in the reverse osmosis membrane FT-30. *J. Membr. Sci.* **1998**, *139*, 1–16.

(22) Roh, I. J. Effect of the physicochemical properties on the permeation performance in fully aromatic crosslinked polyamide thin films. *J. Appl. Polym. Sci.* **2003**, *87*, 569–576.

(23) Roh, I. J.; Greenberg, A. R.; Khare, V. P. Synthesis and characterization of interfacially polymerized polyamide thin films. *Desalination* **2006**, *191*, 279–290.

(24) Toney, M. F.; Mate, C. M.; Leach, K. A.; Pocker, D. Thickness Measurements of Thin Perfluoropolyether Polymer Films on Silicon and Amorphous-Hydrogenated Carbon with X-Ray Reflectivity, ESCA and Optical Ellipsometry. *J. Colloid Interface Sci.* **2000**, *225*, 219–226.

(25) McCrackin, F. L.; Passaglia, E.; Stromberg, R. R.; Steinberg, H. L. Measurement of the Thickness and Refractive Index of Very Thin Films and the Optical Properties of Surfaces by Ellipsometry. *J. Res. Nat. Bur. Sect.* **1963**, *A 67*, 363–377.

(26) Ben-David, A.; Bason, S.; Jopp, J.; Oren, Y.; Freger, V. Partitioning of organic solutes between water and polyamide layer of RO and NF membranes: Correlation to rejection. *J. Membr. Sci.* **2006**, *281*, 480–490.

(27) Coronell, O.; González, M. I.; Mariñas, B. J.; Cahill, D. G. Ionization behavior, stoichiometry of association, and accessibility of functional groups in the active layers of reverse osmosis and nanofiltration membranes. *Environ. Sci. Technol.* **2010**, *44*, 6808–6814.

(28) Tang, C. Y.; Kwon, Y.-N.; Leckie, J. O. Effect of membrane chemistry and coating layer on physiochemical properties of thin film composite polyamide RO and NF membranes I. FTIR and XPS characterization of polyamide and coating layer chemistry. *Desalination* **2009**, *242*, 149–167.

(29) Perry, L. A.; Coronell, O. Reliable, bench-top measurements of charge density in the active layers of thin-film composite and nanocomposite membranes using quartz crystal microbalance technology. *J. Membr. Sci.* **2013**, *429*, 23–33.

(30) Rasband, W.S., ImageJ, U. S. National Institutes of Health, Bethesda, Maryland, USA, http://imagej.nih.gov/ij/, 1997-2014.

(31) Kwak, S.-Y.; Jung, S. G.; Yoon, Y. S.; Ihm, D. W. Details of surface features in aromatic polyamide reverse osmosis membranes characterized by scanning electron and atomic force microscopy. *J. Polym. Sci. Part B Polym. Phys.* **1999**, *37*, 1429–1440.

(32) Attayek, P. J.; Meyer, E. S.; Lin, L.; Rich, G. C.; Clegg, T. B.; Coronell, O. A remotely controlled, semi-automatic target system for Rutherford backscattering spectrometry and elastic recoil detection analyses of polymeric membrane samples. *Nucl. Instruments Methods Phys. Res. Sect. A Accel. Spectrometers, Detect. Assoc. Equip.* **2012**, *676*, 21–25.

(33) Mi, B.; Cahill, D. G.; Mariñas, B. J. Physico-chemical integrity of nanofiltration/reverse osmosis membranes during characterization by Rutherford backscattering spectrometry. *J. Membr. Sci.* **2007**, *291*, 77–85.

(34) Mayer, M. SIMNRA User's Guide, Report IPP 9/113, Max-Planck-Institut fur Plasmaphysik, Garching, Germany, 1997.

(35) Huang, Y.; Paul, D. R. Physical aging of thin glassy polymer films monitored by gas permeability. *Polymer.* **2004**, *45*, 8377–8393.

(36) Irene, E. A. A brief history and state of the art of ellipsometry. In *Ellipsometry at the Nanoscale*; Losurdo, M.; Hingerl, K., Eds.; Springer-Verlag Berlin Heidelberg, 2013; pp. 1–30.

(37) Guide to Using WVASE32-Software for Spectroscopic Ellipsometry Data Acquisition and Analysis, 7.15–7.16.

(38) Tang, C. Y.; Kwon, Y.-N.; Leckie, J. O. Effect of membrane chemistry and coating layer on physiochemical properties of thin film composite polyamide RO and NF membranes II. Membrane physiochemical properties and their dependence on polyamide and coating layers. *Desalination* **2009**, *242*, 168–182.

(39) Coronell, O.; Mariñas, B. J.; Cahill, D. G. Depth heterogeneity of fully aromatic polyamide active layers in reverse osmosis and nanofiltration membranes. *Environ. Sci. Technol.* **2011**, *45*, 4513–4520.

(40) Hirose, M.; Ito, H.; Kamiyama, Y. Effect of skin layer surface structures on the flux behaviour of RO membranes. *J. Membr. Sci.* **1996**, *121*, 209–215.

(41) Pacheco, F. A.; Pinnau, I.; Reinhard, M.; Leckie, J. O. Characterization of isolated polyamide thin films of RO and NF membranes using novel TEM techniques. *J. Membr. Sci.* **2010**, *358*, 51–59.

(42) O'Sullivan, C. K.; Guilbault, G. G. Commercial quartz crystal microbalances—Theory and applications. *Biosens. Bioelectron.* **1999**, *14*, 663–670.

(43) Kim, M.; Lin, N. H.; Lewis, G. T.; Cohen, Y. Surface nano-structuring of reverse osmosis membranes via atmospheric pressure plasma-induced graft polymerization for reduction of mineral scaling propensity. *J. Membr. Sci.* **2010**, *354*, 142–149.

(44) Lin, N. H.; Cohen, Y. QCM study of mineral surface crystallization on aromatic polyamide membrane surfaces. *J. Membr. Sci.* **2011**, *379*, 426–433.

(45) Ellipsometry FAQ http://www.jawoollam.com/faq.html (accessed Apr 9, 2015).

(46) VASE® Ellipsometer http://www.jawoollam.com/vase_home.html (accessed Apr 9, 2015).

(47) Yip, N. Y.; Tiraferri, A.; Phillip, W. A.; Schiffman, J. D.; Hoover, L. A.; Kim, Y. C.; Elimelech, M. Thin-film composite pressure retarded osmosis membranes for sustainable power generation from salinity gradients. *Environ. Sci. Technol.* **2011**, *45*, 4360–4369.

(48) Ramon, G. Z.; Hoek, E. M. V. Transport through composite membranes, part 2: impacts of roughness on permeability and fouling. *J. Membr. Sci.* **2013**, *425-426*, 141–148.

(49) Bowen, W. R.; Welfoot, J. S. Modelling the performance of membrane nanofiltration—Critical assessment and model development. *Chem. Eng. Sci.* **2002**, *57*, 1121–1137.

(50) Kurihara, M.; Hanakawa, M. Mega-ton water system: Japanese national research and development project on seawater desalination and wastewater reclamation. *Desalination* **2013**, *308*, 131–137.

(51) An, Q.; Hung, W.; Lo, S.; Li, Y.; Guzman, M. De; Hu, C.-C.; Lee, K.-R.; Jean, Y.-C.; Lai, J.-Y. Comparison between Free Volume Characteristics of Composite Membranes

Fabricated through Static and Dynamic Interfacial Polymerization Processes. *Macromolecules* **2012**, *45*, 3248–3435.

(52) Kong, C.; Shintani, T.; Kamada, T.; Freger, V.; Tsuru, T. Co-solvent-mediated synthesis of thin polyamide membranes. *J. Membr. Sci.* **2011**, *384*, 10–16.

(53) Kong, C.; Koushima, A.; Kamada, T.; Shintani, T.; Kanezashi, M.; Yoshioka, T.; Tsuru, T. Enhanced performance of inorganic-polyamide nanocomposite membranes prepared by metal-alkoxide-assisted interfacial polymerization. *J. Membr. Sci.* **2011**, *366*, 382–388.

(54) Kong, C.; Kanezashi, M.; Yamomoto, T.; Shintani, T.; Tsuru, T. Controlled synthesis of high performance polyamide membrane with thin dense layer for water desalination. *J. Membr. Sci.* **2010**, *362*, 76–80.

(55) Tang, C. Y.; Kwon, Y.-N.; Leckie, J. O. Probing the nano- and micro-scales of reverse osmosis membranes—A comprehensive characterization of physiochemical properties of uncoated and coated membranes by XPS, TEM, ATR-FTIR, and streaming potential measurements. *J. Membr. Sci.* **2007**, *287*, 146–156.

(56) Tang, C. Y.; Fu, Q. S.; Robertson, A. P.; Criddle, C. S.; Leckie, J. O. Use of reverse osmosis membranes to remove perfluorooctane sulfonate (PFOS) from semiconductor wastewater. *Environ. Sci. Technol.* **2006**, *40*, 7343–7349.

(57) Yin, J.; Kim, E.-S.; Yang, J.; Deng, B. Fabrication of a novel thin-film nanocomposite (TFN) membrane containing MCM-41 silica nanoparticles (NPs) for water purification. *J. Membr. Sci.* **2012**, *423-424*, 238–246.

(58) Ridgway, H. F.; Gale, J. D.; Hughes, Z. E.; Stewart, M. B.; Orbell, J. D.; Gray, S. R. Molecular scale modeling of membrane water treatment processes. In *Functional Nanostructured Materials and Membranes for Water Treatment*; Duke, M.; Zhao, D.; Semiat, R.; Lu, M., Eds.; John Wiley & Sons, 2013; pp. 249–300.

(59) Yan, H.; Miao, X.; Xu, J.; Pan, G.; Zhang, Y.; Shi, Y.; Guo, M.; Liu, Y. The porous structure of the fully-aromatic polyamide film in reverse osmosis membranes. *J. Membr. Sci.* **2015**, *475*, 504–510.

(60) Dow Filmtec. NF90-400 nanofiltration element datasheet, Form No. 609-00345-0312. Available at http://www.dowwaterandprocess.com/en/Products/F/FILMTEC%20NF90_4040 (Accessed on October 26, 2014).

(61) Dow Filmtec. XLE-440 extra low energy RO element datasheet, Form No. 609-00245-0606. Available at http://www.dowwaterandprocess.com/en/products/f/filmtec_xle_4040 (Accessed on October 26, 2014).

(62) Dow Filmtec. SW30HR-380 seawater reverse osmosis element datasheet, Form No. 609-00390-1008. Available at

http://www.dowwaterandprocess.com/en/products/f/filmtec_sw30hr_380 (Accessed on October 26, 2014).

(63) Hydranautics. ESPA3-4040 brackish water reverse osmosis membrane element datasheet. Available at http://www.lenntech.com/Data-sheets/Hydranautics-ESPA3-4040.pdf (Accessed on October 26, 2014).

(64) Hydranautics. SWC4+ 8040 seawater reverse osmosis element datasheet. Available at http://www.lenntech.com/Data-sheets/Hydranautics-SWC4+8040.pdf (Accessed on October 26, 2014).

(65) Bason, S.; Oren, Y.; Freger, V. Ion transport in the polyamide layer of RO membranes: Composite membranes and free-standing films. *J. Membr. Sci.* **2011**, *367*, 119–126.

(66) Marx, K. A. Quartz crystal microbalance: a useful tool for studying thin polymer films and complex biomolecular systems at the solution-surface interface. *Biomacromolecules* **2003**, *4*, 1099–1120.

(67) Bozzola, J. J.; Russell, L. D. *Electron Microscopy: Principles and Techniques for Biologist*; 2nd ed.; Jones and Bartlett, 1999.

(68) Kolev, V.; Freger, V. Hydration, porosity and water dynamics in the polyamide layer of reverse osmosis membranes: A molecular dynamics study. *Polymer.* **2014**, *55*, 1420–1426.

(69) Jeck, S.; Scharfer, P.; Schabel, W.; Kind, M. Water sorption in poly(vinyl alcohol) membranes: an experimental and numerical study of solvent diffusion in a crosslinked polymer. *Chem. Eng. Process.* **2011**, *50*, 543–550.

(70) Ben-David, A.; Oren, Y.; Freger, V. Thermodynamic factors in partitioning and rejection of organic compounds by polyamide composite membranes. *Environ. Sci. Technol.* **2006**, *40*, 7023–7028.

(71) Ciddor, P. E. Refractive index of air: new equations for the visible and near infrared. *Appl. Opt.* **1996**, *35*, 1566–1573.

(72) Braun, M. M.; Pilon, L. Effective optical properties of non-absorbing nanoporous thin films. *Thin Solid Films* **2006**, *496*, 505–514.

(73) Bason, S.; Freger, V. Phenomenological analysis of transport of mono- and divalent ions in nanofiltration. *J. Membr. Sci.* **2010**, *360*, 389–396.

(74) Ding, M.; Ghoufi, A.; Szymczyk, A. Molecular simulations of polyamide reverse osmosis membranes. *Desalination* **2014**, *343*, 48–53.

(75) Ding, M.; Szymczyk, A.; Goujon, F.; Soldera, A.; Ghoufi, A. Structure and dynamics of water confined in a polyamide reverse-osmosis membrane: A molecular-simulation study. *J. Membr. Sci.* **2014**, *458*, 236–244.

(76) Harder, E.; Walters, D. E.; Bodnar, Y. D.; Faibish, R. S.; Roux, B. Molecular dynamics study of a polymeric reverse osmosis membrane. *J. Phys. Chem. B* **2009**, *113*, 10177–10182.

(77) Kotelyanskii, M. J.; Wagner, N. J.; Paulaitis, M. E. Molecular dynamics simulation study of the mechanisms of water diffusion in a hydrated, amorphous polyamide. *Comput. Theor. Polym. Sci.* **1999**, *9*, 301–306.

(78) Yaroshchuk, A.; Martínez-Lladó, X.; Llenas, L.; Rovira, M.; de Pablo, J. Solution-diffusion-film model for the description of pressure-driven trans-membrane transfer of electrolyte mixtures: One dominant salt and trace ions. *J. Membr. Sci.* **2011**, *368*, 192–201.

(79) Paul, D. R. Reformulation of the solution-diffusion theory of reverse osmosis. *J. Membr. Sci.* **2004**, *241*, 371–386.

(80) Xie, W.; Geise, G. M.; Freeman, B. D.; Lee, H.-S.; Byun, G.; McGrath, J. E. Polyamide interfacial composite membranes prepared from m-phenylene diamine, trimesoyl chloride and a new disulfonated diamine. *J. Membr. Sci.* **2012**, *403-404*, 152–161.

(81) Ghosh, A. K.; Jeong, B.-H.; Huang, X.; Hoek, E. M. V. Impacts of reaction and curing conditions on polyamide composite reverse osmosis membrane properties. *J. Membr. Sci.* **2008**, *311*, 34–45.

(82) Song, Y.; Sun, P.; Henry, L. L.; Sun, B. Mechanisms of structure and performance controlled thin film composite membrane formation via interfacial polymerization process. *J. Membr. Sci.* **2005**, *251*, 67–79.

(83) Tang, C. Y.; Kwon, Y.-N.; Leckie, J. O. Probing the nano- and micro-scales of reverse osmosis membranes—A comprehensive characterization of physiochemical properties of uncoated and coated membranes by XPS, TEM, ATR-FTIR, and streaming potential measurements. *J. Membr. Sci.* **2007**, *287*, 146–156.

(84) Bernstein, R.; Kaufman, Y.; Freger, V. Membrane Characterization. In *Encyclopedia of Membrane Science and Technology*; Hoek, E. M. V.; Tarabara, V. V., Eds.; John Wiley & Sons, Inc., 2013; p. 9.

(85) Geise, G. M.; Park, H. B.; Sagle, A. C.; Freeman, B. D.; McGrath, J. E. Water permeability and water/salt selectivity tradeoff in polymers for desalination. *J. Membr. Sci.* **2011**, *369*, 130–138.

(86) Maxwell, C. *Treatise on Electricity and Magnetism, vol. 1*; Oxford University Press, London, 1973.

(87) Cussler, E. L. *Diffusion: Mass Transfer in Fluid Systems*; 3rd ed.; Cambridge University Press: United States of America, 2009; p. 631.

(88) Zhang, X.; Cahill, D. G.; Coronell, O.; Mariñas, B. J. Partitioning of salt ions in FT30 reverse osmosis membranes. *Appl. Phys. Lett.* **2007**, *91*, 181904.

(89) Chen, G.; Li, S.; Zhang, X.; Zhang, S. Novel thin-film composite membranes with improved water flux from sulfonated cardo poly(arylene ether sulfone) bearing pendant amino groups. *J. Membr. Sci.* **2008**, *310*, 102–109.

(90) Rao, A. P.; Joshi, S. V; Trivedi, J. J.; Devmurari, C. V; Shah, V. J. Structure–performance correlation of polyamide thin film composite membranes : effect of coating conditions on film formation. *J. Membr. Sci.* **2003**, *211*, 13–24.

(91) Rana, D.; Kim, Y.; Matsuura, T.; Arafat, H. A. Development of antifouling thin-film-composite membranes for seawater desalination. *J. Membr. Sci.* **2011**, *367*, 110–118.

(92) Li, L.; Zhang, S.; Zhang, X.; Zheng, G. Polyamide thin film composite membranes prepared from isomeric biphenyl tetraacyl chloride and m-phenylenediamine. *J. Membr. Sci.* **2008**, *315*, 20–27.

(93) Ogieglo, W.; van der Werf, H.; Tempelman, K.; Wormeester, H.; Wessling, M.; Nijmeijer, A.; Benes, N. E. n-Hexane induced swelling of thin PDMS films under non-equilibrium nanofiltration permeation conditions , resolved by spectroscopic ellipsometry. *J. Membr. Sci.* **2013**, *431*, 233–243.

(94) Kahle, O.; Wielsch, U.; Metzner, H.; Bauer, J.; Uhlig, C.; Zawatzki, C. Glass transition temperature and thermal expansion behaviour of polymer films investigated by variable temperature spectroscopic ellipsometry. *Thin Solid Films* **1998**, *313-314*, 803–807.

(95) Ogieglo, W.; Wormeester, H.; Wessling, M.; Benes, N. E. Spectroscopic Ellipsometry Analysis of a Thin Film Composite Membrane Consisting of Polysulfone on a Porous α-Alumina Support. *Appl. Mater. Interfaces* **2012**, *4*, 935–943.

(96) Turner, L. A. Zeroth Law of Thermodynamics. *Am. J. Phys.* **1961**, *29*, 71–76.

(97) Yang, K.; Zhu, L.; Xing, B. Adsorption of Polycyclic Aromatic Hydrocarbons by Carbon Nanomaterials. *Environ. Sci. Technol.* **2006**, *40*, 1855–1861.

(98) Lo, S. Anomalous State of Ice. *Mod. Phys.* **1996**, *10*, 909–919.

(99) Metz, S. J.; van de Ven, W. J. C.; Potreck, J.; Mulder, M. H. V; Wessling, M. Transport of water vapor and inert gas mixtures through highly selective and highly permeable polymer membranes. *J. Membr. Sci.* **2005**, *251*, 29–41.

(100) *MWH Water treatment: Principles and design*; Crittenden, J. C.; Trussell, R. R.; Hand, D. W.; Howe, K. J.; Tchobanoglous, G., Eds.; John Wiley & Sons: Hoboken, NY, USA, 2012; p. 1870.

CHAPTER 3: INVESTIGATING THE VOID STRUCTURE OF THE POLYAMIDE ACTIVE LAYERS OF THIN-FILM COMPOSITE MEMBRANES

3.1 Introduction

Thin-film composite (TFC) membranes with polyamide active layers are used in a broad range of applications, including water desalination, hardness removal, water reuse, and energy production.[1–4] Such TFC membranes consist of a top ultrathin (~20-200 nm) polyamide active layer, a microporous polysulfone support (~20-50 μm), and a polyester backing layer (~300 μm).[5,6] The polyamide active layer constitutes the selective barrier to water and solute permeation,[5,7] and thus its physical structure likely plays an essential role in the water permeability and solute rejection properties of the membranes.[8]

The polyamide active layer of TFC membranes has traditionally been assumed to be a dense polymer phase, with voids, if any, no larger than a few nanometers in diameter. This conceptualization of the active layer is reflected in the two mechanistic models commonly used to describe water and solute permeation through polyamide membranes, the solution-diffusion model[9] and the void-flow model.[10] The solution-diffusion model assumes that the active layer is dense without any voids, and the void-flow model assumes the existence of cylindrical nanovoids (typically with a diameter of a few nanometers or less) that stretch across the active layer within an otherwise dense structure. Contrary to this conceptualization of the active layer, recent experimental studies based on cross-sectional TEM images of polyamide active layers[11–15] suggest that globular features visible in the images correspond to voids (i.e., regions without polymer) having tens of nanometers in diameter. It is important to mention that the voids

suggested in these studies are not the same as the voids in the void-flow model, as the voids in the void-flow model connect the feed side and permeate side of membrane active layers and have diameters of a few nanometers while the voids allegedly seen in the TEM images do not seem to connect the feed side and permeate side of membrane active layers and have diameters of tens of nanometers.[10–15]

A different interpretation of the globular features in cross-sectional TEM images of polyamide active layers was proposed by Pacheco *et al.*[16] who indicated that these features correspond to nodules. Based TEM images of the active layer of a brackish water reverse osmosis (RO) membrane in which globular features 20-60 nm in size were visible, Pacheco *et al.* further proposed that active layers are composed of a dense nodular base from which the ridge-and-valley structure extends outwards. Similar features to those interpreted as nodules by Pacheco *et al.* and voids by others[11–15] are visible in TEM images reported by others,[17–19] although they were not identified as nodules or voids.

While it is not settled in the peer-reviewed literature whether the globular features in TEM images discussed here are hollow voids or dense nodules,[20] because the only evidence of this feature are the electron microscopy images themselves, the TEM images reported in the literature[12–19] show that the features are significantly lighter in shade than the rest of the active layer when bright-field imaging is used, indicating that they have a lower electron density than surrounding regions. Therefore, these features are likely hollow voids or correspond to regions of significantly lower polymer density, instead of dense nodules. The postulate that the features are voids is supported by the recent scanning electron microscopy (SEM) work by Yan *et al.*[21] who reported cross-sectional SEM images with features interpreted as voids having diameters of tens to over a hundred of nanometers. If these features are confirmed to be voids, it would have

important implications in the understanding of the mechanisms of permeation of water and contaminants through polyamide membranes since, as described above, current transport models do not account for voids. Confirming the existence of voids in polyamide active layers would also motivate the development of methods to measure volume fractions of voids in active layers to allow for a more accurate understanding of active layer structure and interpretation of active layer characterization data, e.g., partition and diffusion coefficients in polyamide.

Accordingly, the objectives of this study were to evaluate whether (1) the features observed in the TEM cross-sectional images are in fact voids, (2) voids exist in a broad range of TFC membranes, (3) voids account for a significant volume fraction of the active layers, and (4) voids are filled with water when the membranes are immersed in it. To accomplish these objectives, a broad range of TFC membranes were studied, the volume fractions accounted for by the globular features in the active layers were measured by TEM image analyses, and the volume fractions accounted for by voids in their active layers were measured using two non-microscopy techniques - quartz crystal microbalance (QCM) measurements of water uptake by polyamide active layers and spectroscopic ellipsometry estimates of the refractive indices of active layers. The volume fractions obtained for the globular features through TEM image analyses and voids through QCM and ellipsometry analyses were compared to each other. Similar volume fractions obtained with the different analyses methods would provide evidence in support of the hypothesis that the globular features are actually voids, not nodules, as the different methods are based on completely different physical principles. Elemental mapping of membrane cross sections using energy dispersive X-ray spectroscopy and electron energy loss spectroscopy were also used to evaluate the elemental composition of the globular features as to ascertain their nodular or void nature. The QCM measurements also served to assess whether the

voids filled up with water. This study presents experimental results and their corresponding discussion, as well as the implications of the findings to the study and development of polyamide TFC membranes.

3.2 Materials and Methods

(See extended version in the Supporting Information)

3.2.1. Target membranes and sample preparation

Five polyamide TFC membranes of various performance levels were studied: NF90,[22] XLE[23] and SW30HR[24] received as flat sheets in dry state (Dow Filmtec, Minneapolis, MN) and ESPA3[25] and SWC4+[26] received as flat sheets in wet state (Hydranautics, Oceanside, CA). Attenuated total reflectance Fourier transform infrared spectroscopy (ATR-FTIR) analyses (see Figure B.S1.1. in Supporting Information) indicated that all membranes have aromatic polyamide active layers and that the active layer of the SW30HR membrane has a coating, which is likely polyvinyl alcohol.[27] Membrane samples were initially prepared as 2.5×5.0 cm^2 coupons thoroughly rinsed with and stored in ultrapure water (>18 MΩ·cm). Before further sample preparation for TEM, QCM, ellipsometry and atomic force microscopy (AFM) analyses, coupons were blot dried with filter paper and air dried overnight.

3.2.2. TEM analyses

For TEM analyses, a membrane sample preparation procedure similar to that described by Tang et al[17] was used. In brief, membrane samples were dehydrated with 100% ethanol, infiltrated and embedded with LR White resin (London Resin Co., Reading, UK) diluted in ethanol, cured at 48 ℃ for 3 days, and cut into thin (~90-100 nm) slices with a Sorvall MT 6000 Ultramicrotome (RMC Co., Tucson, AR). Three TEM images were taken for each membrane using a JEOL 100CX II TEM (JEOL USA, Peabody, MA) at an acceleration voltage of 80 kV. Control TEM images were obtained for SWC4+ membrane samples dried using supercritical

CO_2 drying, which confirmed that air/ethanol drying did not affect the active layer structure (see Figure B.S1.2 in Supporting Information).

3.2.3. Scanning transmission electron microscopy-energy dispersive X-ray spectroscopy (STEM-EDS) and electron energy loss spectroscopy (STEM-EELS) analyses

Membrane sample preparation and sectioning for STEM-EDS and STEM-EELS analyses were performed in the same manner as for TEM analyses. The STEM-EDS and STEM-EELS analyses of SWC4+ membrane samples were performed with an aberration corrected scanning transmission electron microscope (STEM) FEI Titan (FEI, Houston, TX) at an acceleration voltage of 200 kV. The Titan was equipped with a SuperX EDS system with four Bruker silicon drift detectors (Bruker AXS, Madison, WI) and a Gatan Enfinium spectrometer with high-speed spectrum imaging (Gatan Inc., Pleasanton, CA). Multiple locations on SWC4+ sample cross-sections were analyzed.

3.2.4. SEM analyses

Membrane coupons were removed from the ultrapure water and gently shaken twice to remove excess water. Next, the samples were immersed in liquid nitrogen for 30 seconds, taken out and cracked in air. Secondary electron SEM imaging of membrane cross-sections was performed with a FEI Helios 600 Nanolab Dual Beam System after the samples were coated with a thin film (<5 nm) of Au (60%):Pd (40%) (Ted Pella, Redding, CA) using a Cressington 108 Auto Sputter Coater (Cressington Scientific Instruments, Watford, UK). Triplicate images were taken for each membrane studied.

3.2.5. Active layer isolation

For ellipsometry and AFM analyses, active layers were isolated onto gold-coated QCM sensors and silicon wafers, with the membrane surface facing the sensor/wafer, by peeling off by hand the polyester backing and dissolving the polysulfone support with dimethylformamide (see

details in Supporting Information). The isolation procedure was similar to that described elsewhere,[28] is based on a protocol reported by Freger,[29] and has been successfully used by various research groups[16,21,30] and shown not to affect physico-chemical and transport properties of active layers.[28,31] Any potential gaps created between the isolated active layers and sensor/wafer surfaces due to membrane surface roughness were shown not to affect the active layer void fractions estimated from QCM and ellipsometry analyses as shown in Section 3.3.5.

3.2.6. QCM analyses

A Q-Sense E4 QCM (Biolin Scientific, Lithicum Heights, MD) was used to measure the areal mass (ng·cm^{-2}) of active layer polymer isolated on QCM sensors and the areal mass of water absorbed by active layers. For each membrane, two samples were tested, each with an area of 1.54 cm^2, and for each sample duplicate measurements of water sorption were conducted in each liquid and vapor environments. The mass of active layer isolated on a sensor (m_{AL}) was obtained as described in a previous study[28] from the difference in QCM response between the uncoated sensor and the sensor coated with the active layer. Water uptake in liquid environment (m_l) was obtained from the difference in QCM response to the coated sensor exposed to dry nitrogen (<0.02% relative humidity-RH) and to ultrapure water. Similarly, water sorption in vapor environment (m_v) was obtained from the difference in QCM response to the coated sensor exposed to dry nitrogen and to humidified nitrogen gas at 96% RH. Full details of water sorption measurements in ultrapure water and water vapor can be found in the Supporting Information. In all cases, an uncoated control sensor was exposed to the same liquids or gases as the coated sensors to account for the changes in QCM response caused by variations in the viscosity and density of the fluid to which the sensor was exposed.[28,32,33] All experiments were performed at 22 ±0.02 ℃.

3.2.7. Ellipsometry analyses

The refractive indices of the membrane active layers were obtained using spectroscopic ellipsometry. Samples consisted of active layers isolated on silicon wafers. Triplicate samples were analyzed for each membrane, and three locations (0.3 cm^2 each) were analyzed in each sample using a variable angle spectroscopic ellipsometer (J.A. Woollam Co., Lincoln, NE). Data acquisition was performed at incidence angles of 65 °, 70 ° and 75 ° and wavelength range of 380-1000 nm using the Autoretarder feature. Data analysis was performed using the software WVASE® (J.A. Woollam Co.) where the overall sample structure was modeled as a thin polymer layer on a 2-nm thick silicon dioxide layer[34] supported by a 1-mm thick silicon substrate. Cauchy dispersion formulae[35] were used to describe the optical properties of the polymer layer by selecting the appropriate option in the WVASE® software whose database also contains the well-known optical constants for silicon and silicon dioxide. The refractive index and thickness of the active layers were obtained with the WVASE® software by fitting the data to the model until a minimized mean squared error of less than 20 was reached.

3.2.8. AFM analyses

Membrane surface roughness and active layer thickness was characterized with an Asylum Research MFP-3D AFM (Santa Barbara, CA) and Tap300Al tips (BudgetSensors, Sofia, Bulgaria) in tapping mode. For surface roughness measurements, 2.5×5.0 cm^2 membrane coupons were rinsed and dried as described above. For each membrane sample, the membrane surface topography was obtained by scanning the AFM tip in tapping mode over the membrane sample surface, covering areas of 10×10 μm^2. Surface roughness was reported as root-mean-square roughness and was calculated from the surface topography profiles as described by Kwak *et al.*[36] For active layer thickness measurements, a procedure similar to that described by Freger[29] (see details in Supporting Information and Chapter 2) was used. Briefly, active layers

isolated on silicon wafers were gently scratched with a sharp razor to expose the surface of the wafer and obtain multiple polyamide thin strips. The AFM analysis was then used to obtain topography profiles covering areas ~30 ×30 μm^2 in size, which allowed the determination of the average thickness of the isolated polyamide film from the difference of the average height of the polyamide surface and the average height of the silicon wafer surface. Triplicate samples of each membrane were analyzed for each surface roughness and active layer thickness measurements.

3.3. Results and Discussion

3.3.1. Presence of globular features in active layers

Figure 3.1 shows representative cross-sectional bright-field TEM and SEM images of the NF90, ESPA3 and SWC4+ membranes. Similar images (not shown) were obtained for the XLE and SW30HR membranes. For each membrane, the region corresponding to the active layer is outlined in red dotted lines. For all membranes, the TEM images show well-defined features, lighter in color than the surrounding polyamide, similar to the features identified as voids[11–15] and nodules[16] in the literature. The grayscale contrast between any two regions in TEM images is produced by the difference in the number of electrons of the analysis beam that pass through the two regions of the sample.[37] Areas with lower electron density (i.e., fewer or smaller atoms) allow for the transmission of a higher number of electrons of the analysis beam, resulting in corresponding lighter image areas in bright-field TEM images. Thus, the significantly lighter color of the globular features with respect to the surrounding polymer indicates that they either are voids or correspond to regions with a significantly lower polymer density than the surrounding polyamide.

The color contrast in the secondary electron SEM images in Figure 1 provides an indication of the cross-sectional topology of the membrane samples.[37] Dark areas correspond to

depressions (from which secondary electrons generated cannot reach the detector), which are indicative of the existence of voids in the active layers. The SEM images in Figure 3.1 are consistent with those reported by Yan *et al.*[21] and show that the active layer cross sections feature distinct depressions of similar size as the globular features observed in the TEM images. This supports the hypothesis that the active layers are not continuous dense polymer films, but rather have voids in them. Thus, the TEM and SEM evidence together indicate that the active layer globular features identified as voids by some[11–15,21] and nodules by others[16] commonly exist in polyamide RO and NF membranes of a broad performance range.

3.3.2. Volume fraction of active layer accounted for by globular features from TEM image analyses

Image analysis of the TEM micrographs was performed in order to estimate the volume fractions of the active layers occupied by the globular features. For each TEM image, the software ImageJ 1.47v[38] was used to obtain the area of the active layer and the area of the globular features. The areal fraction of the active layer occupied by the features in a given image ($f_{feature,i}^{areal}$) was calculated as the ratio between the total features area and the total active layer area. It was assumed that for any given membrane, the average areal fraction occupied by the

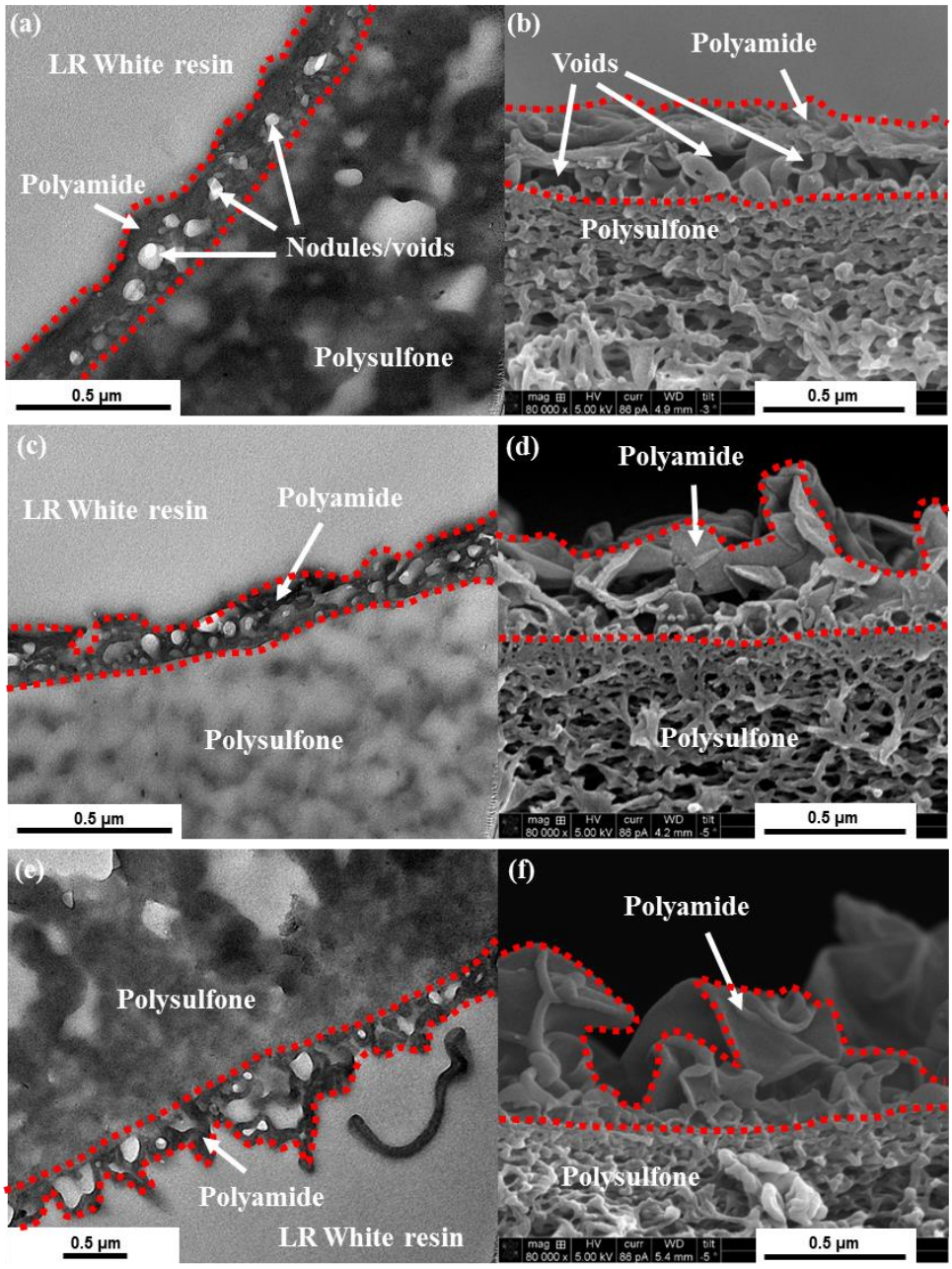

Figure 3.1. Cross-sectional TEM and SEM images of samples of the (a,b) NF90, (c,d) ESPA3, and (e,f) SWC4+ membranes. For any given membrane, the TEM and SEM images do not correspond to the exact same cross section. The perimeter of the active layers of all membranes is outlined in red dotted lines, and examples of globular features (i.e., nodules/voids) in the active layers are indicated by arrows for the NF90 membrane. The nodules/voids are also visible in the images of the ESPA3 and SWC4+ membranes.

features obtained from arbitrary 2D TEM images was representative of the corresponding 3D volume fraction ($f_{feature}^{volume}$) as given by

$$f_{feature}^{volume} = \left(\frac{1}{m}\right)\sum_{i=1}^{m} f_{feature,i}^{areal}\,, \tag{3.1}$$

where *m* corresponds to the number of TEM images analyzed. The features volume fractions calculated using this approach are shown in Figure 3.2 as empty bars and were all in the 27-32% range. An analysis of variance (ANOVA) F-test of the results indicates that, with a 95% confidence level, all features volume fractions are *not* statistically different from each other. The SEM images were not used to obtain the void fractions because: (1) the cut to obtain the cross sections for SEM (i.e., liquid nitrogen freezing followed by breakage by hand) is not controlled or clean as it is for TEM (i.e., ultramicrotome cut), and (2) it is a very subjective task to distinguish the polyamide and void regions that are on the focus plane of the SEM image from those that are also visible in the image but are a few/several nanometers behind or before the focus plane.

3.3.3. Void volume fraction from water uptake measurements.

Table 3.1 presents the results for water uptake ($ng \cdot cm^{-2}$) by active layers when exposed to ultrapure water and humidified nitrogen gas at 96% RH. The results show that for all membranes, water uptake was significantly larger (2-5 fold) when the active layer was exposed to liquid water than when it was exposed to humidified nitrogen gas. From a thermodynamic equilibrium perspective, if the active layer were a dense polymer phase, the water uptake by the active layer should be the same when exposed to liquid water as when exposed to humidified nitrogen gas at 100% RH (and, by extension, very similar to when exposed to humidified nitrogen gas at 96% RH). This is because both environments represent a water activity of ≈1

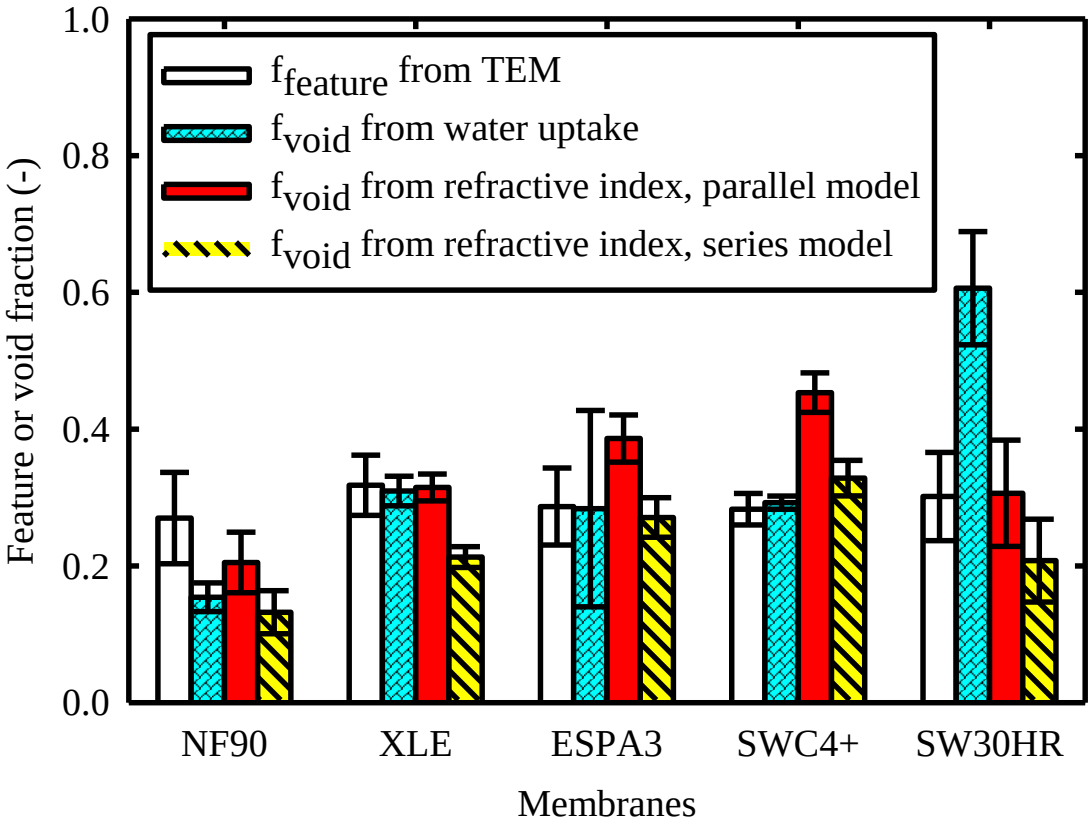

Figure 3.2. Feature volume fractions ($f_{feature}^{volume}$) and void volume fractions (f_{void}) in the active layers of five commercial polyamide thin-film composite membranes. Feature volume fractions (empty bars) were obtained from analyses of TEM cross-sectional images. Void volume fractions were obtained using (i) water uptake measurements with a QCM and Equation 3.3 (blue brick bars), and (ii) refractive index estimates by spectroscopic ellipsometry and Equations 4 (parallel model, solid red bars) and 5 (series model, cross hatched yellow bars). For each membrane, the reported values were obtained as follows. The feature volume fraction corresponds to the average of the values obtained for triplicate images. The void volume fraction from water uptake measurements corresponds to the average of the values obtained for duplicate samples (1.54 cm^2 each), where duplicate measurements were taken in each sample. The void fraction from refractive index measurements corresponds to the average of the values obtained for triplicate samples, where three locations (0.3 cm^2 each) were analyzed in each sample. The error bars for the feature volume fractions represent standard deviation. All other error bars represent the propagated error obtained in calculations using the uncertainties in Table 3.1.

outside the active layer, and thermodynamics indicates that it is the water activity outside the active layer, not the water state (i.e., liquid or vapor), that determines the activity of water inside the active layer (see detailed thermodynamic discussion in the Supporting Information). For this reason, other researchers in previous studies[30,39] have also performed water sorption experiments with humidified inert gases at water vapor activities near unity (i.e., 95% RH or 0.95 water activity). Thus, the different water uptake results in Table 3.1 with liquid water from those with humidified nitrogen gas indicate that the active layers are not dense polymer films.

The larger water uptake from the liquid phase compared with that from the humidified nitrogen gas phase can be explained by the existence of permeable voids within the active layer as depicted in Figure 3.3. From thermodynamics (see Supporting Information), when the active layers were exposed to humidified nitrogen gas, both water and nitrogen partitioned into the polyamide phase and saturated the voids. Nitrogen mass uptake by polyamide was negligible because the baseline readings were performed with the active layers exposed to pure dry nitrogen, and the partial pressure (i.e., activity) of nitrogen in humidified nitrogen gas at 96% RH (98,680 Pa) is only 2.6% lower than the partial pressure of nitrogen in pure dry nitrogen (101,325 Pa). Likewise, humidified nitrogen uptake by the voids contributed a negligible mass increase because the densities of dry (1,157 $kg \cdot m^{-3}$) and humidified (1,146 $kg \cdot m^{-3}$) nitrogen gas are within 1% of each other (see derivation of densities in Supporting Information). Therefore, given that the nitrogen mass uptake by polyamide and humidified nitrogen gas mass uptake by the voids were negligible, then the mass increase measured during tests with humidified nitrogen gas corresponds to the mass uptake associated with water uptake by polyamide (m_v).

As discussed above, water uptake by polyamide was the same when the active layers were exposed to liquid water as when they were exposed to humidified nitrogen gas. However,

Table 3.1. Polymer mass (m_{AL}), water uptake in humidified nitrogen (m_v), water uptake in liquid water (m_l), thickness (δ), and refractive index at 589 nm (n_{AL}) of membrane active layers.

Membrane	Application	m_{AL} [a,d] (ng·cm^{-2})	m_v [a,d] (ng·cm^{-2})	m_l [a,d] (ng·cm^{-2})	δ [b,e] (nm)	n_{AL} [c,e] (-)
NF90	Nanofiltration	17257 ± 128	2163 ± 95	4302 ± 390	120 ± 13	1.56 ± 0.03
XLE	Brackish water	14060 ± 1065	1763 ± 199	5252 ± 167	136 ± 23	1.48 ± 0.01
ESPA3	Brackish water	13767 ± 915	1682 ± 7	4872 ± 1732	76 ± 12	1.43 ± 0.02
SWC4+	Seawater	13415 ± 1588	1868 ± 470	5029 ± 2	113 ± 14	1.38 ± 0.02
SW30HR	Seawater	18558 ± 842	2309 ± 33	11377 ± 1621	176 ± 25	1.49 ± 0.05

Notes: [a] Areal masses (m_{AL}, m_v, m_l) were obtained from duplicate measurements in each of two samples (1.54 cm^2 each). [b] Active layer thickness (δ) was obtained from analyses of triplicate samples (30×30 μm^2 analysis area in each). [c] Active layer refractive index (n_{AL}) was obtained from analyses of three locations in each of triplicate samples (a total of 9 points per membrane, each point having an area of 0.3 cm^2). [d] Uncertainties represent the difference between the average result for either sample and the average of the two samples analyzed. [e] Uncertainties represent standard deviations.

since polyamide is permeable to water, exposure of the active layers to liquid water would also result in water filling the voids. The total mass uptake measured during tests with liquid water (m_l) can therefore be used to calculate the mass uptake associated to the liquid water that filled the voids as $m_l - m_v$. Then the water uptake measurements can be used to calculate the void fraction in active layers (f_{void}) using the expression

$$f_{void} = \frac{total\ void\ volume}{active\ layer\ volume} = \frac{(m_l - m_v)\rho_{AL}}{\rho_w m_{AL}}, \quad (3.2)$$

where m_l (ng·cm^{-2}) and m_v (ng·cm^{-2}) correspond to the water uptake when active layers were exposed to liquid water and humidified nitrogen, respectively, and m_{AL} (ng·cm^{-2}), ρ_{AL}=1.24 g·cm^{-3},[39,40] and ρ_w=1.0 g·cm^{-3} are the active layer polymer mass, active layer density, and water density, respectively. Notice that the thickness of the active layer sample analyzed is accounted for by the m_{AL}/ρ_{AL} ratio. In Equation 3.2, it is assumed that the swelling of active layers in liquid water is the same as in water vapor. While there is no reason to believe that this is not the case, even in the worst-case scenario where no swelling occurred under humidified nitrogen gas but swelling under liquid water were in the 2-35% range reported in the literature for aromatic polyamide active layers,[29,41] the error in the void fractions estimated with Equation 3.2 would be at most 35%.

Void fractions of the active layers studied were calculated using Equation 3.2 and the corresponding results are presented in Figure 3.2 as (blue) brick bars. The features volume fractions obtained from TEM image analysis and the void fractions calculated from water uptake measurements were compared through Welch's t-tests. Results show that, with a 95% confidence level, the features volume fractions and void fractions are significantly different only for the SW30HR membrane. For the other four membranes, the features volume fractions and void fractions are statistically the same. It is not known why the SW30HR void fraction

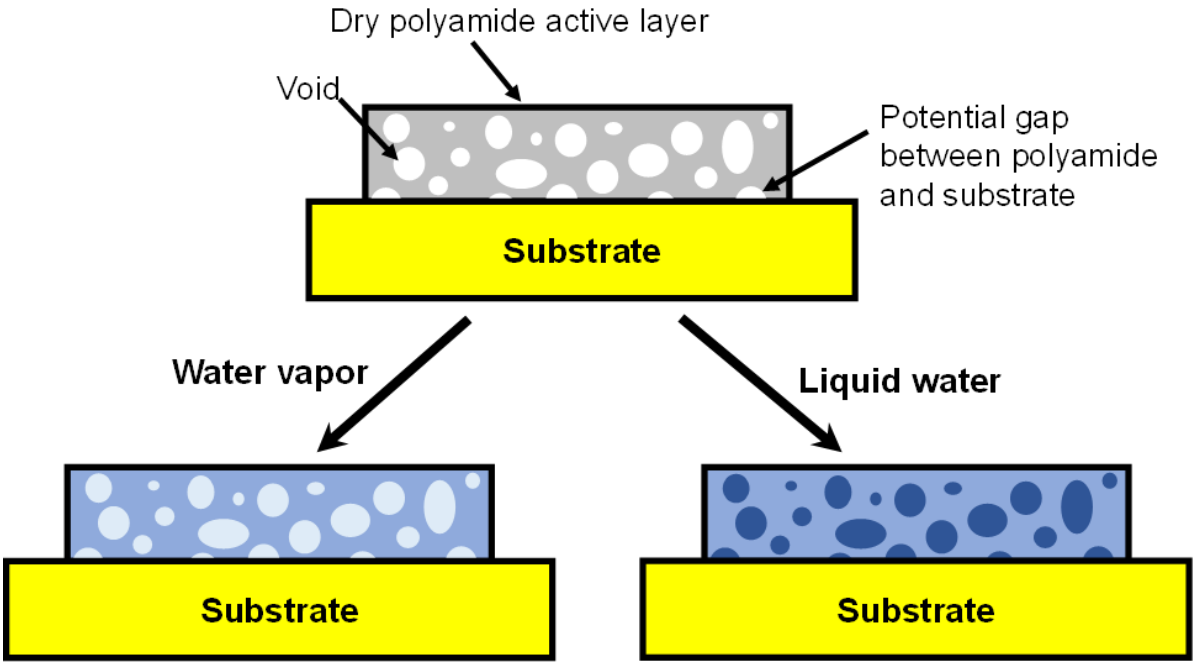

Figure 3.3. Illustration of an isolated polyamide active layer when exposed to dry nitrogen (top), water vapor via humidified nitrogen gas (bottom left) and liquid water (bottom right). When the active layer is exposed to humidified nitrogen gas, nitrogen and water partition into the polyamide phase and the voids saturate with humidified nitrogen. In contrast, when the active layer is exposed to liquid water, water partitions into the polyamide phase and bulk water, not humidified gas, fills the voids within the active layer. Any potential gaps existing between the isolated active layers and sensor surfaces due to the roughness of the active layer were shown to not affect the active layer void fractions estimated from QCM and ellipsometry analyses.

obtained from water uptake measurements is significantly larger than the features volume fraction obtained from TEM image analyses, but it is reasonable to speculate that it may be related to the PVA coating in its active layer. SW30HR is the only membrane tested that had a coating, and PVA has a significantly higher water absorption (30 wt%[42]) compared to fully-aromatic polyamide (11-20 wt% in the literature[30,39] and 12-14 wt% in this study). Nevertheless, the agreement between the features volume fractions obtained from TEM image analyses and the void fractions obtained from water uptake measurements for all active layers made of only polyamide indicates that the features are likely voids, not dense nodules.

To further evaluate the void nature of the globular features, STEM-EDS and STEM-EELS analyses of SWC4+ membrane cross-sections were performed. Figure 3.4 shows a representative dark-field STEM image (left), and corresponding nitrogen and sulfur (middle) and carbon (right) STEM-EDS mappings. In the dark-field STEM image, the nodules appear as darker regions compared to the surrounding polymer. In the STEM-EDS elemental mappings, dark regions within the red and blue areas correspond to regions where nitrogen content and carbon content, respectively, are significantly lower (or absent) compared to the surrounding polyamide. Similar observations were made in STEM-EELS images (Figure 3.5). Therefore, STEM-EDS/EELS images confirm that the features are voids or have significantly lower polymer density compared to the surrounding polyamide.

3.3.4. Void fraction from refractive indices

Table 3.1 presents the refractive indices at a light wavelength of 589 nm obtained for the active layers studied by spectroscopic ellipsometry. Assuming that the active layers have voids in them, as supported by the TEM, STEM-EDS/EELS, SEM and QCM results above, one can conceptualize the active layers as a composite having polyamide as the matrix and voids as the dispersed phase. Therefore, the refractive index measured by ellipsometry constitutes the

effective refractive index of the active layer (n_{AL}) and can be related to the refractive indices of polyamide at 589 nm ($n_{polymer}$=1.70)[43] and air (n_{void}=1)[44] filling the voids using effective-medium approximation (EMA) models.[45]

The EMA models treat heterogeneous media as a homogeneous medium with some effective properties. For the case of a solid-air composite like polyamide active layers, the effective properties (e.g., refractive index) are assumed to be independent of the heterogeneity of void size, void size distribution, and spatial distribution of voids. Two of the most commonly used EMA models for the calculation of effective refractive indices are the parallel and series models given by[45]

$$n_{AL} = (1 - f_{void})n_{polymer} + f_{void}n_{void}, \quad (3.3)$$

and

$$\frac{1}{n_{AL}} = \frac{1-f_{void}}{n_{polymer}} + \frac{f_{void}}{n_{void}}, \quad (3.4)$$

respectively. These two models cover a wide range of the variability among the refractive index values obtained using the different existing EMA models, with the parallel and series models giving values in the higher and lower ends of the spectrum, respectively.[45]

Void fractions were calculated using both the parallel and series models and n_{AL} values obtained by ellipsometry and Equations 3.3 and 3.4, and present the corresponding results in Figure 3.2. Welch's t-tests (95% confidence level) were performed comparing the void fractions obtained from ellipsometry analyses to the features volume fractions obtained from TEM analyses and the void fractions obtained from water uptake measurements. Results showed that for all possible comparisons (i.e., f_{void} from series model versus $f_{feature}^{volume}$ from TEM results, f_{void} from parallel model versus f_{void} from QCM results, etc.), only one of the membranes (SWC4+)

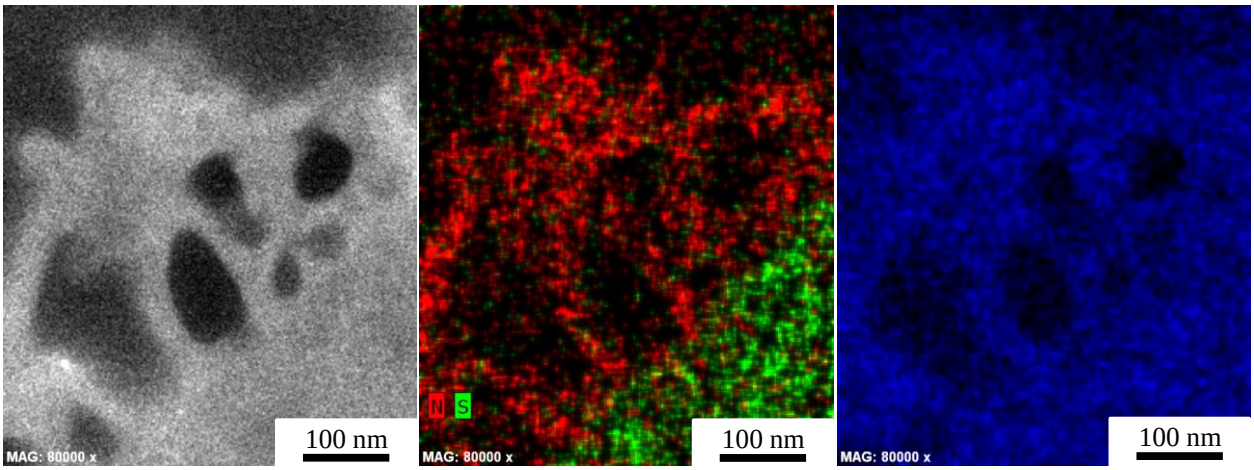

Figure 3.4. Dark-field STEM image (left), and corresponding nitrogen and sulfur (middle) and carbon (right) STEM-EDS mappings, of a cross section of the active layer of a SWC4+ membrane sample.

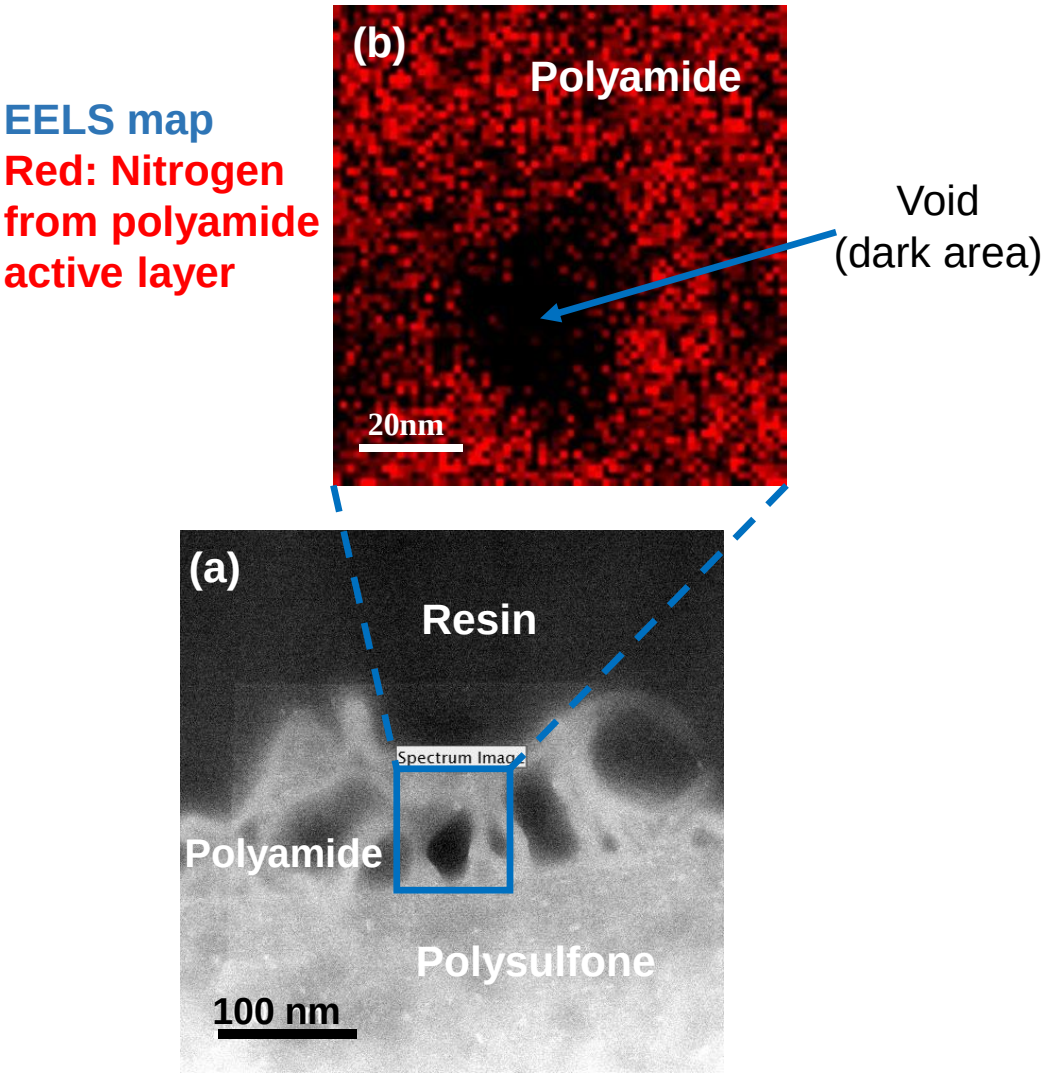

Figure 3.5. Representative (a) dark-field STEM image and (b) corresponding nitrogen EELS mapping of a cross-section of the active layer of a SWC4+ RO membrane sample. The red area in the EELS mapping corresponds to regions containing nitrogen which is present in polyamide. The dark area within the red area corresponds to a localized region where nitrogen content is significantly lower (or absent) compared to the surrounding polyamide, therefore indicating the presence of a void.

studied had a void fraction obtained from refractive index values that was statistically different from the features volume fraction obtained from TEM images or the void fraction obtained from water uptake tests. The agreement between ellipsometry, TEM and QCM results further supports the existence of voids in the active layers as well as the void nature of the globular features.

3.3.5. Effect of membrane surface roughness and active layer thickness on void fractions estimated by water uptake and refractive index measurements

As described in the Materials and Methods, water uptake measurements involved the isolation of the active layers onto QCM sensors. Given that the surface of the active layers faced the sensors, there was the possibility that the roughness of the active layers may have resulted in gaps between the sensor and the polyamide phase (see Figure 3.3). If these gaps filled with liquid water during QCM measurements, then the water uptake (m_l) measurements, and the corresponding void fractions calculated with Equation 3.2 would be biased towards larger values. Thus, it was evaluated whether water uptake and surface roughness were correlated to each other. Towards this purpose, Figure 3.6(a) plotted water uptake normalized by active layer polymer mass (m_l/m_{AL}) in the *y*-axis and membrane surface roughness normalized by active layer thickness (σ/δ) in the *x*-axis. Both active layer roughness and thickness were measured using AFM analysis and the results are presented in Table 3.1. As observed in Figure 3.6(a), a higher surface roughness did not result in a higher water uptake when the active layer was exposed to liquid water. In fact, a linear fit of the data indicates a negative slope (-0.17) with a poor goodness-of-fitting (R^2=0.26). Thus, it was concluded that surface roughness did not significantly affect the void fraction calculated based on water uptake measurements and Equation 3.2.

Using a similar reasoning as that used for water uptake measurements with a QCM, it could be argued that there is the possibility that the gaps introduced by the surface roughness between the polyamide film and the silicon wafer may have biased the measured refractive indices and corresponding calculated void fractions towards lower and higher values, respectively. Thus, it was evaluated whether refractive indices and surface roughness were correlated to each other. As observed in Figure 3.6(b), a higher surface roughness was not strongly correlated to a lower refractive index, with a linear fit of the data indicating a very small negative slope (-0.0831) with a poor goodness-of-fitting (R^2=0.25). Thus, it was concluded that the surface roughness did not significantly affect the void fraction obtained from refractive indices measured with ellipsometry.

In a similar manner to the analysis performed for the effect of membrane surface roughness, the liquid water uptake normalized by active layer polymer mass (m_l / m_{AL}) versus active layer thickness (δ) was plotted (not shown) and it was found that there was not a significant correlation between normalized water uptake and active layer thickness (i.e., slope = -0.0002 and R^2=0.007 when the outlier results of the coated active layer of the SW30HR membrane were excluded, and slope = 0.0026 and R^2=0.51 including the SW30HR results). A plot of the active layer refractive indices versus active layer thicknesses also showed no significant correlation between the two parameters (i.e., slope = -0.0007 and R^2=0.13 including the results for all membranes). Therefore, the results indicate that active layer thickness did not bias the void fractions calculated based on water uptake measurements or refractive indices.

3.3.6. Size and interconnectivity of voids

The existence of voids with diameters >1 nm (including >100 nm) is directly supported by the TEM[11–19] and SEM[11,21] images reported elsewhere, as well as the TEM,

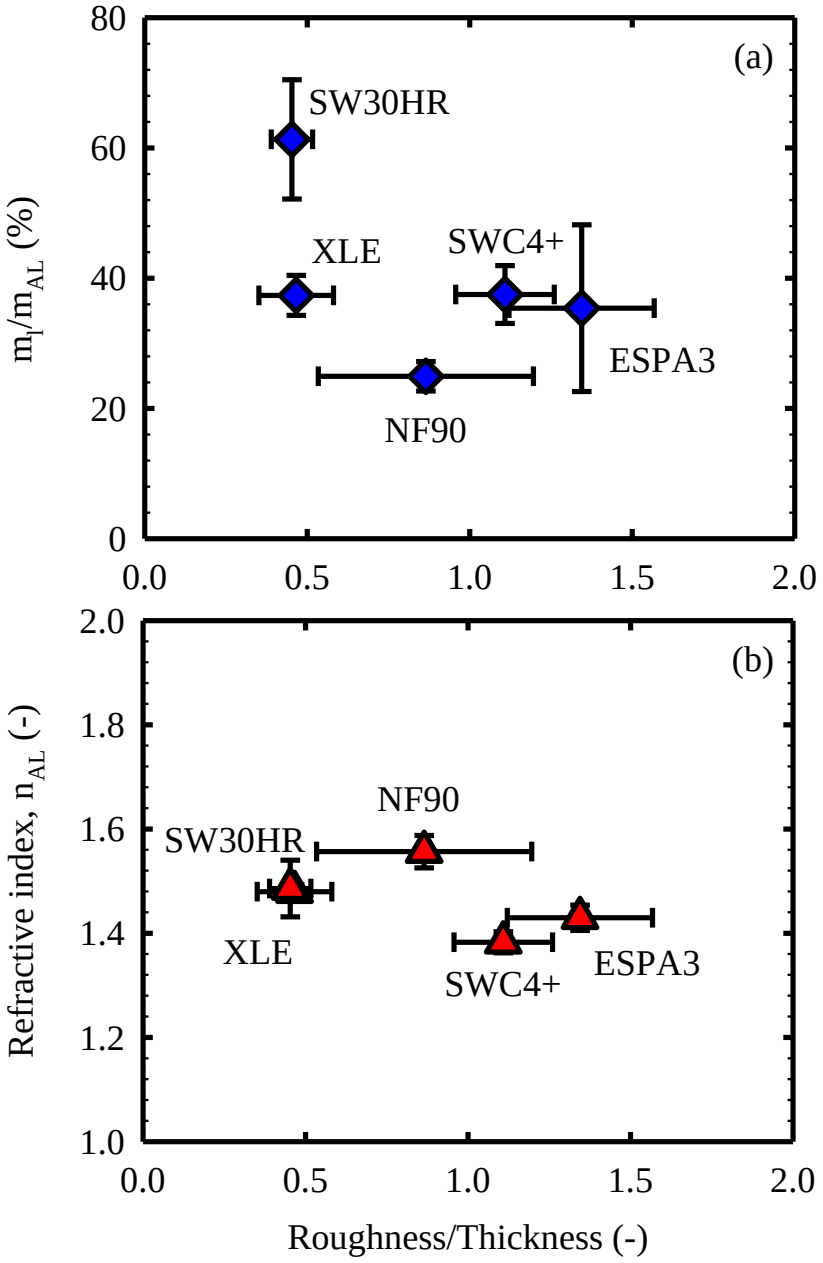

Figure 3.6. (a) Water uptake when the active layer is exposed to liquid water (m_l) normalized by active layer polymer mass (m_{AL}), and (b) refractive index as a function of root-mean-square membrane surface roughness (σ) normalized by active layer thickness (δ). The calculated roughness values for the NF90, XLE, ESPA3, SWC4+, and SW30HR membranes were 104 ±38, 63 ±11, 102 ±6, 125 ±7, and 80 ±2, respectively. Error bars represent the propagated error obtained in calculations using the roughness uncertainties reported above and the uncertainties for all other parameters reported in Table 3.1.

STEM-EDS/EELS and SEM images reported in this study. Given that RO/NF membranes have high levels of sodium chloride rejection (i.e., >85% for NF90[22] and >99% for all others[23–26]), the existence of voids larger than 1 nm in their active layers indicates that if the voids are interconnected, then the interconnectivity is such that the voids do not form passageways from the feed side to the permeate side; however, this does not exclude the possibility of some level of interconnectivity between voids. This conclusion is supported by the TEM images in this and other studies[11–19] which show clearly defined voids but not clearly defined passageways from the feed to the permeate side. Additionally, the lack of interconnectivity between the voids and the feed side is supported by TEM images reported by Pacheco *et al.*[16] which show that the filtration of aqueous solutions containing 10 nm and 30 nm gold nanoparticles resulted in nanoparticle deposition on the active layer surface, not inside the active layer. Finally, SEM images reported by Yan *et al.*[21] suggest that there is some level of interconnectivity between the voids, and perhaps between the voids and the backside of the active layer, but not between the voids and the feed side. Comprehensive characterization of the topology of the voids in polyamide active layer requires further research and is beyond of the scope of this study.

3.3.7. Implications on RO/NF science and technology

Existing analytical, numerical and atomistic approaches for modelling the transport of water and solutes through RO/NF membranes[8,9,20,40,46–53] and the active layer formation[20,40,47–49] do not take into account the existence of voids. Therefore, future transport modelling efforts should evaluate the importance of the presence of voids in active layers (e.g., water/solute partitioning events at polyamide-water interfaces at the voids' walls, non-constant water/solute diffusion coefficients in the active layer), and active layer formation modeling efforts should target a more accurate active layer structure that includes the voids. The results from this study provide quantitative ranges of void volume fractions and sizes that can be used as initial

simulation values in transport modeling and calibration values in active layer formation modeling. Also, given that there is no evidence that the voids have been taken into account in membrane optimization efforts, this work reveals to membrane developers that there is an untapped complex parameter (i.e., void size distribution, volume fraction, and topology) that could potentially be optimized to develop improved membranes.

3.4. Conclusion

The presence of voids in the aromatic polyamide active layers of TFC membranes for water purification was studied using a selection of commercial membranes with a broad range of performance levels. The study was partly motivated by conflicting interpretations in the literature of globular features observed in cross-sectional electron microscopy images of polyamide TFC membranes that some authors [11,12,14,15] have interpreted as voids and some others as nodules [16]. We evaluated the void or nodular nature of the globular features using TEM and SEM imaging as well as STEM-EDS and STEM-EELS elemental mapping, measured the volume fraction of the active layer occupied by the features using TEM image analysis and measured the void volume fraction in active layers using water sorption and refractive index analyses. Our results and discussion support the following conclusions:

- The globular features observed in TEM images are voids, not nodules. This conclusion is supported by (i) the matching volume fractions occupied by the features (TEM image analyses) and volume fraction occupied by voids (water sorption and refractive index analyses) in the active layers, and (ii) the elemental mapping results by STEM-EDS and STEM-EELS.
- The voids are a common feature of aromatic polyamide active layers as they were observed in the active layers of all five TFC membranes studied which covered a broad

range of performance levels including nanofiltration, brackish water RO and seawater RO.

- Voids accounted for a significant volume fraction (15-32%) of the membrane active layers.
- Voids are filled with liquid water when the membranes are immersed in it.
- The voids in polyamide active layers do not form passageways connecting the feed and permeate sides, but rather are cavities disconnected from the feed side. Further research is required to assess whether the voids are interconnected to each other.

In addition to the findings above, this study contributed three different methods to measure void volume fraction in active layers, and experimentally measured void volume fractions that can be used as input or calibration parameters in future modeling studies of active layer formation or water and solute transport. The confirmation of the existence of voids as common features in the polyamide active layers of TFC membranes indicates that the voids are an active layer property that could potentially be targeted for optimization towards the development of improved membranes.

3.5. Acknowledgments

The author thanks Dr. Rene Lopez for helpful discussion about ellipsometry and Yingchi Liu and Chengcheng Feng for their help in ellipsometry experiments. The author also thanks Wallace Ambrose and Amar S. Kumbhar (TEM), Yang Liu (STEM-EDS/EELS), and Carrie Donley (SEM) for assistance in acquisition of microscopy images and helpful discussions. The TEM, AFM and ellipsometry analyses were conducted at the Chapel Hill Analytical and Nanofabrication Laboratory in Chapel Hill, NC. The STEM-EDS/EELS analyses were performed at the Analytical Instrumentation Facility of the North Carolina State University. This

work was supported by the National Science Foundation (NSF) Grants Opportunities for Academic Liaison with Industry (GOALI) and Chemical and Biological Separations programs under Award#1264690, and NSF Environmental Engineering program under Award#1336532.

3.6. Supporting Information Available

Materials and methods (extended version). Thermodynamics of water partitioning into active layers exposed to liquid water and humidified nitrogen gas. Mass density of dry and humidified nitrogen gas. This information is available in Appendix 8.

REFERENCES

(1) Greenlee, L. F.; Lawler, D. F.; Freeman, B. D.; Marrot, B.; Moulin, P. Reverse osmosis desalination: water sources, technology, and today's challenges. *Water Res.* **2009**, *43*, 2317–2348.

(2) Jacangelo, J. G.; Trussell, R. R.; Watson, M. Role of membrane technology in drinking water treatment in the United States. *Desalination* **1997**, *113*, 119–127.

(3) Van der Bruggen, B.; Everaert, K.; Wilms, D.; Vandecasteele, C. Application of nanofiltration for removal of pesticides, nitrate and hardness from ground water: rejection properties and economic evaluation. *J. Membr. Sci.* **2001**, *193*, 239–248.

(4) Yip, N. Y.; Tiraferri, A.; Phillip, W. A.; Schiffman, J. D.; Hoover, L. A.; Kim, Y. C.; Elimelech, M. Thin-film composite pressure retarded osmosis membranes for sustainable power generation from salinity gradients. *Environ. Sci. Technol.* **2011**, *45*, 4360–4369.

(5) Petersen, R. J. Composite reverse osmosis and nanofiltration membranes. *J. Membr. Sci.* **1993**, *83*, 81–150.

(6) Lee, K. P.; Arnot, T. C.; Mattia, D. A review of reverse osmosis membrane materials for desalination—Development to date and future potential. *J. Membr. Sci.* **2011**, *370*, 1–22.

(7) Bellona, C.; Drewes, J. E.; Xu, P.; Amy, G. Factors affecting the rejection of organic solutes during NF/RO treatment—A literature review. *Water Res.* **2004**, *38*, 2795–2809.

(8) Ramon, G. Z.; Hoek, E. M. V. Transport through composite membranes, part 2: impacts of roughness on permeability and fouling. *J. Membr. Sci.* **2013**, *425-426*, 141–148.

(9) Wijmans, J. G.; Baker, R. W. The solution-diffusion model: a review. *J. Membr. Sci.* **1995**, *107*, 1–21.

(10) Bowen, W. R.; Welfoot, J. S. Modelling the performance of membrane nanofiltration—Critical assessment and model development. *Chem. Eng. Sci.* **2002**, *57*, 1121–1137.

(11) Kurihara, M.; Hanakawa, M. Mega-ton water system: Japanese national research and development project on seawater desalination and wastewater reclamation. *Desalination* **2013**, *308*, 131–137.

(12) An, Q.; Hung, W.; Lo, S.; Li, Y.; Guzman, M. De; Hu, C.-C.; Lee, K.-R.; Jean, Y.-C.; Lai, J.-Y. Comparison between Free Volume Characteristics of Composite Membranes Fabricated through Static and Dynamic Interfacial Polymerization Processes. *Macromolecules* **2012**, *45*, 3248–3435.

(13) Kong, C.; Shintani, T.; Kamada, T.; Freger, V.; Tsuru, T. Co-solvent-mediated synthesis of thin polyamide membranes. *J. Membr. Sci.* **2011**, *384*, 10–16.

(14) Kong, C.; Koushima, A.; Kamada, T.; Shintani, T.; Kanezashi, M.; Yoshioka, T.; Tsuru, T. Enhanced performance of inorganic-polyamide nanocomposite membranes prepared by metal-alkoxide-assisted interfacial polymerization. *J. Membr. Sci.* **2011**, *366*, 382–388.

(15) Kong, C.; Kanezashi, M.; Yamomoto, T.; Shintani, T.; Tsuru, T. Controlled synthesis of high performance polyamide membrane with thin dense layer for water desalination. *J. Membr. Sci.* **2010**, *362*, 76–80.

(16) Pacheco, F. A.; Pinnau, I.; Reinhard, M.; Leckie, J. O. Characterization of isolated polyamide thin films of RO and NF membranes using novel TEM techniques. *J. Membr. Sci.* **2010**, *358*, 51–59.

(17) Tang, C. Y.; Kwon, Y.-N.; Leckie, J. O. Probing the nano- and micro-scales of reverse osmosis membranes—A comprehensive characterization of physiochemical properties of uncoated and coated membranes by XPS, TEM, ATR-FTIR, and streaming potential measurements. *J. Membr. Sci.* **2007**, *287*, 146–156.

(18) Tang, C. Y.; Fu, Q. S.; Robertson, A. P.; Criddle, C. S.; Leckie, J. O. Use of reverse osmosis membranes to remove perfluorooctane sulfonate (PFOS) from semiconductor wastewater. *Environ. Sci. Technol.* **2006**, *40*, 7343–7349.

(19) Yin, J.; Kim, E.-S.; Yang, J.; Deng, B. Fabrication of a novel thin-film nanocomposite (TFN) membrane containing MCM-41 silica nanoparticles (NPs) for water purification. *J. Membr. Sci.* **2012**, *423-424*, 238–246.

(20) Ridgway, H. F.; Gale, J. D.; Hughes, Z. E.; Stewart, M. B.; Orbell, J. D.; Gray, S. R. Molecular scale modeling of membrane water treatment processes. In *Functional Nanostructured Materials and Membranes for Water Treatment*; Duke, M.; Zhao, D.; Semiat, R.; Lu, M., Eds.; John Wiley & Sons, 2013; pp. 249–300.

(21) Yan, H.; Miao, X.; Xu, J.; Pan, G.; Zhang, Y.; Shi, Y.; Guo, M.; Liu, Y. The porous structure of the fully-aromatic polyamide film in reverse osmosis membranes. *J. Membr. Sci.* **2015**, *475*, 504–510.

(22) Dow Filmtec. NF90-400 nanofiltration element datasheet, Form No. 609-00345-0312. Available at http://www.dowwaterandprocess.com/en/Products/F/FILMTEC%20NF90_4040 (Accessed on October 26, 2014).

(23) Dow Filmtec. XLE-440 extra low energy RO element datasheet, Form No. 609-00245-0606. Available at http://www.dowwaterandprocess.com/en/products/f/filmtec_xle_4040 (Accessed on October 26, 2014).

(24) Dow Filmtec. SW30HR-380 seawater reverse osmosis element datasheet, Form No. 609-00390-1008. Available at http://www.dowwaterandprocess.com/en/products/f/filmtec_sw30hr_380 (Accessed on October 26, 2014).

(25) Hydranautics. ESPA3-4040 brackish water reverse osmosis membrane element datasheet. Available at http://www.lenntech.com/Data-sheets/Hydranautics-ESPA3-4040.pdf (Accessed on October 26, 2014).

(26) Hydranautics. SWC4+ 8040 seawater reverse osmosis element datasheet. Available at http://www.lenntech.com/Data-sheets/Hydranautics-SWC4+8040.pdf (Accessed on October 26, 2014).

(27) Tang, C. Y.; Kwon, Y.-N.; Leckie, J. O. Effect of membrane chemistry and coating layer on physiochemical properties of thin film composite polyamide RO and NF membranes I. FTIR and XPS characterization of polyamide and coating layer chemistry. *Desalination* **2009**, *242*, 149–167.

(28) Perry, L. A.; Coronell, O. Reliable, bench-top measurements of charge density in the active layers of thin-film composite and nanocomposite membranes using quartz crystal microbalance technology. *J. Membr. Sci.* **2013**, *429*, 23–33.

(29) Freger, V. Swelling and morphology of the skin layer of polyamide composite membranes: an atomic force microscopy study. *Environ. Sci. Technol.* **2004**, *38*, 3168–3175.

(30) Lee, J.; Doherty, C. M.; Hill, A. J.; Kentish, S. E. Water vapor sorption and free volume in the aromatic polyamide layer of reverse osmosis membranes. *J. Membr. Sci.* **2013**, *425-426*, 217–226.

(31) Bason, S.; Oren, Y.; Freger, V. Ion transport in the polyamide layer of RO membranes: Composite membranes and free-standing films. *J. Membr. Sci.* **2011**, *367*, 119–126.

(32) Marx, K. A. Quartz crystal microbalance: a useful tool for studying thin polymer films and complex biomolecular systems at the solution-surface interface. *Biomacromolecules* **2003**, *4*, 1099–1120.

(33) O'Sullivan, C. K.; Guilbault, G. G. Commercial quartz crystal microbalances—Theory and applications. *Biosens. Bioelectron.* **1999**, *14*, 663–670.

(34) Huang, Y.; Paul, D. R. Physical aging of thin glassy polymer films monitored by gas permeability. *Polymer.* **2004**, *45*, 8377–8393.

(35) Irene, E. A. A brief history and state of the art of ellipsometry. In *Ellipsometry at the Nanoscale*; Losurdo, M.; Hingerl, K., Eds.; Springer-Verlag Berlin Heidelberg, 2013; pp. 1–30.

(36) Kwak, S.-Y.; Jung, S. G.; Yoon, Y. S.; Ihm, D. W. Details of surface features in aromatic polyamide reverse osmosis membranes characterized by scanning electron and atomic force microscopy. *J. Polym. Sci. Part B Polym. Phys.* **1999**, *37*, 1429–1440.

(37) Bozzola, J. J.; Russell, L. D. *Electron Microscopy: Principles and Techniques for Biologist*; 2nd ed.; Jones and Bartlett, 1999.

(38) Rasband, W.S., ImageJ, U. S. National Institutes of Health, Bethesda, Maryland, USA, http://imagej.nih.gov/ij/, 1997-2014.

(39) Zhang, X.; Cahill, D. G.; Coronell, O.; Mariñas, B. J. Absorption of water in the active layer of reverse osmosis membranes. *J. Membr. Sci.* **2009**, *331*, 143–151.

(40) Kolev, V.; Freger, V. Hydration, porosity and water dynamics in the polyamide layer of reverse osmosis membranes: A molecular dynamics study. *Polymer.* **2014**, *55*, 1420–1426.

(41) Dražević, E.; Košutić, K.; Freger, V. Permeability and selectivity of reverse osmosis membranes: Correlation to swelling revisited. *Water Res.* **2014**, *49*, 444–452.

(42) Jeck, S.; Scharfer, P.; Schabel, W.; Kind, M. Water sorption in poly(vinyl alcohol) membranes: an experimental and numerical study of solvent diffusion in a crosslinked polymer. *Chem. Eng. Process.* **2011**, *50*, 543–550.

(43) Ben-David, A.; Oren, Y.; Freger, V. Thermodynamic factors in partitioning and rejection of organic compounds by polyamide composite membranes. *Environ. Sci. Technol.* **2006**, *40*, 7023–7028.

(44) Ciddor, P. E. Refractive index of air: new equations for the visible and near infrared. *Appl. Opt.* **1996**, *35*, 1566–1573.

(45) Braun, M. M.; Pilon, L. Effective optical properties of non-absorbing nanoporous thin films. *Thin Solid Films* **2006**, *496*, 505–514.

(46) Bason, S.; Freger, V. Phenomenological analysis of transport of mono- and divalent ions in nanofiltration. *J. Membr. Sci.* **2010**, *360*, 389–396.

(47) Ding, M.; Ghoufi, A.; Szymczyk, A. Molecular simulations of polyamide reverse osmosis membranes. *Desalination* **2014**, *343*, 48–53.

(48) Ding, M.; Szymczyk, A.; Goujon, F.; Soldera, A.; Ghoufi, A. Structure and dynamics of water confined in a polyamide reverse-osmosis membrane: A molecular-simulation study. *J. Membr. Sci.* **2014**, *458*, 236–244.

(49) Harder, E.; Walters, D. E.; Bodnar, Y. D.; Faibish, R. S.; Roux, B. Molecular dynamics study of a polymeric reverse osmosis membrane. *J. Phys. Chem. B* **2009**, *113*, 10177–10182.

(50) Kotelyanskii, M. J.; Wagner, N. J.; Paulaitis, M. E. Molecular dynamics simulation study of the mechanisms of water diffusion in a hydrated, amorphous polyamide. *Comput. Theor. Polym. Sci.* **1999**, *9*, 301–306.

(51) Yaroshchuk, A.; Martínez-Lladó, X.; Llenas, L.; Rovira, M.; de Pablo, J. Solution-diffusion-film model for the description of pressure-driven trans-membrane transfer of

electrolyte mixtures: One dominant salt and trace ions. *J. Membr. Sci.* **2011**, *368*, 192–201.

(52) Kotelyanskii, M. J.; Wagner, N. J.; Paulaitis, M. E. Atomistic simulation of water and salt transport in the reverse osmosis membrane FT-30. *J. Membr. Sci.* **1998**, *139*, 1–16.

(53) Paul, D. R. Reformulation of the solution-diffusion theory of reverse osmosis. *J. Membr. Sci.* **2004**, *241*, 371–386.

(54) Xie, W.; Geise, G. M.; Freeman, B. D.; Lee, H.-S.; Byun, G.; McGrath, J. E. Polyamide interfacial composite membranes prepared from m-phenylene diamine, trimesoyl chloride and a new disulfonated diamine. *J. Membr. Sci.* **2012**, *403-404*, 152–161.

(55) Ghosh, A. K.; Jeong, B.-H.; Huang, X.; Hoek, E. M. V. Impacts of reaction and curing conditions on polyamide composite reverse osmosis membrane properties. *J. Membr. Sci.* **2008**, *311*, 34–45.

(56) Song, Y.; Sun, P.; Henry, L. L.; Sun, B. Mechanisms of structure and performance controlled thin film composite membrane formation via interfacial polymerization process. *J. Membr. Sci.* **2005**, *251*, 67–79.

(57) Mi, B.; Coronell, O.; Mariñas, B. J.; Watanabe, F.; Cahill, D. G.; Petrov, I. Physico-chemical characterization of NF/RO membrane active layers by Rutherford backscattering spectrometry. *J. Membr. Sci.* **2006**, *282*, 71–81.

(58) Tang, C. Y.; Kwon, Y.-N.; Leckie, J. O. Probing the nano- and micro-scales of reverse osmosis membranes—A comprehensive characterization of physiochemical properties of uncoated and coated membranes by XPS, TEM, ATR-FTIR, and streaming potential measurements. *J. Membr. Sci.* **2007**, *287*, 146–156.

(59) Coronell, O.; González, M. I.; Mariñas, B. J.; Cahill, D. G. Ionization behavior, stoichiometry of association, and accessibility of functional groups in the active layers of reverse osmosis and nanofiltration membranes. *Environ. Sci. Technol.* **2010**, *44*, 6808–6814.

(60) Bernstein, R.; Kaufman, Y.; Freger, V. Membrane Characterization. In *Encyclopedia of Membrane Science and Technology*; Hoek, E. M. V.; Tarabara, V. V., Eds.; John Wiley & Sons, Inc., 2013; p. 9.

(61) Geise, G. M.; Park, H. B.; Sagle, A. C.; Freeman, B. D.; McGrath, J. E. Water permeability and water/salt selectivity tradeoff in polymers for desalination. *J. Membr. Sci.* **2011**, *369*, 130–138.

(62) Maxwell, C. *Treatise on Electricity and Magnetism, vol. 1*; Oxford University Press, London, 1973.

(63) Cussler, E. L. *Diffusion: Mass Transfer in Fluid Systems*; 3rd ed.; Cambridge University Press: United States of America, 2009; p. 631.

(64) Zhang, X.; Cahill, D. G.; Coronell, O.; Mariñas, B. J. Partitioning of salt ions in FT30 reverse osmosis membranes. *Appl. Phys. Lett.* **2007**, *91*, 181904.

(65) Coronell, O.; Mariñas, B. I.; Cahill, D. G. Accessibility and ion exchange stoichiometry of ionized carboxylic groups in the active layer of FT30 reverse osmosis membrane. *Environ. Sci. Technol.* **2009**, *43*, 5042–5048.

(66) Chen, G.; Li, S.; Zhang, X.; Zhang, S. Novel thin-film composite membranes with improved water flux from sulfonated cardo poly(arylene ether sulfone) bearing pendant amino groups. *J. Membr. Sci.* **2008**, *310*, 102–109.

(67) Rao, A. P.; Joshi, S. V; Trivedi, J. J.; Devmurari, C. V; Shah, V. J. Structure–performance correlation of polyamide thin film composite membranes : effect of coating conditions on film formation. *J. Membr. Sci.* **2003**, *211*, 13–24.

(68) Rana, D.; Kim, Y.; Matsuura, T.; Arafat, H. A. Development of antifouling thin-film-composite membranes for seawater desalination. *J. Membr. Sci.* **2011**, *367*, 110–118.

(69) Li, L.; Zhang, S.; Zhang, X.; Zheng, G. Polyamide thin film composite membranes prepared from isomeric biphenyl tetraacyl chloride and m-phenylenediamine. *J. Membr. Sci.* **2008**, *315*, 20–27.

(70) Ogieglo, W.; van der Werf, H.; Tempelman, K.; Wormeester, H.; Wessling, M.; Nijmeijer, A.; Benes, N. E. n-Hexane induced swelling of thin PDMS films under non-equilibrium nanofiltration permeation conditions , resolved by spectroscopic ellipsometry. *J. Membr. Sci.* **2013**, *431*, 233–243.

(71) Kahle, O.; Wielsch, U.; Metzner, H.; Bauer, J.; Uhlig, C.; Zawatzki, C. Glass transition temperature and thermal expansion behaviour of polymer films investigated by variable temperature spectroscopic ellipsometry. *Thin Solid Films* **1998**, *313-314*, 803–807.

(72) Ogieglo, W.; Wormeester, H.; Wessling, M.; Benes, N. E. Spectroscopic Ellipsometry Analysis of a Thin Film Composite Membrane Consisting of Polysulfone on a Porous α-Alumina Support. *Appl. Mater. Interfaces* **2012**, *4*, 935–943.

(73) Turner, L. A. Zeroth Law of Thermodynamics. *Am. J. Phys.* **1961**, *29*, 71–76.

(74) Yang, K.; Zhu, L.; Xing, B. Adsorption of Polycyclic Aromatic Hydrocarbons by Carbon Nanomaterials. *Environ. Sci. Technol.* **2006**, *40*, 1855–1861.

(75) Lo, S. Anomalous State of Ice. *Mod. Phys.* **1996**, *10*, 909–919.

(76) Metz, S. J.; van de Ven, W. J. C.; Potreck, J.; Mulder, M. H. V; Wessling, M. Transport of water vapor and inert gas mixtures through highly selective and highly permeable polymer membranes. *J. Membr. Sci.* **2005**, *251*, 29–41.

(77) *MWH Water treatment: Principles and design*; Crittenden, J. C.; Trussell, R. R.; Hand, D. W.; Howe, K. J.; Tchobanoglous, G., Eds.; John Wiley & Sons: Hoboken, NY, USA, 2012; p. 1870.

CHAPTER 4: CORRELATION OF ACTIVE LAYER THICKNESS, WATER PARTITIONING AND WATER DIFFUSIVITY TO THE WATER PERMEABILITY OF POLYAMIDE THIN-FILM COMPOSITE MEMBRANES

4.1. Introduction

Thin-film composite (TFC) membranes are widely used in reverse osmosis (RO) and naonofiltration (NF) processes in a broad range of water purification applications, including desalination, hardness removal, and water reuse.[1–3] Such RO/NF membranes have a multi-layer structure consisting of an active layer (~20-200 nm), a polysulfone support layer (~30 μm) and a polyester fabric backing (~300 μm).[4,5] The polyamide active layer is typically made of polyamide, and often –for treatment of treated effluent, and sea, brackish and ground water– of fully aromatic polyamide.[4] The polyamide active layer plays the role of the selective barrier in water and solute transport through the membranes, and therefore its structure and properties have great impact on membrane performance.[4,6,7]

Fully aromatic polyamide active layers are prepared by interfacial polymerization between *m*-phenylenediamine (MPD) in aqueous solution and trimesoyl chloride (TMC) in an organic solvent.[4] It is well known that when using this base chemistry,[8–11] variations in the active layer casting protocols (e.g., MPD concentration, TMC concentration, reaction time, etc.) result in membranes with a wide range of performance levels. Also, the active layers of these membranes have very similar physico-chemical properties, such as elemental composition, chemical signature, charge density and degree of polymer crosslinking.[12–15] Therefore, it is not well understood which resulting active layer properties determine the different membrane water permeabilities.

The transport of water through the active layers of polyamide RO/NF membranes is often described by the solution-diffusion model,[16] which illustrates the transport as a three step process: 1) water molecules first dissolve into the active layer from the feed water, 2) then move across the active layer through diffusion, and (3) finally partition out of the active layer to the permeate. The solution-diffusion model describes the water permeability of a membrane active layer using the water permeability coefficient A (m^2 s^{-1} Pa^{-1}), which is given by[16]

$$A = \frac{DK}{\delta}\frac{C_{H_2O}v}{RT} \quad , \tag{4.1}$$

where K (-) is the partition coefficient of water into the active layer, D (m^2 s^{-1}) is the diffusion coefficient of water within the active layer, δ (m) is the thickness of the active layer, C_{H_2O} (mol m^{-3}) is the molar concentration of bulk water, v (m^3 mol^{-1}) is the molar volume of liquid water, R (m^3 Pa K^{-1} mol^{-1}) is the ideal gas constant, and T (K) is the absolute temperature.

Given that C_{H_2O}, v, R and T are either constants or operational parameters, Equation 4.1 indicates that water permeability (A) is determined by the partition coefficient (K), the diffusion coefficient (D) and the thickness of the active layer (δ). Thus, to understand why membranes with active layers made of fully aromatic polyamide, having similar physico-chemical properties, have significantly different water permeabilities, there is a need to investigate how strongly correlated each δ, K and D are to A. Conclusions from such a study would also inform membrane developers on which membrane properties (δ, K and/or D) should be targeted for tailoring towards the production of improved membranes.

To investigate the correlation of δ, K and D to A in fully aromatic polyamide active layers, each of δ, K and D needs to be characterized. In Chapter 2, several methods for measuring active layer thickness were compared to each other, and it was concluded that AFM, profilometry, RBS, QCM and ellipsometry give consistent and accurate results, and that

ellipsometry is the overall most advantageous method in terms of accuracy, ease of use and equipment availability. However, the partition and the diffusion coefficients of water in polyamide active layers have not been thoroughly characterized in the peer-reviewed literature. The very limited work on characterizing *K* and *D* is likely the result of the experimental difficulties associated with quantifying water content in the ultrathin polyamide active layers, which requires nanoscale spatial resolution for partitioning characterization and better than microsecond temporal resolution for diffusion characterization.

There are only two studies[17,18] reported in the literature that have characterized water partitioning into the active layers of commercial RO/NF. Zhang *et al.*[17] and Lee *et al.*[18] measured water uptake by polyamide active layers of commercial RO membranes using a quartz crystal microbalance (QCM) and active layers isolated on a QCM sensor. Zhang *et al.*[17] obtained water uptake values of 11.2 wt% and 12.8 wt% for the FT30 RO (A =5×10^{-12} m·s^{-1}·Pa^{-1}) and LF10 RO membranes (A =6.8×10^{-12} m·s^{-1}·Pa^{-1}), respectively, while Lee *et al.*[18] obtained a water uptake value of 20.1 wt% for the SW30 RO membrane (A =4.8×10^{-12} m·s^{-1}·Pa^{-1} was not reported in the study but was calculated in this chapter based on the values of water uptake, active layer thickness (185nm) and diffusion coefficient (0.43×10^{-9} m^2 s^{-1}) reported in the study of Lee *et al.*), which was approximately 57-80% higher than the water uptake values obtained by Zhang *et al.* Since these two studies focused only on RO membranes and did not obtain consistent results, there is a need to characterize water partitioning in a set of polyamide RO/NF membranes with a wider range of performance levels (i.e., NF, brackish water RO and seawater RO) to better understand water partitioning into polyamide active layers and its correlation to water permeability.

Zhang *et al.* and Lee *et al.* also calculated the corresponding water diffusion coefficients for the membranes they studied using the water permeability coefficients, active layer thicknesses and water uptake values they obtained and Equation 4.1.[17,18] While Zhang *et al.* obtained water diffusion coefficients for FT30 RO and LF10 RO membranes of 0.8×10^{-9} m^2 s^{-1} and 1.2×10^{-9} m^2 s^{-1}, respectively,[17] Lee et al obtained a significantly lower water diffusion coefficient of 0.43×10^{-9} m^2 s^{-1} for the SW30 RO membrane.[18] In addition to these two studies, Kotelyanskii *et al.*[19] obtained a water diffusion coefficient range of 0.71-0.85 $\times10^{-9}$ m^2 s^{-1} through atomistic simulations that mimicked the active layer of the FT30 membrane. The range of values obtained by Kotelyanskii *et al.* was comparable to the values obtained by Zhang *et al.* but nearly twice as high as the value obtained by Lee *et al.* All three studies have focused only on RO membranes, therefore, there is a need to characterize water diffusion in a set of polyamide RO/NF membranes with a wider range of performance levels to better understand water diffusion within active layers and its correlation to water permeability.

In addition to the knowledge gaps in the literature identified above for characterizing water partitioning and diffusion coefficients in polyamide active layers, no study in the literature has taken into account the void structure of polyamide active layers when characterizing water transport through RO/NF membranes. As demonstrated in Chapter 3, voids account for 15-32% of the active layer volume, and therefore potentially impact the interpretation of characterization results and/or experimental approaches used for active layer characterization. For example, while the water sorption studies of Zhang *et al.*[17] and Lee *et al.*[18] discussed above measured water uptake by exposing the active layers to water vapor, the results in Chapter 3 show that very different water uptake results were obtained by exposing the active layers to liquid water, which is the environment that closely mimics the manner in which the membranes are used in a water

treatment plant. Therefore, to reach sound conclusions in terms of what active layer properties are most strongly correlated to water permeability, there is a need to interpret A, δ, K and D results while considering of the void structure of the active layer.

To address the literature knowledge gaps identified above, the objective of this study was to characterize the water permeability (A) of several commercial membranes, the thickness of their active layers (δ), and the partition (K) and diffusion coefficients (D) of water in their active layers, and evaluate through statistical analysis which of δ, K or D accounts for most of the differences in A among different membranes. The corresponding analyses were performed taking into account the void structure of the active layer.

4.2. Materials and Methods

4.2.1. Membranes and Sample Preparation

Five polyamide RO/NF membranes were studied, including NF90 (NF),[20] XLE (brackish water RO)[21] and SW30HR(seawater RO)[22] (Dow Filmtec, Minneapolis, MN), and ESPA3(brackish water RO)[23] and SWC4+(seawater RO)[24] (Hydranautics, Oceanside, CA). The membranes were received as flat sheets, which were then cut into 2.5×5.0 cm^2 coupons for thickness, water uptake and void volume fraction analyses and 14.6 cm^2 circle coupons for water permeation tests. All membrane coupons were thoroughly rinsed with and stored in ultrapure water (>18 MΩ·cm) until used. For thickness and water uptake analyses, membrane active layers were isolated onto silicon wafers and gold-coated QCM sensors, respectively, using the active layer isolation procedure described in Chapter 2, which has been used by various studies[18,25–27] and has been reported not to affect the integrity of the active layers.[28,29] In brief, the active layer isolation procedure has eight steps: 1) dry a membrane coupon between two filter papers by applying fingertip pressure; 2) peel off the polyester backing layer by hand leaving

behind the polyamide-polysulfone composite; 3) place the composite on a substrate (silicon wafer for thickness measurements and QCM sensors for water absorption tests) with the polyamide layer facing the substrate; 4) secure the polyamide-polysulfone composite to the substrate using a customized stainless steel frame with an open window on the polysulfone side; 5) dissolve the polysulfone layer by applying dimethylformamide (DMF) onto the sample through the open window and discard the polysulfone-DMF solution after 1 min, and repeat this step 15 times; 6) when most of the polysulfone has been dissolved and removed from the sample surface, dry the sample in air overnight; 7) dip the sample in fresh DMF for 4 h and air dry the sample overnight again in order to remove any polysulfone that still remains attached to the polyamide layer after step 6; 8) rinse the sample with ultrapure water and gently dry the sample with ultrapure nitrogen gas.

4.2.2. Water Permeation Tests

The water permeability coefficient (A) was obtained from permeation experiments using ultrapure water. A Sterlitech^{TM} (Kent, WA) HP4750 dead-end stirred filtration system with an effective membrane area of 14.6 cm^2 was used for the tests, which were performed at a temperature of 20±2^{o}C and an applied transmembrane pressure (ΔP) of 0.67 MPa. The mass of the permeate was measured with an electronic balance and the filtration time was measured with a stopwatch until the system reached a stabilized water flux (J_v, m·s^{-1}). The water permeability coefficient (A) was calculated as[16]

$$J_v = A(\Delta P - \Delta\pi), \tag{4.2}$$

where $\Delta\pi$ (Pa) is the transmembrane osmotic pressure which was zero since ultrapure water was used as the feed solution. For each membrane, duplicate samples were tested for water permeation. For each type of membrane studied, the samples tested for water permeation, active

layer thickness and water uptake were obtained from a single flat-sheet membrane, from the vicinity of each other, in order to avoid additional variability in membrane properties caused by taking membrane samples far from each other.

4.2.3. Ellipsometry Analyses

Active layer thickness was measured using spectroscopic ellipsometry as described in Chapter 2. Analyses were performed with a spectroscopic ellipsometer (J.A. Woollam Co. Inc., Lincoln, NE) at incidence angles of 65 °, 70 ° and 75 ° and wavelength range of 380-100 nm using the Autoretarder feature. Triplicate samples of each membrane were analyzed and each sample was tested at three locations (0.3 cm^2 each location) to obtain the average thickness of the membrane active layer. For data analyses, the structure of each sample was modeled as a composite consisting of a top polymer layer, an intermediate 2-nm thick silicon dioxide layer[30] and a 1-mm thickness silicon base layer. The polymer layer was simulated with the Cauchy dispersion formula,[31] and the thickness and refractive index of the membrane active layer were obtained by fitting the experimental data to the Cauchy model until reaching a minimized mean squared error lower than 20. Additional details of ellipsometry analyses for measurement of active layer thickness were described in Chapter 2.

4.2.4. QCM Analyses

QCM analyses were used to obtain the areal mass of polymer in the active layers (m_{AL}, ng cm^{-2}), the areal mass of water uptake by the active layers when exposed to humidified nitrogen gas at 96% relative humidity (m_v, ng cm^{-2}), and the areal mass of water uptake by the active layers when exposed to liquid water (m_l, ng cm^{-2}). Analyses were performed as described in Chapter 3 using a Q-Sense E4 QCM (Biolin Scientific, Lithicum Heights, MD) and QCM sensors before and after active layers were isolated on them. For each sensor, four tests were performed as follows: (1) uncoated sensor exposed to dry nitrogen gas (<0.02% RH); (2) coated

sensor (i.e., sensor coated with the active layer) exposed to dry nitrogen gas; (3) coated sensor exposed to humidified nitrogen gas at 96% RH; and (4) coated sensor exposed to ultrapure water. The areal mass of the active layer isolated on QCM sensors (m_{AL}) was obtained from the difference in QCM response between tests 1 and 2, the areal mass of water uptake under humidified nitrogen gas (m_v) was obtained from the difference in QCM response between tests 2 and 3, and the areal mass of water uptake under liquid water (m_l) was obtained from the difference in QCM response between tests 2 and 4. Water uptake tests under humidified nitrogen gas were performed using Q-Sense humidity modules (Biolin Scientific, Lithicum Heights, MD), which had two chambers separated by a GORE^{TM} membrane (W. L. Gore & Associates, Newark, DE). For each test, the sensor was placed in the inner chamber of the module and the dry or humidified nitrogen stream (<0.1 psi) flowed through the outer chamber until the system (consisting of the outer chamber, the inner chamber and the sample) reached equilibrium as indicated by a change of areal mass lower than 3.6 ng·cm^{-2}·min^{-1}. Water uptake tests in liquid water were performed using Q-Sense flow modules (Biolin Scientific, Lithicum Heights, MD), in which liquid water flowed through the same chamber in which the sensor was placed. In order to ensure laminar conditions and negligible disturbance of the sensor, the water flow rate was adjusted to 0.1 mL·min^{-1}. During each QCM experiment, an uncoated sensor that served as a control sensor was tested in parallel to account for changes in QCM response caused by the differences in the viscosity and density of the fluid used (i.e., dry nitrogen gas, humidified nitrogen gas and liquid water).[29,32,33] Duplicate samples (1.54 cm^2 each) of each membrane were tested at a temperature of 22 ±0.02 ℃, which prevented water condensation during experiments as the dew point at 96% RH is 21 ℃.

4.2.5. TEM Analyses

Transmission electron microscopy (TEM) cross-sectional images of the SW30HR membrane were obtained as described in Chapter 3. Membrane samples were prepared with a procedure similar to that described by Tang *et al.*[34] Briefly, membrane samples were first dehydrated with 100% ethanol three consecutive times (15 min each time), then infiltrated and embedded with LR White resin (London Resin Co., Reading, UK) for 1 h (50%v/v of resin and ethanol), 2 h (67% v/v of resin and ethanol), 3 h (100% v/v of resin and ethanol) and another 2h (100% v/v of resin and ethanol), and cured at 48 ℃ for 3 days. At last, the samples were cut into thin slices (~90-100 nm) with a Sorvall MT 6000 Ultramicrotome (RMC Co., Tucson, AR). Triplicate images were taken for the SW30HR membrane at an acceleration voltage of 80 kV with a JEOL 100CX II TEM (JEOL USA, Peabody, MA) at a magnification of 72,000×.

4.3. Results and Discussion

4.3.1. Correlation between water permeability and intensive and extensive properties of membrane active layer

While Equation 4.1 shows that the water permeability (A) of a membrane is a function of the thickness (δ), water partition coefficient (K) and water diffusion coefficient (D) of the membrane active layer, studies in the peer-reviewed literature have typically used the water permeance (P) of membrane active layer as given by

$$P = A \times \delta = DK\frac{C_{H_2O}v}{RT} \quad (4.3)$$

as a descriptor of the water permeation properties of the active layer polymer instead of using K and D independently.[35–37] This approach of combining K and D into one single parameter P is typically followed because of the experimental difficulties associated with characterizing the water partition and diffusion coefficients in polyamide active layers as described in Section 4.1. Since both D and K are intensive properties of membrane active layers (i.e., properties that do

not change with the dimensions of the active layer), P is also an intensive property. On the other hand, δ is an extensive property of membrane active layers (i.e., a property that changes with the dimensions of the active layer). Therefore, the water permeability of a membrane, A, is a function of the intensive property P and the extensive property δ as given by

$$A = \frac{P}{\delta}. \tag{4.4}$$

Thus, if a given membrane has a water permeability that is twice as large as the water permeability of another membrane, it is possible that the two membranes have active layers with the same overall intensive property (P) but the first membrane simply has an active layer half as thick as that of the second membrane (i.e., they differ in the extensive property, δ_{AL}). It is also possible that the two membranes have active layers with the same extensive property (δ), but they have different water partition coefficients and/or diffusion coefficients (i.e., they differ in their overall intensive property, P).

To understand whether the differences in the water permeabilities, A, of commercial polyamide RO/NF membranes were mostly accounted for by the differences in the actual properties of the active layer material and structure (represented with the intensive property, P_{AL}) or the amount of material in the active layer (represented with the extensive property, δ_{AL}), the correlations between A and P_{AL} and A and δ_{AL} were studied. The subscript "AL" is used for the thickness measurements and permeance values calculated from thickness measurements to indicate that they constitute values descriptive of the overall active layer (i.e., polymer and voids). The A and δ_{AL} values obtained for the five membranes studied from water permeation tests and ellipsometry analyses, respectively, are summarized in Table 4.1, and P_{AL} values calculated as the product of A and δ_{AL} are summarized in Table 4.2. For all membranes, the water permeability coefficient was in the 0.12(±0.03)-2.24(±0.09)$\times 10^{-11}$ m s^{-1} Pa^{-1} range, the

active layer thickness (δ_{AL}) was in the 90(±3)-157(±5) nm range, and the water permeance (P_{AL}) was in the 0.18(±0.04)-2.94(±0.29)×10^{-18} m^2 s^{-1} Pa^{-1} range.

To evaluate the correlation of δ_{AL} and P_{AL} to A, the A values were plotted as a function of δ_{AL} and P_{AL} in Figures 4.1(a) and 4.1(b), respectively. Figure 4.1 shows that while the most water permeable membrane in this study (NF90) had a value of A that was ~19 times higher than the A value of the least water permeable membrane (SW30HR), the thickest active layer was only less than twice as thick as the thinnest active layer. By contrast, the largest P_{AL} value of these membranes was ~16 times higher than the smallest P_{AL}. Linear regression analyses were performed on the correlations between A and δ_{AL} and A and P_{AL}. The goodness of fitting (R^2) between A and δ_{AL} was only 0.05 while the R^2 value between A and P_{AL} was close to 1 (0.95). The small R^2 value between A and δ_{AL} suggests that the differences in A among different membranes are not accounted for by the differences in δ_{AL} (the extensive property), but rather by the differences in P_{AL} (the overall intensive water transport property).

While the above calculations are based on Equation 4.1, which is the widely accepted approach used to study the intensive water transport properties of the active layers of RO/NF membranes (P_{AL}, K_{AL} and D_{AL}),[17,18] Equation 4.1 is used in the literature under the assumption that the active layer is a continuous polymer film.[16] Thus, the values of P_{AL}, K_{AL} and D_{AL}

Table 4.1. Permeability coefficient (A), active layer thickness (δ_{AL}), areal mass of active layer (m_{AL}), water uptake humidified (96% RH) nitrogen gas (m_v), water uptake in liquid water (m_l) and volume fraction of voids (f_{void}) for five commercial polyamide RO/NF membranes.

Membrane	$A \times 10^{11}$ (m s^{-1} Pa^{-1})	δ_{AL} [a] (nm)	m_{AL} [b] (ng cm^{-2})	m_v [b] (ng cm^{-2})	m_l [b] (ng cm^{-2})	f_{void} [c] (-)
NF90	2.24 ± 0.09	131 ± 12	17257 ± 128	2163 ± 95	4302 ± 390	0.15 ± 0.02
XLE	1.99 ± 0.10	135 ± 4	14060 ± 1065	1763 ± 199	5252 ± 167	0.31 ± 0.02
ESPA3	1.48 ± 0.01	90 ± 3	13767 ± 915	1682 ± 7	4872 ± 1732	0.28 ± 0.14
SWC4+	0.28 ± 0.03	116 ± 17	13415 ± 1588	1868 ± 470	5029 ± 2	0.29 ± 0.01
SW30HR	0.12 ± 0.03	157 ± 5	18558 ± 842	2309 ± 33	11377 ± 1621	0.30 ± 0.06

Notes: [a] Active layer thickness (δ_{AL}) obtained from ellipsometry analyses has been reproduced from Chapter 2 for the convenience of the reader. [b] Areal mass of active layer (m_{AL}), water uptake under humidified nitrogen gas (m_v), and water uptake in liquid water (m_l) values have been reproduced from Chapter 3 (Table 3.1) for convenience of the reader. [c] Volume fraction of voids (f_{void}) has been reproduced from Chapter 3 (Table 3.1) for the convenience of the reader. f_{void} values correspond to those obtained from water uptake measurements, except for the SW30HR membrane for which it corresponds to that obtained using TEM image analysis.

Table 4.2. Active layer thickness (δ_{AL}), polymer thickness of active layer (δ_P), active layer permeance (P_{AL}), polymer permeance of active layer (P_P), effective water partition coefficient into active layer (K_{AL}), water partition coefficient into active layer polymer (K_P), water partition coefficient into active layer polymer ignoring voids (K_P'), effective water diffusion coefficient in active layer (D_{AL}), water diffusion coefficient in active layer polymer (D_P) and water diffusion coefficient in active layer polymer ignoring voids (D_P') for the five commercial polyamide RO/NF membranes.

Membrane	δ_{AL}[a] (nm)	δ_P (nm)	$P_{AL}\times10^{18}$ ($m^2\ s^{-1}\ Pa^{-1}$)	$P_P\times10^{18}$ ($m^2\ s^{-1}\ Pa^{-1}$)	K_{AL} (-)	K_P (-)	K_P' (-)	$D_{AL}\times10^9$ ($m^{-2}\ s$)	$D_P\times10^9$ ($m^{-2}\ s$)	D_P'$\times10^9$ ($m^{-2}\ s$)
NF90	131 ± 12	111 ± 18	2.94 ± 0.29	1.90 ± 0.40	0.33 ± 0.04	0.19 ± 0.03	0.16 ± 0.02	1.22 ± 0.20	1.33 ± 0.35	2.42 ± 0.34
XLE	135 ± 4	94 ± 7	2.69 ± 0.15	1.15 ± 0.13	0.39 ± 0.02	0.19 ± 0.03	0.13 ± 0.02	0.94 ± 0.07	0.83 ± 0.14	2.80 ± 0.36
ESPA3	90 ± 3	65 ± 31	1.33 ± 0.04	0.61 ± 0.42	0.54 ± 0.19	0.26 ± 0.13	0.19 ± 0.01	0.33 ± 0.12	0.32 ± 0.27	0.97 ± 0.04
SWC4+	116 ± 17	82 ± 12	0.32 ± 0.06	0.15 ± 0.03	0.44 ± 0.06	0.23 ± 0.07	0.16 ± 0.05	0.10 ± 0.02	0.09 ± 0.03	0.27 ± 0.09
SW30HR	157 ± 5	110 ± 24	0.18 ± 0.04	0.08 ± 0.03	0.72 ± 0.11	0.21 ± 0.05	0.15 ± 0.01	0.03 ± 0.01	0.05 ± 0.02	0.17 ± 0.04

Notes: [a] Active layer thickness has been reproduced from Table 4.1 for the convenience of the reader.

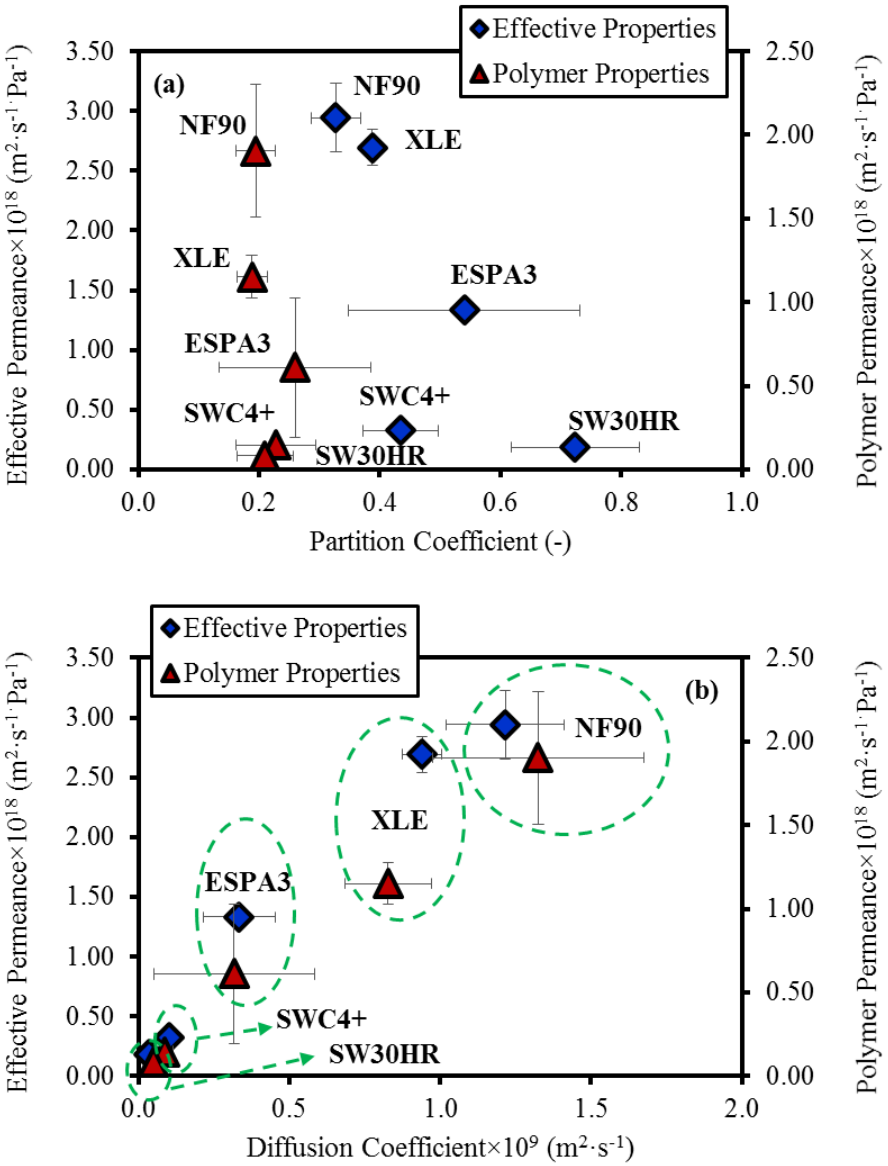

Figure 4.1. (a) Membrane water permeability (A) as a function of thickness of membrane active layer (effective active layer thickness δ_{AL} and polymer thickness δ_P), and (b) membrane water permeability (A) as a function of permeance of active layer (effective active layer permeance P_{AL} and polymer permeance P_P) of five commercial polyamide RO/NF membranes. Error bars for A and δ_{AL} represent the uncertainties of the two and three measurements, respectively, for each membrane. Error bars for δ_P, P_{AL} and P_P represent propagated errors obtained in calculations using Equations 4.6, 4.3 and 4.8, respectively, and the uncertainties in Table 4.1.

reported in the literature have been believed to be properties of the active layer polymer (polyamide).[17,18] The continuous polymer film assumption is inaccurate because, as concluded in Chapter 3, a significant volume fraction (15-32%) of the active layer of polyamide RO/NF membranes is occupied by voids. Therefore the active layer is not a continuous polymer film, but rather a composite film consisting of a polyamide matrix and voids as a dispersed phase. The composite nature of the active layer means that the water transport properties discussed above and reported in the literature (P_{AL}, K_{AL} and D_{AL}) are effective properties of the active layer, not properties of the polymer (polyamide) material. For example, in the real-world water purification applications of RO/NF membranes, the membranes are immersed in liquid water and the voids are filled with water according to the findings in Chapter 3. Therefore, when the membranes are being used for water purification processes, the effective water partition coefficient into the active layer (K_{AL}) is different from the water partition coefficient into the polyamide polymer alone (K_P). Similarly, water diffuses both in the polymer and in the voids, which leads to an effective water diffusion coefficient in the active layer (D_{AL}) that is different from the water diffusion coefficient in the polyamide polymer (D_P). Since permeance is the product of the water partition and diffusion coefficients, then the effective permeance of the active layer (P_{AL}) is also different from the permeance of polyamide polymer (P_P). A similar argument can be made about the active layer thickness. The measured thickness (δ_{AL}) corresponds to the effective (i.e., total) thickness of the active layer, but one can also define a 'polymer' thickness (δ_P) descriptive of the polymer volume only, excluding the volume of the voids. The difference between effective properties of active layers and properties of polyamide polymer is demonstrated in Figure 4.2.

While it is important to study the effective properties (δ_{AL}, P_{AL}, K_{AL} and D_{AL}) because they are descriptive of the net active layer performance when they are used in real-world applications, it is also very important to study the properties of the active layer polymer because if one were to optimize the active layer, only the water transport properties of the polymer, not of the voids, can be modified for active layer optimization. For the voids, only their geometrical properties (i.e., size, volume fraction, spatial distribution) could potentially be modified. Accordingly, the correlation of the polymer intensive (P_P) and extensive (δ_P) properties with A was studied. In order to calculate the properties of the active layer polymer, the void volume fractions (f_{void}, which will be called simply as 'void fraction' from here on) of the membrane active layers obtained in Chapter 3, and reproduced in Table 4.1, were used.

For the NF90, XLE, ESPA3 and SWC4+ membranes, void fractions were calculated with the results from the water uptake tests as

$$f_{void} = \frac{(m_l - m_v)\rho_{AL}}{\rho_w m_{AL}}, \quad (4.5)$$

where m_l (ng cm^{-2}) is the water uptake in liquid water environment, m_v (ng cm^{-2}) is the water uptake in humidified nitrogen environment, m_{AL} (ng cm^{-2}) and ρ_{AL} (1.24 g cm^{-3})[17,38] are the areal mass and density of the active layer, respectively, and ρ_w (1.0 g cm^{-3}) is the water density. The values of m_l, m_v and m_{AL} were reproduced in Table 4.1 as well. For the SW30HR membrane, the void fraction was obtained by image analyses of TEM cross-sectional images of the active layer, not from Equation 4.5. This is because, as discussed in Chapter 3, the active layer of the SW30HR membrane has a polyvinyl alcohol (PVA) coating that seemingly results in calculation artifacts with Equation 4.5 given the high water sorption by PVA.

The polymer thickness values were calculated as

$$\delta_P = \delta_{AL}(1 - f_{void}), \quad (4.6)$$

using the void fractions listed in Table 4.1 and the active layer thickness values measured with ellipsometry. The corresponding results are listed in Table 4.2. While the active layer thicknesses (δ_{AL}) for the five membranes was in the 90±3 to 157±5 nm range, the polymer thicknesses (δ_P) of their active layers was in the 65±31 to 111±18 nm range. The permeance of the active layer polymer was obtained based on Maxwell's effective-medium approximation theory[39] as

$$\frac{P_{AL}}{P_P} = \frac{1+2\alpha+2f_{void}(1-\alpha)}{1+2\alpha-f_{void}(1-\alpha)}, \quad (4.7)$$

where $\alpha = P_P/P_{void}$ and P_{void} is the permeance of the voids, $m^2\ s^{-1}\ Pa^{-1}$. Given that bulk water diffusion (i.e., in the voids) is orders of magnitude larger than in the polymer,[17–19] $\alpha \to 0$ and Equation 4.7 can be simplified to

$$P_P = P_{AL}\frac{1-f_{void}}{1+2f_{void}}. \quad (4.8)$$

The results for the permeance of the active layer polymer calculated with Equation 4.8 are listed in Table 4.2. While the active layer permeance (P_{AL}) values were in the $0.18\pm0.04\times10^{-18}$ to $2.94\pm0.29\times10^{-18}$ $m^2\ s^{-1}\ Pa^{-1}$ range, the polymer permeance (P_P) values were in the $0.08\pm0.03\times10^{-18}$ to $1.90\pm0.4\times10^{-18}$ $m^2\ s^{-1}\ Pa^{-1}$ range. Therefore, the values of P_{AL} and P_P in Table 4.2 suggest that the existence of the voids increased the permeance of the active layer by a factor of 1.5-2.3 (P_{AL}/P_P) compared to the active layer polymer without voids. In other words, if there were no voids, the permeance of the active layer would have been lower (i.e., equal to that of the polymer).

To evaluate the correlation of δ_P and P_P to A, the A values were plotted as a function of δ_P and P_P in Figures 4.1(a) and 4.1(b), respectively. Linear regression analyses were performed for the correlations between A and δ_P and between A and P_P. The analyses yielded a R^2 value of

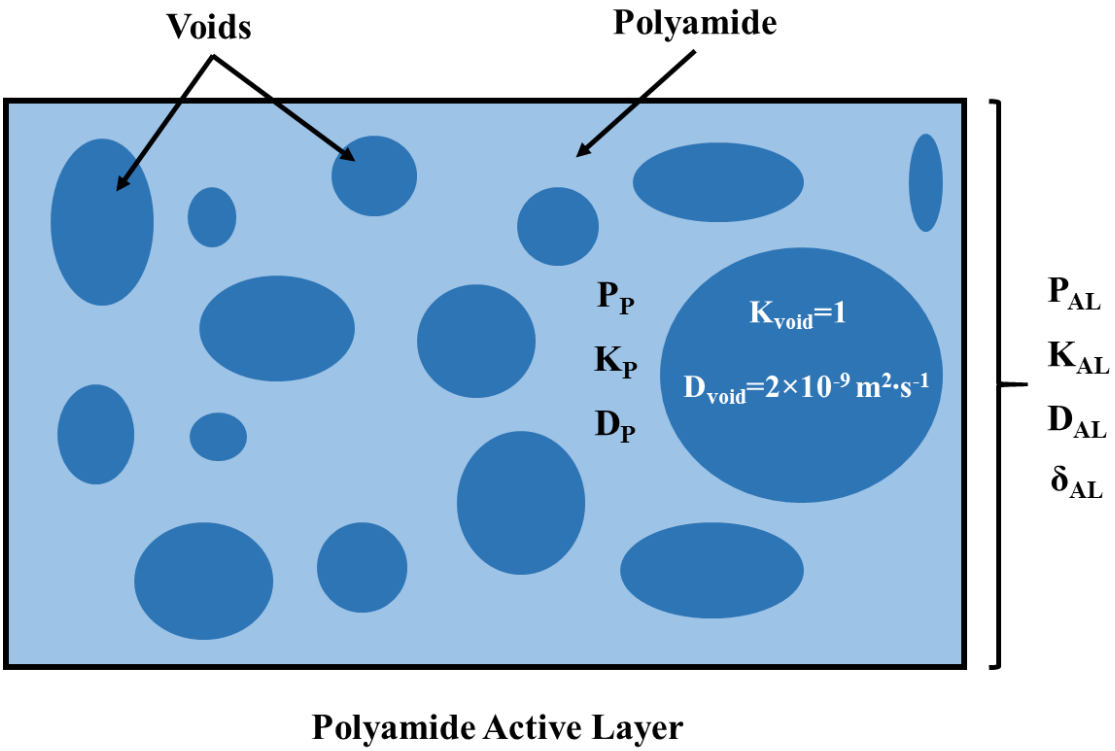

Figure 4.2. Effective water permeance (P_{AL}), water partition coefficient (K_{AL}), water diffusion coefficient (D_{AL}) and thickness (δ_{AL}) of membrane active layer, and water permeance (P_P), water partition coefficient (K_P), water diffusion coefficient (D_P) and thickness (δ_P) of active layer polymer (polyamide).

0.002 between A and δ_P and a R^2 value of 0.86 between A and P_P. The small R^2 value between A and δ_P suggests that the differences in A among different membranes are not accounted for by the differences in δ_P (the extensive property), but rather by the differences in P_P (the overall intensive water transport property). In fact, while the values of A varied from $0.12 \pm 0.03 \times 10^{-11}$ to $2.24 \pm 0.09 \times 10^{-11}$ m s^{-1} Pa^{-1} for the five membranes, an analysis of variance (ANOVA) found that their δ_P values were *not* statistically different from each other. Therefore, Figure 4.1 shows that, based on the studies of both the effective properties of active layers (δ_{AL} and P_{AL}) and the polymer properties of active layers ($\delta_P$and P_P), the differences in the water permeabilities among the five membranes are mostly accounted for by the differences in water permeance, not by the differences in thickness.

4.3.2. Effective and Polyamide Water Partition Coefficients

Effective partition coefficients of water in membrane active layers (K_{AL}) were obtained from the water uptake measurements in liquid water as given by

$$K_{AL} = \frac{m_l}{MW_{H_2O} C_{H_2O} \delta_{AL}}. \quad (4.9)$$

In Equation 4.9, it is assumed that the membrane does not swell by a significant amount when immersed in liquid water. While active layer swelling was not measured in this study, other studies in the literature have reported 13±6% swelling observed for SWC4+ membrane, 7±2% swelling for ESPA and 4.8±4.4% for ESPA1 membrane, and 35±2% for XLE membrane.[15,27] Therefore, while active layer swelling was not characterized in this study, errors in the water partition coefficients estimated with Equation 4.9 are expected to be at most 35%. The values of K_{AL} for the five membranes studied were in the range of 0.33(±0.04) – 0.72(±0.11) and are listed in Table 4.2.

Water partition coefficients in the active layers polymer (K_P) were obtained from the water uptake measurements in humidified nitrogen gas as given by

$$K_P = \frac{m_v}{MW_{H_2O} C_{H_2O} \delta_P} . \quad (4.10)$$

The polymer thickness δ_P was used in the calculation instead of the active layer thickness δ_{AL}, because water uptake by the voids under humidified nitrogen gas was negligible and only the polymer was responsible for the mass increase (m_v) caused by water uptake, according to the findings in Chapter 3. The values of K_P for the five membranes studied were in the range of 0.19(±0.03) – 0.26(±0.13) and are listed in Table 4.2. A comparison of the values of K_{AL} and K_P indicates that the existence of voids within membrane active layer increased the partition coefficient of the active layer by a factor of 1.7-3.4 (K_{AL}/K_P). The increased partition coefficient of the active layer caused by the voids can be explained by the fact that the water partition coefficient of active layer polymer (K_P) is smaller than 1 while the water partition coefficient of voids is 1 (as the voids are filled with water when the membrane is in contact with liquid water). Therefore, the effective water partition coefficient of the active layer (K_{AL}), which is a function of the partitioning into polymer and voids, is higher than the water partition coefficient of the polymer (K_P).

As discussed in Section 4.1, Zhang *et al.* obtained water uptake values by active layers of FT30 and LF10 membranes under humidified nitrogen gas and Lee *et al.* obtained water uptake value by active layer of SW30 membrane also under humidified helium gas.[17,18] Zhang *et al.* also calculated the concentration of water in the membrane active layers (C_m, mol m^{-3}), but did not take into account in the calculations the void fractions of the active layers because of a lack of awareness of the existence of the voids. Similarly, the value of C_m for the SW30 membrane active layer can also be calculated for the study of Lee *et al.* based on the water uptake value

they reported, though they did not report the value of C_m in their study. Because of the unawareness of the existence of the voids, the C_m values they obtained and the corresponding values of K that can be calculated from their study are neither effective active layer properties (as the water uptake tests were conducted under humidified nitrogen gas instead of liquid water) nor polymer properties of membrane active layers (as the existence of voids was not accounted for). The values of C_m obtained by Zhang *et al.* were 7.7×10^3 mol m^{-3} and 8.7×10^3 mol m^{-3} for the FT30 and LF10 RO membranes,[17] respectively, so the corresponding partition coefficients calculated as $K = C_m/C_{H_2O}$ are 0.14 and 0.16 for the FT30 and LF10 RO membranes, respectively. The values of C_m calculated based on the study of Lee *et al.* is 15.4×10^3 mol m^{-3} for the SW30 membrane and the corresponding value of *K* is 0.28.

While Zhang *et al.* used similar water uptake tests under humidified nitrogen gas as the tests used in this study to obtain the K_P values, the water partition coefficients obtained from their study are smaller than the values of K_P obtained for the four RO membranes in this study (average K_P of 0.22 ± 0.03 for the four RO membranes) because they did not take into account the existence of voids within membrane active layers. In fact, if the existence of voids were ignored in the present study (i.e., f_{pore} = 0), the water partition coefficients of active layer polymer (K_P') would have been calculated to be 0.16 ± 0.02 for NF90, 0.13 ± 0.02 for XLE, 0.19 ± 0.01 for ESPA3, 0.16 ± 0.05 for SWC4+ and 0.15 ± 0.01 for SW30HR as shown in Table 4.2, with an average of 0.16 ± 0.02 for the four RO membranes (XLE, ESPA3, SWC4+ and SW30HR membranes). This average value is not statistically different from the partition coefficients obtained by Zhang *et al.* While Lee *et al.* used a different water uptake measurement technique and obtained a 2 times higher water uptake by the SW30 membrane active layer compared to this study for the SW30HR membrane and the study of Zhang *et al.*, the partition coefficient

calculated from the Lee *et al.* study is only 1.3 times higher than the value of K_P for the SW30HR membrane. Therefore, not taking into account the existence of voids could lead to an underestimation of the partition coefficient of the active layer polymer by a factor of 1.2-1.4 (K_P'/K_P) in membrane characterization.

4.3.3. Effective and Polyamide Water Diffusion Coefficients.

To the author's knowledge, water diffusion coefficients in active layers of RO/NF membranes have not been experimentally measured, because of the extremely small time scale of water diffusion in the active layers. The time scale (t) of one-dimensional diffusion in active layers (i.e., perpendicular to the membrane surface) can be estimated as[40]

$$t = \frac{L^2}{2D}, \tag{4.11}$$

where L is the length scale of the diffusion (i.e., active layer thickness) and D is the water diffusion coefficient in the active layer. Since the active layer thickness is not larger than 200 nm (based on ellipsometry measurements of the five membranes in this study) and the water diffusion coefficient in membrane active layers has been estimated to be in the range of 0.43-1.2 $\times 10^{-9}$ m^2 s^{-1} in the literature,[17–19] a conservative estimate of the time scale of diffusion using the largest L = 200 nm and the smallest $D = 0.43 \times 10^{-9}$ m^2 s^{-1} yields $t = 4.7 \times 10^{-5}$ s. This small time scale of diffusion indicates that equilibrium of water content between the active layer and the environment is almost instantaneous, and therefore, measuring water diffusion coefficients in polyamide active layers represents a big experimental challenge.

As alternatives, studies in the peer-reviewed literature have estimated water diffusion coefficients of membrane active layers using atomistic simulations[19] or using Equation 4.1 and experimental values of A, δ and K.[17,18] However, in the latter approach, the values of K used in the calculations corresponded to the K_P' values described in the previous section which are

neither the effective property nor the polymer property of the active layer. Correspondingly, the calculated water diffusion coefficients do not represent the effective or polymer water diffusion coefficient.

In this study, both the effective diffusion coefficients of water in membrane active layers (D_{AL}) and water diffusion coefficients in active layer polymer (D_P) were calculated as

$$D_{AL} = \frac{P_{AL}}{K_{AL}} \frac{RT}{C_{H_2O} v} \tag{4.12}$$

and

$$D_P = \frac{P_P}{K_P} \frac{RT}{C_{H_2O} v}, \tag{4.13}$$

respectively, and the corresponding results are presented in Table 4.2. While the D_{AL} of the five membranes ranged from $0.03 \pm 0.01 \times 10^{-9}$ m^2 s^{-1} to $1.22 \pm 0.2 \times 10^{-9}$ m^2 s^{-1}, the D_P of the five membranes ranged from $0.05 \pm 0.02 \times 10^{-9}$ m^2 s^{-1} to $1.33 \pm 0.35 \times 10^{-9}$ m^2 s^{-1}. An analysis of the values of D_P and D_{AL} indicates that the existence of voids within membrane active layers changed the water diffusion coefficient in active layers by a factor of 0.7-1.2 (D_{AL}/D_P), i.e., the existence of the voids increased water diffusion for some membranes (XLE, ESPA3 and SWC4+ membranes) and reduced water diffusion for other membranes (NF90 and SW30HR membranes).

The change of water diffusion coefficient due to the existence of the voids is likely a result of a combination of several effects. Since the voids were filled with water in the measurement of K_{AL} which was used in the calculation of D_{AL} and the water diffusion coefficient in bulk water is higher than the water diffusion coefficient in the active layer polymer (D_P), the existence of the voids could have led to an overall higher water diffusion coefficient of the active layer (D_{AL}) which is a function of the diffusion in the polymer and the voids. This explains the increased water diffusion for XLE, ESPA3 and SWC4+ membranes. However, there is another

important effect of the voids on water diffusion in membrane active layers that may lead to a decreased effective water diffusion coefficient. Because of the existence of the voids, the path of water diffusion through membrane active layers changes. While the exact path of water diffusion in the active layers is not known in this study and has not been studied in the literature, there are only two possible paths for a water molecule to diffuse through the active layer. The first possible path is that the water molecule diffuses through the polymer and voids, and the second possible path is that the water molecule does not diffuse through the voids and only diffuses along the polymer around the voids. If a water molecule diffuses following the first path, then the movement of the water molecule through the active layer is divided into several stages by the alternation of polymer and voids on the path of the movement, and each stage would involve the water molecule dissolving into the polymer, diffusing through the polymer, dissolving into the voids (bulk water) then diffusing through the voids. This complex multistage path could potentially slow down the movement of water through the active layer, as each partitioning step (dissolving into the polymer or into the voids) takes extra time, and therefore the effective water diffusion coefficient (D_{AL}) could be smaller than the water diffusion coefficient in the polymer (D_P). On the other hand, if a water molecule diffuses through the active layer following the second possible path (i.e., only diffuses along the polymer but not through the voids), then it would have to detour in the polymer around the voids, which makes the diffusion path longer than the thickness of the active layer and thus results in a smaller effective water diffusion coefficient of the active layer (D_{AL}). This effect explains the reduced water diffusion for NF90 and SW30HR membranes. Both the effect of high diffusion coefficient in the voids (which increases the overall water diffusion in the active layer) and the effect of diffusion path change (which reduces the overall water diffusion in the active layer) exist for

each membrane active layer. Therefore, the effect of the voids on the diffusion of water through membrane active layers is a combination of both effects and can result in increased or reduced effective water diffusion coefficient (D_{AL}).

As discussed earlier, Zhang *et al.* and Lee *et al.* calculated water diffusion coefficients for RO membranes with Equation 4.1 and the partition coefficients obtained in their study, and reported the diffusion coefficient of 0.8×10^{-9} m^2 s^{-1} and 1.2×10^{-9} m^2 s^{-1} for the FT30 (seawater RO) and the LF10 (brackish water RO) membranes,[17] respectively, and the diffusion coefficient of 0.43×10^{-9} m^2 s^{-1} for the SW30 (seawater RO) membrane.[18] These values are considerably higher (4.8-16.0 times) than the D_P values obtained in this chapter for the seawater RO membranes. This discrepancy in water diffusion coefficients can be explained by the underestimation of water partition coefficients in the Zhang *et al.* and Lee *et al.* studies, as demonstrated in Section 4.3.2, and the higher water permeability coefficients in their studies compared to the water permeability coefficients obtained in this chapter. In fact, if the existence of voids were ignored in this chapter (i.e., f_{void} = 0), the diffusion coefficients reported by Zhang et al and Lee et al would be only 1.6-4.7 times higher than the water diffusion coefficients in the active layer polymer ($D_P{}'$) calculated from $K_P{}'$ and Equation 4.13 (see Table 4.2). Therefore, unawareness of the existence of voids could lead to an overestimation of the water diffusion coefficient in the active layer polymer by a factor of 1.8-3.4 (D_P'/D_P) in membrane characterization. Table 4.2 shows that the D_P' value of the NF90 membrane ($2.42 \pm 0.34 \times 10^{-9}$ m^2 s^{-1}) is higher than the water diffusion coefficient in bulk water (2×10^{-9} m^2 s^{-1}),[17] and this unreasonably high D_P' value is an evidence of the overestimation of water diffusion coefficients in membrane active layers when the existence of the voids is not taken into account.

4.3.4. Correlation between water permeability (A) and the water partition (K) and diffusion (D) coefficients in polyamide active layers

As concluded in Section 4.3.1, the differences in water permeabilities among the different membranes studied is mostly accounted for by the differences in the permeance (an intensive property) of their active layers. This conclusion was reached from the point of view of both the effective and polymer properties of the active layers. Since permeance is a function of the water partition and diffusion coefficients, here it is further evaluated whether the water permeance of membrane active layers is a stronger function of the partition coefficient or of the diffusion coefficient. Thus, Figure 4.3 shows the active layer permeance plotted as a function of water partition coefficient (panel (a)) and water diffusion coefficient (panel (b)) for both the effective active layer properties and the polymer properties of the active layers.

It can be observed from Figure 4.3 that the differences in effective permeance among the active layers studied are mostly accounted for by the differences in the effective water diffusion coefficients in the active layers rather than by the differences in their effective water partition coefficients. Similarly, the differences in polyamide permeance among membrane active layers are mostly accounted for by the differences in the water diffusion coefficients in polyamide, rather than by the differences in the water partition coefficients in polyamide. While the R^2 obtained from linear regression analysis of the correlation between P_{AL} and K_{AL} was 0.57, the R^2 of the correlation between P_{AL} and D_{AL} was close to 1 (0.97), which supports the observation from Figure 4.3 that the differences in the effective permeance among membranes are mostly accounted for by the differences in diffusion coefficients. In fact, an ANOVA shows that, with a 95% confidence level, the effective partition coefficients of the active layers of the five membranes studied are not statistically different from each other but their effective diffusion coefficients are statistically different from each other. Similarly, while the R^2 obtained from

linear regression analysis of the correlation between P_P and K_P is only 0.27, the R^2 of the correlation between P_P and D_P is close to 1 (0.99), which supports the observation from Figure 4.3 that the differences in polymer permeance among membranes are mostly accounted for by the differences in water diffusion coefficients in polyamide. An ANOVA test with a 95% confidence level shows that the water partition coefficients into polyamide are not statistically different among membranes but that the water diffusion coefficients in polyamide are statistically different from each other. Thus, the results of the ANOVA tests indicate that the effective water partition coefficients into the active layers, as well as the water partition coefficients into polyamide, were statistically the same among the five membranes studied.

Since the differences in the water permeabilities were most strongly correlated to the differences in active layer permeance, and the differences in active layer permeance were mostly accounted for by the different water diffusion coefficients in active layers, it can be concluded that the differences in water permeabilities among membranes are mostly accounted for by the differences in water diffusion coefficients in the active layers. This conclusion can be reached by analysis of either the effective water transport properties of membrane active layers or water transport properties of polyamide.

4.3.5. Correlation between void fraction (f_{void}) and water permeance (P), water partition coefficient (K) and water diffusion coefficient (D)

As demonstrated in Sections 4.3.1-4.3.3, the existence of voids in the active layers of the five RO/NF membranes studied increased the water permeance (P) of the active layers by a factor of 1.5-2.3, increased the water partitioning (K) of the active layer by a factor of 1.7-3.4, and changed the water diffusivity (D) of the active layers by a factor of 0.7-1.2, compared to the

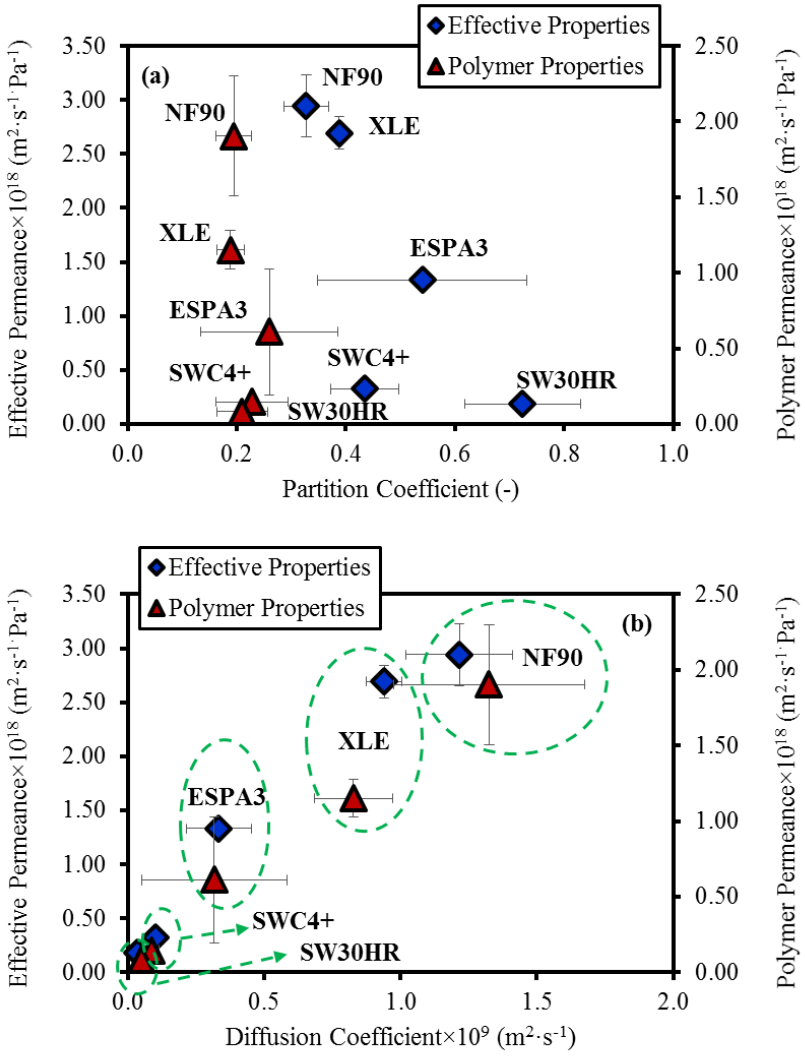

Figure 4.3 (a) Active layer permeance (effective permeance P_{AL} and polymer permeance P_P) as a function of the water partition coefficient into the active layer (effective partition coefficient $K_{AL}$and polymer partition coefficient K_P), and (b) active layer permeance (effective permeance P_{AL} and polymer permeance P_P) as a function of the water diffusion coefficient in the active layer (effective diffusion coefficient $D_{AL}$and polymer diffusion coefficient D_P) of five commercial polyamide RO/NF membranes. Error bars for P_{AL}, K_{AL} and D_{AL} represent propagated errors obtained in calculations using Equations 4.3, 4.9 and 4.12, respectively, and the uncertainties in Tables 4.1 and 4.2. Error bars for P_P, K_P and D_P represent propagated errors obtained in calculations using Equations 4.8, 4.10 and 4.13, respectively, and the uncertainties in Tables 4.1 and 4.2.

corresponding water transport properties in the active layer polymers (polyamide). Thus, in this section, it was evaluated whether there was a strong correlation between the void fraction in the active layers and the water permeance, water partition and water diffusion coefficients.

Figure 4.4 plots the water permeance (panel (a)), water partition coefficient (panel (b)) and water diffusion coefficient (panel (c)) of membrane active layers as a function of void membrane active layers. No obvious correlation can be observed from Figure 4.4 between void fraction and permeance, water partition coefficient or water diffusion coefficient. Consistent with this observation, linear regression analyses yields R^2 values of 0.33, 0.62, 0.29, 0.08, 0.46 and 0.59 for the correlations between P_{AL} and f_{void}, P_P and f_{void}, K_{AL} and f_{void}, K_P and f_{void}, and D_{AL} and f_{void} and D_P and f_{void}. Also, ANOVA tests show that the void fractions of the five membranes are not significantly different from each other. It is important to note that despite the lack of a strong correlation observed in this study between void fraction and the various water transport properties of the active layers, our analyses was limited to void fraction and did not take into account other void properties such as average size, size distribution and spatial distribution. Therefore, it remains as future work to investigate quantitatively how void properties other than void fraction (or the combination of them) affect the water transport properties of membrane active layers. This avenue of research is important because the void structure of membrane active layers is an untapped parameter in membrane development that can potentially be optimized to produce improved membranes.

4.4. Conclusion

In this chapter, the water transport properties (permeance, water partition coefficient and water diffusion coefficient) of the active layers of RO/NF membranes were characterized and their correlation to water permeability of the membranes was evaluated by statistical analyses.

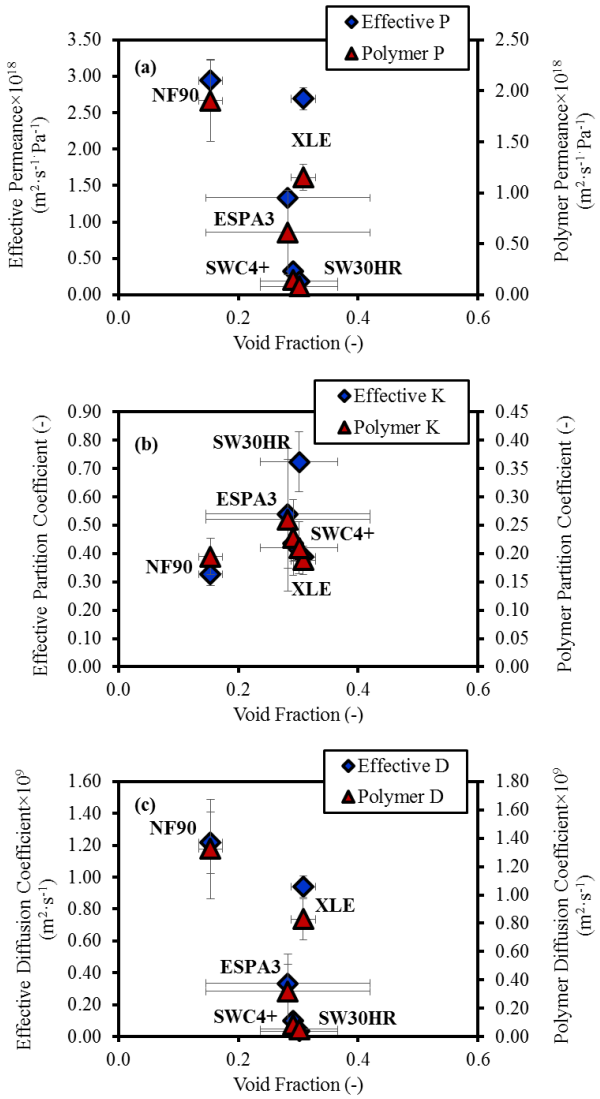

Figure 4.4. (a) Active layer permeance (effective permeance P_{AL} and polymer permeance P_P) as a function of void fraction of the active layer, (b) water partition coefficient into the active layer (effective partition coefficient K_{AL} and polymer partition coefficient K_P) as a function of void fraction of the active layer, and (c) water diffusion coefficient in the active layer (effective diffusion coefficient D_{AL} and polymer diffusion coefficient D_P) as a function of void fraction of the active layer. Error bars for void fractions of the NF90, XLE, ESPA3 and SWC4+ membranes represent propagated errors obtained in calculations using Equation 4.5 and uncertainties in Table 4.1. The error bar for the void fraction of the SW30HR membrane represents the uncertainty of three measurements from TEM analyses. Error bars for permeance, water partition coefficients and water diffusion coefficients were obtained as described in the captions of Figures 4.1 and 4.3.

For each water transport property, both effective active layer values and active layer polymer values were obtained. The analyses performed yielded the following conclusions:

- The effective water permeance of the active layers of the five membranes ranged from $0.18 \pm 0.04 \times 10^{-18}$ to $2.94 \pm 0.29 \times 10^{-18}$ m^2 s^{-1} Pa^{-1} and the corresponding water permeance of polyamide ranged from $0.08 \pm 0.03 \times 10^{-18}$ to $1.90 \pm 0.4 \times 10^{-18}$ m^2 s^{-1} Pa^{-1}. Thus, the presence of the voids in the membrane active layers increased the water permeance of the active layers by a factor of 1.5-2.3 compared to cases where the active layer had had no voids.
- The effective water partition coefficients of the active layers of the five membranes ranged from 0.33 ± 0.04 to 0.72 ± 0.11 and the corresponding water partition coefficients of polyamide ranged from 0.19 ± 0.03 to 0.26 ± 0.13. Thus, the presence of the voids in the membrane active layers increased the water partition coefficients of the active layers by a factor of 1.7-3.4 compared to cases where the active layer had had no voids.
- The effective water diffusion coefficients of the active layers of the five membranes ranged from $0.03 \pm 0.01 \times 10^{-9}$ m^2 s^{-1} to $1.22 \pm 0.2 \times 10^{-9}$ m^2 s^{-1} and the corresponding water diffusion coefficients of polyamide ranged from $0.05 \pm 0.02 \times 10^{-9}$ m^2 s^{-1} to $1.33 \pm 0.35 \times 10^{-9}$ m^2 s^{-1}. Thus, the presence of the voids in the membrane active layers changed the water diffusion coefficients of the active layers by a factor of 0.7-1.2 compared to cases where the active layer had had no voids.
- Among active layer thickness, water partition coefficient and water diffusion coefficient, the differences in the water permeabilities of the RO/NF membranes tested were mostly accounted for by the differences in the water diffusion coefficients in their

active layers, from the point of view of both effective properties of membrane active layers and polyamide properties.

- There was not a clear correlation between void fraction and water permeance, water partition coefficient or water diffusion coefficient of membrane active layers.

4.5. Acknowledgements

The author would like to thank Dr. Rene Lopez for helpful discussion about ellipsometry and Yingchi Liu and Chengcheng Feng for their help on ellipsometry experiments. The author would also like to thank Wallace Ambrose and Amar S. Kumbhar (TEM) for their help in acquiring the TEM images for the SW30HR membranes at the Chapel Hill Analytical and Nanofabrication Laboratory at Chapel Hill, NC. This work was supported by the National Science Foundation (NSF) Grants Opportunities for Academic Liason with Industry (GOALI) and Chemical and Biological Separations programs under Award#1264690, and NSF Environmental Engineering program under Award#1336532. The author was partially supported by the Okun Scholarship.

REFERENCES

(1) Greenlee, L. F.; Lawler, D. F.; Freeman, B. D.; Marrot, B.; Moulin, P. Reverse osmosis desalination: water sources, technology, and today's challenges. *Water Res.* **2009**, *43*, 2317–2348.

(2) Jacangelo, J. G.; Trussell, R. R.; Watson, M. Role of membrane technology in drinking water treatment in the United States. *Desalination* **1997**, *113*, 119–127.

(3) Van der Bruggen, B.; Everaert, K.; Wilms, D.; Vandecasteele, C. Application of nanofiltration for removal of pesticides, nitrate and hardness from ground water: rejection properties and economic evaluation. *J. Membr. Sci.* **2001**, *193*, 239–248.

(4) Petersen, R. J. Composite reverse osmosis and nanofiltration membranes. *J. Membr. Sci.* **1993**, *83*, 81–150.

(5) Lee, K. P.; Arnot, T. C.; Mattia, D. A review of reverse osmosis membrane materials for desalination—Development to date and future potential. *J. Membr. Sci.* **2011**, *370*, 1–22.

(6) Bellona, C.; Drewes, J. E.; Xu, P.; Amy, G. Factors affecting the rejection of organic solutes during NF/RO treatment—A literature review. *Water Res.* **2004**, *38*, 2795–2809.

(7) Ramon, G. Z.; Hoek, E. M. V. Transport through composite membranes, part 2: impacts of roughness on permeability and fouling. *J. Membr. Sci.* **2013**, *425-426*, 141–148.

(8) Xie, W.; Geise, G. M.; Freeman, B. D.; Lee, H.-S.; Byun, G.; McGrath, J. E. Polyamide interfacial composite membranes prepared from m-phenylene diamine, trimesoyl chloride and a new disulfonated diamine. *J. Membr. Sci.* **2012**, *403-404*, 152–161.

(9) Ghosh, A. K.; Jeong, B.-H.; Huang, X.; Hoek, E. M. V. Impacts of reaction and curing conditions on polyamide composite reverse osmosis membrane properties. *J. Membr. Sci.* **2008**, *311*, 34–45.

(10) Kong, C.; Kanezashi, M.; Yamomoto, T.; Shintani, T.; Tsuru, T. Controlled synthesis of high performance polyamide membrane with thin dense layer for water desalination. *J. Membr. Sci.* **2010**, *362*, 76–80.

(11) Song, Y.; Sun, P.; Henry, L. L.; Sun, B. Mechanisms of structure and performance controlled thin film composite membrane formation via interfacial polymerization process. *J. Membr. Sci.* **2005**, *251*, 67–79.

(12) Mi, B.; Coronell, O.; Mariñas, B. J.; Watanabe, F.; Cahill, D. G.; Petrov, I. Physico-chemical characterization of NF/RO membrane active layers by Rutherford backscattering spectrometry. *J. Membr. Sci.* **2006**, *282*, 71–81.

(13) Tang, C. Y.; Kwon, Y.-N.; Leckie, J. O. Probing the nano- and micro-scales of reverse osmosis membranes—A comprehensive characterization of physiochemical properties of

uncoated and coated membranes by XPS, TEM, ATR-FTIR, and streaming potential measurements. *J. Membr. Sci.* **2007**, *287*, 146–156.

(14) Coronell, O.; González, M. I.; Mariñas, B. J.; Cahill, D. G. Ionization behavior, stoichiometry of association, and accessibility of functional groups in the active layers of reverse osmosis and nanofiltration membranes. *Environ. Sci. Technol.* **2010**, *44*, 6808–6814.

(15) Dražević, E.; Košutić, K.; Freger, V. Permeability and selectivity of reverse osmosis membranes: Correlation to swelling revisited. *Water Res.* **2014**, *49*, 444–452.

(16) Wijmans, J. G.; Baker, R. W. The solution-diffusion model: a review. *J. Membr. Sci.* **1995**, *107*, 1–21.

(17) Zhang, X.; Cahill, D. G.; Coronell, O.; Mariñas, B. J. Absorption of water in the active layer of reverse osmosis membranes. *J. Membr. Sci.* **2009**, *331*, 143–151.

(18) Lee, J.; Doherty, C. M.; Hill, A. J.; Kentish, S. E. Water vapor sorption and free volume in the aromatic polyamide layer of reverse osmosis membranes. *J. Membr. Sci.* **2013**, *425-426*, 217–226.

(19) Kotelyanskii, M. J.; Wagner, N. J.; Paulaitis, M. E. Atomistic simulation of water and salt transport in the reverse osmosis membrane FT-30. *J. Membr. Sci.* **1998**, *139*, 1–16.

(20) Dow Filmtec. NF90-400 nanofiltration element datasheet, Form No. 609-00345-0312. Available at http://www.dowwaterandprocess.com/en/Products/F/FILMTEC%20NF90_4040 (Accessed on October 26, 2014).

(21) Dow Filmtec. XLE-440 extra low energy RO element datasheet, Form No. 609-00245-0606. Available at http://www.dowwaterandprocess.com/en/products/f/filmtec_xle_4040 (Accessed on October 26, 2014).

(22) Dow Filmtec. SW30HR-380 seawater reverse osmosis element datasheet, Form No. 609-00390-1008. Available at http://www.dowwaterandprocess.com/en/products/f/filmtec_sw30hr_380 (Accessed on October 26, 2014).

(23) Hydranautics. ESPA3-4040 brackish water reverse osmosis membrane element datasheet. Available at http://www.lenntech.com/Data-sheets/Hydranautics-ESPA3-4040.pdf (Accessed on October 26, 2014).

(24) Hydranautics. SWC4+ 8040 seawater reverse osmosis element datasheet. Available at http://www.lenntech.com/Data-sheets/Hydranautics-SWC4+8040.pdf (Accessed on October 26, 2014).

(25) Pacheco, F. A.; Pinnau, I.; Reinhard, M.; Leckie, J. O. Characterization of isolated polyamide thin films of RO and NF membranes using novel TEM techniques. *J. Membr. Sci.* **2010**, *358*, 51–59.

(26) Yan, H.; Miao, X.; Xu, J.; Pan, G.; Zhang, Y.; Shi, Y.; Guo, M.; Liu, Y. The porous structure of the fully-aromatic polyamide film in reverse osmosis membranes. *J. Membr. Sci.* **2015**, *475*, 504–510.

(27) Freger, V. Swelling and morphology of the skin layer of polyamide composite membranes: an atomic force microscopy study. *Environ. Sci. Technol.* **2004**, *38*, 3168–3175.

(28) Bason, S.; Oren, Y.; Freger, V. Ion transport in the polyamide layer of RO membranes: Composite membranes and free-standing films. *J. Membr. Sci.* **2011**, *367*, 119–126.

(29) Perry, L. A.; Coronell, O. Reliable, bench-top measurements of charge density in the active layers of thin-film composite and nanocomposite membranes using quartz crystal microbalance technology. *J. Membr. Sci.* **2013**, *429*, 23–33.

(30) Huang, Y.; Paul, D. R. Physical aging of thin glassy polymer films monitored by gas permeability. *Polymer.* **2004**, *45*, 8377–8393.

(31) Irene, E. A. A brief history and state of the art of ellipsometry. In *Ellipsometry at the Nanoscale*; Losurdo, M.; Hingerl, K., Eds.; Springer-Verlag Berlin Heidelberg, 2013; pp. 1–30.

(32) Marx, K. A. Quartz crystal microbalance: a useful tool for studying thin polymer films and complex biomolecular systems at the solution-surface interface. *Biomacromolecules* **2003**, *4*, 1099–1120.

(33) O'Sullivan, C. K.; Guilbault, G. G. Commercial quartz crystal microbalances—Theory and applications. *Biosens. Bioelectron.* **1999**, *14*, 663–670.

(34) Tang, C. Y.; Kwon, Y.-N.; Leckie, J. O. Probing the nano- and micro-scales of reverse osmosis membranes—A comprehensive characterization of physiochemical properties of uncoated and coated membranes by XPS, TEM, ATR-FTIR, and streaming potential measurements. *J. Membr. Sci.* **2007**, *287*, 146–156.

(35) Bernstein, R.; Kaufman, Y.; Freger, V. Membrane Characterization. In *Encyclopedia of Membrane Science and Technology*; Hoek, E. M. V.; Tarabara, V. V., Eds.; John Wiley & Sons, Inc., 2013; p. 9.

(36) Paul, D. R. Reformulation of the solution-diffusion theory of reverse osmosis. *J. Membr. Sci.* **2004**, *241*, 371–386.

(37) Geise, G. M.; Park, H. B.; Sagle, A. C.; Freeman, B. D.; McGrath, J. E. Water permeability and water/salt selectivity tradeoff in polymers for desalination. *J. Membr. Sci.* **2011**, *369*, 130–138.

(38) Kolev, V.; Freger, V. Hydration, porosity and water dynamics in the polyamide layer of reverse osmosis membranes: A molecular dynamics study. *Polymer.* **2014**, *55*, 1420–1426.

(39) Maxwell, C. *Treatise on Electricity and Magnetism, vol. 1*; Oxford University Press, London, 1973.

(40) Cussler, E. L. *Diffusion: Mass Transfer in Fluid Systems*; 3rd ed.; Cambridge University Press: United States of America, 2009; p. 631.

CHAPTER 5: CONCLUSIONS

This dissertation focused on elucidating which parameter among water partitioning, water diffusion and active layer thickness accounts for the differences in water permeability among polyamide reverse osmosis (RO) and nanofiltration (NF) membranes. To accomplish this, the research plan focused on: (i) comparing analytical techniques for measuring active layers of RO/NF membranes to determine the preferred techniques to use to obtain facile and accurate measurements; (ii) confirming the existence of voids in active layers of RO/NF membranes with a broad range of performance levels, and evaluating the volume fractions of active layers occupied by voids; (iii) quantifying water partition coefficients and water diffusion coefficients of membrane active layers; and (iv) elucidating which parameter among active layer thickness, water partition coefficient and water diffusion coefficient accounts for most of the differences in water productivity among RO/NF membranes.

Seven techniques were compared in determining the preferred techniques for measuring thickness of membrane active layers: scanning electron microscope (SEM), transmission electron microscopy (TEM), atomic force microscopy (AFM), Rutherford backscattering spectrometry (RBS), quartz crystal microbalance (QCM), profilometry and ellipsometry. Voids in membrane active layers were investigated using TEM, QCM, spectroscopic ellipsometry, SEM, scanning transmission electron microscopy-energy dispersive X-ray spectroscopy (STEM-EDS) and STEM-electron energy loss spectroscopy (STEM-EELS). Water partition coefficients in membrane active layers were measured using water sorption tests with a QCM, and water diffusion coefficients in membrane active layers were calculated from measured water partition

coefficients, water permeability coefficients measured through permeation tests, and active layer thicknesses measured using ellipsometry. Major outcomes of this dissertation are:

1. It was found that AFM, RBS, QCM, profilometry and ellipsometry produced consistent thickness results compared to each other and thus likely produced the most accurate measurements of active layer thickness for RO/NF membranes given that they operate under several completely different physical principles.

2. Thickness results for membrane active layers obtained with SEM and TEM were, in general, higher than non-electron microscopy techniques; therefore, SEM and TEM should only be used for rough estimation of active layer thickness.

3. Ellipsometry is considered the preferred technique for measuring the thickness of active layers of RO/NF membranes, AFM and profilometry are appropriate techniques to use when an ellipsometry is not available, and RBS and QCM are ideal techniques to use when the active layer volumetric mass density is known.

4. Active layer thicknesses for the six commercial RO/NF membranes studied were in the range of 14-176 nm, the average density of their active layers was 1.20 ± 0.20 g m^{-3}, and the average density of the active layers of the uncoated fully aromatic polyamide membranes was 1.26 ± 0.21 g m^{-3}.

5. Voids were found to exist in the polyamide active layers of all RO/NF membranes studied, which consisted of a group of five membranes having a broad range of performance levels (i.e., NF, brackish water RO and seawater RO).

6. The volume fractions accounted for by voids in the polyamide active layers of the five commercial RO/NF membranes studied was quantified through image analyses of

cross-sectional TEM micrographs, water uptake tests using a QCM, and ellipsometry and was found to be to be in the range of 15-32%.

7. Voids in the active layers were found to be filled with water when the membranes were immersed in water.

8. The presence of voids in the active layers was found to increase the effective water permeance of the active layer, increase the effective partition coefficient of water into the active layer, and decrease or increase the effective diffusion coefficient of water in the active layer, compared to the corresponding values in the active layer polymer alone.

9. The effective water permeance of the active layers of five commercial RO/NF membranes was found to range from $0.18 \pm 0.04 \times 10^{-18}$ to $2.94 \pm 0.29 \times 10^{-18}$ m^2 s^{-1} Pa^{-1}; the corresponding water permeance of polyamide alone was found to range from $0.08 \pm 0.03 \times 10^{-18}$ to $1.90 \pm 0.4 \times 10^{-18}$ m^2 s^{-1} Pa^{-1}.

10. The effective water partition coefficients into the active layers of five commercial RO/NF membranes were found to range from 0.33 ± 0.04 to 0.72 ± 0.11; the corresponding water partition coefficients into polyamide alone were found to range from 0.19 ± 0.03 to 0.26 ± 0.13.

11. The effective water diffusion coefficients in the active layers of five commercial RO/NF membranes were found to range from $0.03 \pm 0.01 \times 10^{-9}$ m^2 s^{-1} to $1.22 \pm 0.2 \times 10^{-9}$ m^2 s^{-1}; the corresponding water diffusion coefficients in polyamide alone were found to range from $0.05 \pm 0.02 \times 10^{-9}$ m^2 s^{-1} to $1.33 \pm 0.35 \times 10^{-9}$ m^2 s^{-1}.

12. Among active layer thickness, water partition coefficient and water diffusion coefficient in active layers, the difference in water diffusion coefficients was found to

account for most of the difference in water permeabilities among membrane active layers having the same chemistry (fully aromatic polyamide), from the point of view of both effective properties of membrane active layers and properties of polyamide alone.

CHAPTER 6: FUTURE WORK

Through comparing thickness measurement techniques, investigating the void structure of membrane active layers and studying water transport properties of membrane active layers, this dissertation has provided useful tools and raised questions that open avenues for future research. Three questions that arose from this dissertation are:

1. What are the properties of the voids that affect the water transport properties (e.g., water permeance, water partition coefficient and water diffusion coefficient) of active layers of RO/NF membranes? As discussed in Chapter 4, the voids that were found to exist in polylamide active layers increase water permeance, increase water partition coefficient and increase or decrease water diffusion coefficient in membrane active layers. However, as shown in Section 4.3.5, no strong correlation was observed between void fraction and water permeance, water partition coefficient and water diffusion coefficient. Therefore, the correlation between other properties of the voids and water transport properties (permeance, partition and diffusion coefficients) of membrane active layers remains to be studied. The properties of voids that are reasonable candidates to study include average size, size distribution, and spatial resolution.

2. How does the existence of voids affect solute transport through membrane active layers? As shown in chapter 4, existence of voids has significant effects on the water transport properties of membrane active layers. Therefore, it is reasonable to speculate that the voids also affect the solute transport properties of active layers. Since this study has only focused on the water transport properties, it remains to be studied how the

existence of voids affect the solute partition coefficient and solute diffusion coefficient of active layers of RO/NF membranes.

3. What are the parameters in membrane fabrication that affect the properties of the voids in membrane active layers? Since Chapter 4 has found that the voids have significant effects on water transport properties of membrane active layers, if future research discovers how the properties of the voids affect water transport properties as proposed in the first question of this section, it would be very beneficial to perform further research on how the membrane fabrication process can be modified to change the properties of voids for the purpose of improving water permeability of membrane active layers, particularly the water diffusion coefficient which was shown to account for most of the differences in water permeability among different membranes. Similarly, further research can also be performed into modifying the membrane fabrication process to change the properties of voids for the purpose of improving solute rejection of RO/NF membranes. Parameters in membrane fabrication that are reasonable candidates to study include concentration of *m*-phenylenediamine, concentration of trimesoyl chloride, polymerization time, curing condition (e.g., time and temperature, dry or wet), solvent, incorporation of nanoparticles, etc.

APPENDIX 1: RESULTS OF TRANSMISSION ELECTRON MICROSCOPY (TEM) ANALYSES OF ACTIVE LAYER THICKNESS

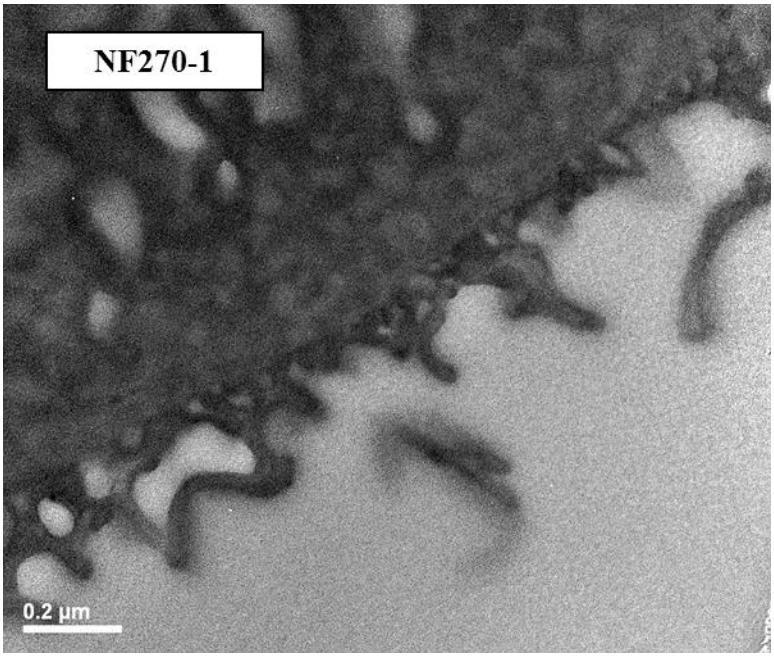

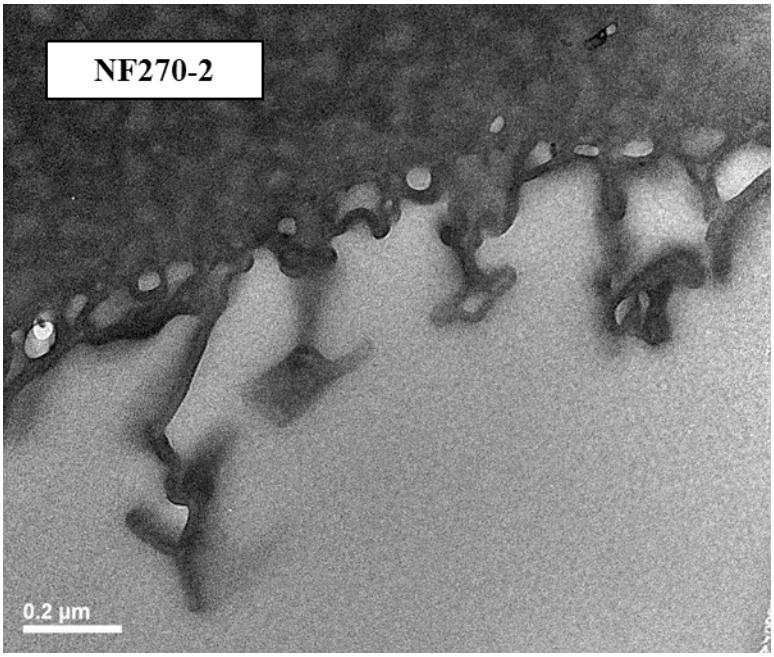

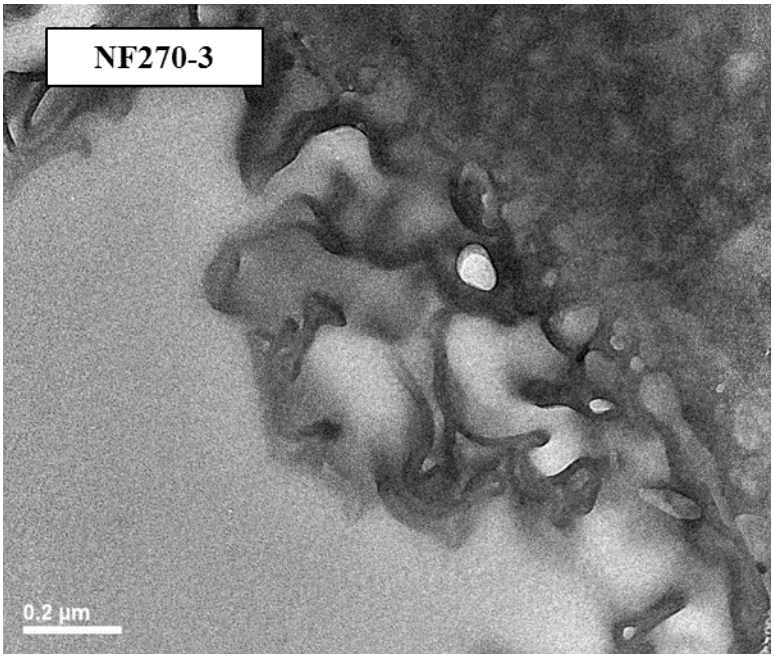
NF270-3
0.2 µm

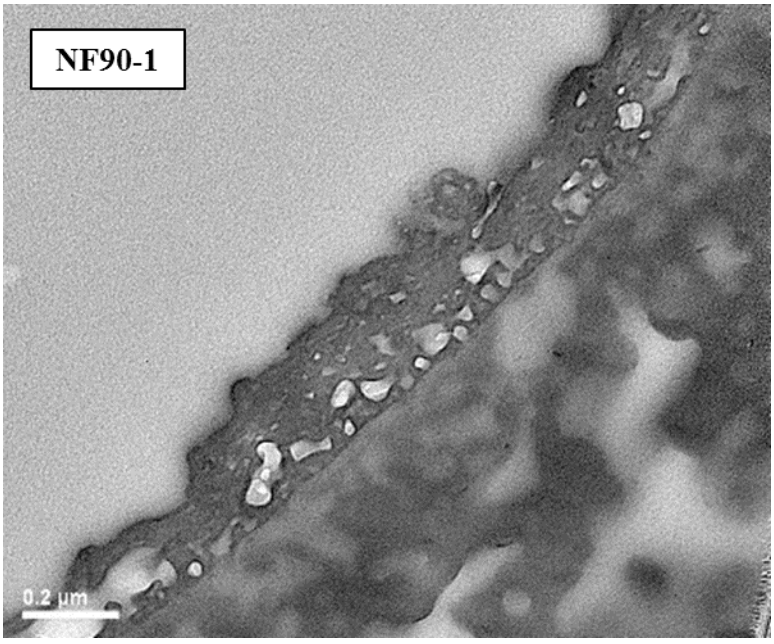
NF90-1
0.2 µm

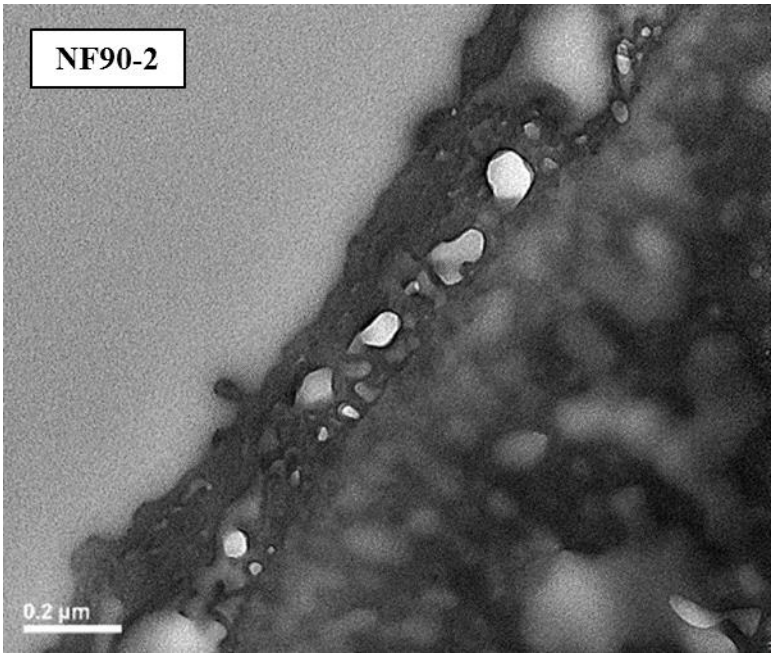
NF90-2
0.2 µm

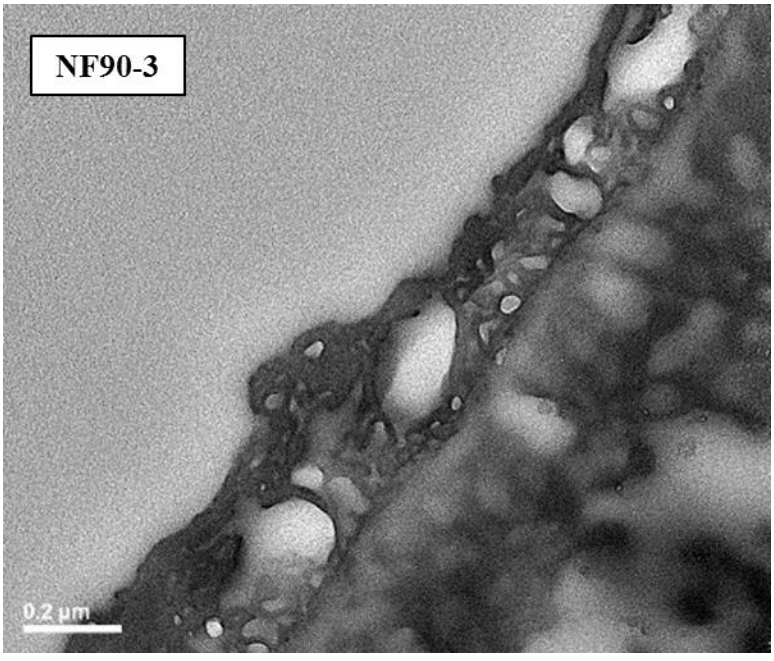
NF90-3
0.2 µm

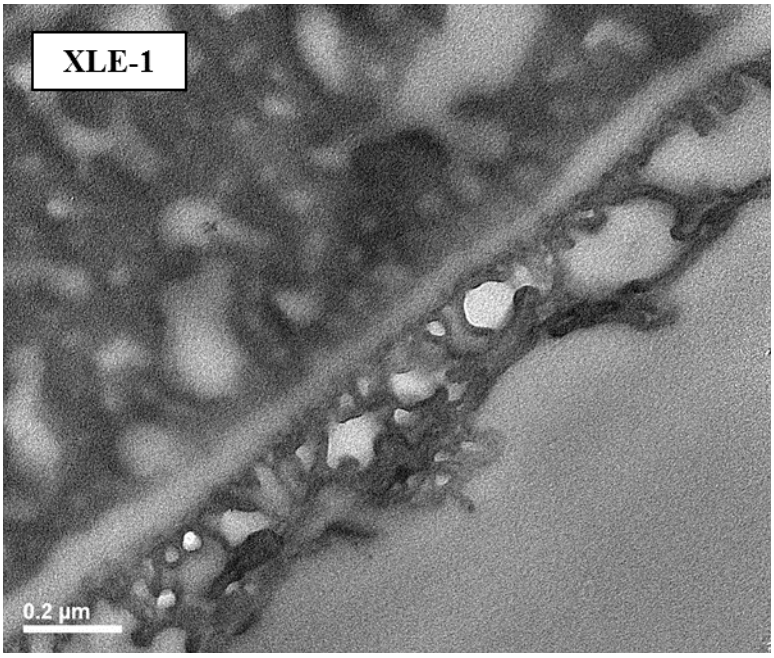
XLE-1
0.2 µm

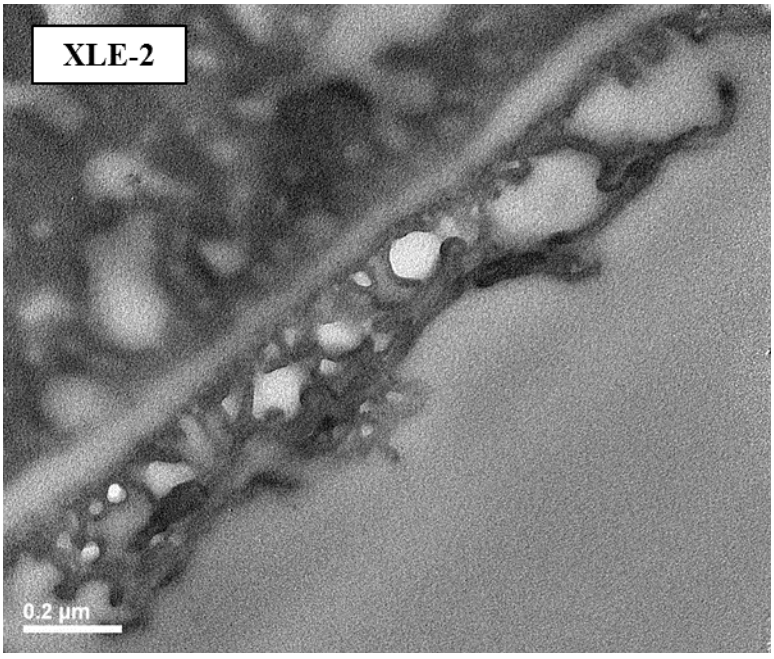
XLE-2
0.2 µm

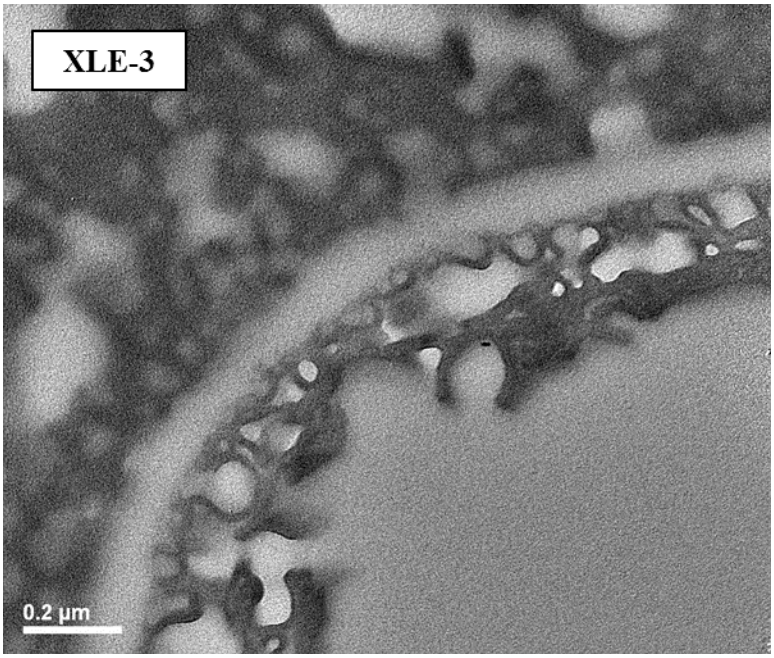
XLE-3
0.2 µm

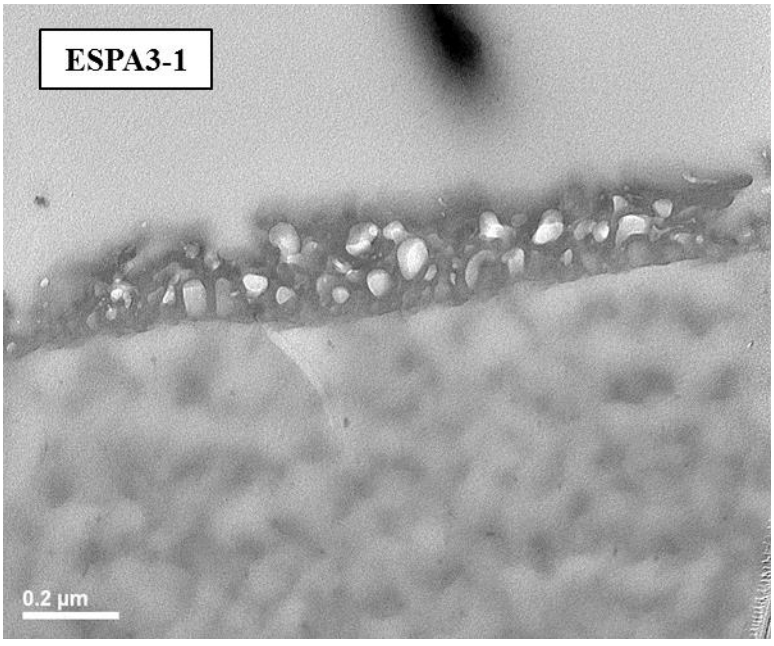
ESPA3-1
0.2 µm

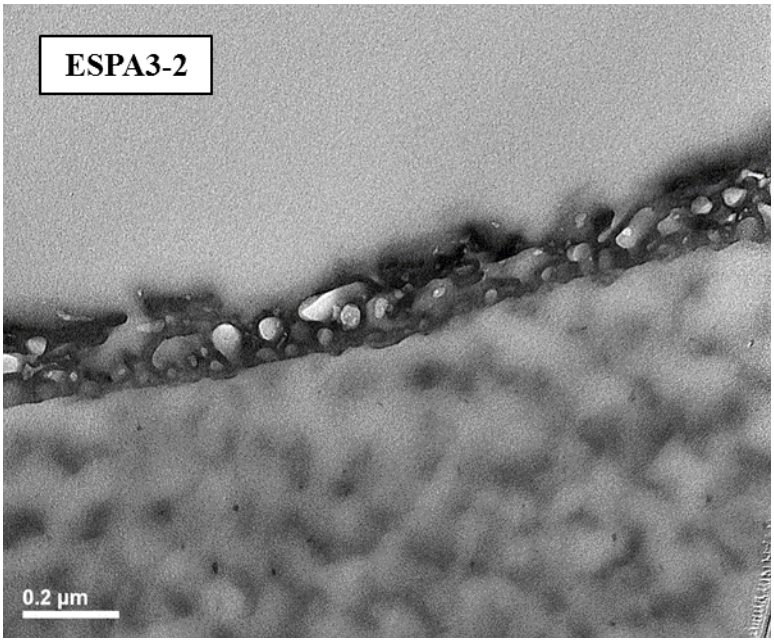
ESPA3-2
0.2 µm

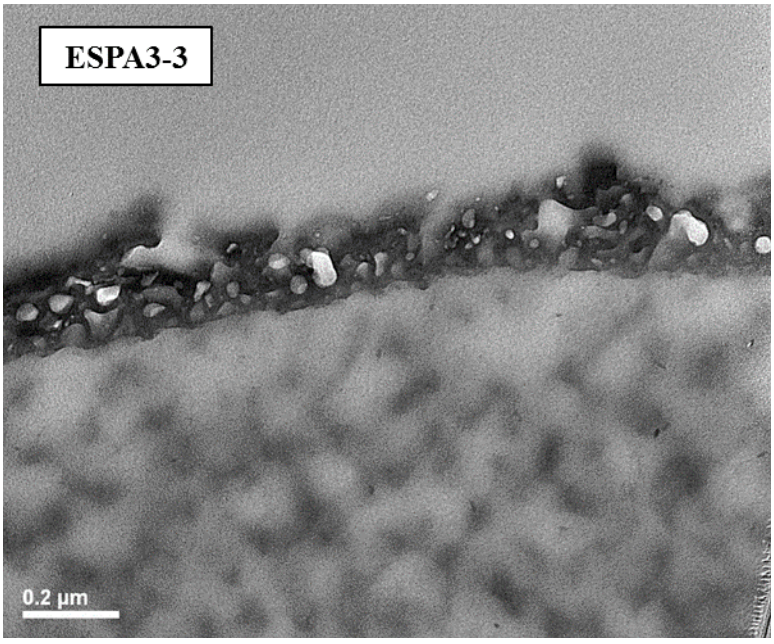
ESPA3-3
0.2 µm

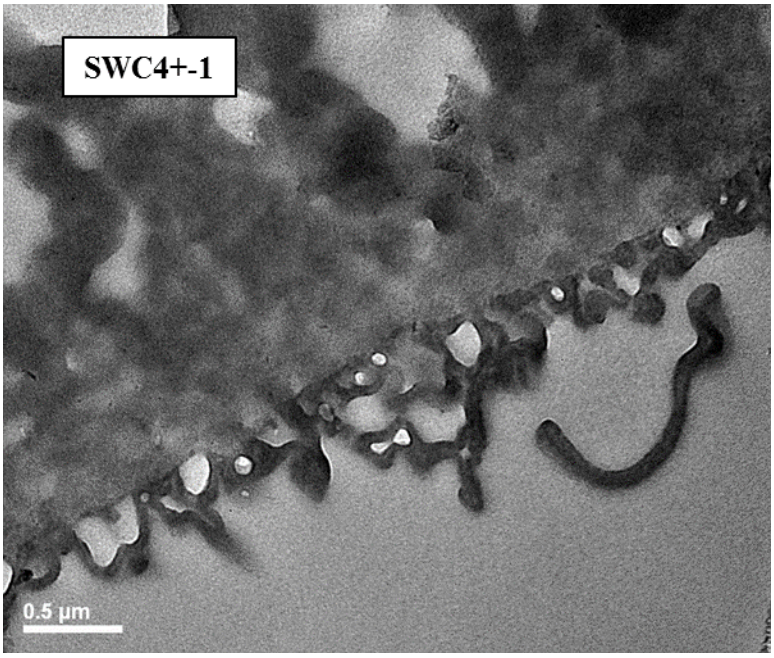
SWC4+-1
0.5 µm

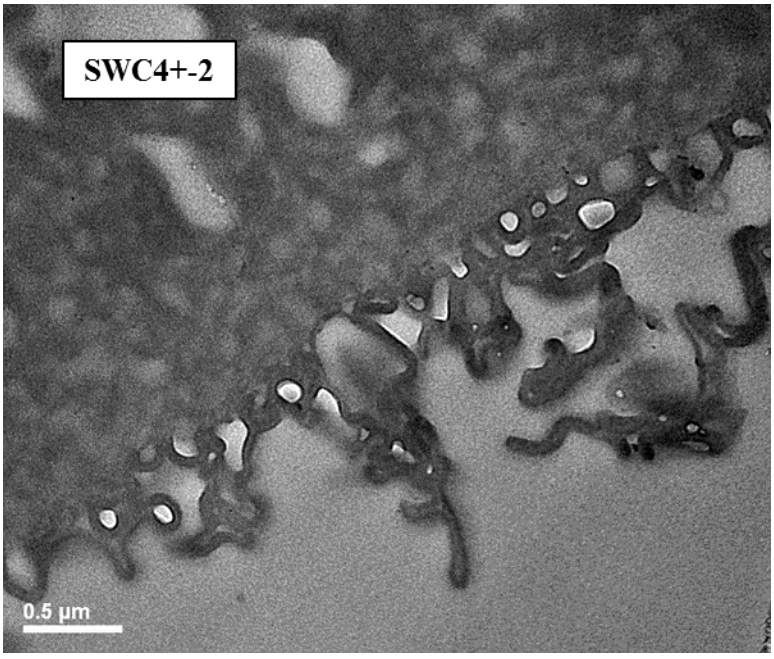
SWC4+-2
0.5 µm

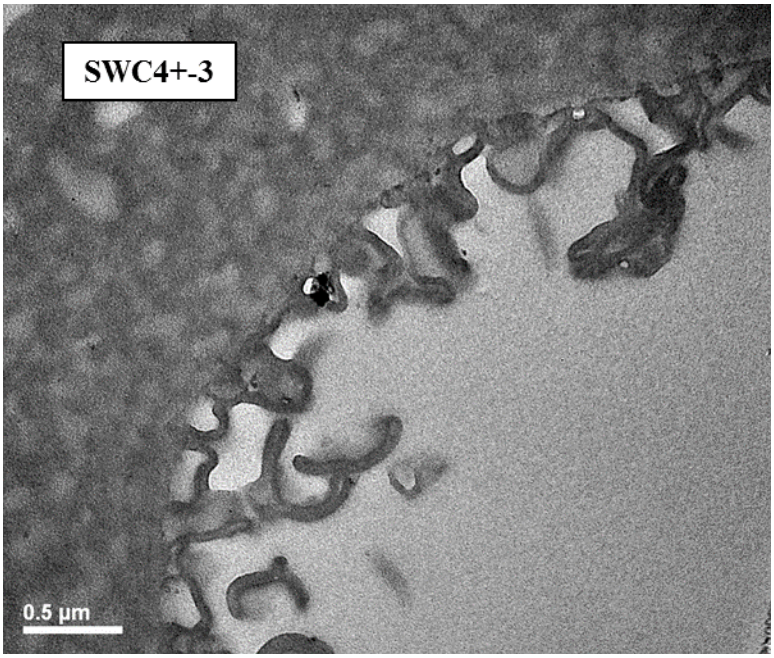
SWC4+-3
0.5 µm

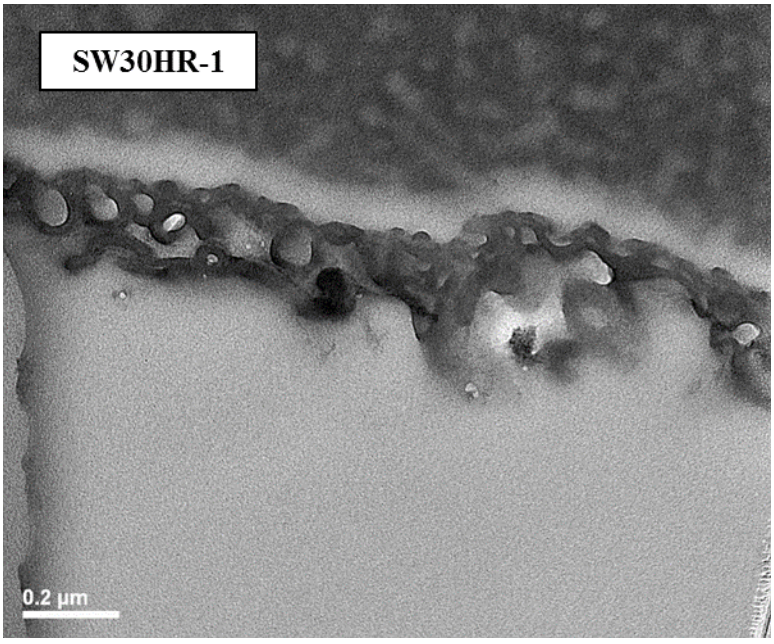
SW30HR-1
0.2 µm

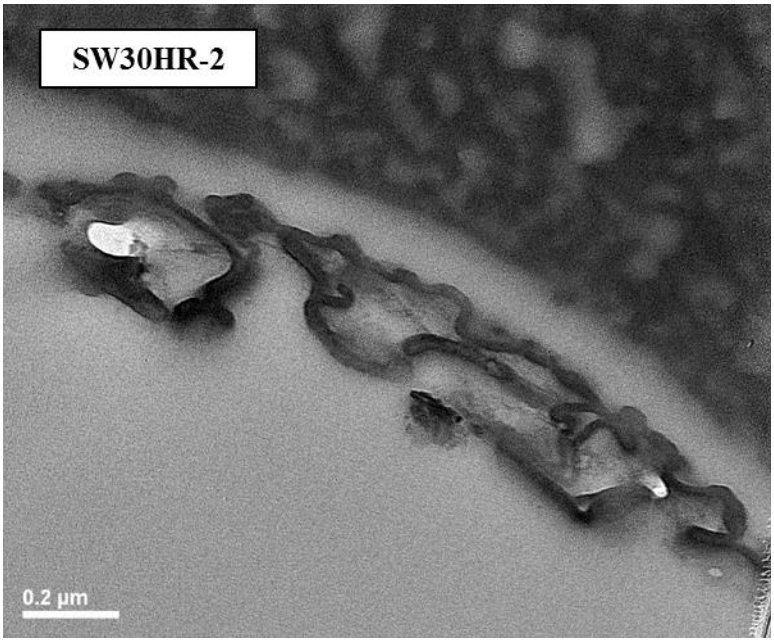
SW30HR-2
0.2 µm

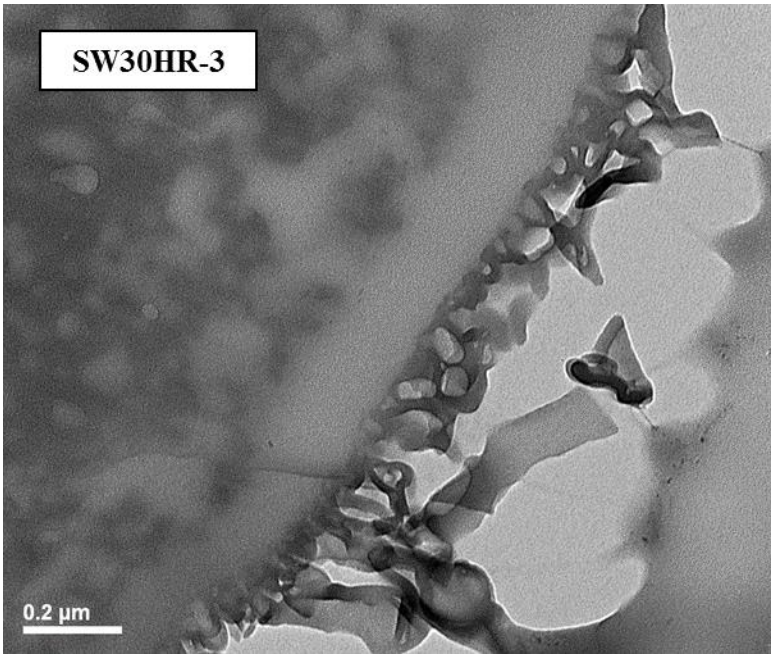
SW30HR-3
0.2 µm

APPENDIX 2: RESULTS OF SCANNING ELECTRON MICROSCOPE (SEM) ANALYSES OF ACTIVE LAYER THICKNESS

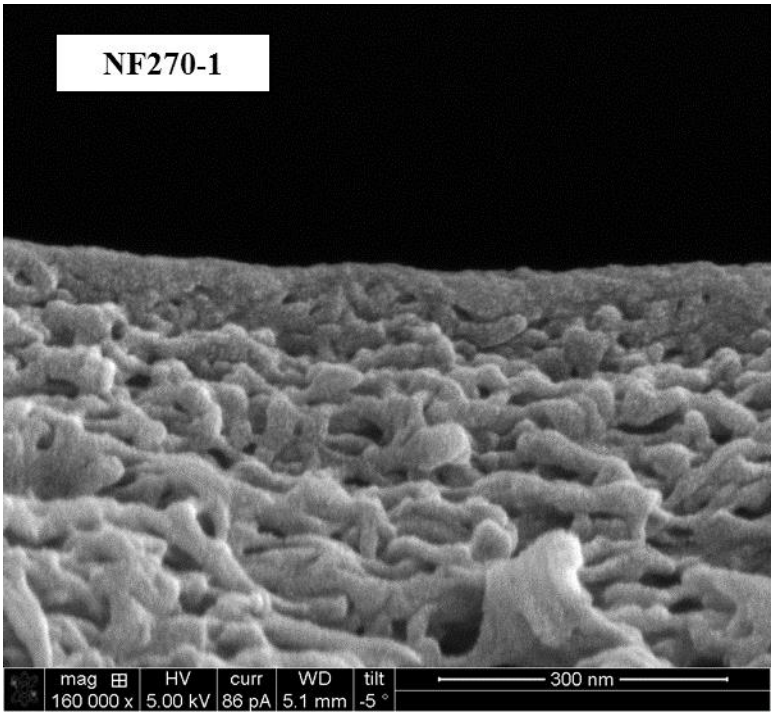

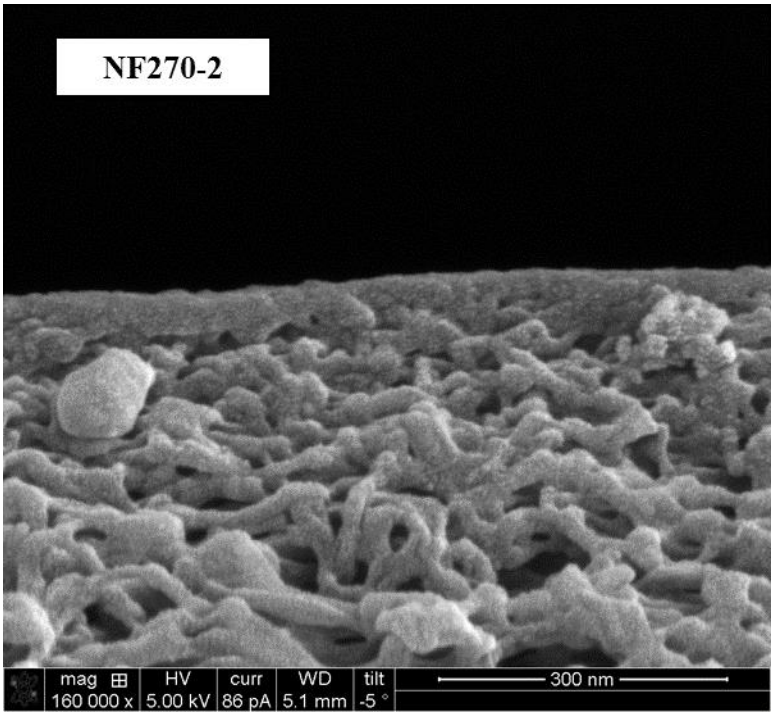

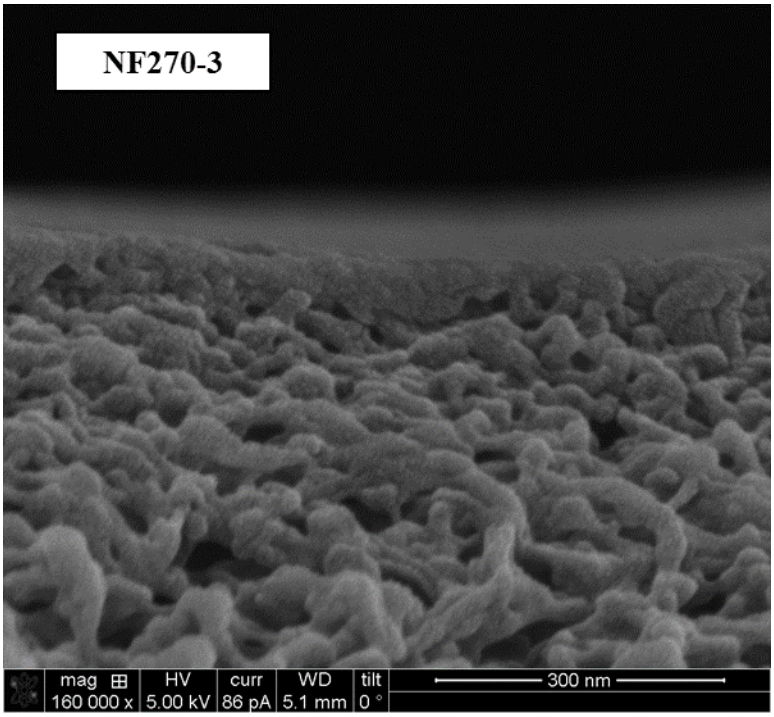
NF270-3
mag
160 000 x
HV
5.00 kV
curr
86 pA
WD
5.1 mm
tilt
0 °
300 nm

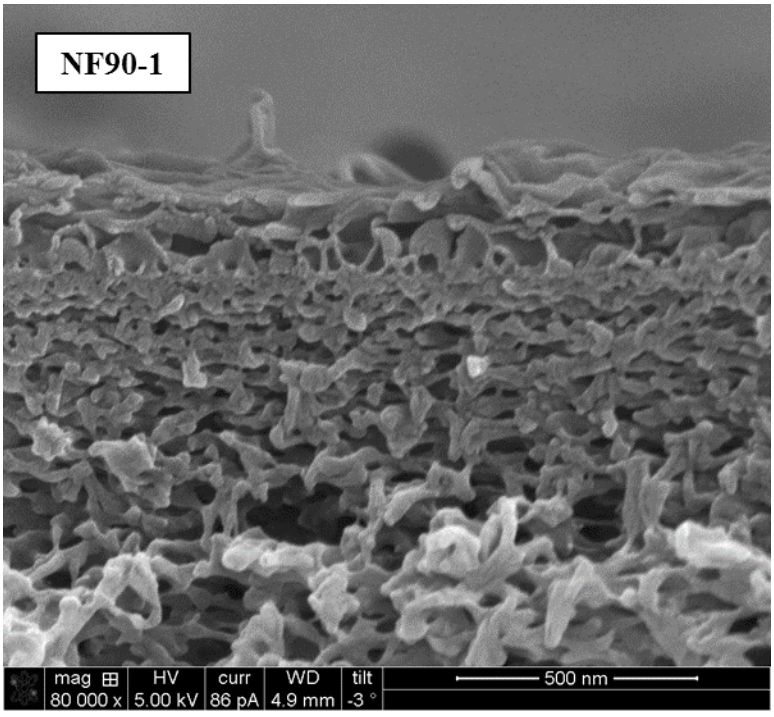
NF90-1
mag
80 000 x
HV
5.00 kV
curr
86 pA
WD
4.9 mm
tilt
-3 °
500 nm

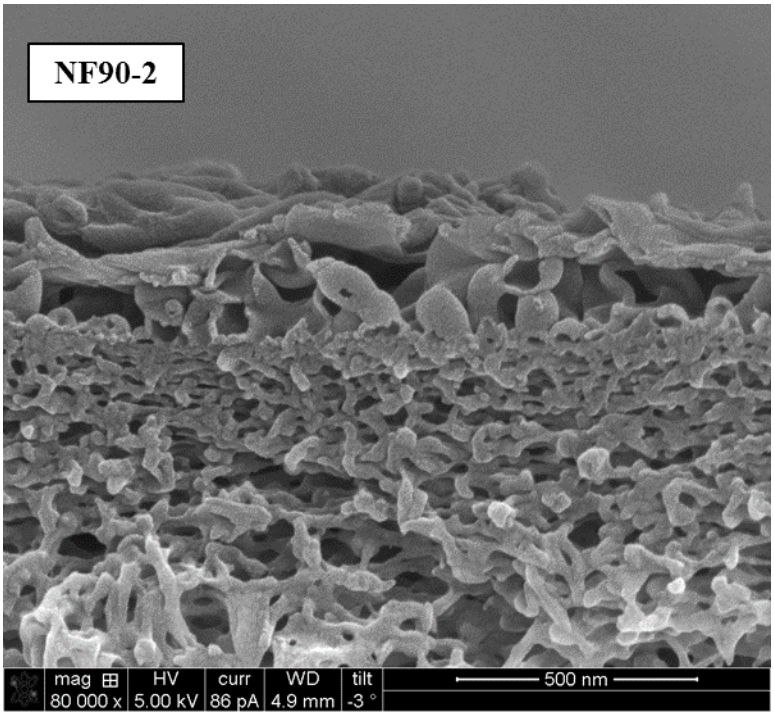
NF90-2
mag
80 000 x
HV
5.00 kV
curr
86 pA
WD
4.9 mm
tilt
-3 °
500 nm

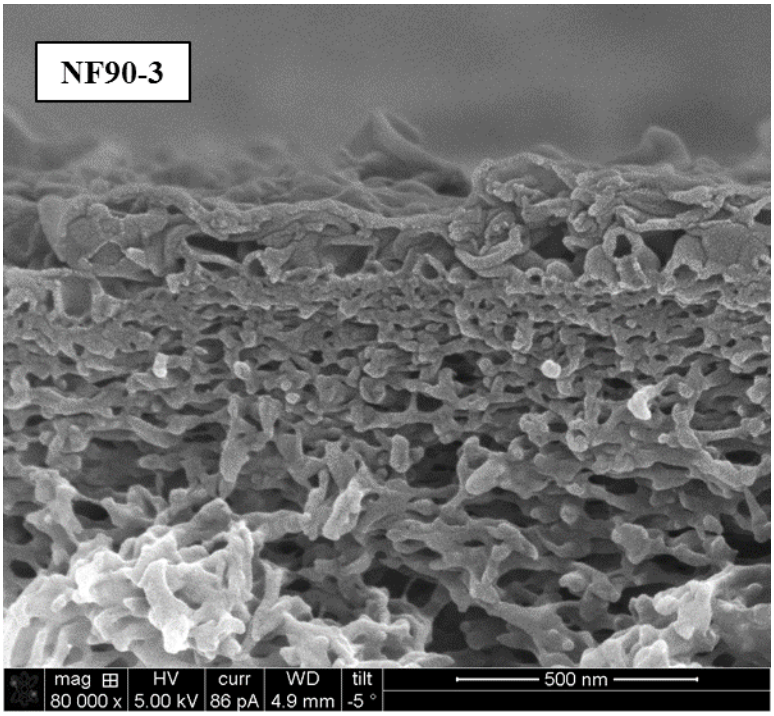
NF90-3
mag
80 000 x
HV
5.00 kV
curr
86 pA
WD
4.9 mm
tilt
-5 °
500 nm

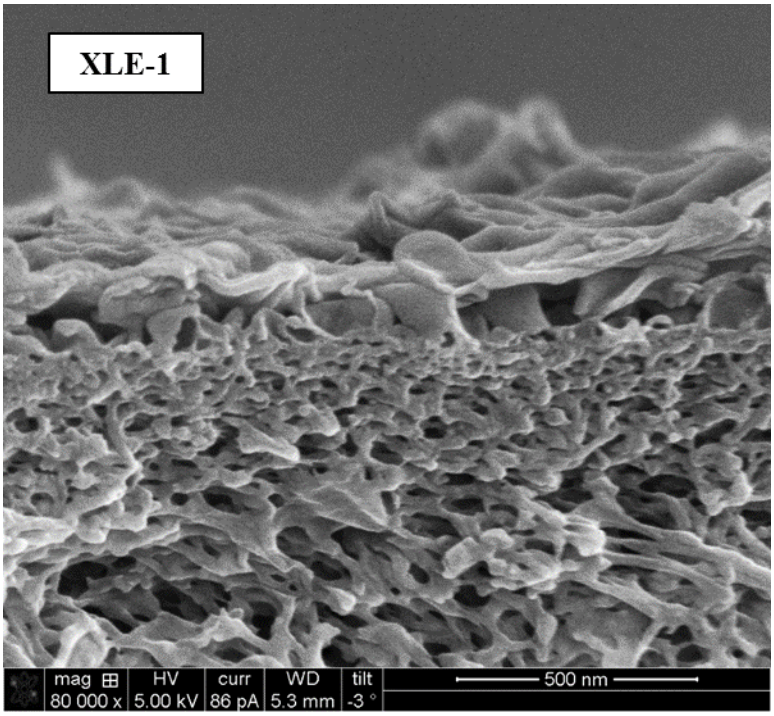
XLE-1
mag
80 000 x
HV
5.00 kV
curr
86 pA
WD
5.3 mm
tilt
-3 °
500 nm

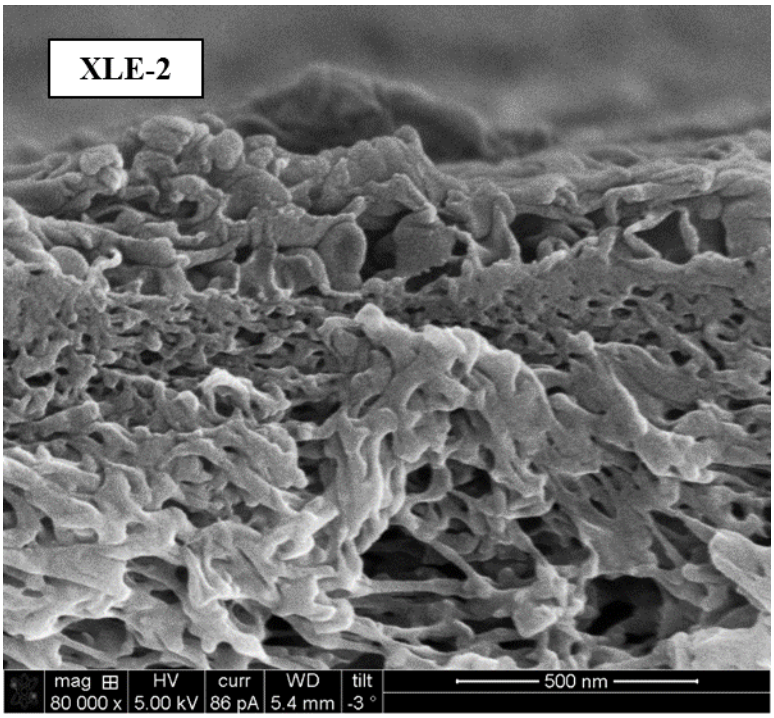
XLE-2
mag
80 000 x
HV
5.00 kV
curr
86 pA
WD
5.4 mm
tilt
-3 °
500 nm

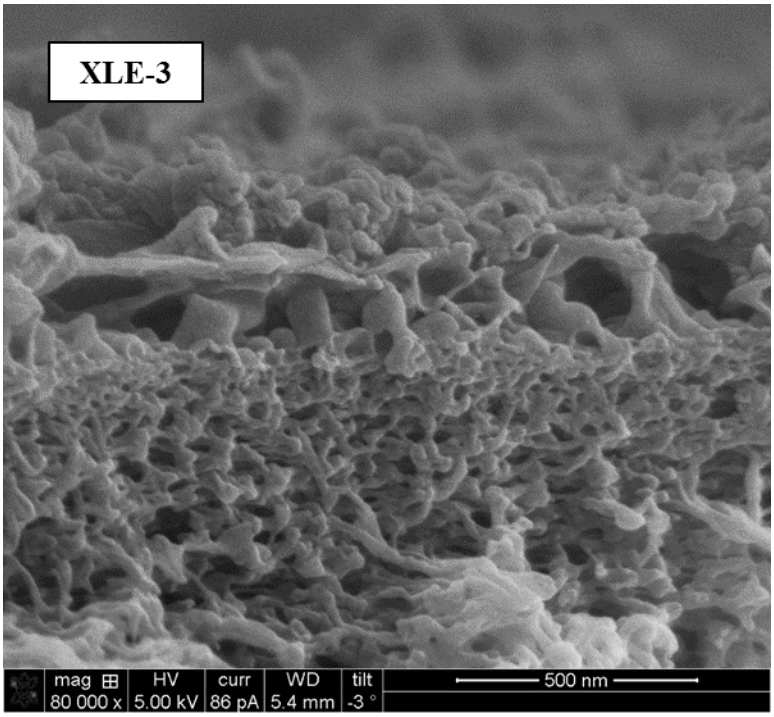
XLE-3
mag
80 000 x
HV
5.00 kV
curr
86 pA
WD
5.4 mm
tilt
-3 °
500 nm

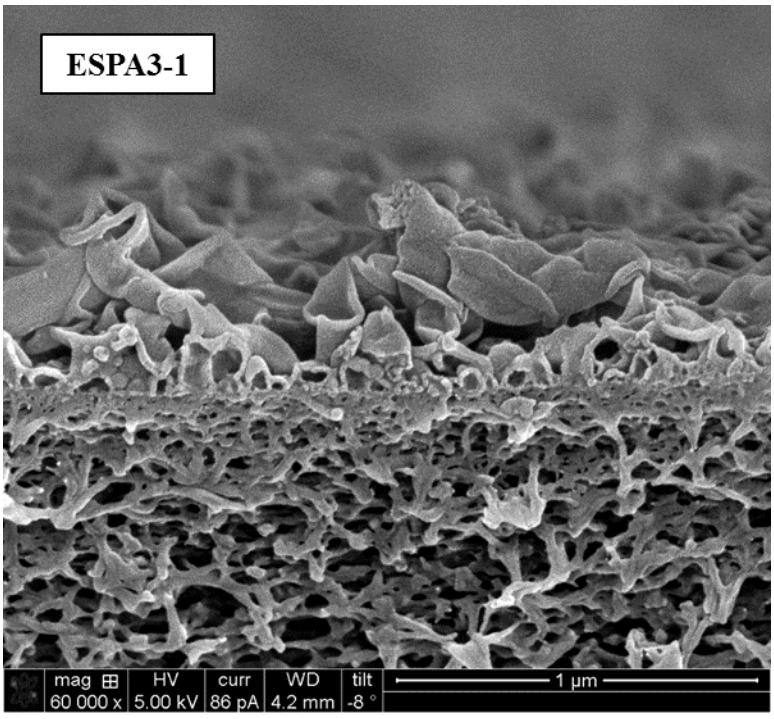
ESPA3-1
mag
60 000 x
HV
5.00 kV
curr
86 pA
WD
4.2 mm
tilt
-8 °
1 µm

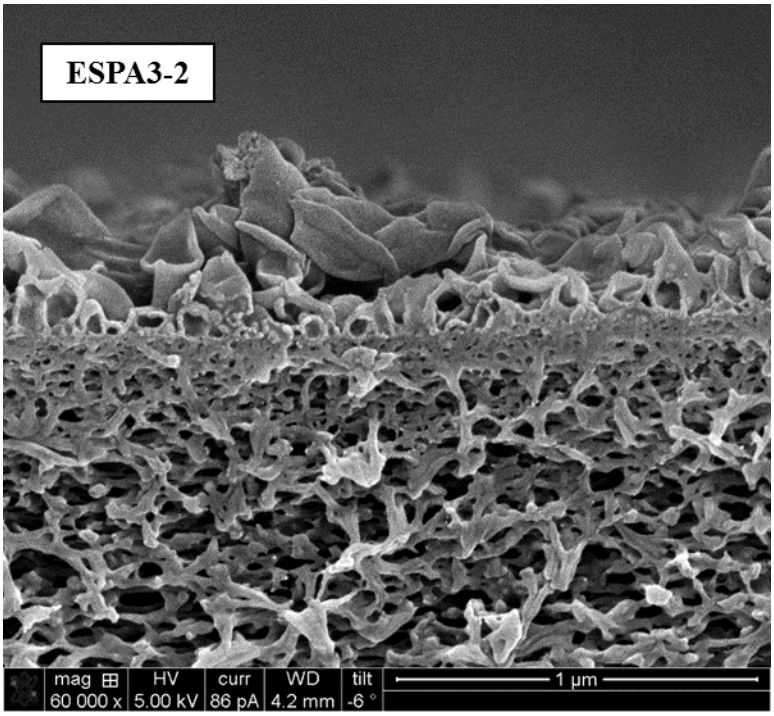
ESPA3-2
mag
60 000 x
HV
5.00 kV
curr
86 pA
WD
4.2 mm
tilt
-6 °
1 µm

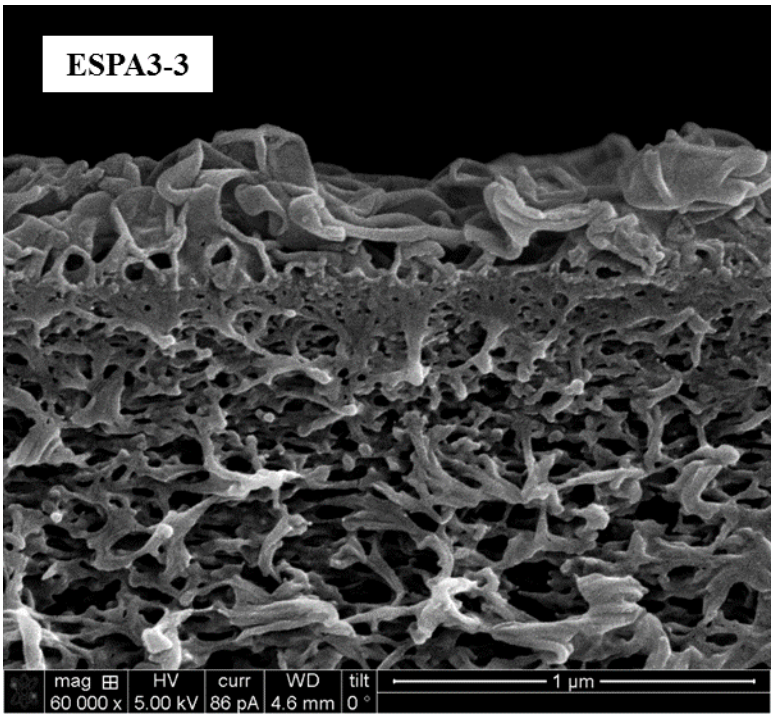
ESPA3-3
mag
60 000 x
HV
5.00 kV
curr
86 pA
WD
4.6 mm
tilt
0 °
1 µm

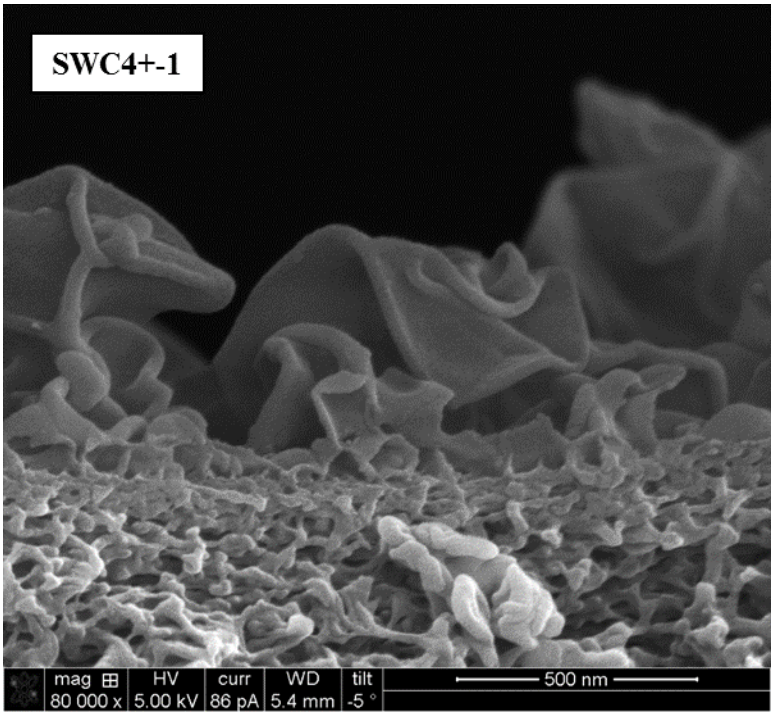
SWC4+-1
mag
80 000 x
HV
5.00 kV
curr
86 pA
WD
5.4 mm
tilt
-5 °
500 nm

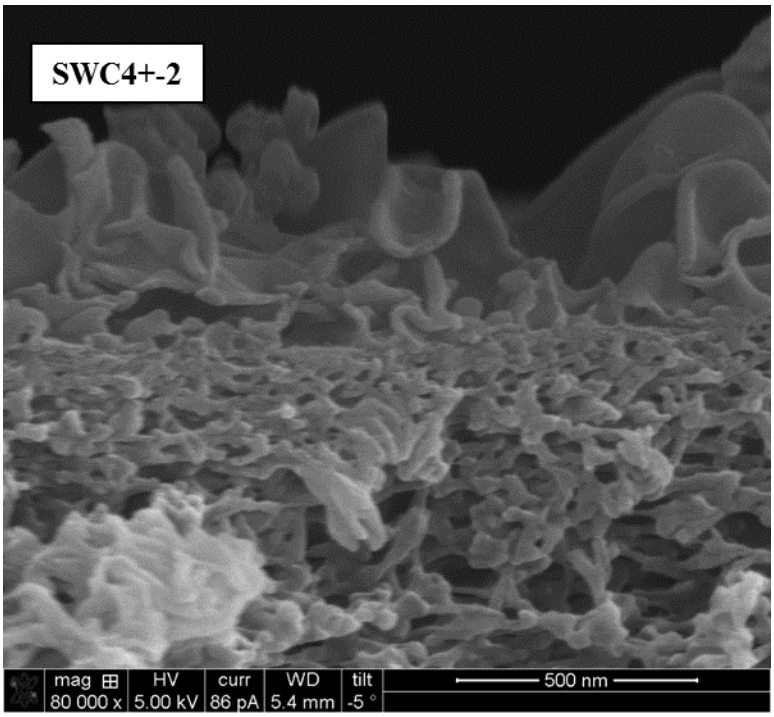
SWC4+-2
mag
80 000 x
HV
5.00 kV
curr
86 pA
WD
5.4 mm
tilt
-5 °
500 nm

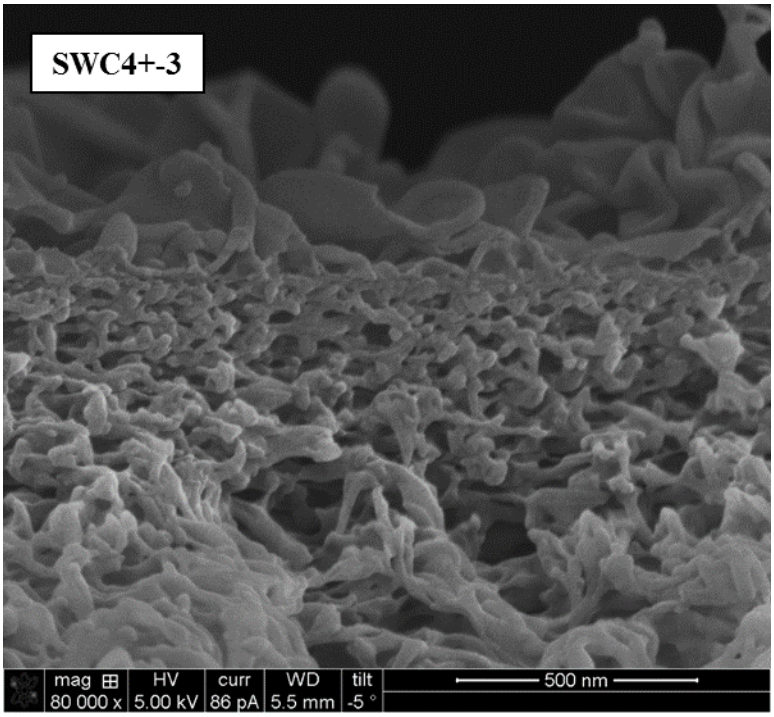
SWC4+-3
mag
80 000 x
HV
5.00 kV
curr
86 pA
WD
5.5 mm
tilt
-5 °
500 nm

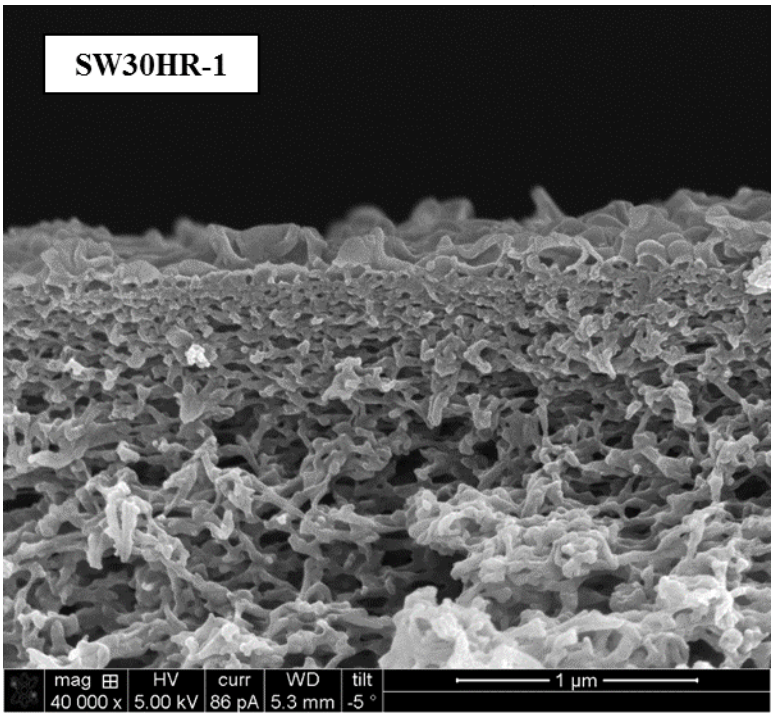
SW30HR-1
mag
40 000 x
HV
5.00 kV
curr
86 pA
WD
5.3 mm
tilt
-5 °
1 µm

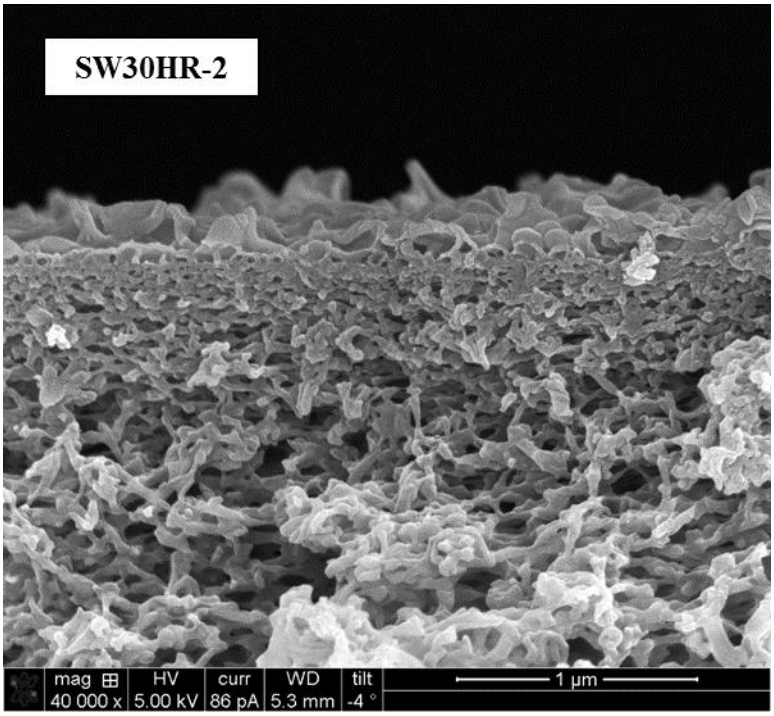
SW30HR-2
mag
40 000 x
HV
5.00 kV
curr
86 pA
WD
5.3 mm
tilt
-4 °
1 µm

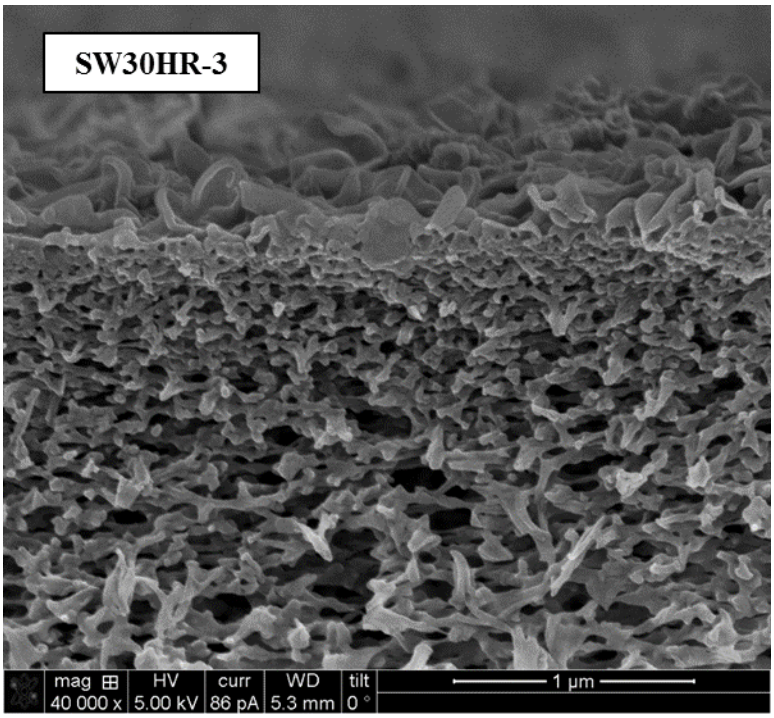
SW30HR-3
mag
40 000 x
HV
5.00 kV
curr
86 pA
WD
5.3 mm
tilt
0 °
1 µm

APPENDIX 3: RESULTS OF RUTHERFORD BACKSCATTERING SPECTROMETRY (RBS) ANALYSES OF ACTIVE LAYER THICKNESS

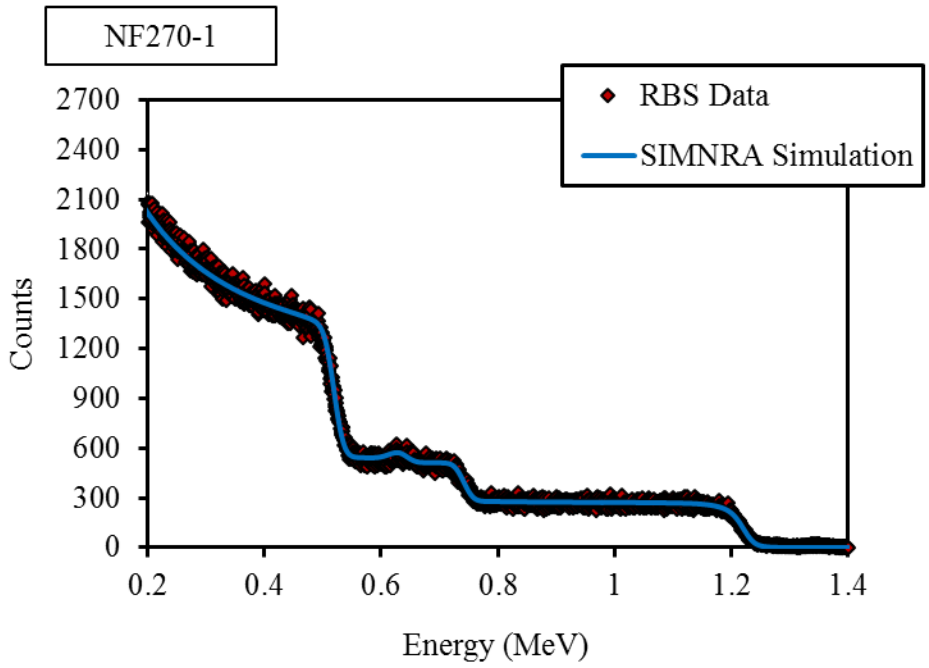

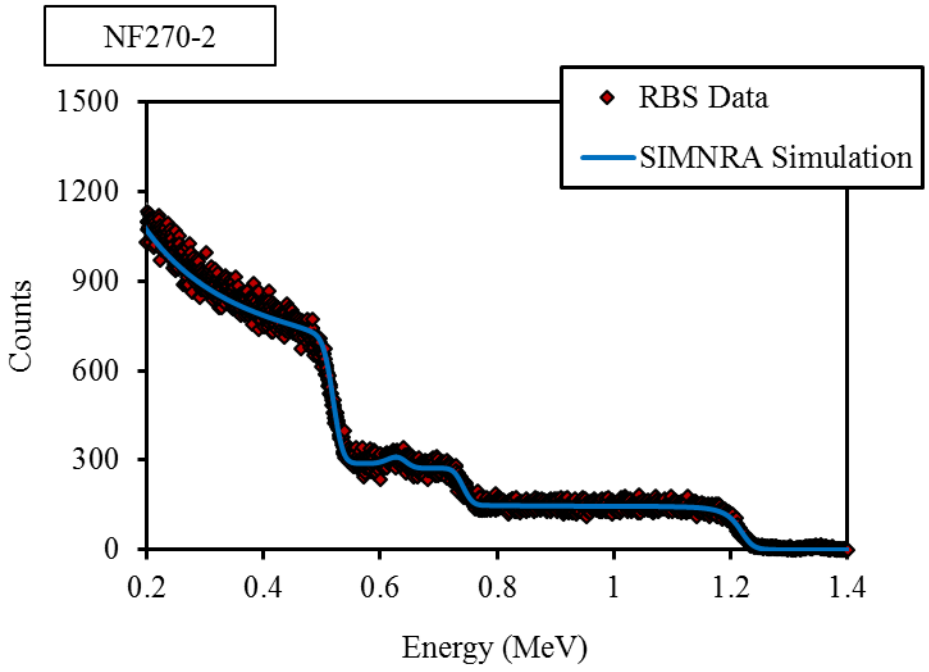

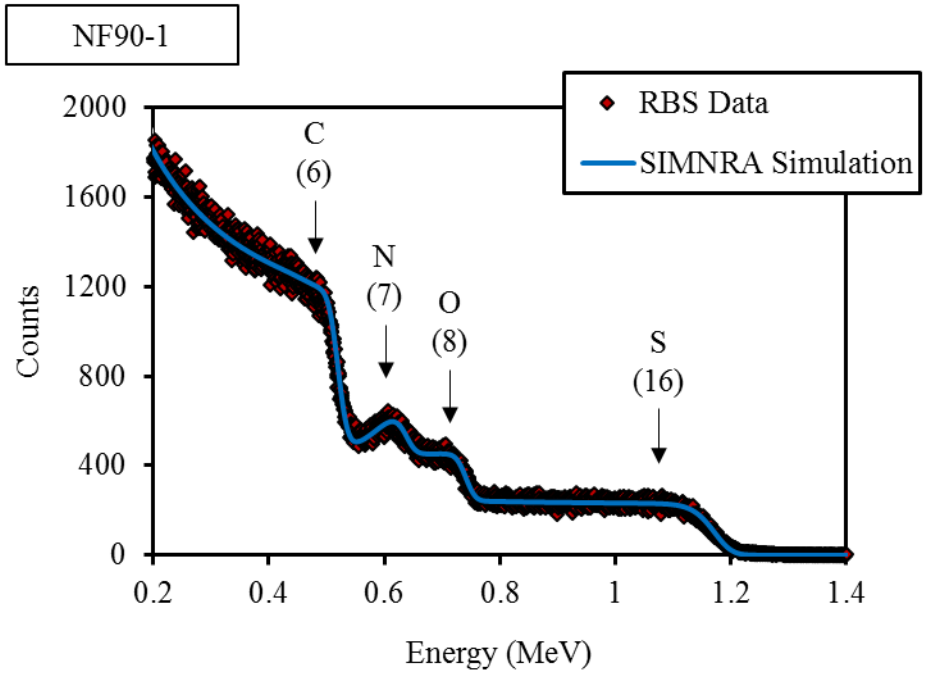
NF90-1
RBS Data
SIMNRA Simulation
C
(6)
N
(7)
O
(8)
S
(16)
Counts
Energy (MeV)
2000
1600
1200
800
400
0
0.2
0.4
0.6
0.8
1
1.2
1.4

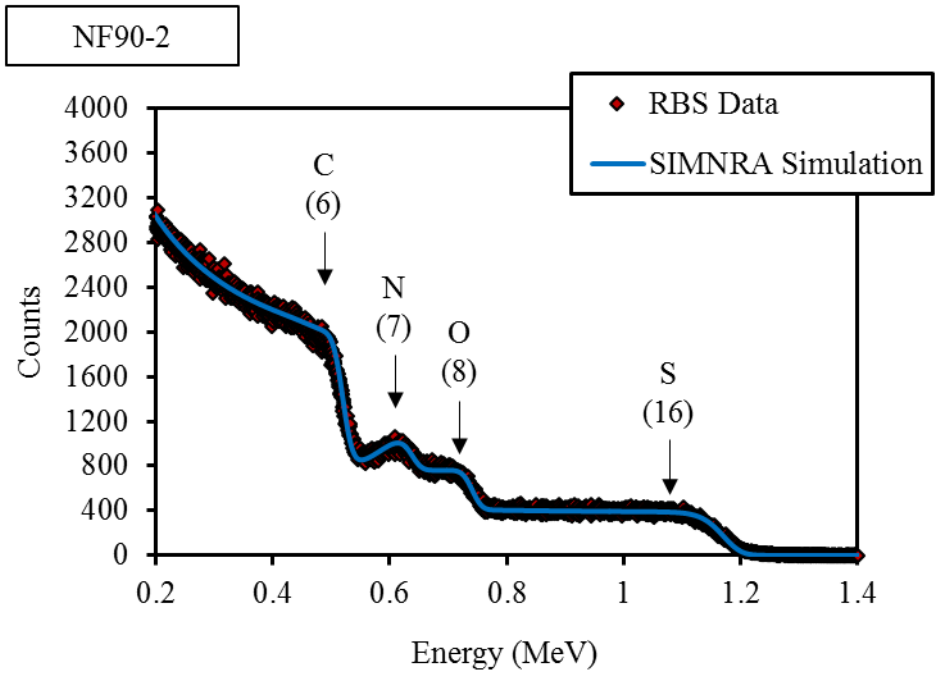
NF90-2
RBS Data
SIMNRA Simulation
C
(6)
N
(7)
O
(8)
S
(16)
Counts
Energy (MeV)
4000
3600
3200
2800
2400
2000
1600
1200
800
400
0
0.2
0.4
0.6
0.8
1
1.2
1.4

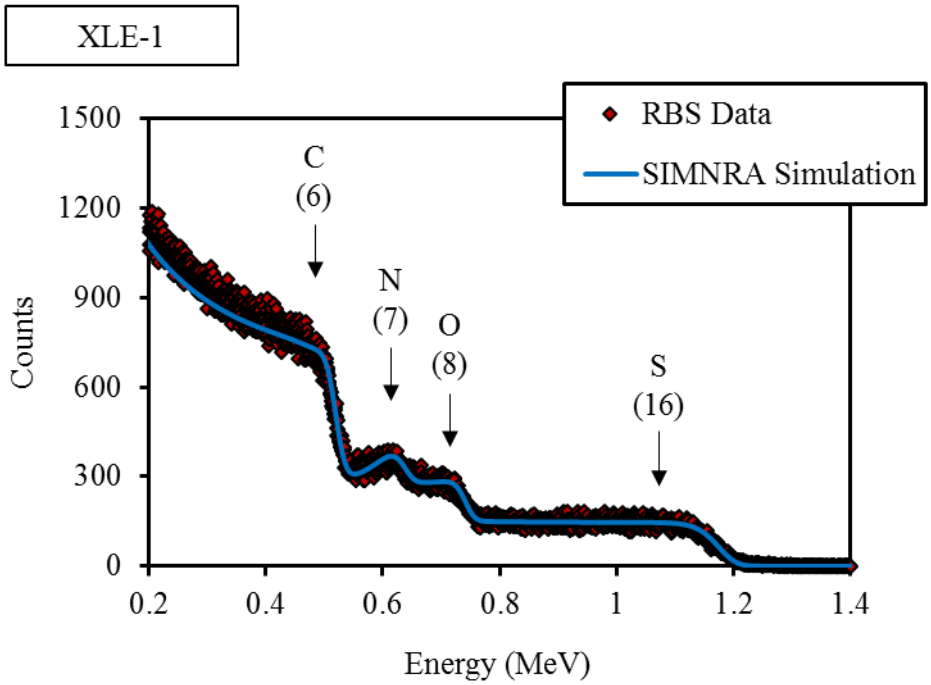
XLE-1
RBS Data
SIMNRA Simulation
C
(6)
N
(7)
O
(8)
S
(16)
Counts
Energy (MeV)
0
300
600
900
1200
1500
0.2
0.4
0.6
0.8
1
1.2
1.4

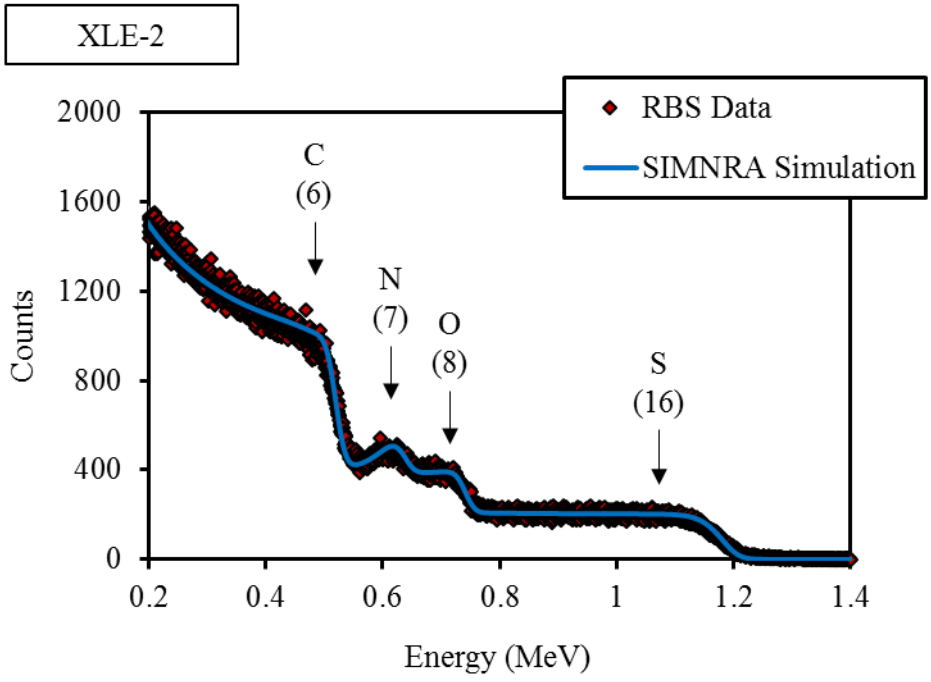
XLE-2
RBS Data
SIMNRA Simulation
C
(6)
N
(7)
O
(8)
S
(16)
Counts
Energy (MeV)
0
400
800
1200
1600
2000
0.2
0.4
0.6
0.8
1
1.2
1.4

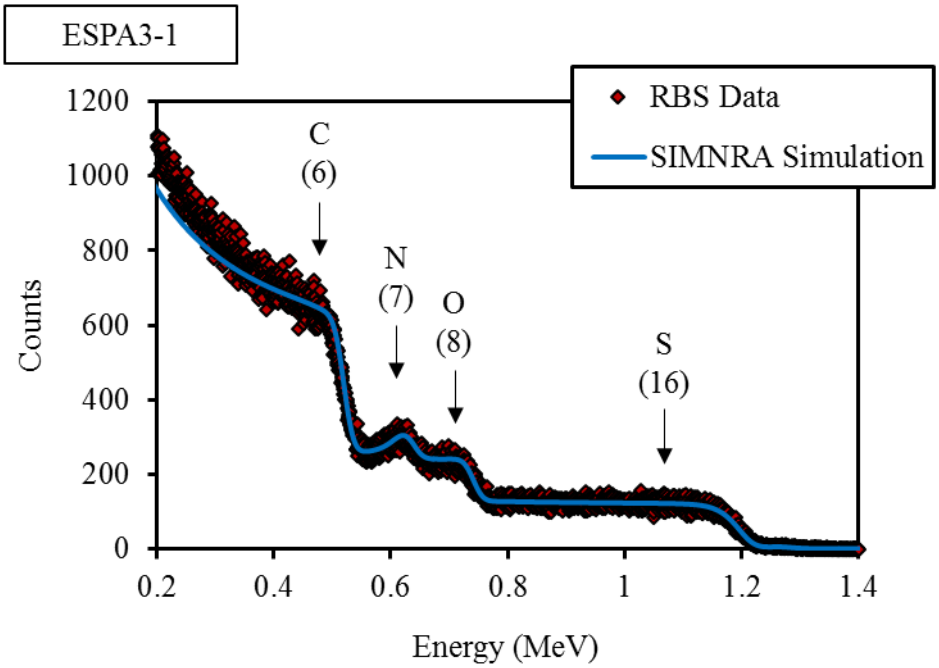
ESPA3-1
RBS Data
SIMNRA Simulation
C
(6)
N
(7)
O
(8)
S
(16)
Counts
Energy (MeV)
0
200
400
600
800
1000
1200
0.2
0.4
0.6
0.8
1
1.2
1.4

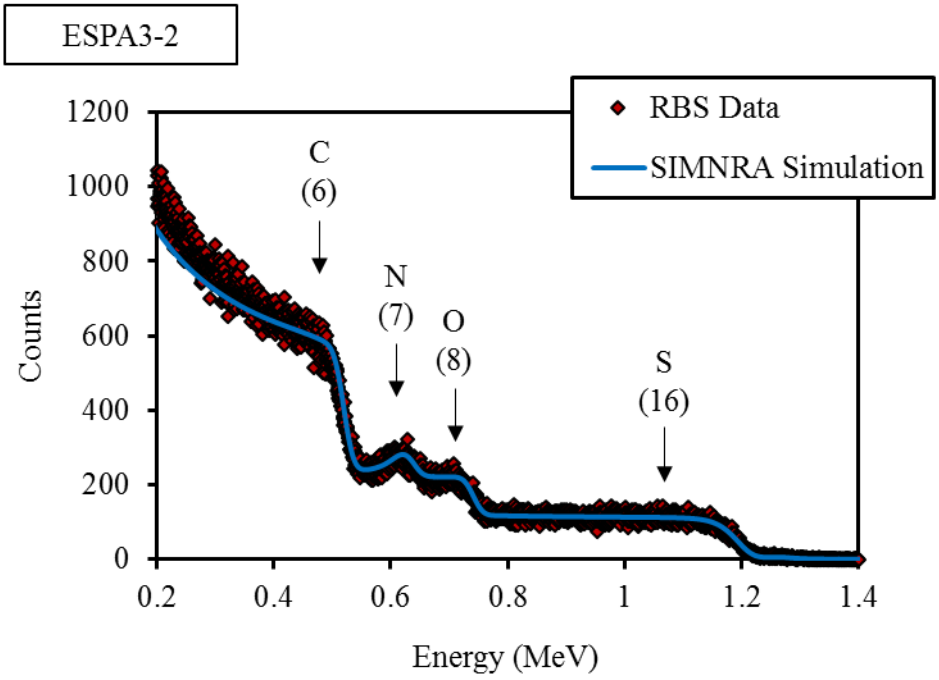
ESPA3-2
RBS Data
SIMNRA Simulation
C
(6)
N
(7)
O
(8)
S
(16)
Counts
Energy (MeV)
0
200
400
600
800
1000
1200
0.2
0.4
0.6
0.8
1
1.2
1.4

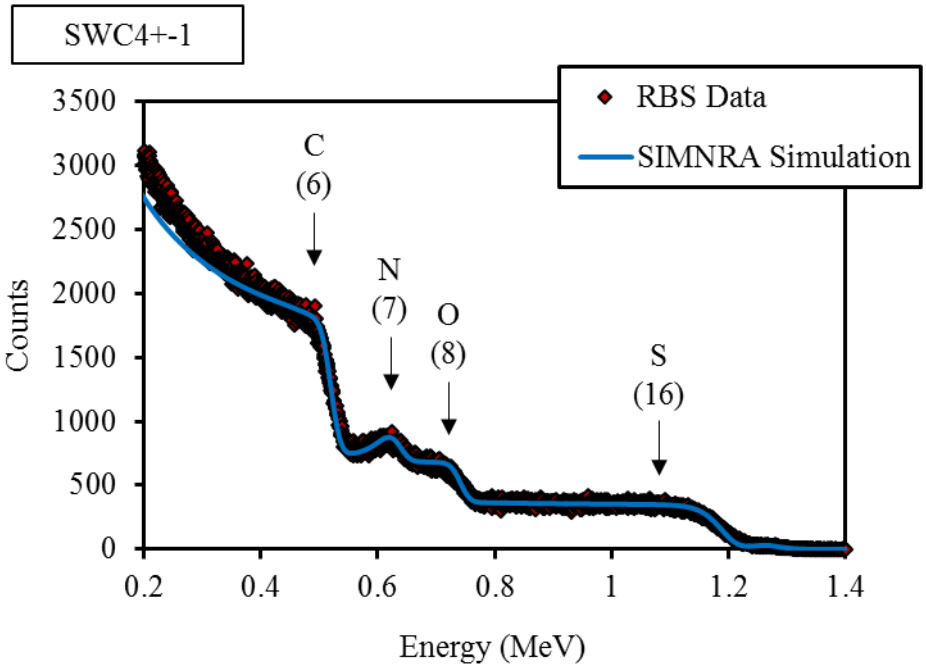
SWC4+-1
RBS Data
SIMNRA Simulation
C
(6)
N
(7)
O
(8)
S
(16)
Counts
Energy (MeV)
0
500
1000
1500
2000
2500
3000
3500
0.2
0.4
0.6
0.8
1
1.2
1.4

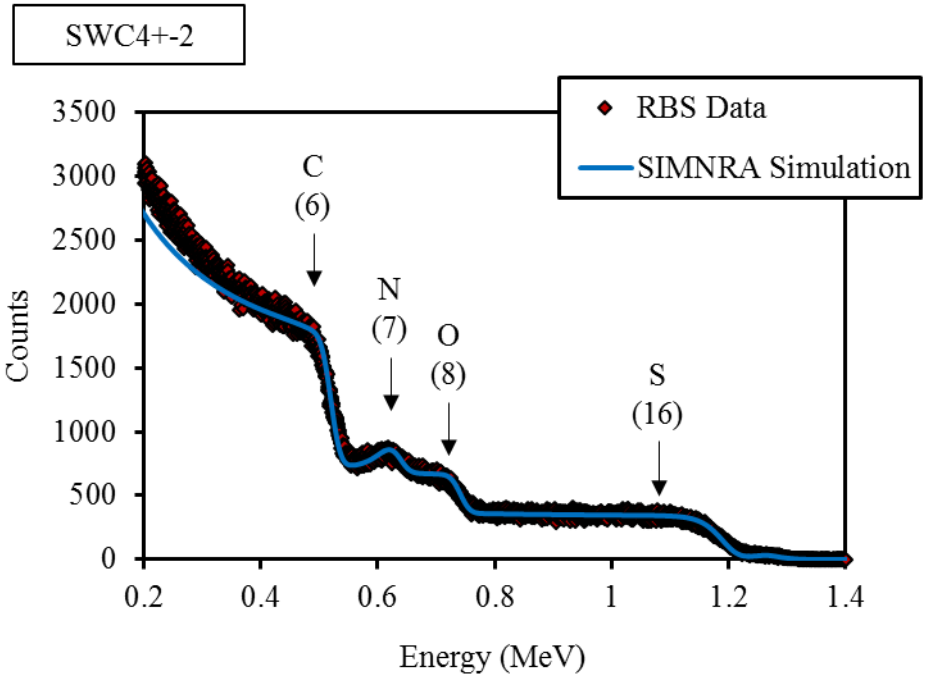
SWC4+-2
RBS Data
SIMNRA Simulation
C
(6)
N
(7)
O
(8)
S
(16)
Counts
Energy (MeV)
0
500
1000
1500
2000
2500
3000
3500
0.2
0.4
0.6
0.8
1
1.2
1.4

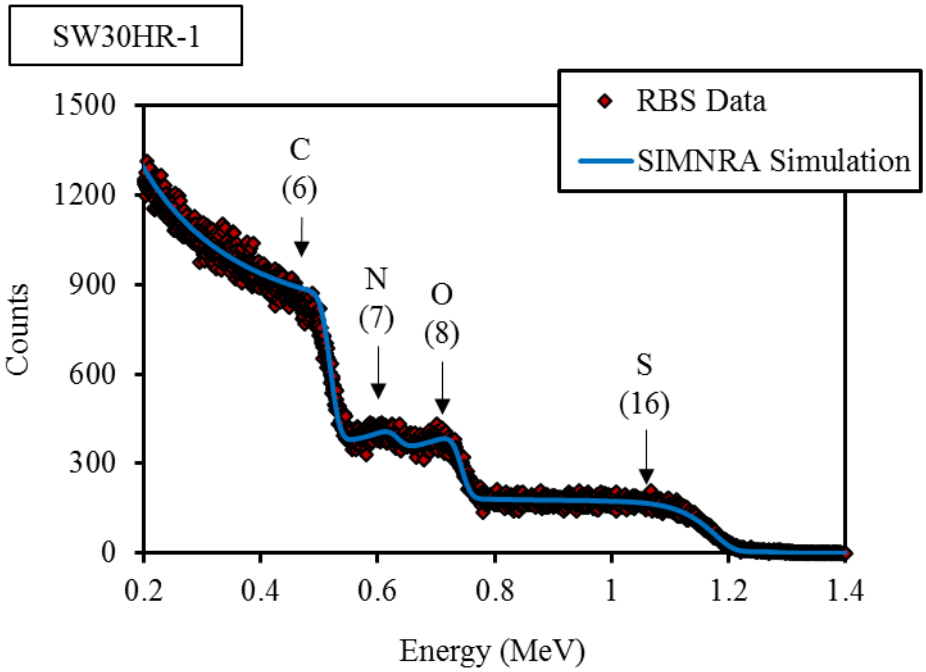
SW30HR-1
RBS Data
SIMNRA Simulation
C
(6)
N
(7)
O
(8)
S
(16)
Counts
Energy (MeV)
0
300
600
900
1200
1500
0.2
0.4
0.6
0.8
1
1.2
1.4

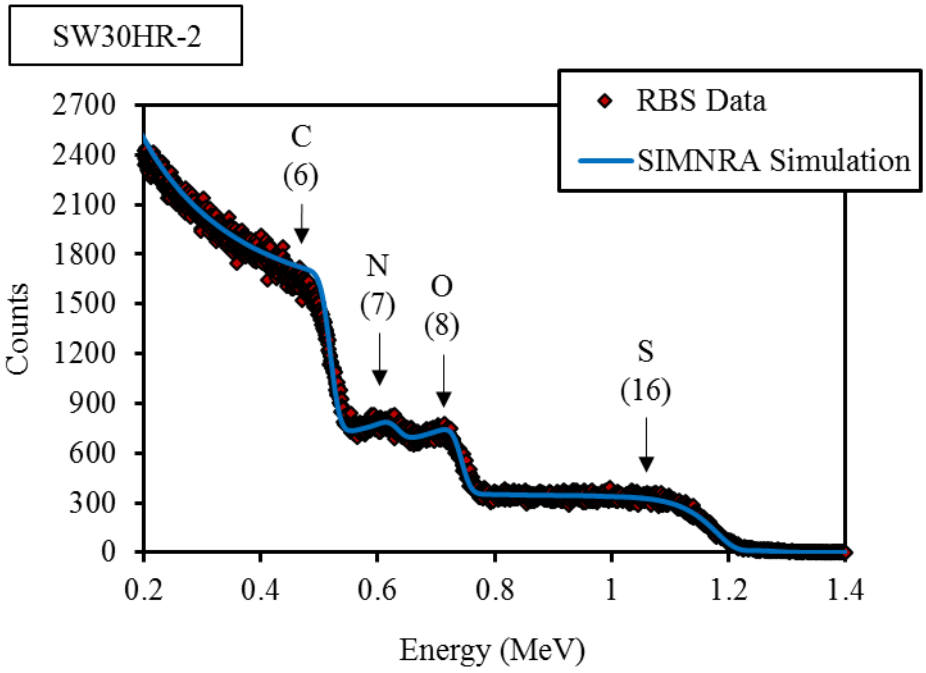
SW30HR-2
RBS Data
SIMNRA Simulation
C
(6)
N
(7)
O
(8)
S
(16)
Counts
Energy (MeV)
0
300
600
900
1200
1500
1800
2100
2400
2700
0.2
0.4
0.6
0.8
1
1.2
1.4

APPENDIX 4: RESULTS OF ATOMIC FORCE MICROSCOPY (AFM) ANALYSES OF ACTIVE LAYER THICKNESS

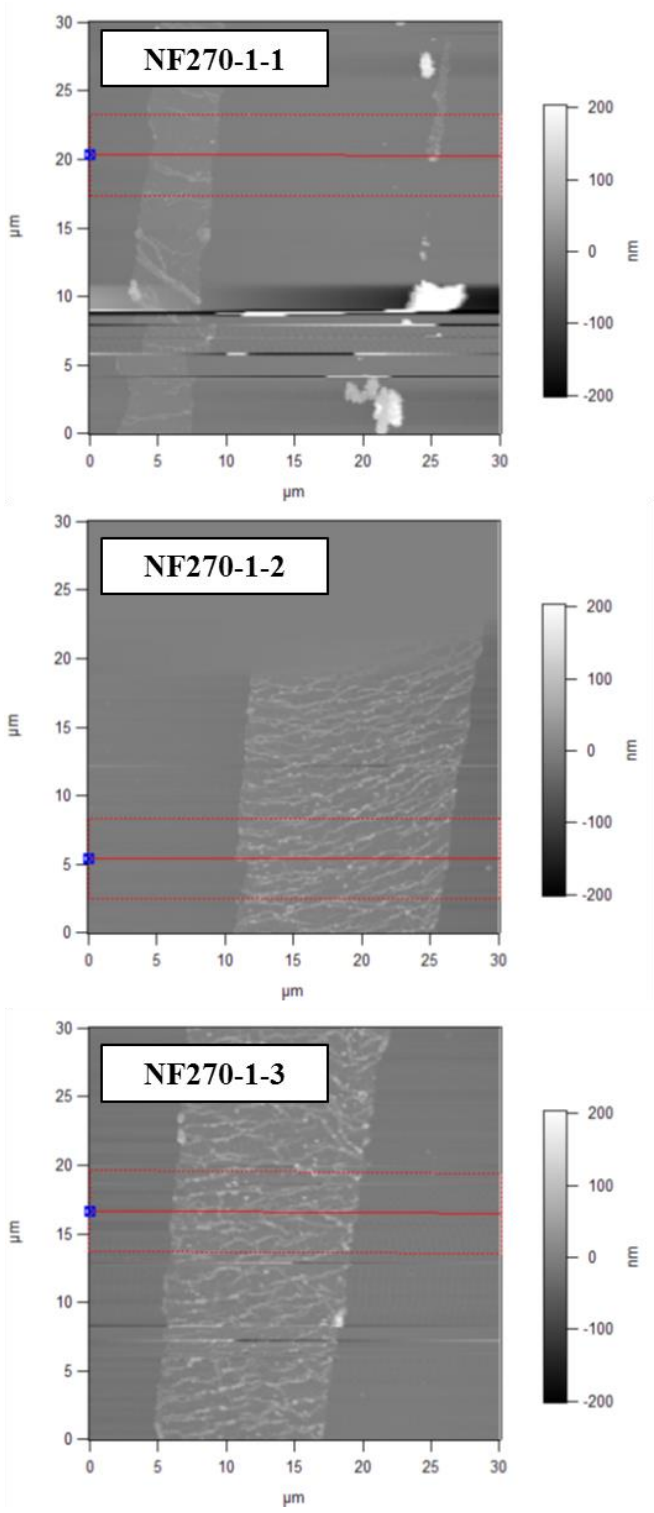

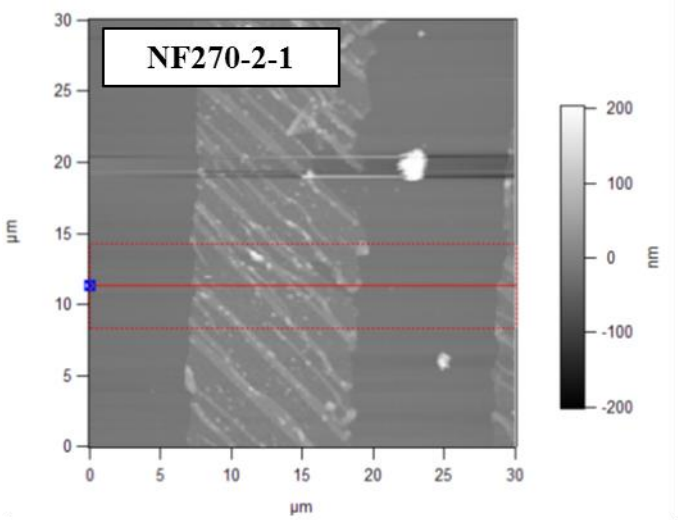
NF270-2-1
30
25
20
15
10
5
0
µm
0
5
10
15
20
25
30
µm
200
100
0
-100
-200
nm

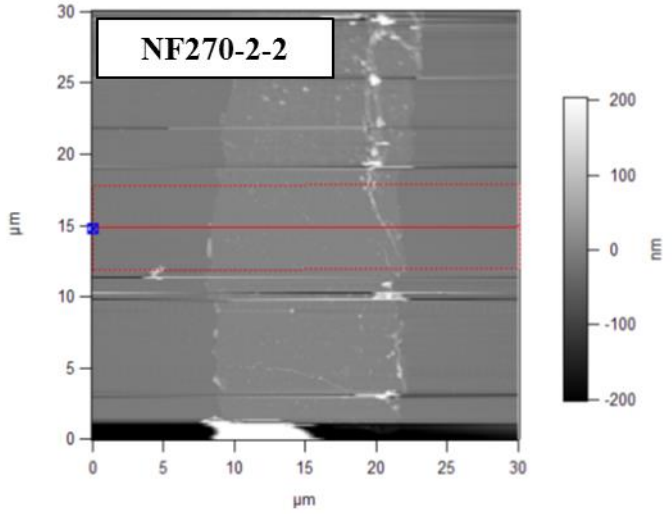
NF270-2-2
30
25
20
15
10
5
0
µm
0
5
10
15
20
25
30
µm
200
100
0
-100
-200
nm

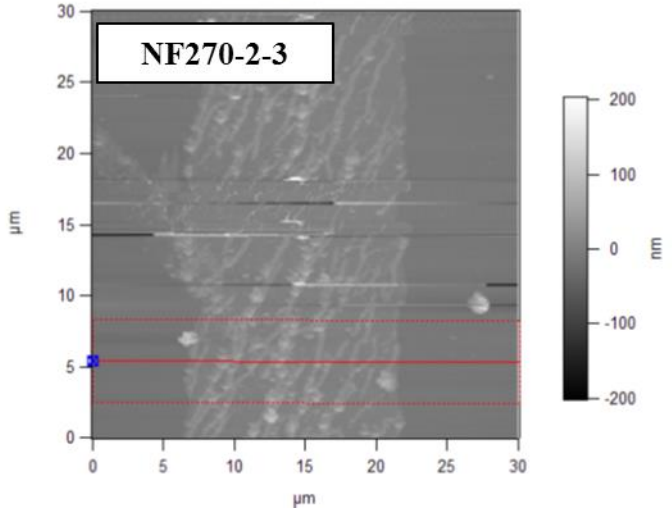
NF270-2-3
30
25
20
15
10
5
0
µm
0
5
10
15
20
25
30
µm
200
100
0
-100
-200
nm

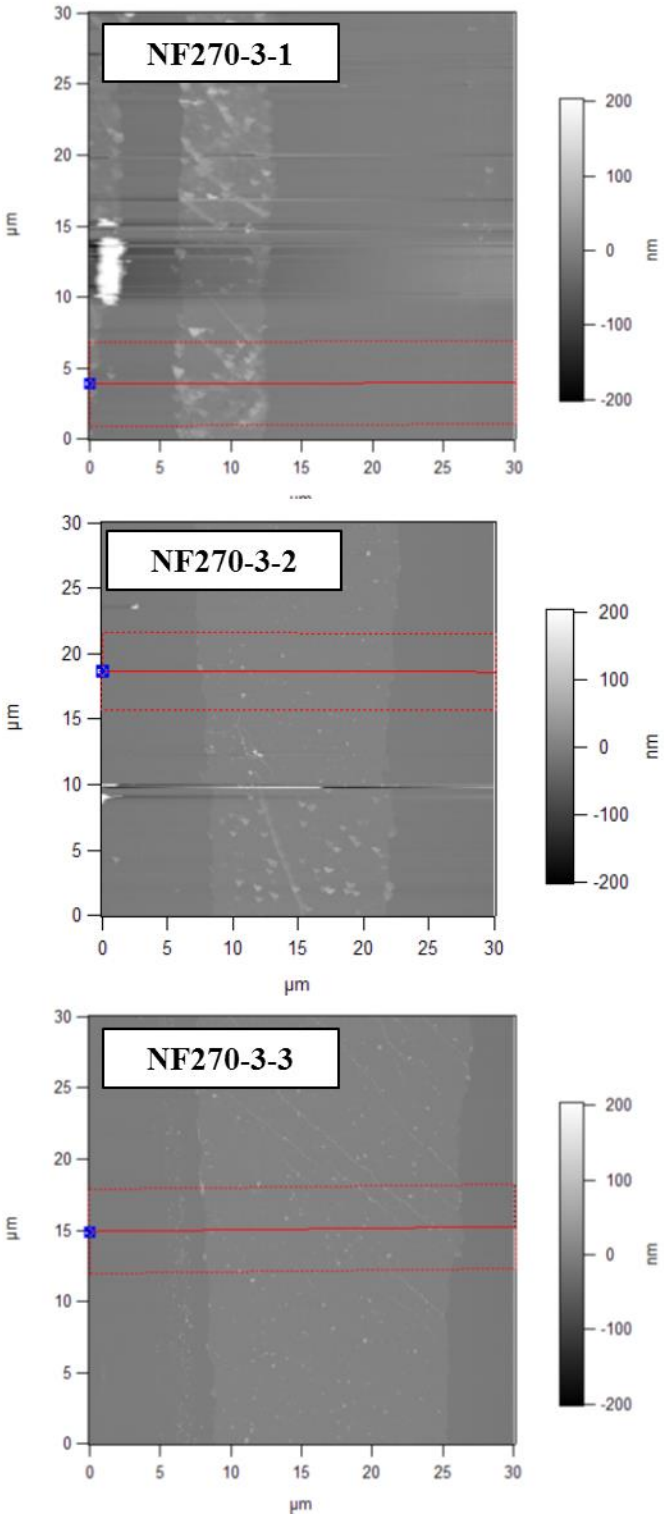
NF270-3-1
NF270-3-2
NF270-3-3
µm
nm
200
100
0
-100
-200
0
5
10
15
20
25
30

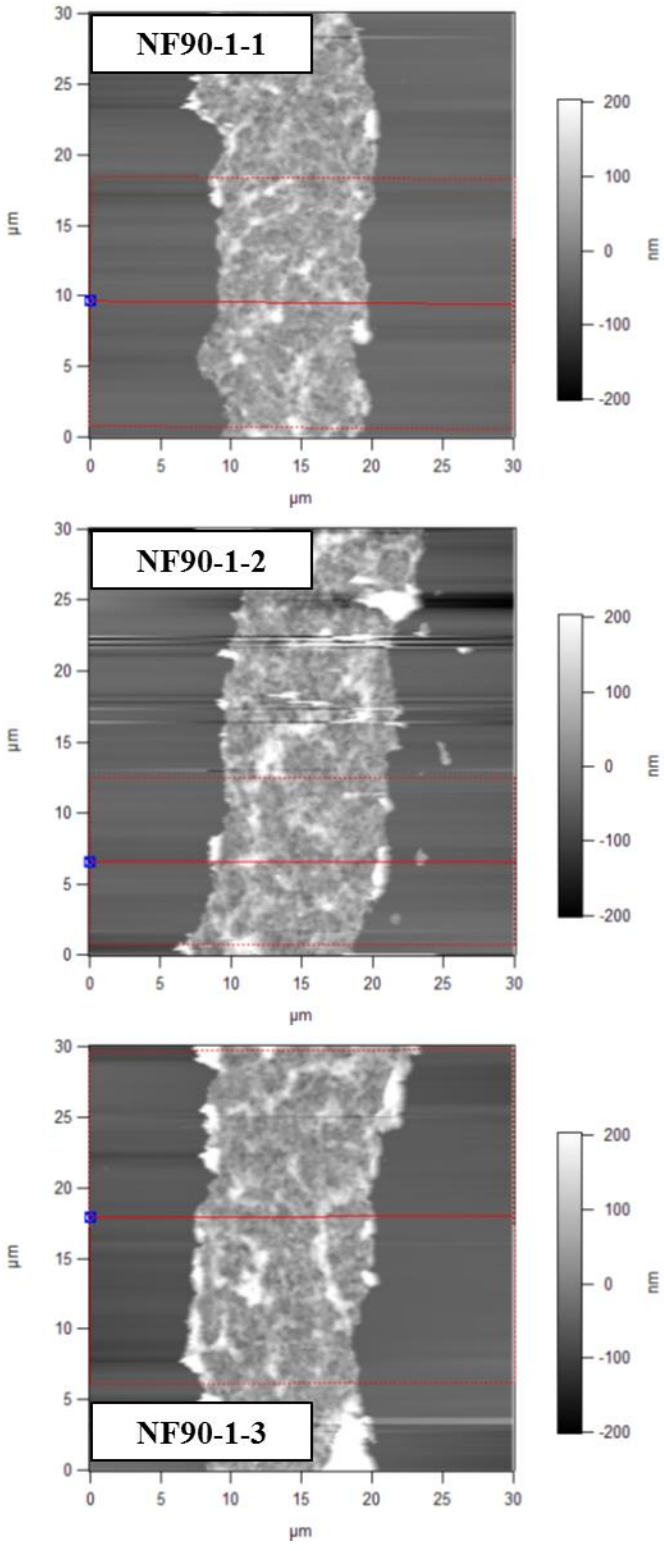
NF90-1-1
NF90-1-2
NF90-1-3
µm
nm
200
100
0
-100
-200
0
5
10
15
20
25
30

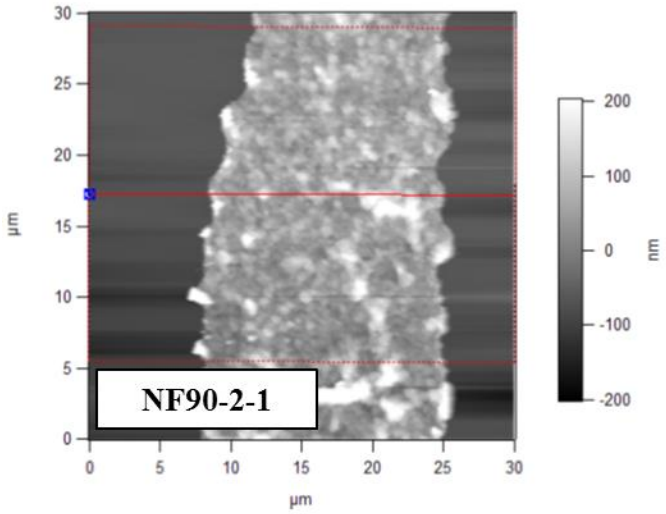
NF90-2-1
μm
nm
200
100
0
-100
-200

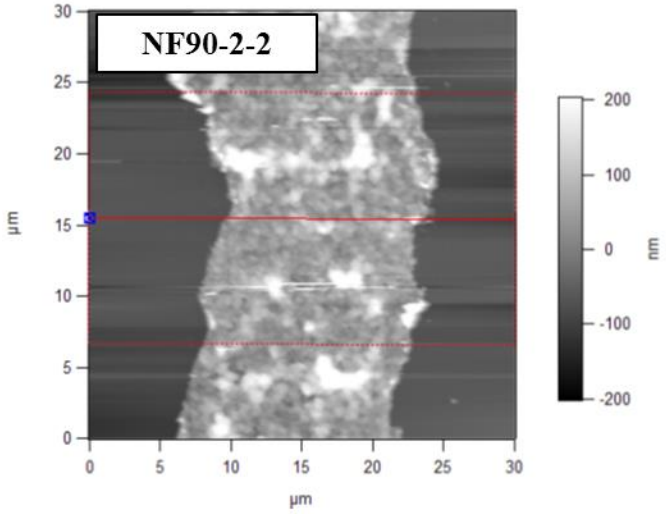
NF90-2-2
μm
nm
200
100
0
-100
-200

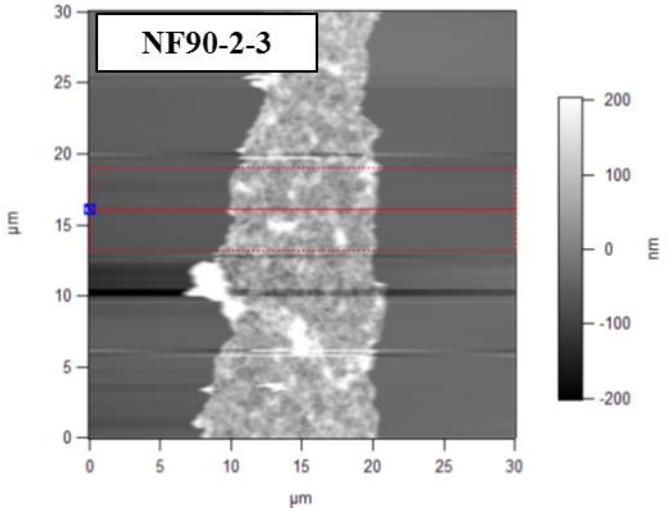
NF90-2-3
μm
nm
200
100
0
-100
-200

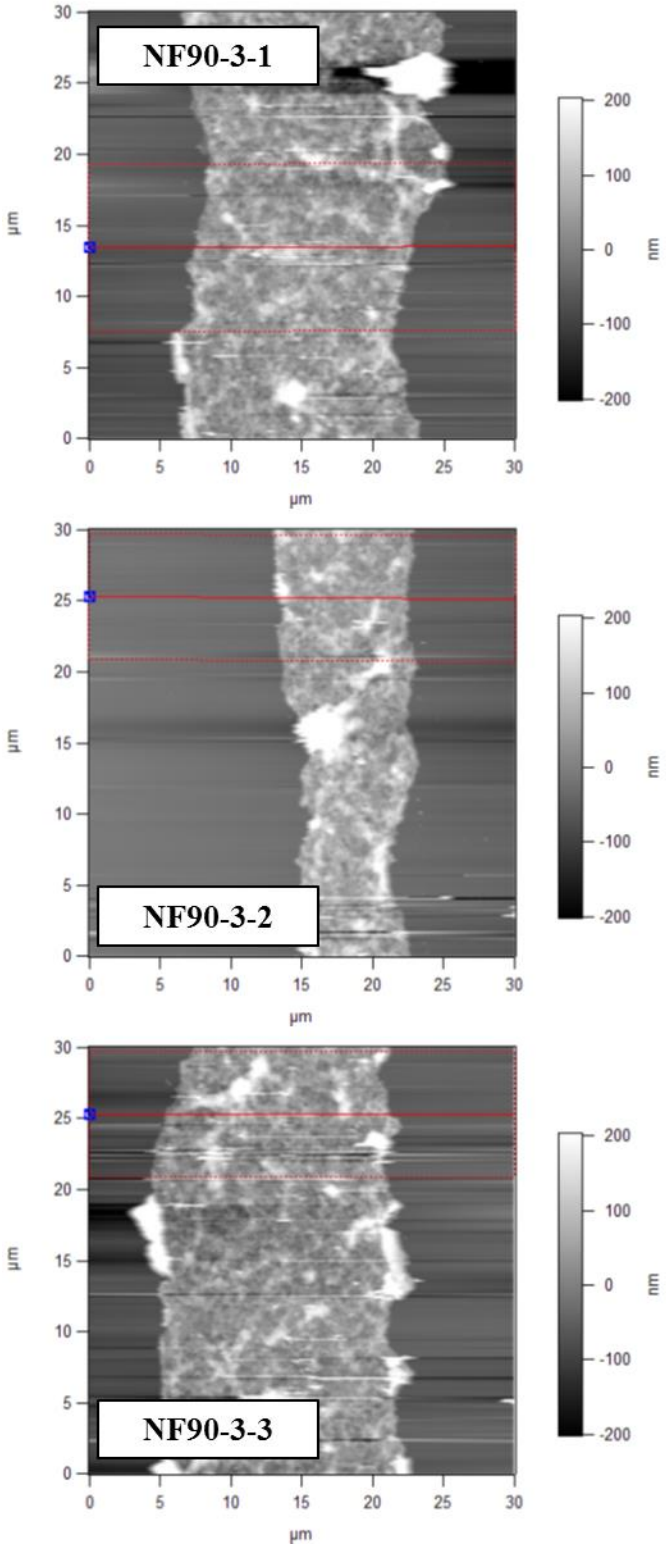
NF90-3-1
NF90-3-2
NF90-3-3
µm
nm
200
100
0
-100
-200
0
5
10
15
20
25
30

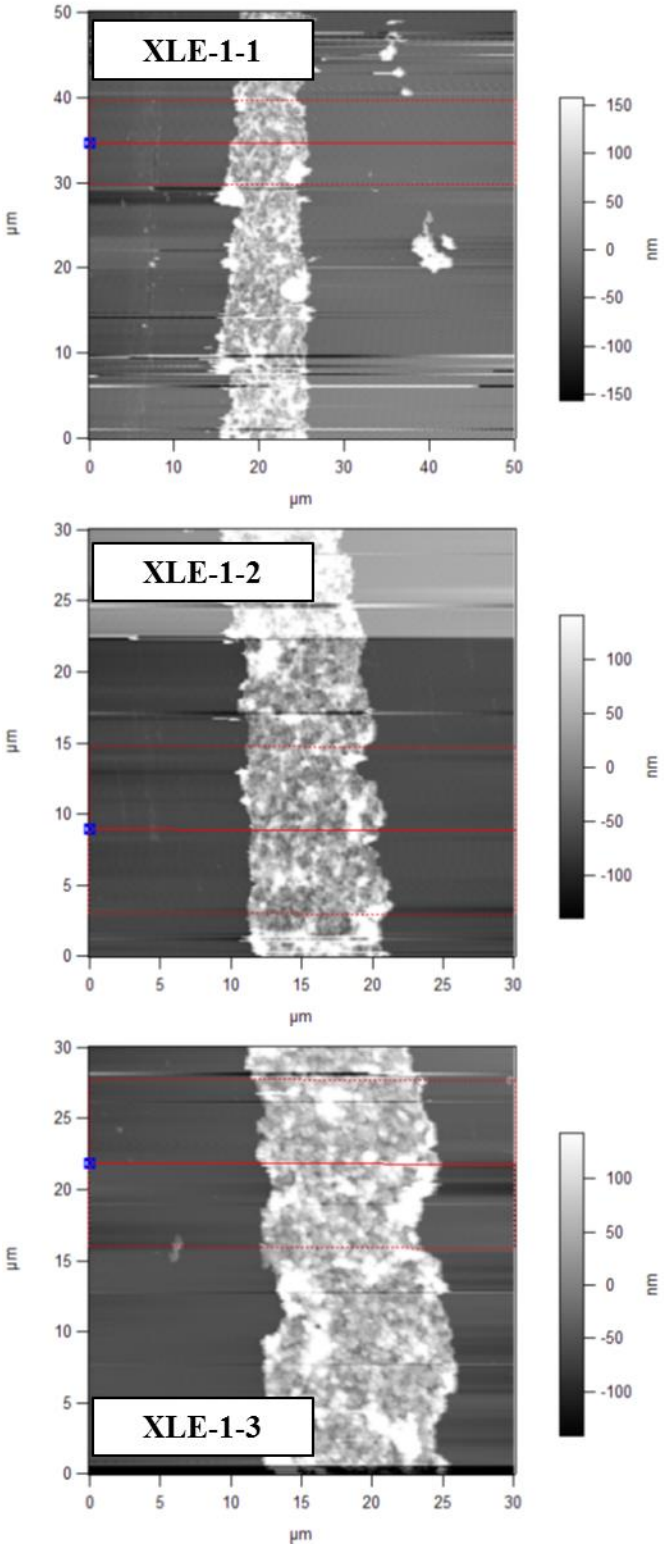
XLE-1-1
XLE-1-2
XLE-1-3
µm
nm

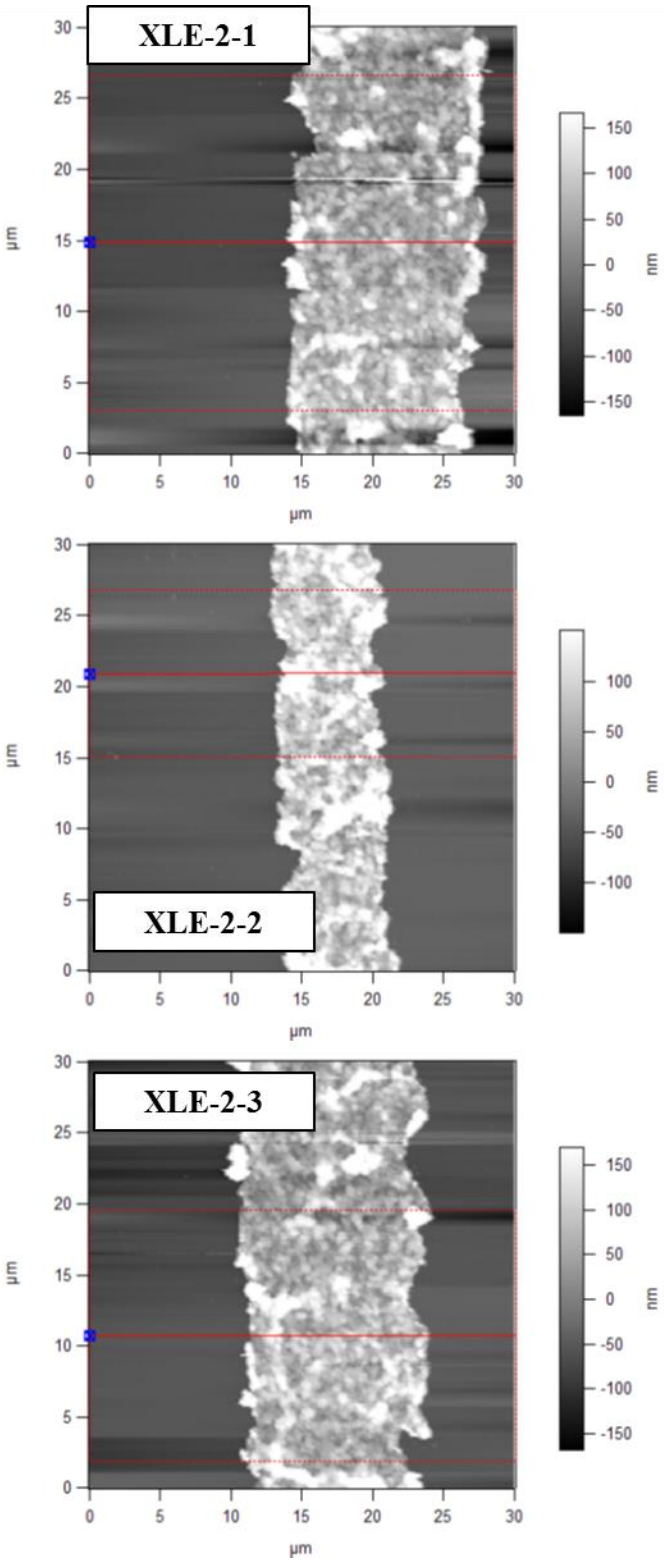
XLE-2-1
XLE-2-2
XLE-2-3
µm
nm
150
100
50
0
-50
-100
-150

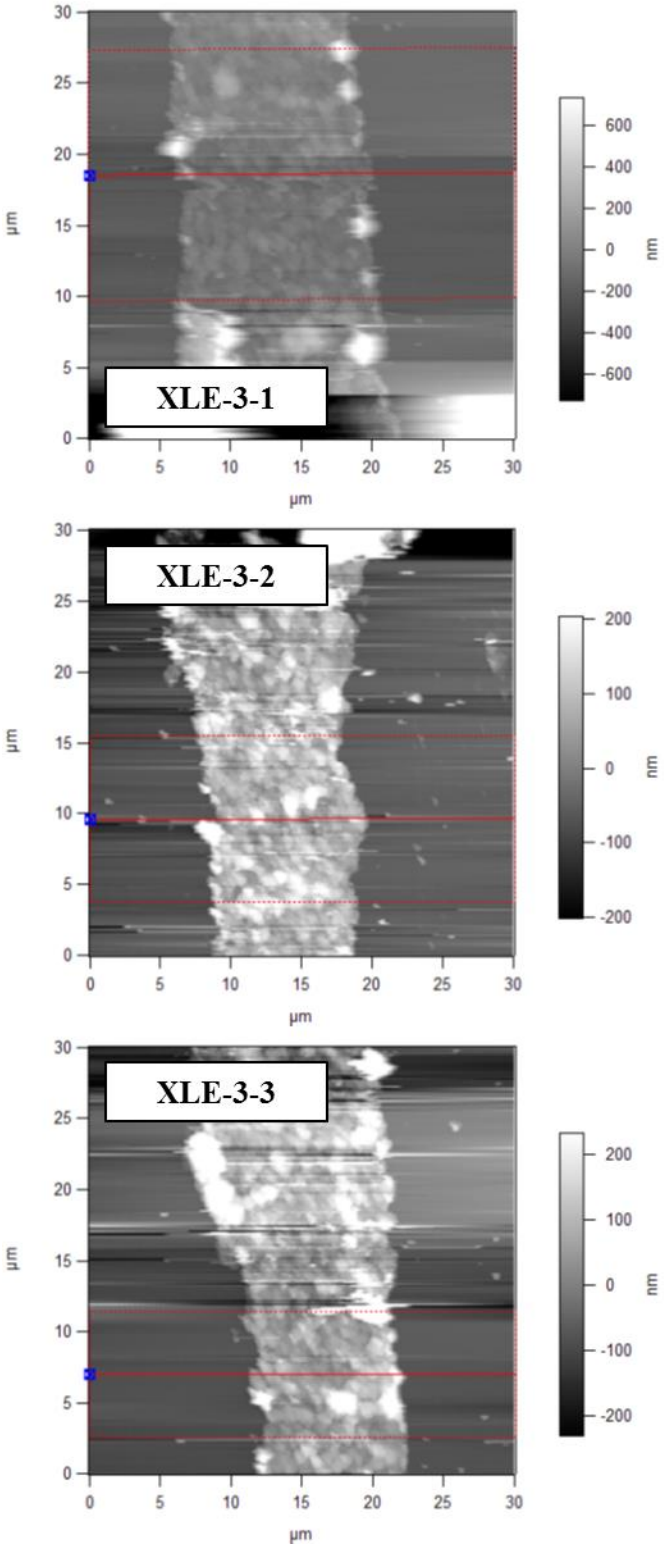
XLE-3-1
XLE-3-2
XLE-3-3
μm
nm

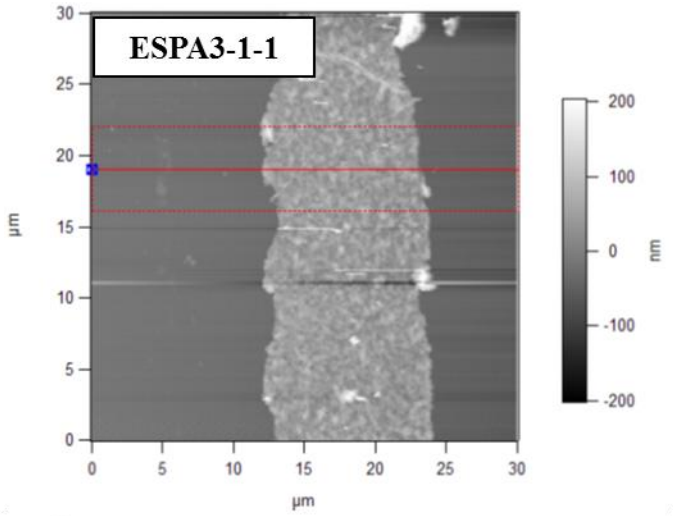
ESPA3-1-1
30
25
20
15
10
5
0
µm
0
5
10
15
20
25
30
µm
200
100
0
-100
-200
nm

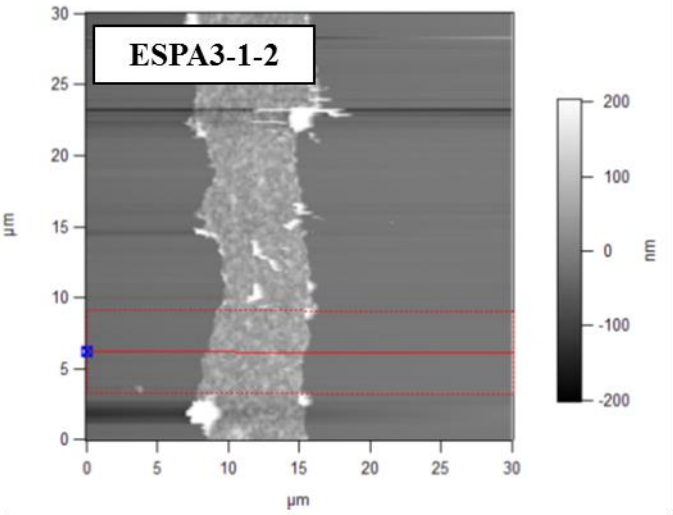
ESPA3-1-2
30
25
20
15
10
5
0
µm
0
5
10
15
20
25
30
µm
200
100
0
-100
-200
nm

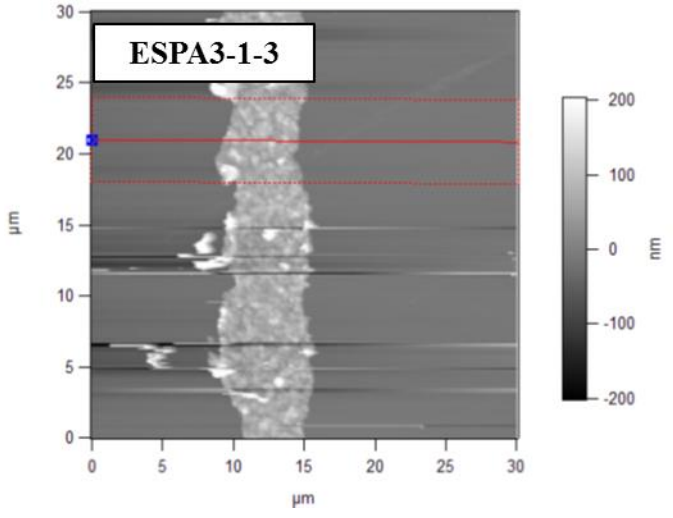
ESPA3-1-3
30
25
20
15
10
5
0
µm
0
5
10
15
20
25
30
µm
200
100
0
-100
-200
nm

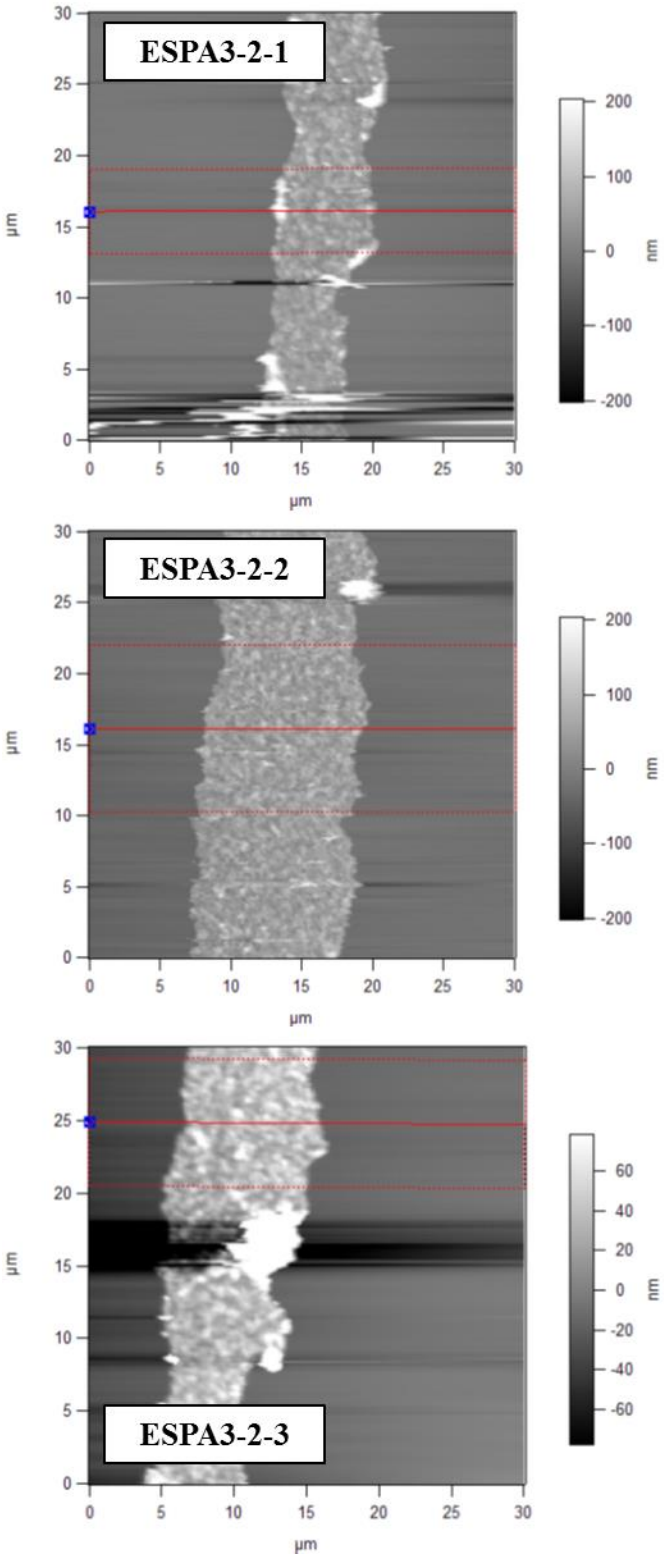
ESPA3-2-1
ESPA3-2-2
ESPA3-2-3
µm
nm
0
5
10
15
20
25
30
200
100
0
-100
-200
60
40
20
-20
-40
-60

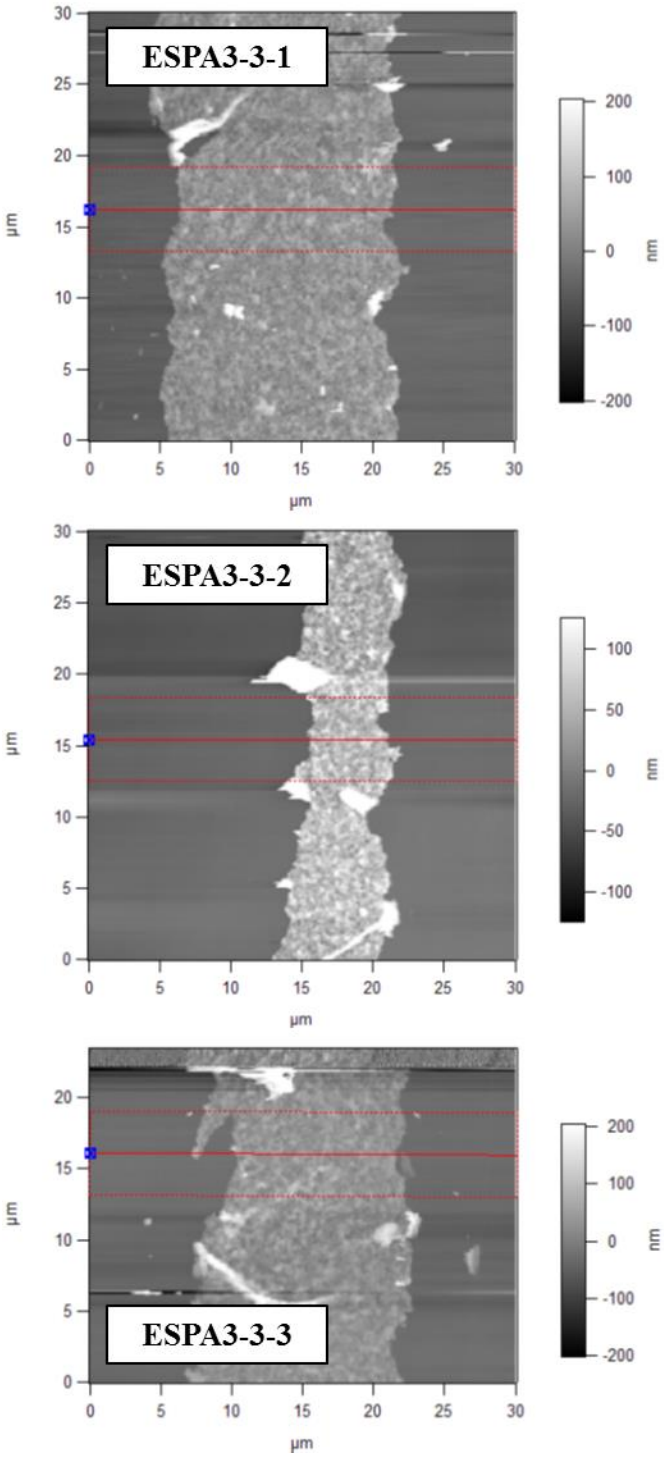
ESPA3-3-1
ESPA3-3-2
ESPA3-3-3
µm
nm

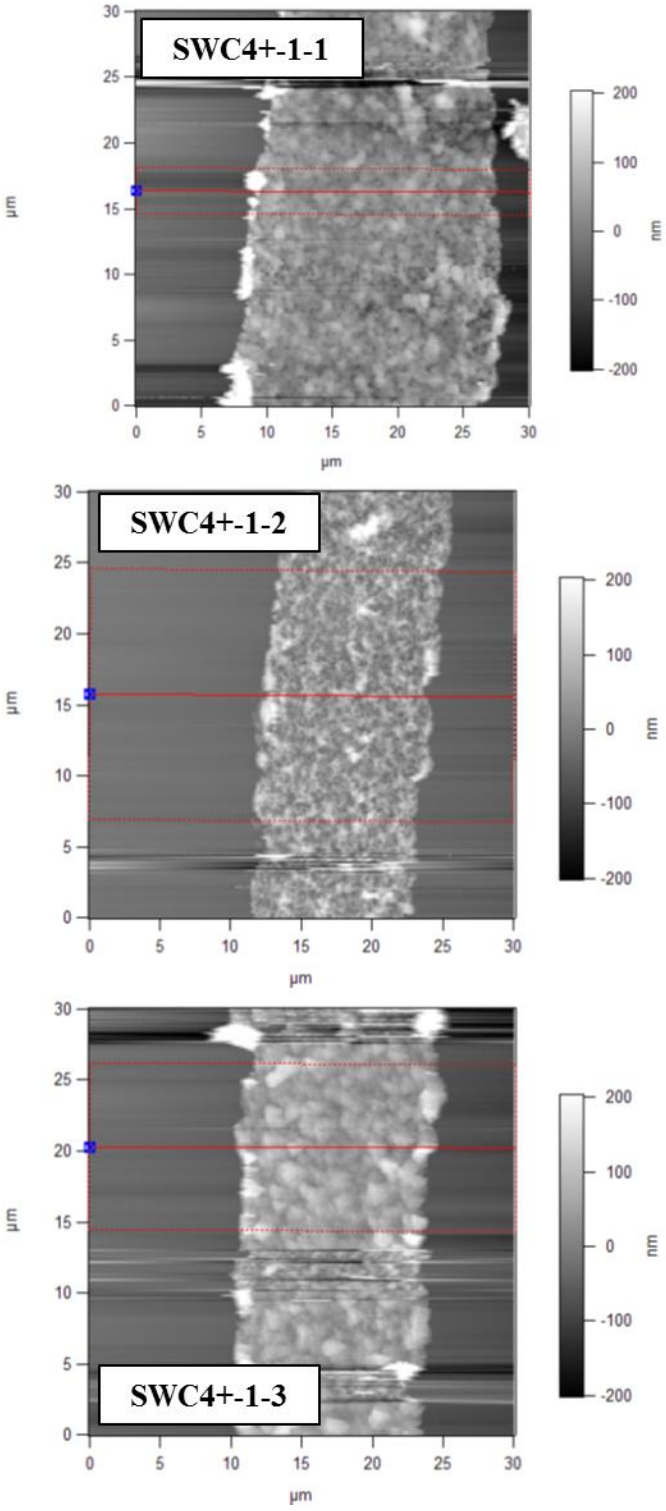
SWC4+-1-1
SWC4+-1-2
SWC4+-1-3
µm
nm
200
100
0
-100
-200
0
5
10
15
20
25
30

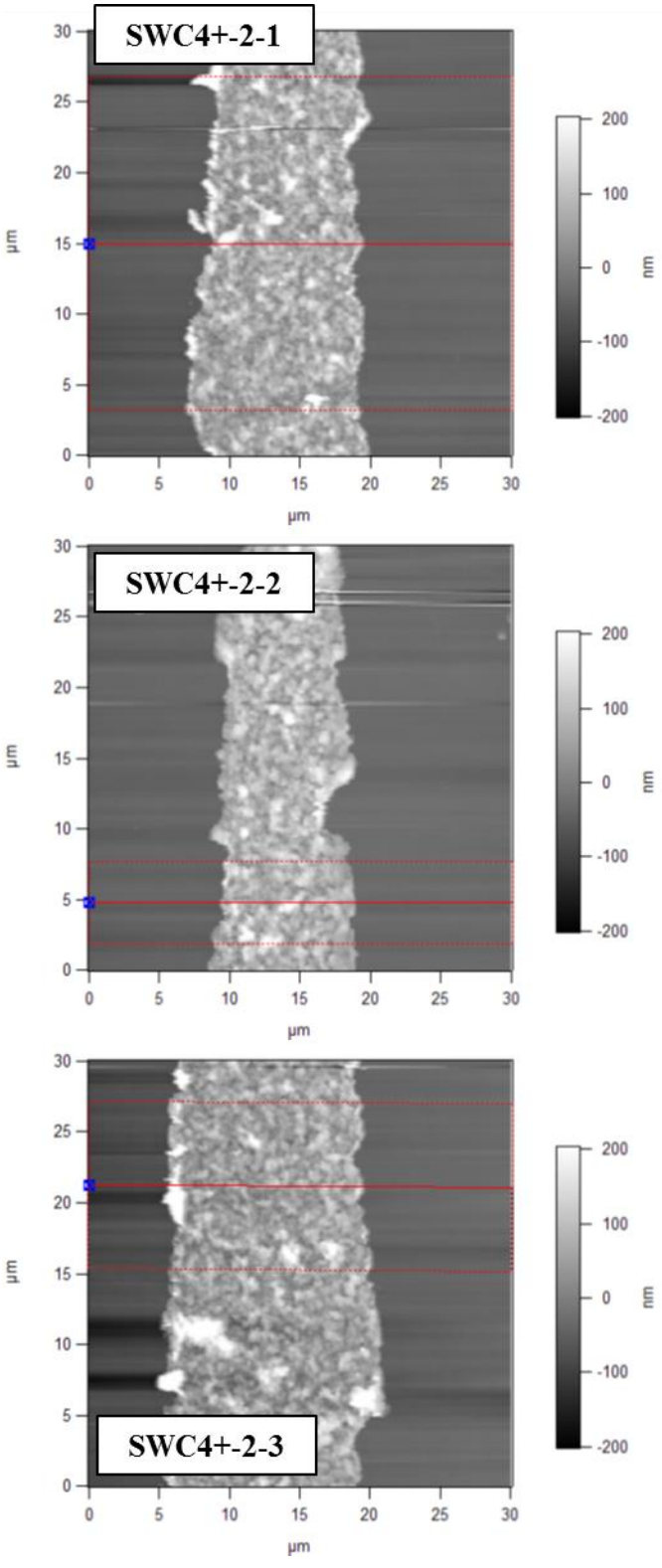
SWC4+-2-1
SWC4+-2-2
SWC4+-2-3
µm
nm
200
100
0
-100
-200
0
5
10
15
20
25
30

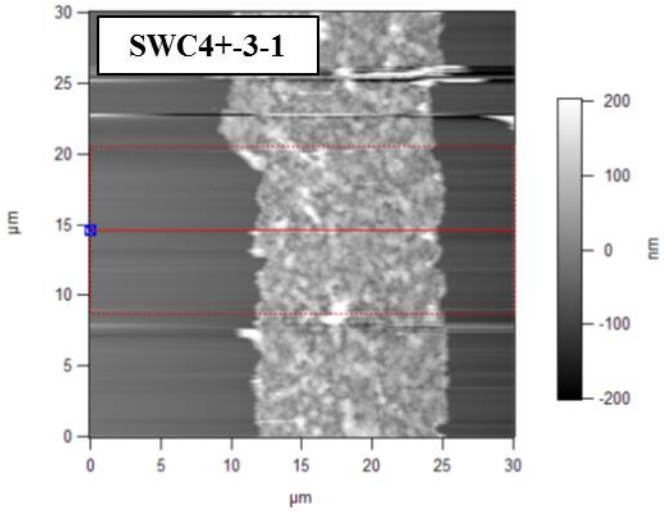
SWC4+-3-1
30
25
20
15
10
5
0
µm
0
5
10
15
20
25
30
µm
200
100
0
-100
-200
nm

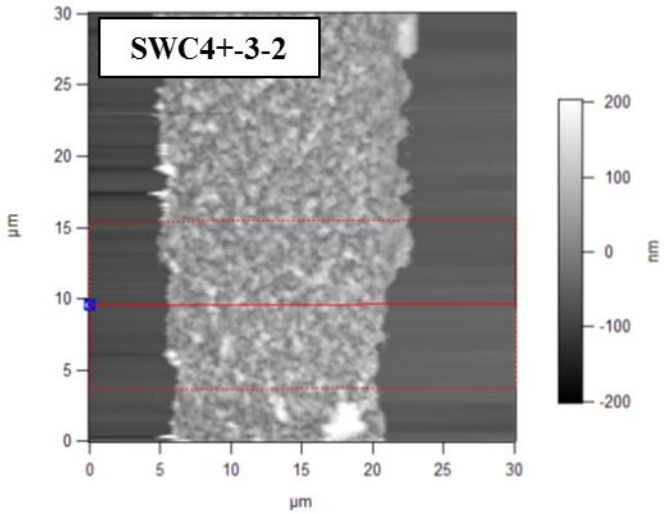
SWC4+-3-2
30
25
20
15
10
5
0
µm
0
5
10
15
20
25
30
µm
200
100
0
-100
-200
nm

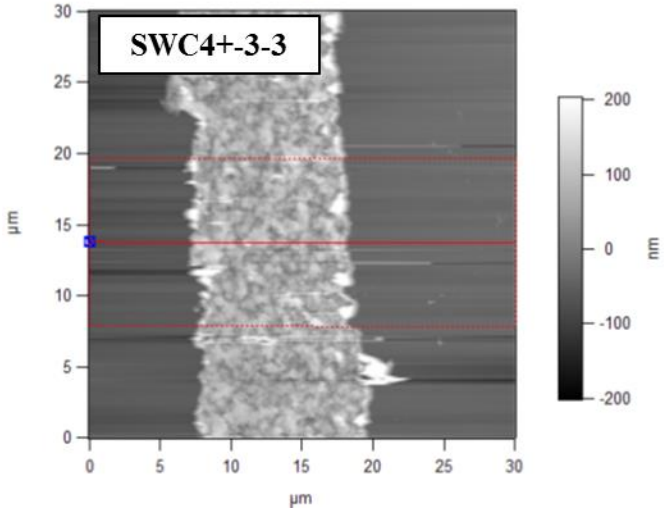
SWC4+-3-3
30
25
20
15
10
5
0
µm
0
5
10
15
20
25
30
µm
200
100
0
-100
-200
nm

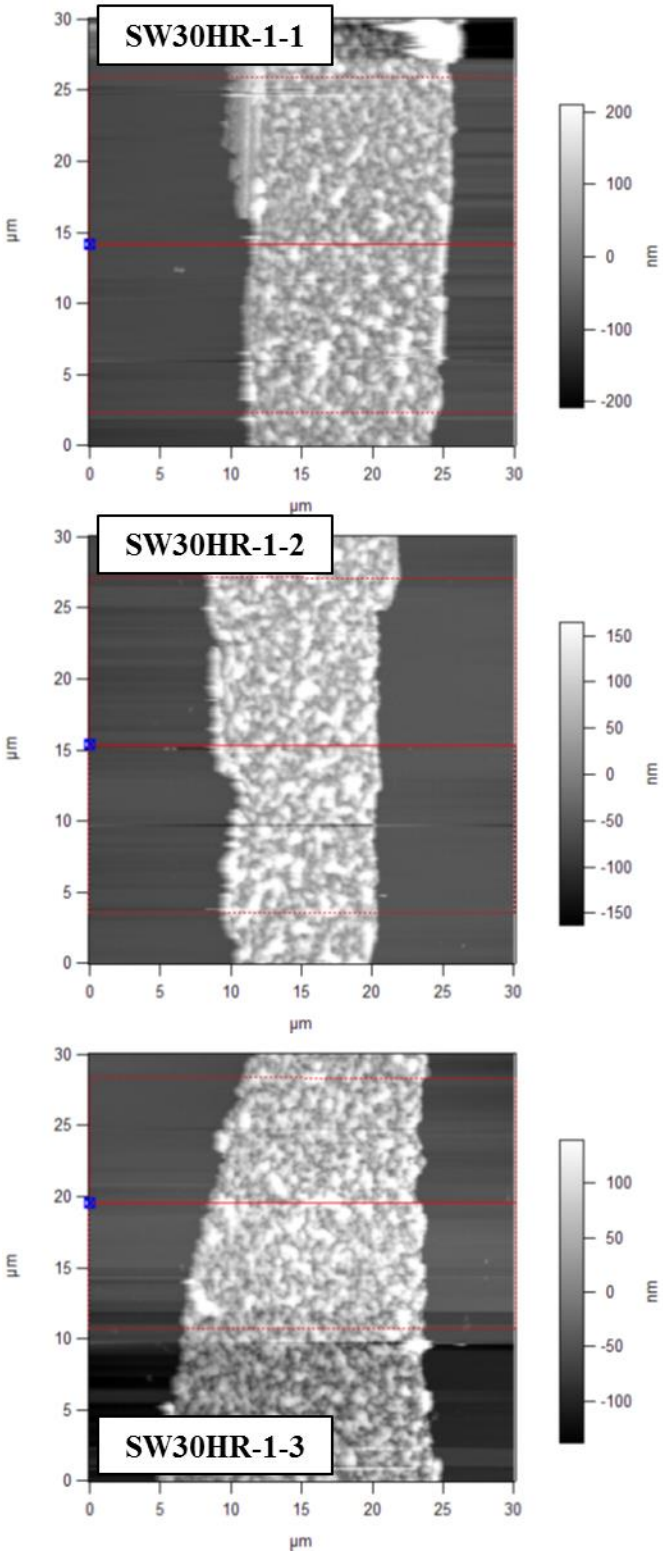
SW30HR-1-1
SW30HR-1-2
SW30HR-1-3
μm
nm

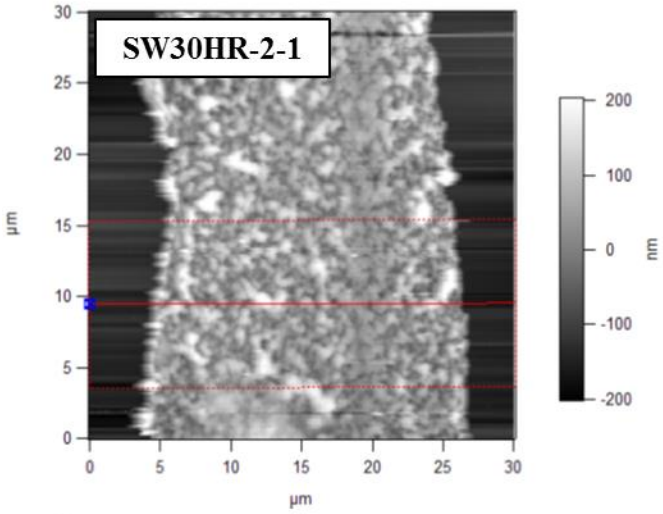
SW30HR-2-1
30
25
20
15
10
5
0
µm
0
5
10
15
20
25
30
µm
200
100
0
-100
-200
nm

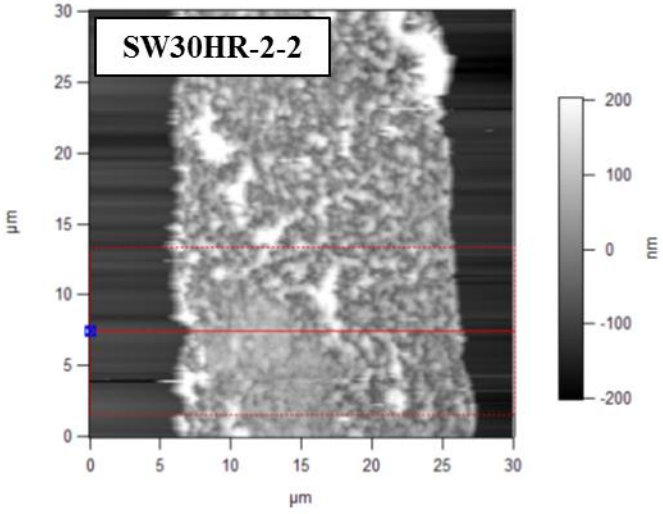
SW30HR-2-2
30
25
20
15
10
5
0
µm
0
5
10
15
20
25
30
µm
200
100
0
-100
-200
nm

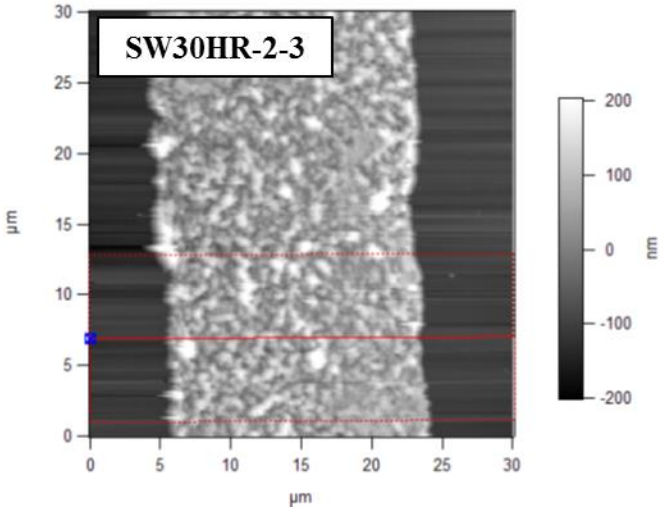
SW30HR-2-3
30
25
20
15
10
5
0
µm
0
5
10
15
20
25
30
µm
200
100
0
-100
-200
nm

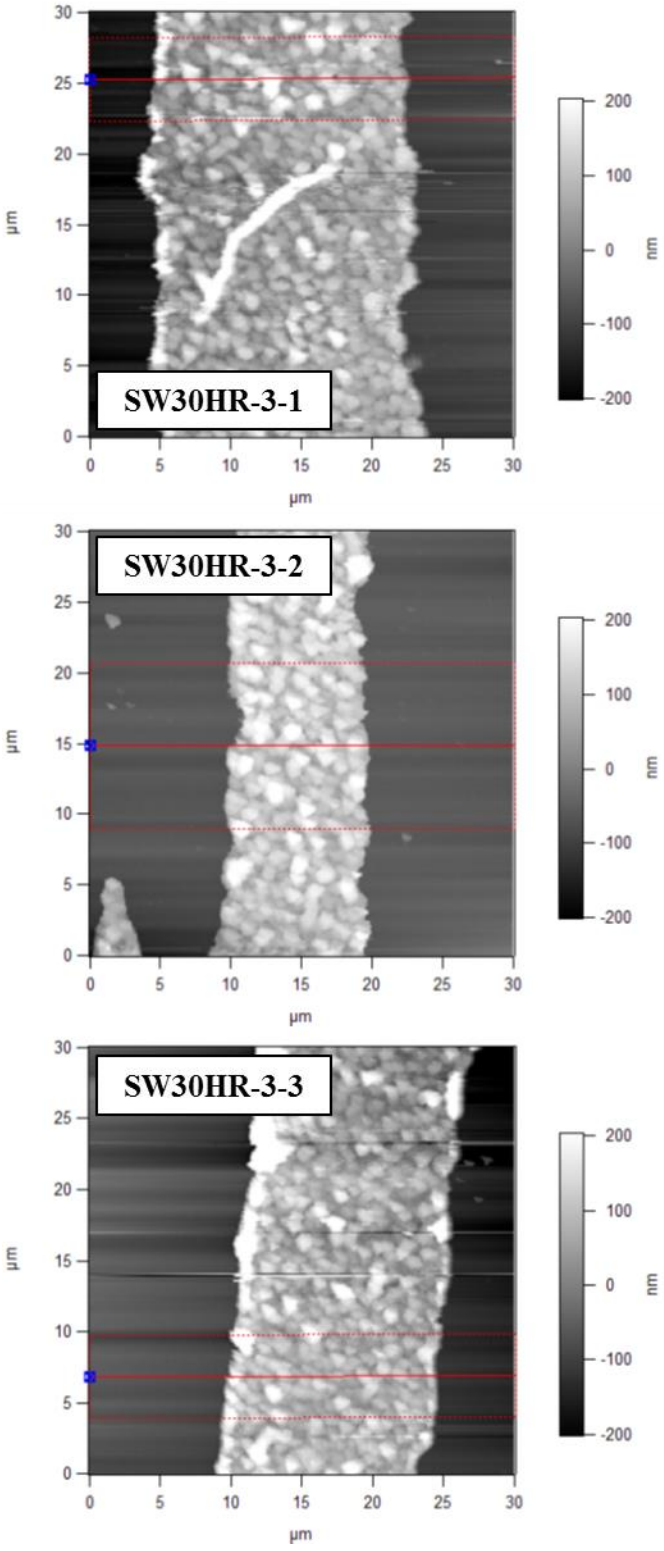
SW30HR-3-1
SW30HR-3-2
SW30HR-3-3
μm
nm
200
100
0
-100
-200
0
5
10
15
20
25
30

APPENDIX 5: RESULTS OF QUARTZ CRYSTAL MICROBALANCE (QCM) ANALYSES OF ACTIVE LAYER THICKNESS

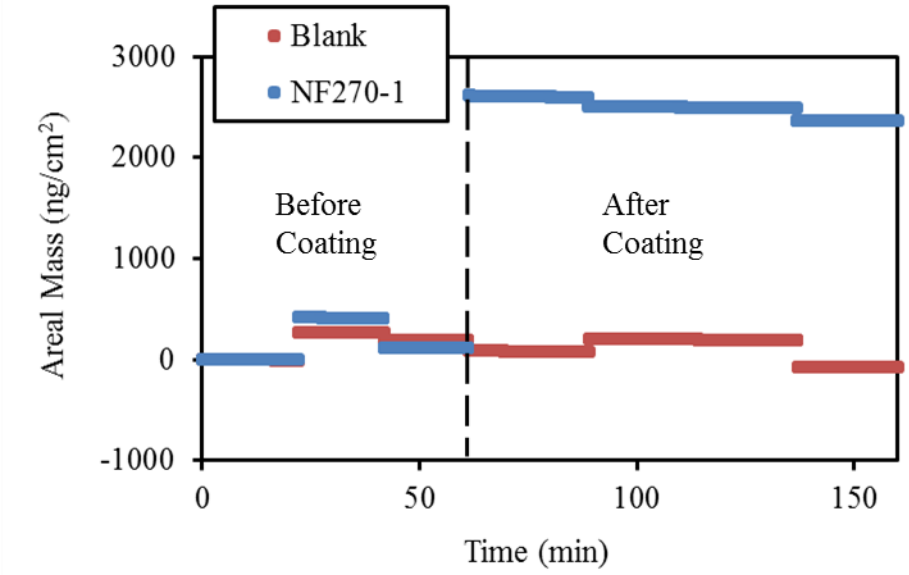

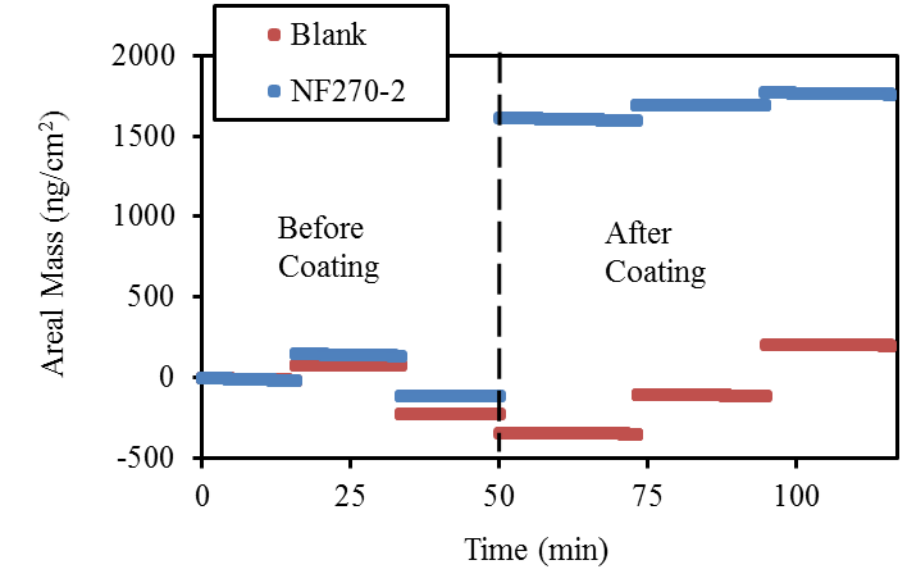

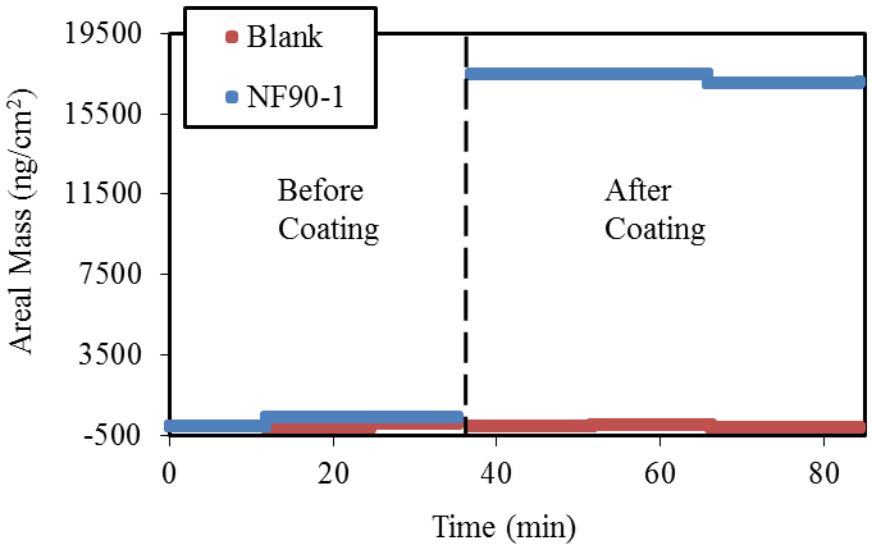
Blank
NF90-1
Before Coating
After Coating
Areal Mass (ng/cm²)
19500
15500
11500
7500
3500
-500
0
20
40
60
80
Time (min)

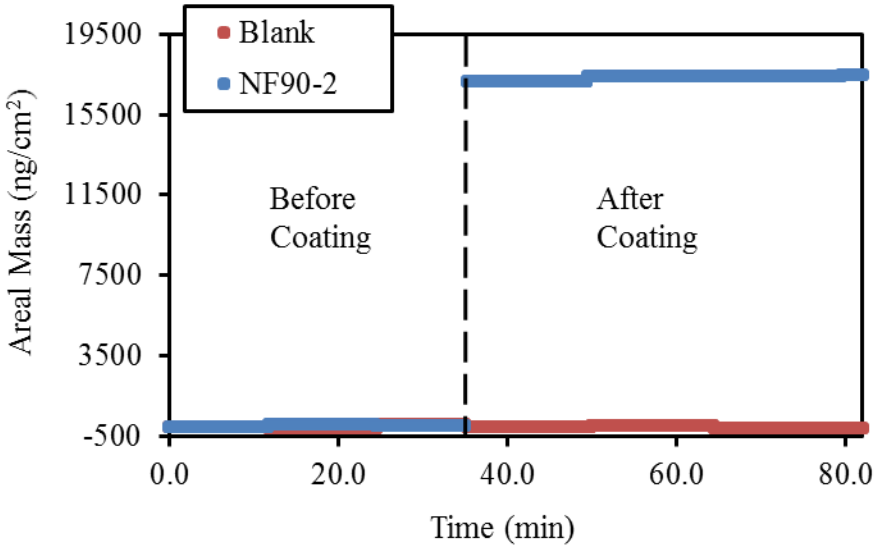
Blank
NF90-2
Before Coating
After Coating
Areal Mass (ng/cm²)
19500
15500
11500
7500
3500
-500
0.0
20.0
40.0
60.0
80.0
Time (min)

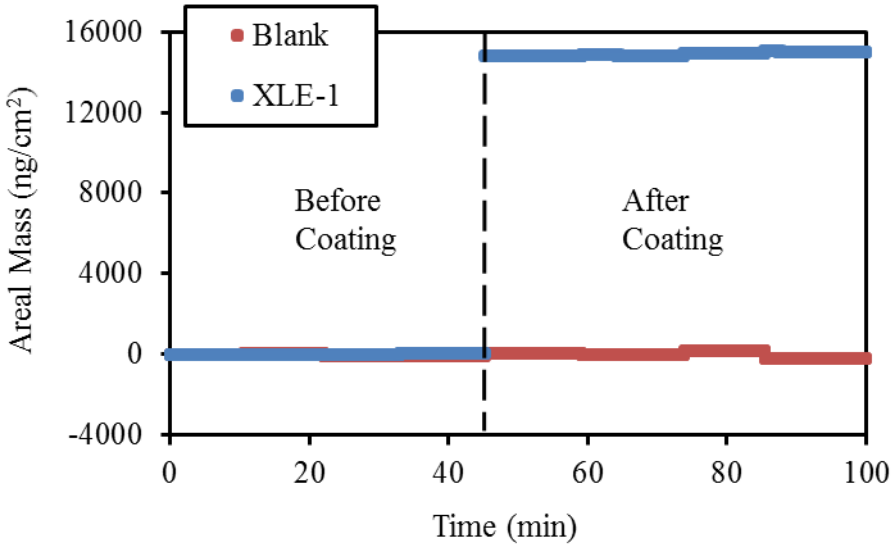
Blank
XLE-1
Before Coating
After Coating
Areal Mass (ng/cm²)
16000
12000
8000
4000
0
-4000
0
20
40
60
80
100
Time (min)

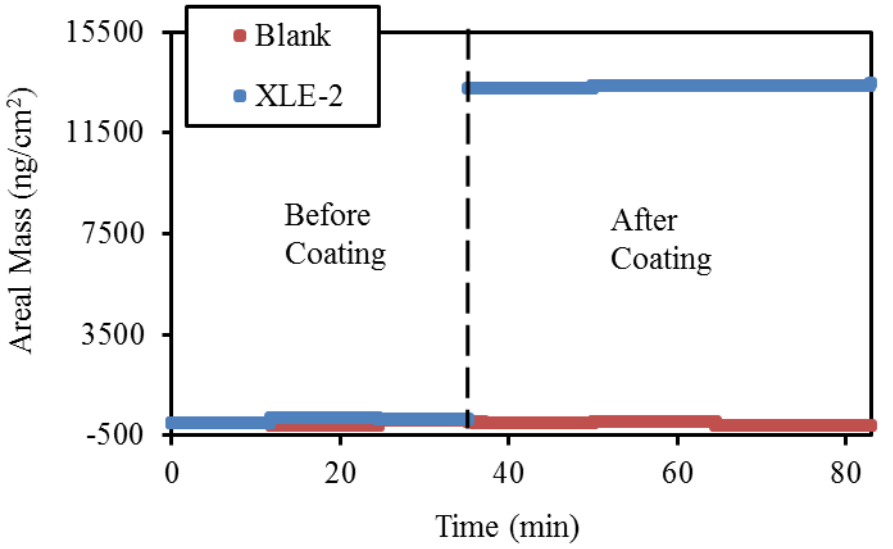
Blank
XLE-2
Before Coating
After Coating
Areal Mass (ng/cm²)
15500
11500
7500
3500
-500
0
20
40
60
80
Time (min)

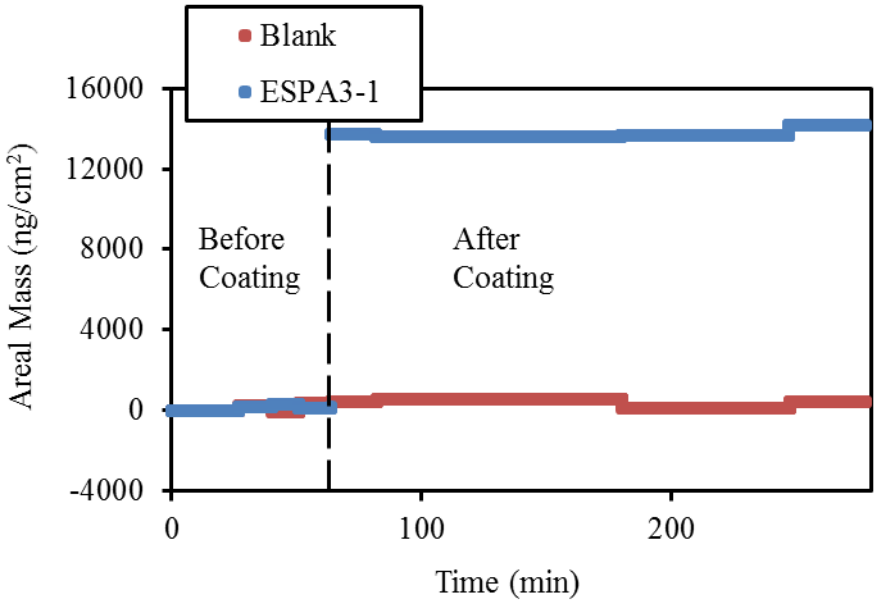
Blank
ESPA3-1
16000
12000
8000
4000
0
-4000
Areal Mass (ng/cm²)
Before Coating
After Coating
0
100
200
Time (min)

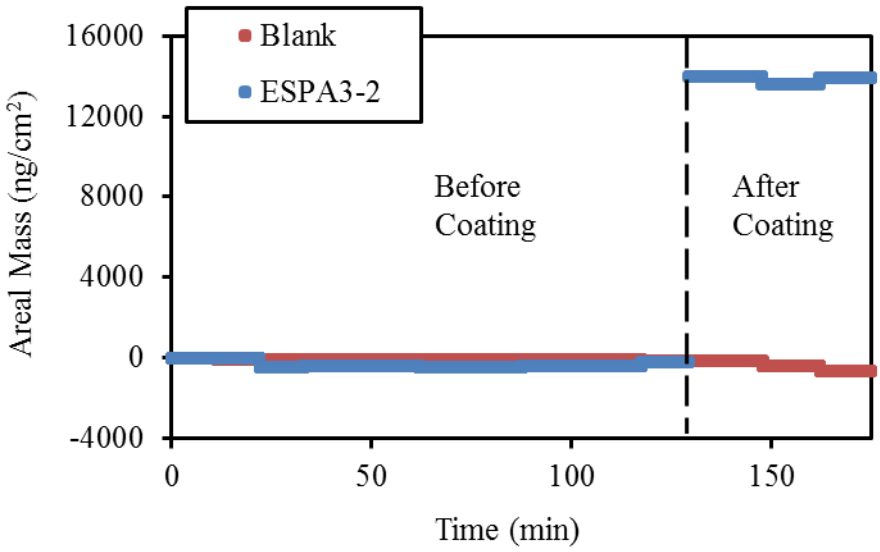
Blank
ESPA3-2
16000
12000
8000
4000
0
-4000
Areal Mass (ng/cm²)
Before Coating
After Coating
0
50
100
150
Time (min)

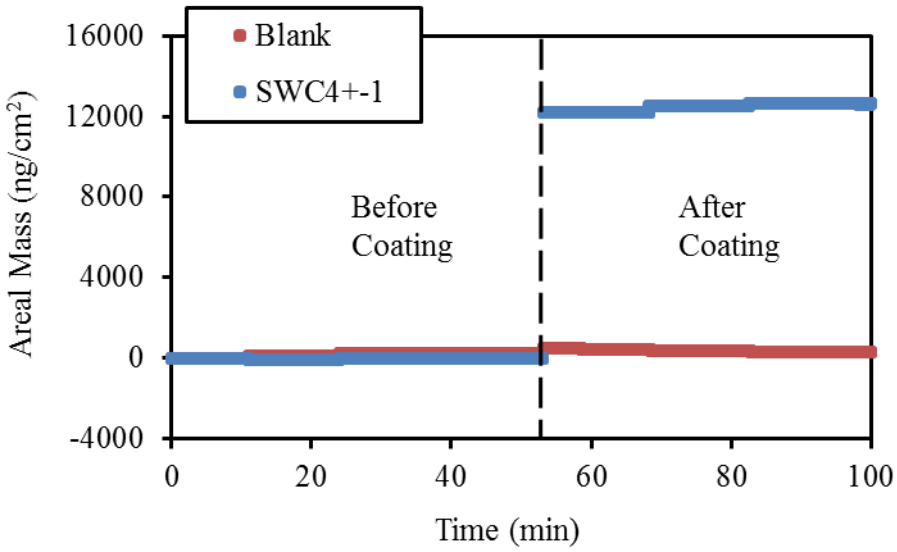
Blank
SWC4+-1
Before Coating
After Coating
Areal Mass (ng/cm²)
16000
12000
8000
4000
0
-4000
0
20
40
60
80
100
Time (min)

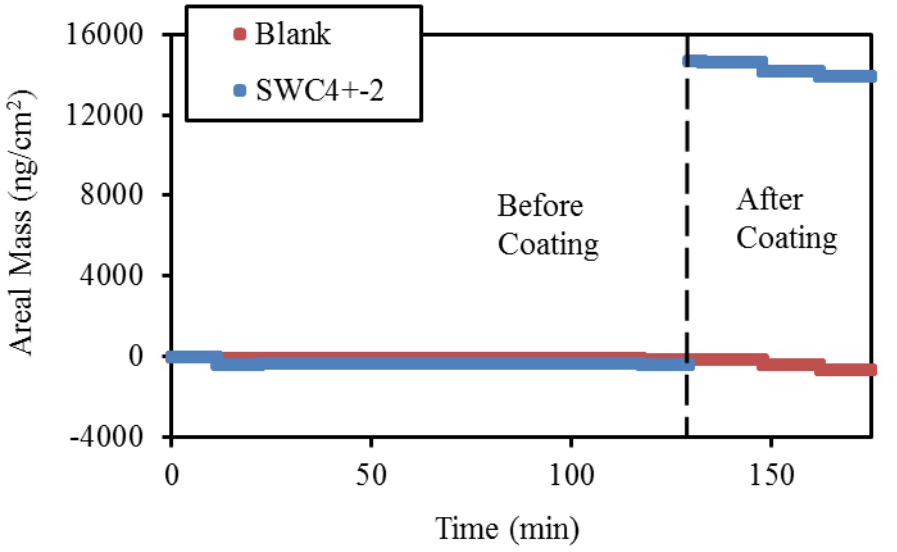
Blank
SWC4+-2
Before Coating
After Coating
Areal Mass (ng/cm²)
16000
12000
8000
4000
0
-4000
0
50
100
150
Time (min)

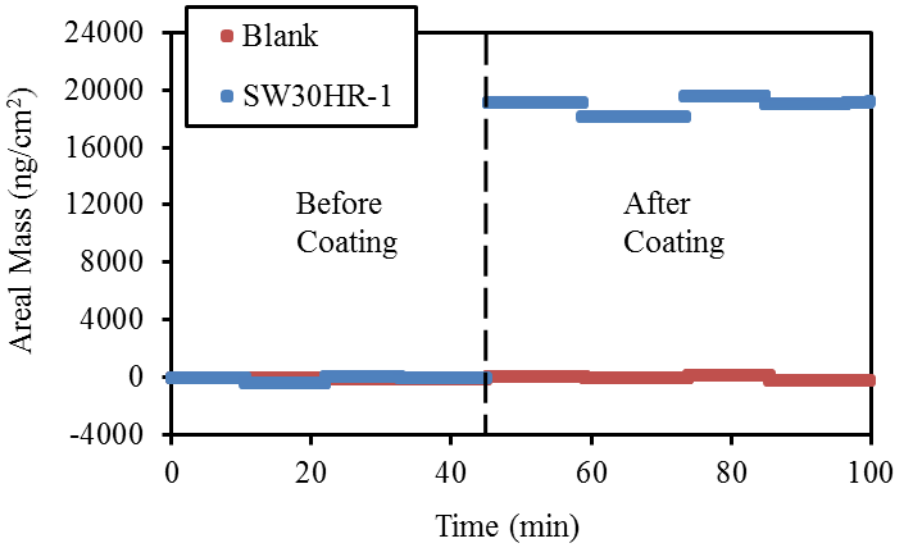
Blank
SW30HR-1
Before Coating
After Coating
Areal Mass (ng/cm²)
Time (min)
24000
20000
16000
12000
8000
4000
0
-4000
0
20
40
60
80
100

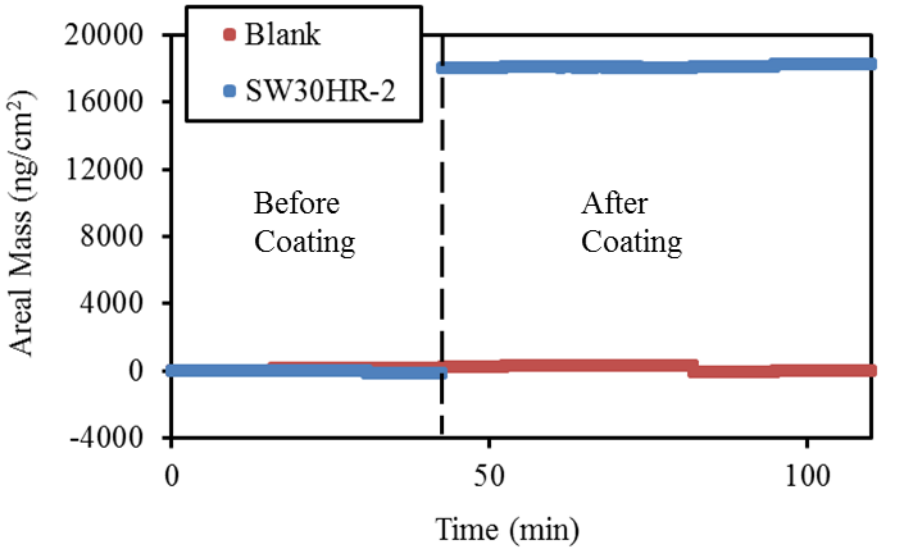
Blank
SW30HR-2
Before Coating
After Coating
Areal Mass (ng/cm²)
Time (min)
20000
16000
12000
8000
4000
0
-4000
0
50
100

APPENDIX 6: RESULTS OF PROFILOMETRY ANALYSES OF ACTIVE LAYER THICKNESS

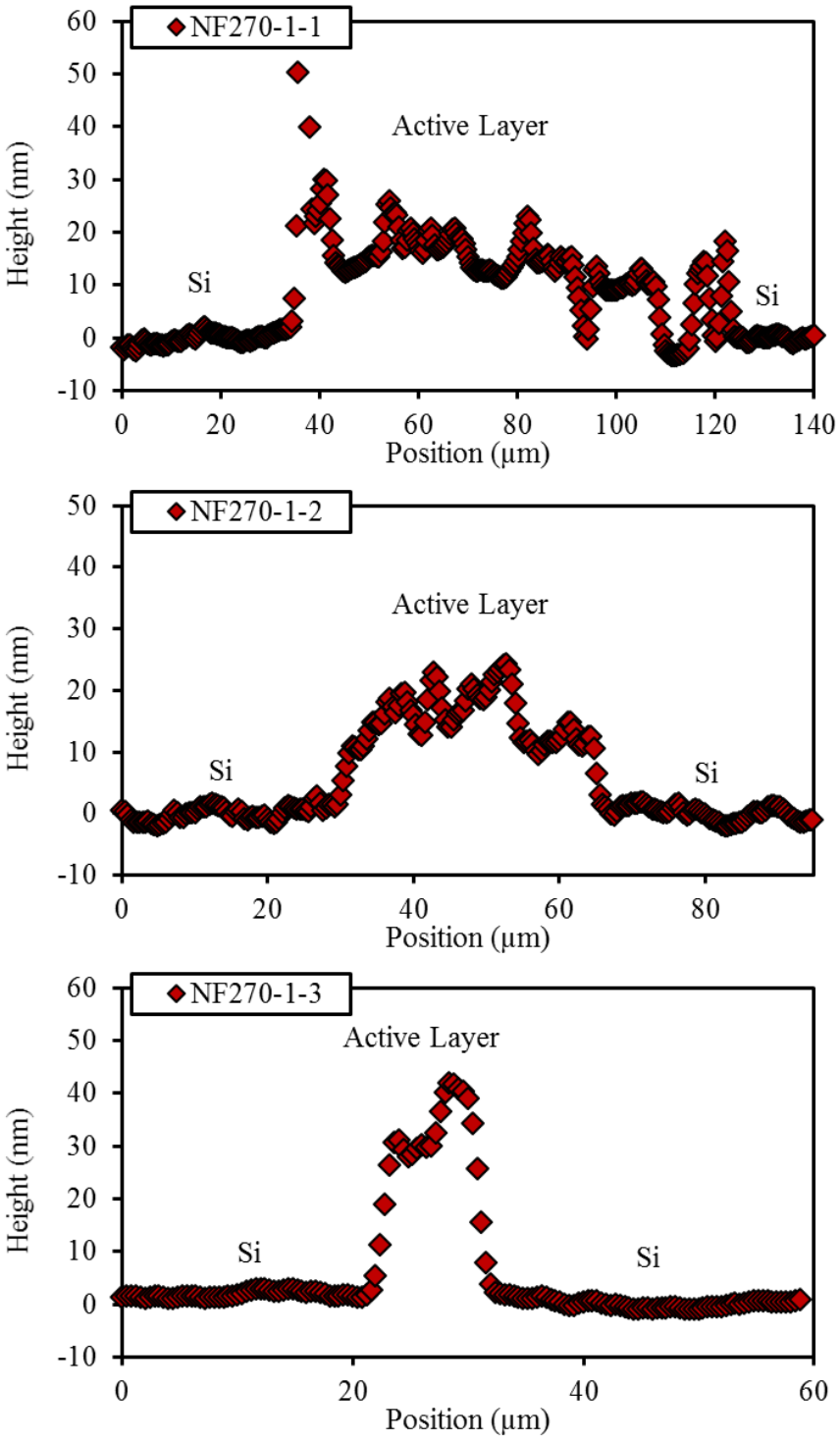

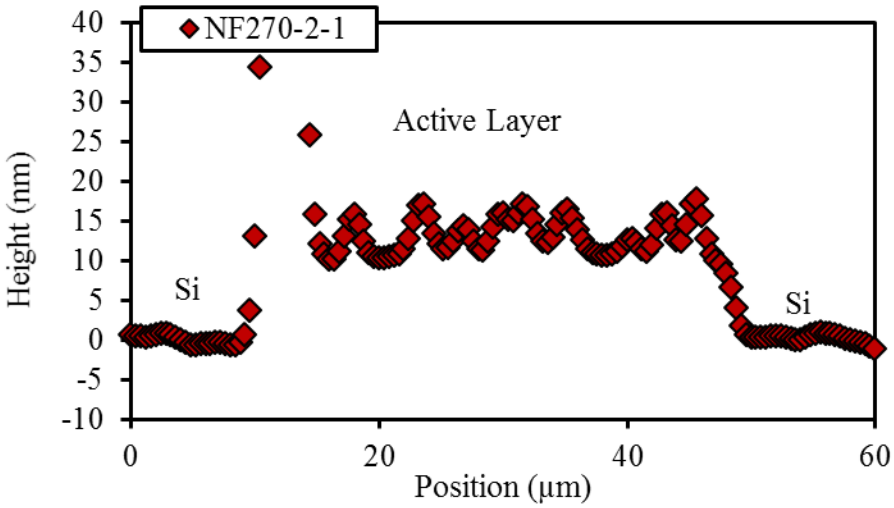
NF270-2-1
Active Layer
Si
Si
Height (nm)
Position (μm)
40
35
30
25
20
15
10
5
0
-5
-10
0
20
40
60

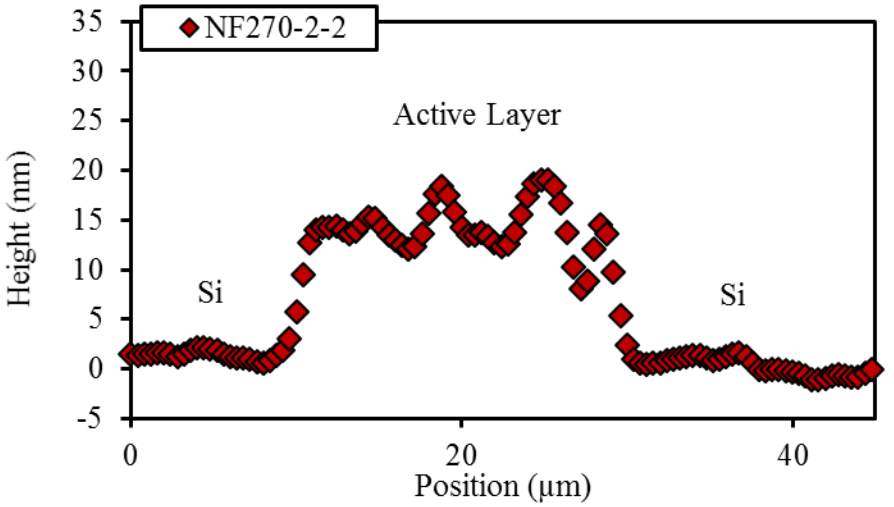
NF270-2-2
Active Layer
Si
Si
Height (nm)
Position (μm)
35
30
25
20
15
10
5
0
-5
0
20
40

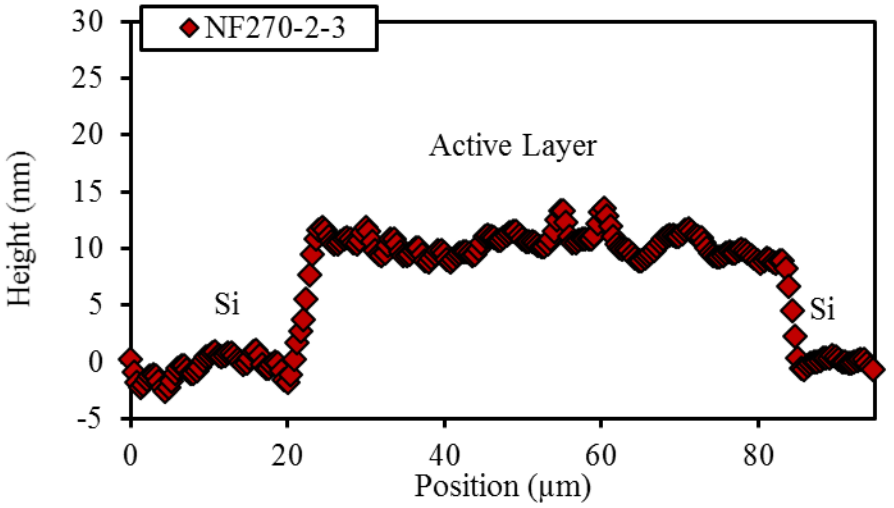
NF270-2-3
Active Layer
Si
Si
Height (nm)
Position (μm)
30
25
20
15
10
5
0
-5
0
20
40
60
80

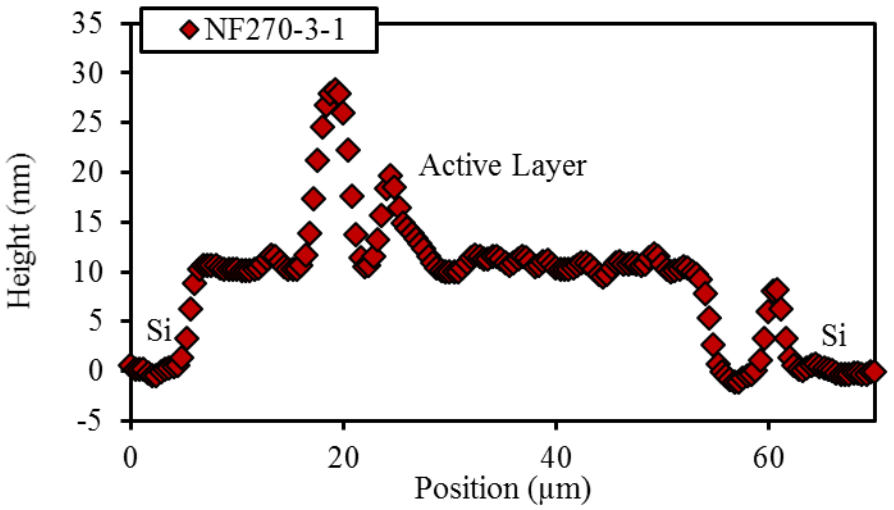
NF270-3-1
Height (nm)
Position (μm)
Active Layer
Si
Si
35
30
25
20
15
10
5
0
-5
0
20
40
60

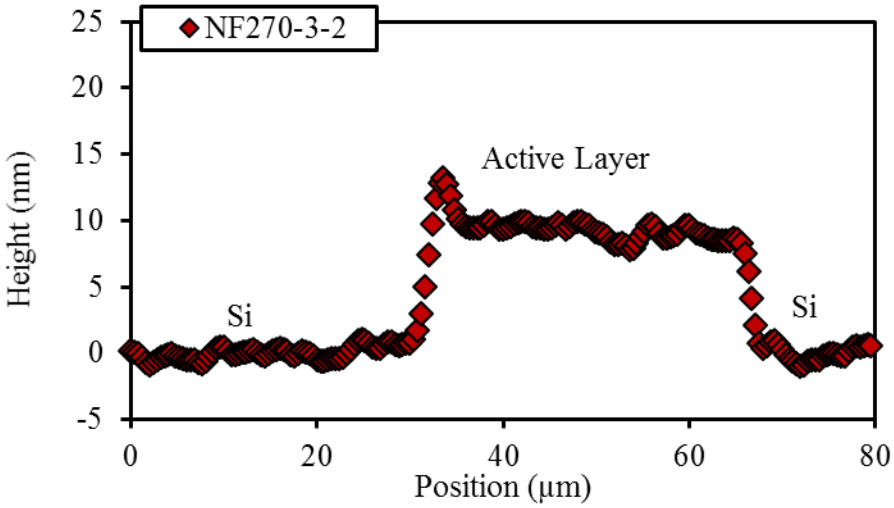
NF270-3-2
Height (nm)
Position (μm)
Active Layer
Si
Si
25
20
15
10
5
0
-5
0
20
40
60
80

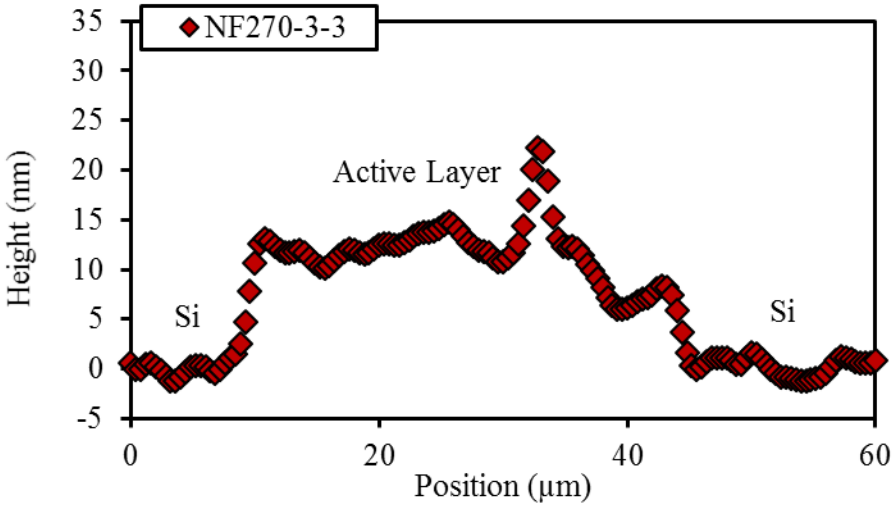
NF270-3-3
Height (nm)
Position (μm)
Active Layer
Si
Si
35
30
25
20
15
10
5
0
-5
0
20
40
60

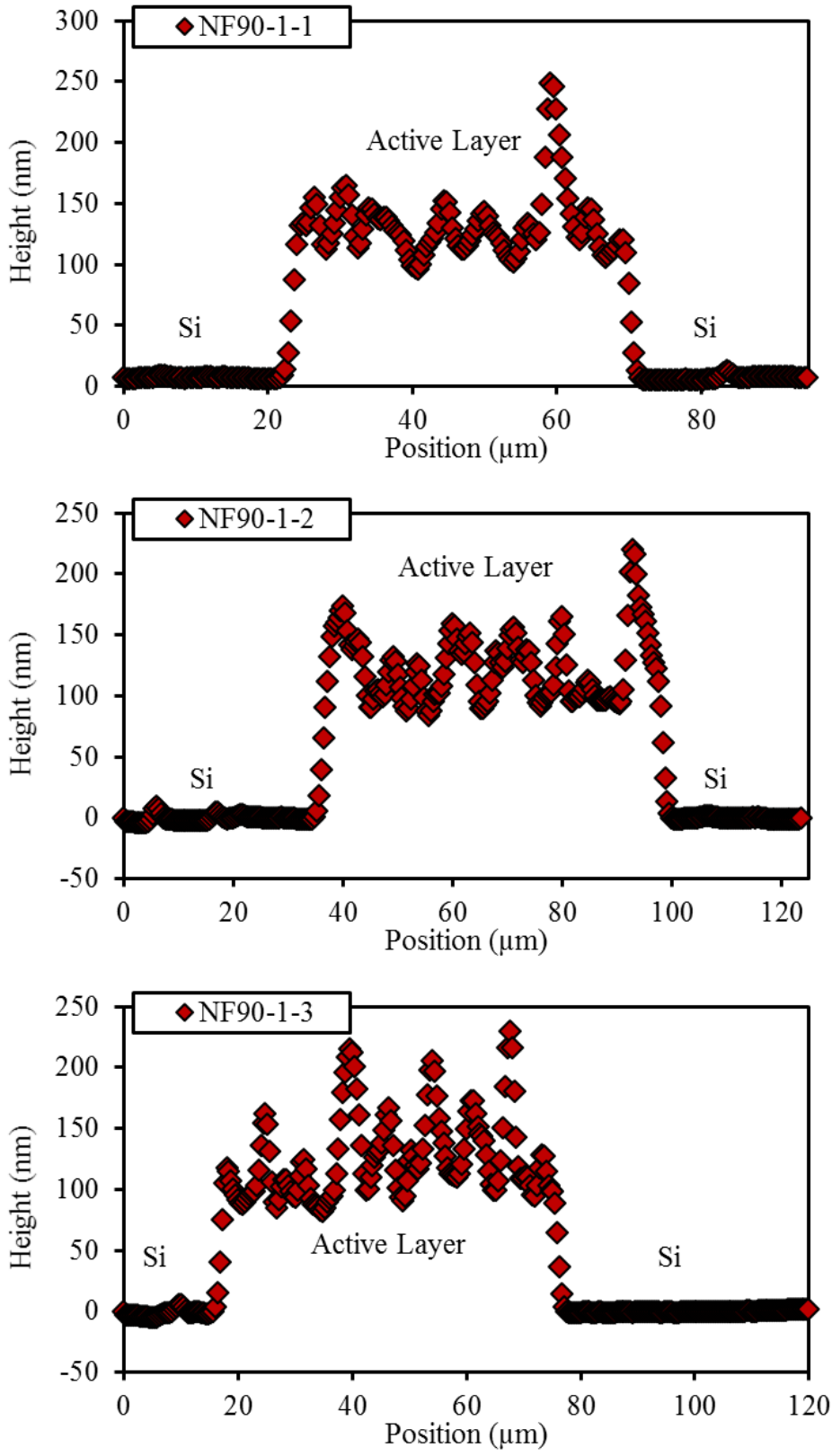
NF90-1-1
Active Layer
Si
Si
Height (nm)
Position (μm)
NF90-1-2
Active Layer
Si
Si
Height (nm)
Position (μm)
NF90-1-3
Active Layer
Si
Si
Height (nm)
Position (μm)

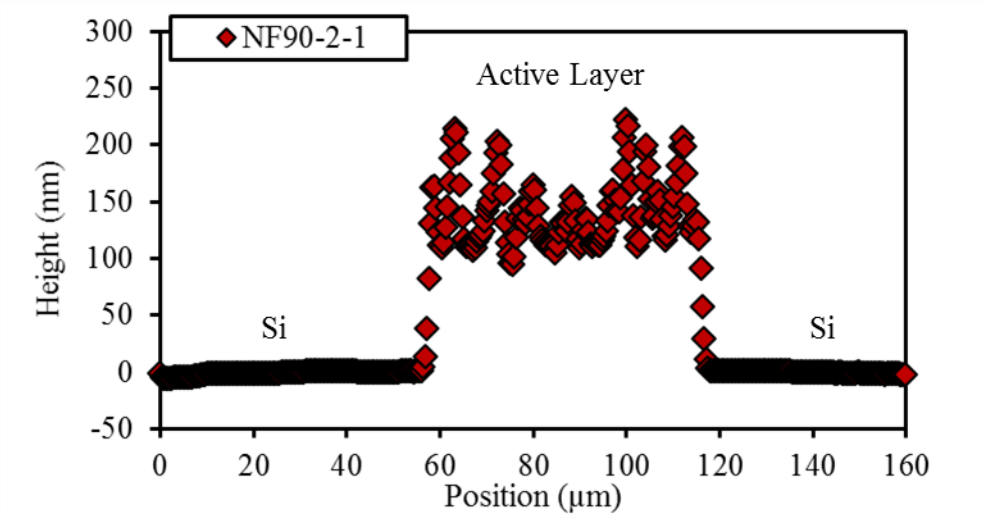
NF90-2-1
Active Layer
Si
Si
Height (nm)
Position (μm)
300
250
200
150
100
50
0
-50
0
20
40
60
80
100
120
140
160

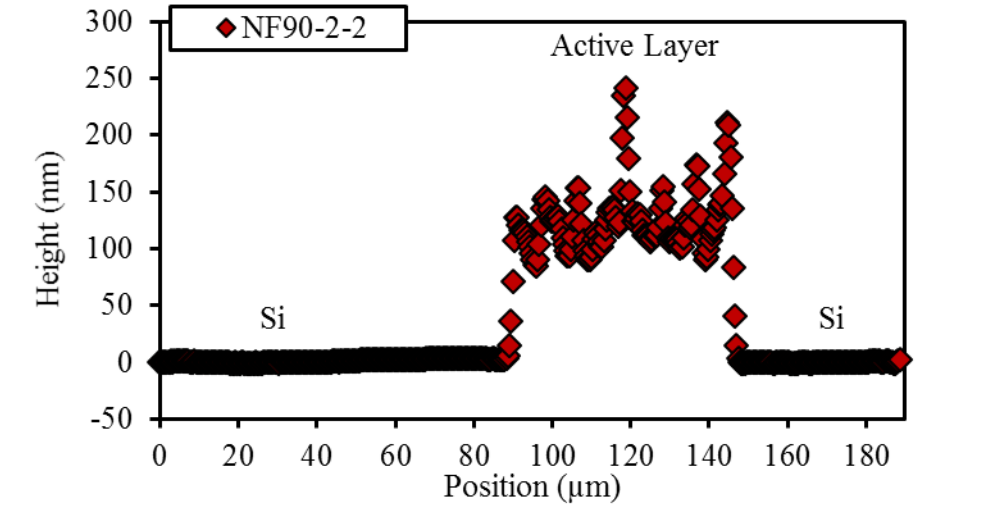
NF90-2-2
Active Layer
Si
Si
Height (nm)
Position (μm)
300
250
200
150
100
50
0
-50
0
20
40
60
80
100
120
140
160
180

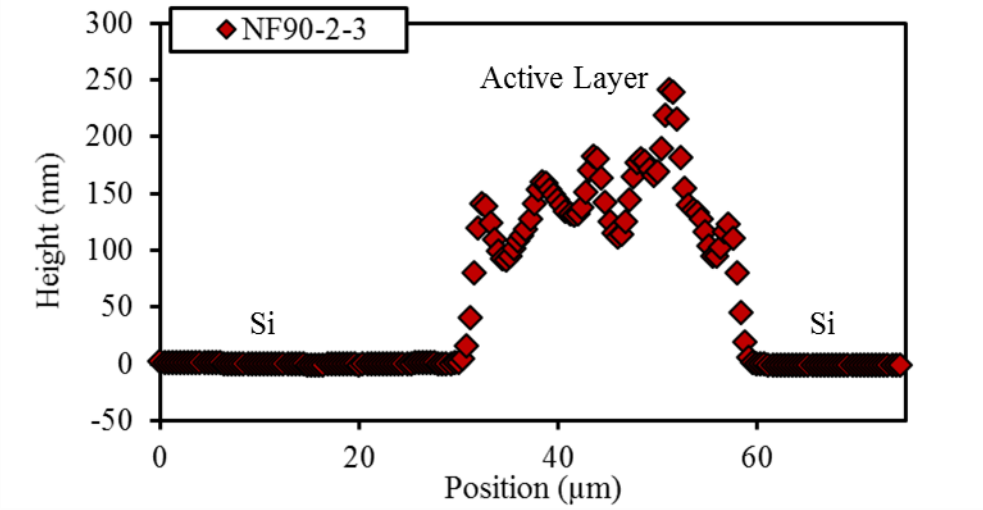
NF90-2-3
Active Layer
Si
Si
Height (nm)
Position (μm)
300
250
200
150
100
50
0
-50
0
20
40
60

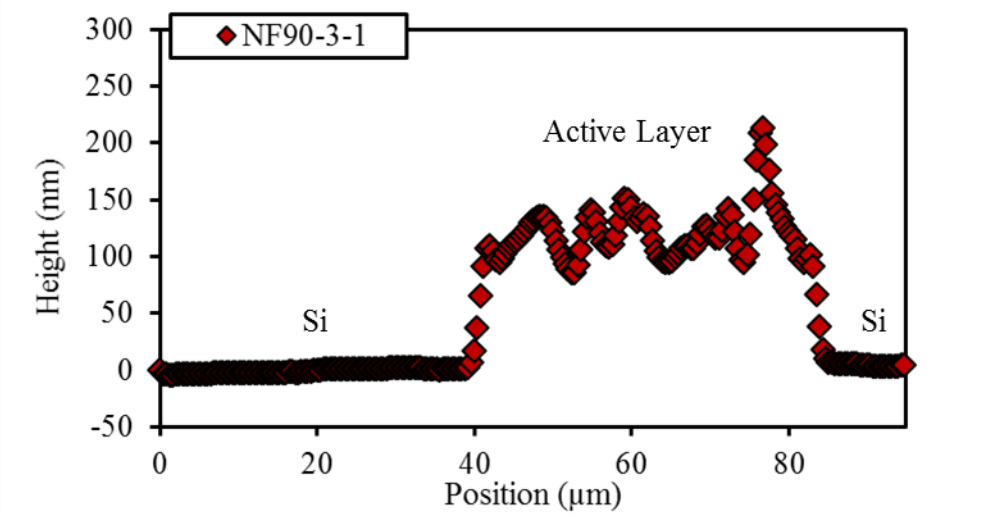
NF90-3-1
Active Layer
Si
Si
Height (nm)
Position (μm)
300
250
200
150
100
50
0
-50
0
20
40
60
80

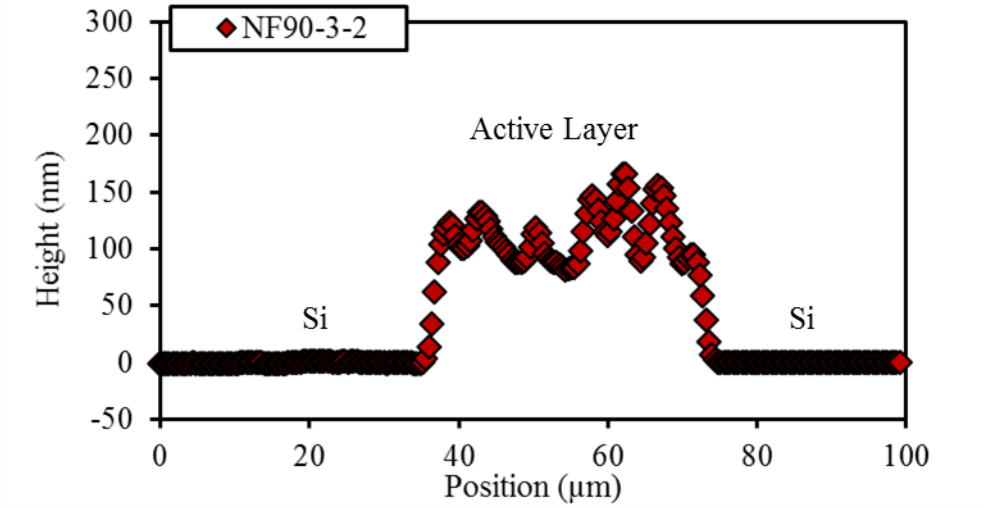
NF90-3-2
Active Layer
Si
Si
Height (nm)
Position (μm)
300
250
200
150
100
50
0
-50
0
20
40
60
80
100

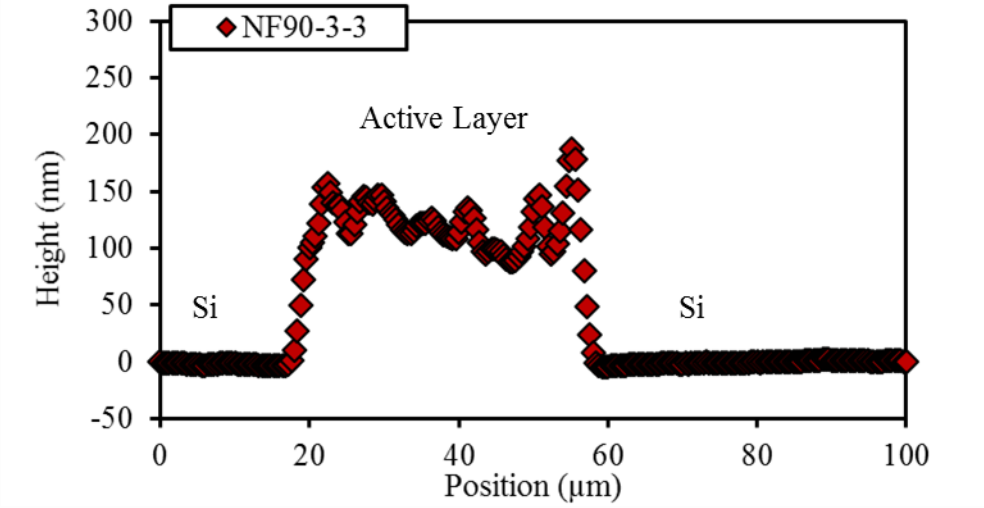
NF90-3-3
Active Layer
Si
Si
Height (nm)
Position (μm)
300
250
200
150
100
50
0
-50
0
20
40
60
80
100

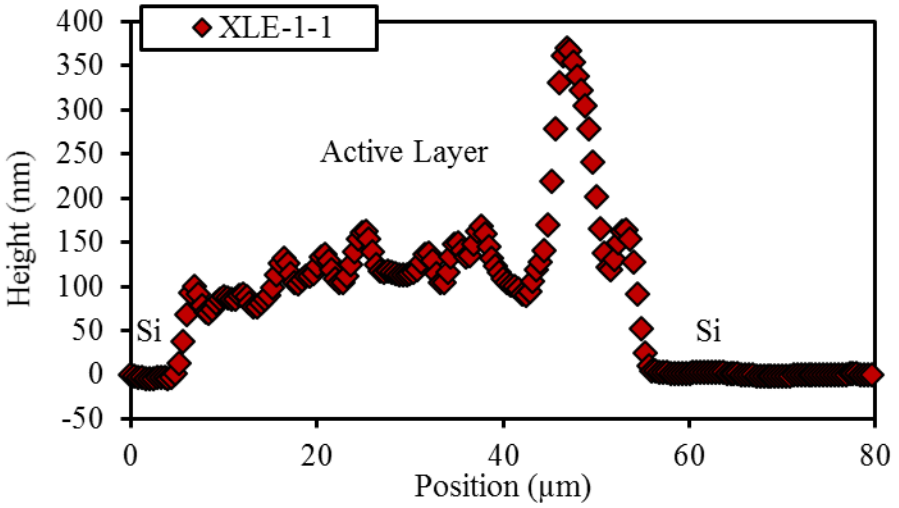
XLE-1-1
Active Layer
Si
Si
Height (nm)
Position (μm)
400
350
300
250
200
150
100
50
0
-50
0
20
40
60
80

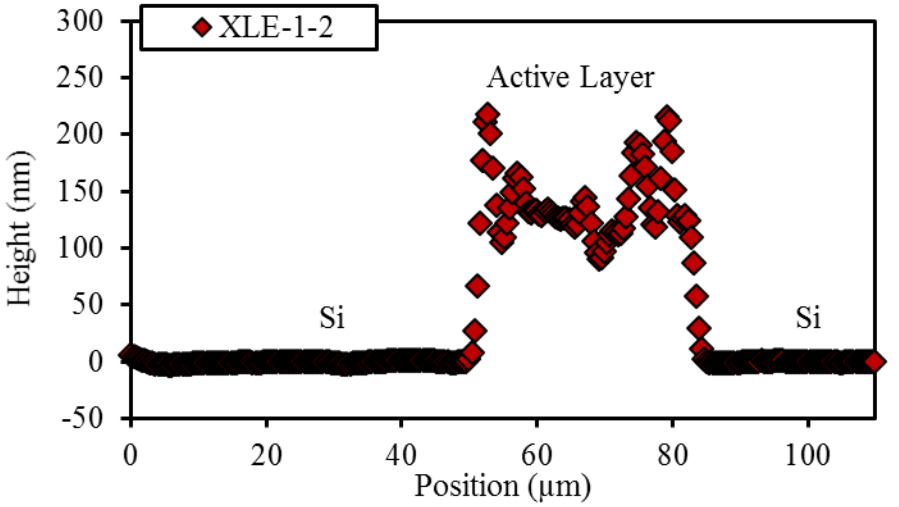
XLE-1-2
Active Layer
Si
Si
Height (nm)
Position (μm)
300
250
200
150
100
50
0
-50
0
20
40
60
80
100

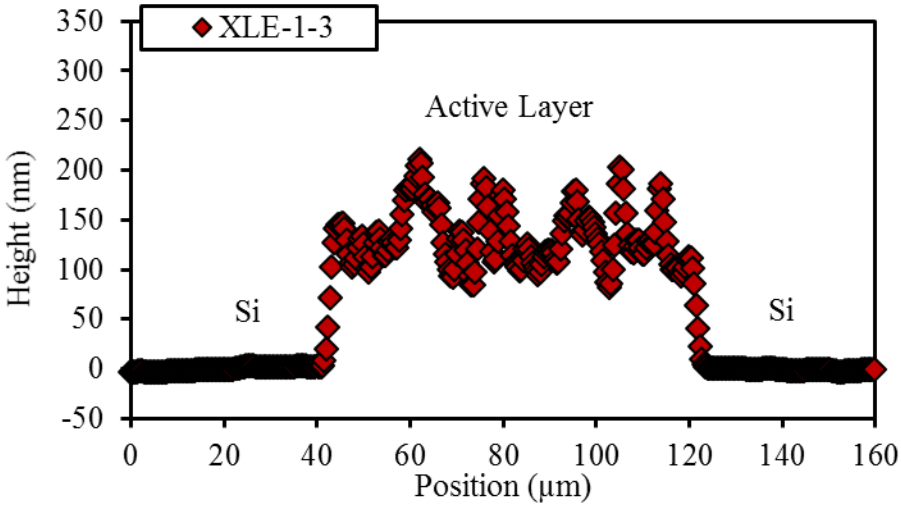
XLE-1-3
Active Layer
Si
Si
Height (nm)
Position (μm)
350
300
250
200
150
100
50
0
-50
0
20
40
60
80
100
120
140
160

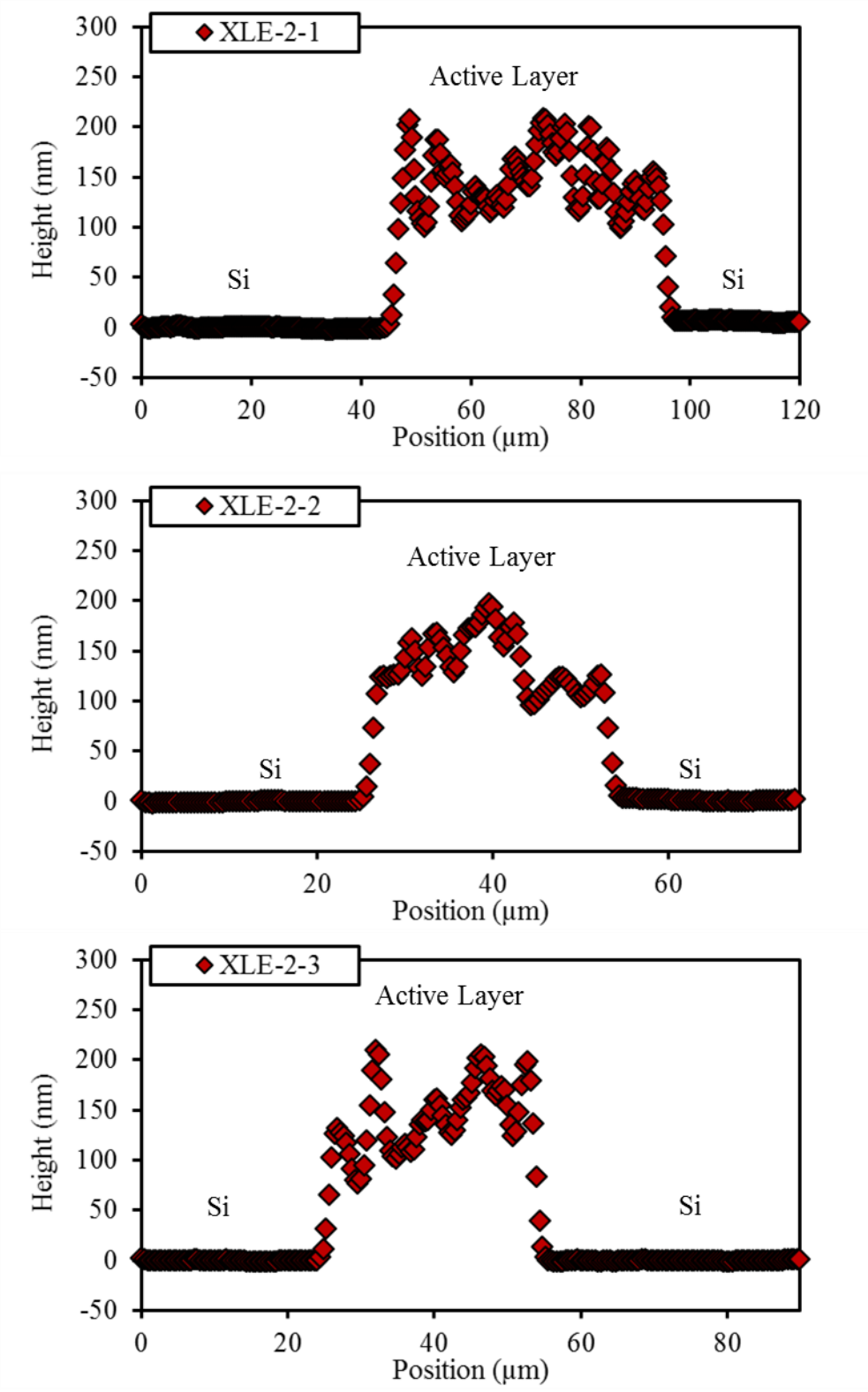
XLE-2-1
Active Layer
Si
Si
Height (nm)
Position (μm)
XLE-2-2
Active Layer
Si
Si
Height (nm)
Position (μm)
XLE-2-3
Active Layer
Si
Si
Height (nm)
Position (μm)

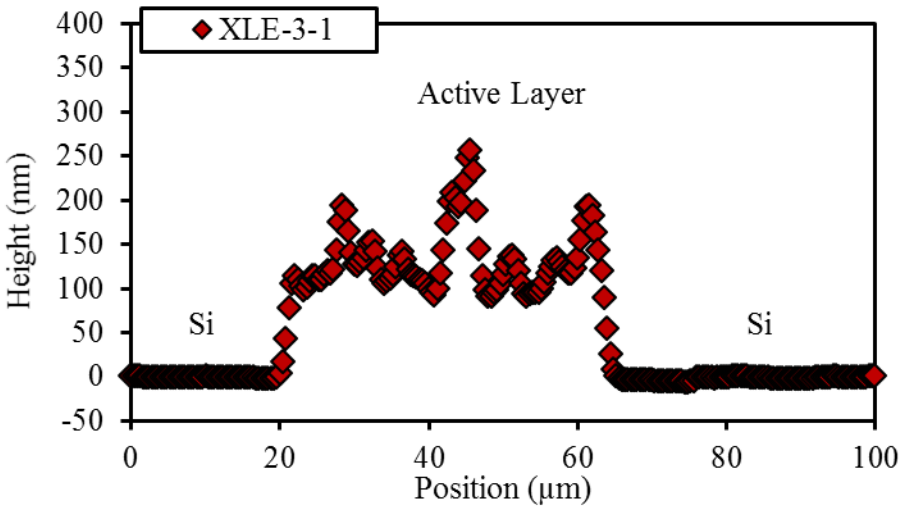
XLE-3-1
Active Layer
Si
Si
Height (nm)
Position (μm)
400
350
300
250
200
150
100
50
0
-50
0
20
40
60
80
100

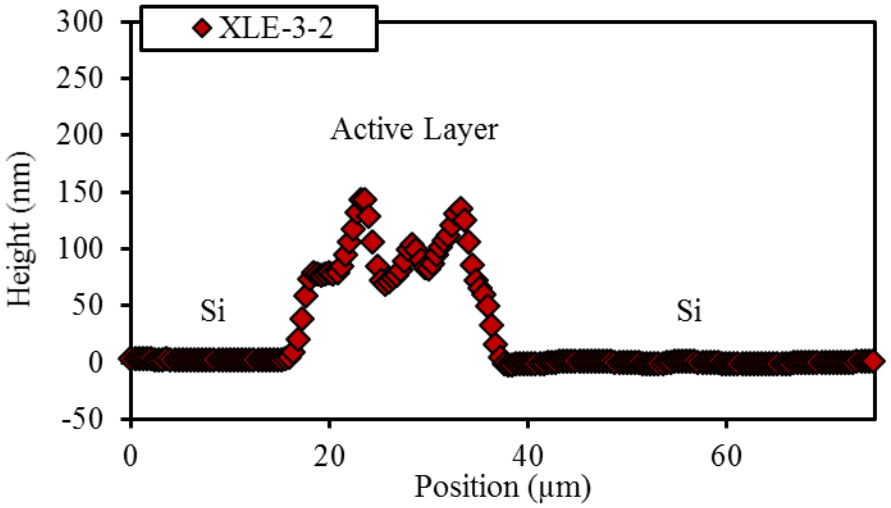
XLE-3-2
Active Layer
Si
Si
Height (nm)
Position (μm)
300
250
200
150
100
50
0
-50
0
20
40
60

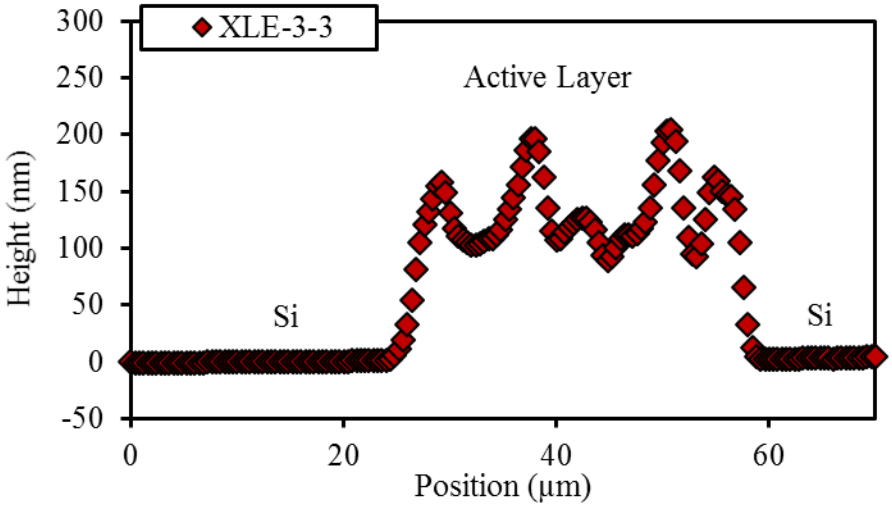
XLE-3-3
Active Layer
Si
Si
Height (nm)
Position (μm)
300
250
200
150
100
50
0
-50
0
20
40
60

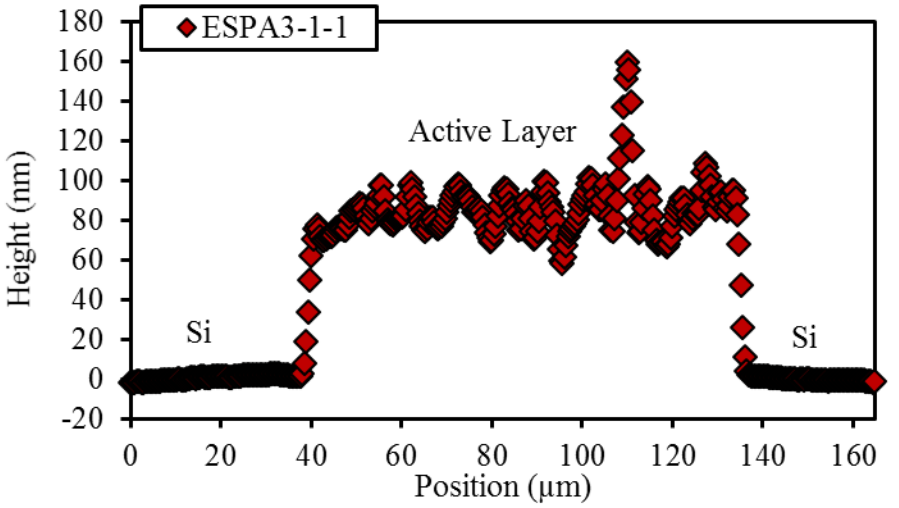
ESPA3-1-1
Active Layer
Si
Si
Height (nm)
Position (μm)
180
160
140
120
100
80
60
40
20
0
-20
0
20
40
60
80
100
120
140
160

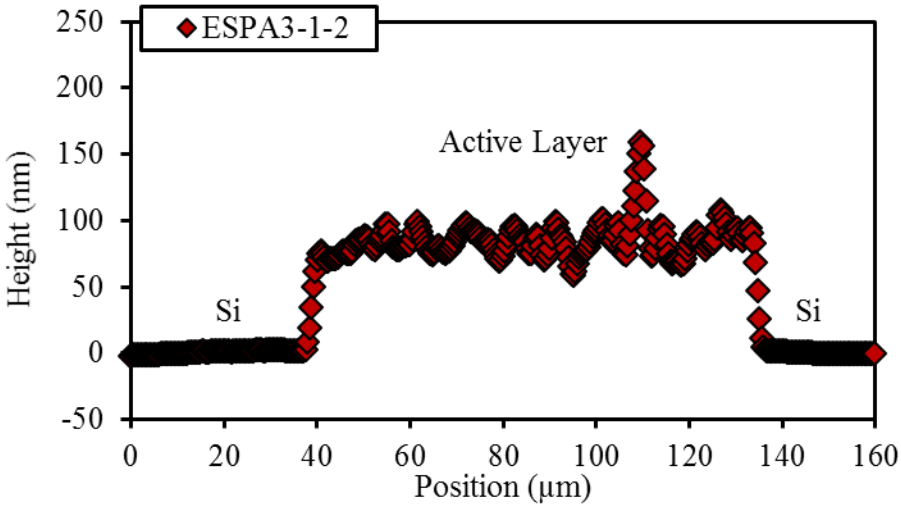
ESPA3-1-2
Active Layer
Si
Si
Height (nm)
Position (μm)
250
200
150
100
50
0
-50
0
20
40
60
80
100
120
140
160

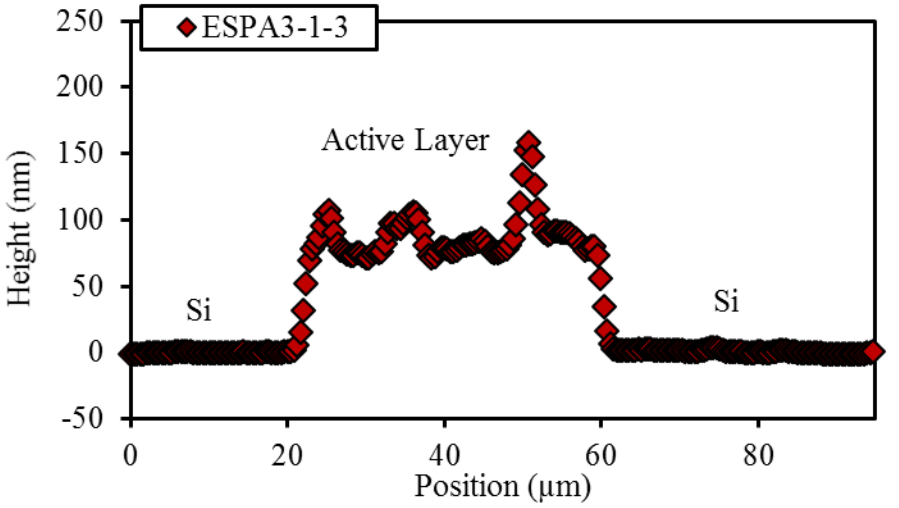
ESPA3-1-3
Active Layer
Si
Si
Height (nm)
Position (μm)
250
200
150
100
50
0
-50
0
20
40
60
80

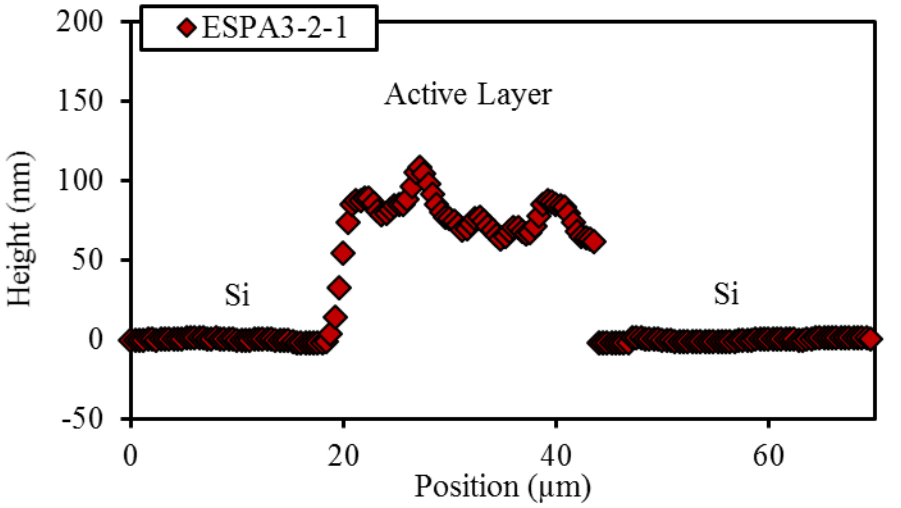
ESPA3-2-1
Active Layer
Si
Si
Height (nm)
Position (μm)
200
150
100
50
0
-50
0
20
40
60

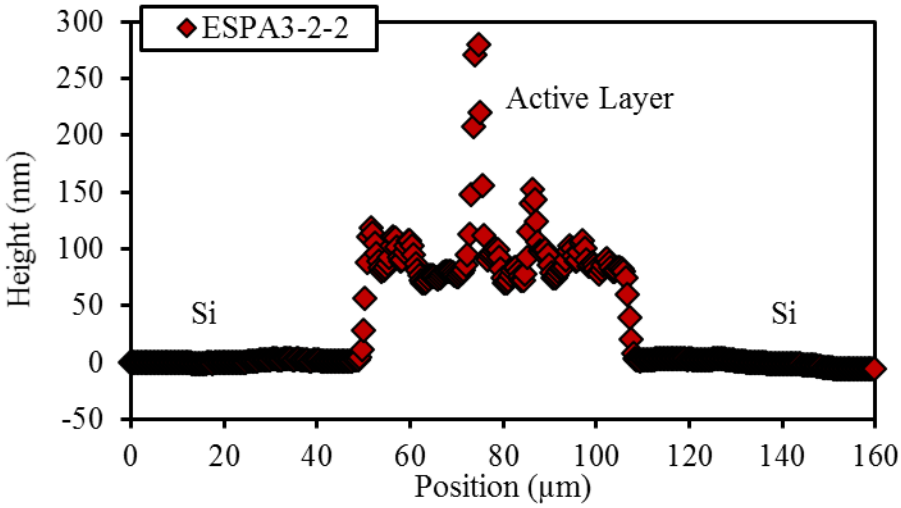
ESPA3-2-2
Active Layer
Si
Si
Height (nm)
Position (μm)
300
250
200
150
100
50
0
-50
0
20
40
60
80
100
120
140
160

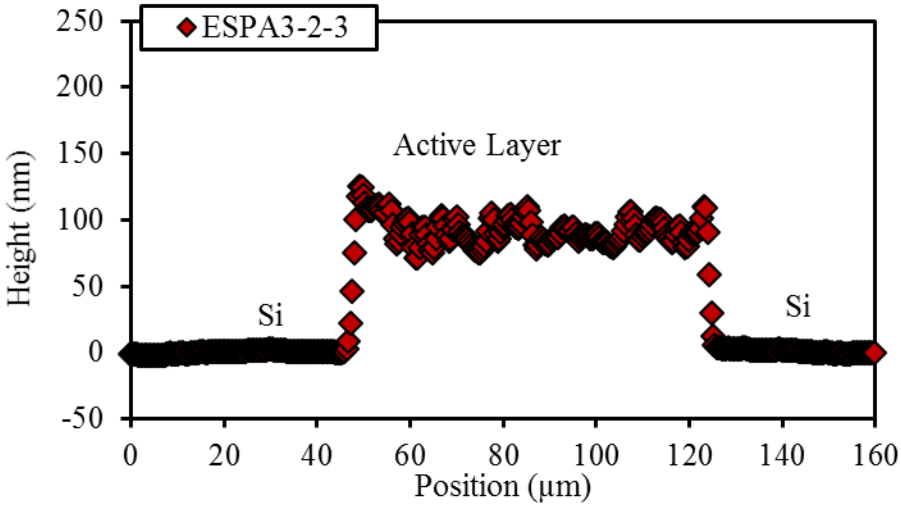
ESPA3-2-3
Active Layer
Si
Si
Height (nm)
Position (μm)
250
200
150
100
50
0
-50
0
20
40
60
80
100
120
140
160

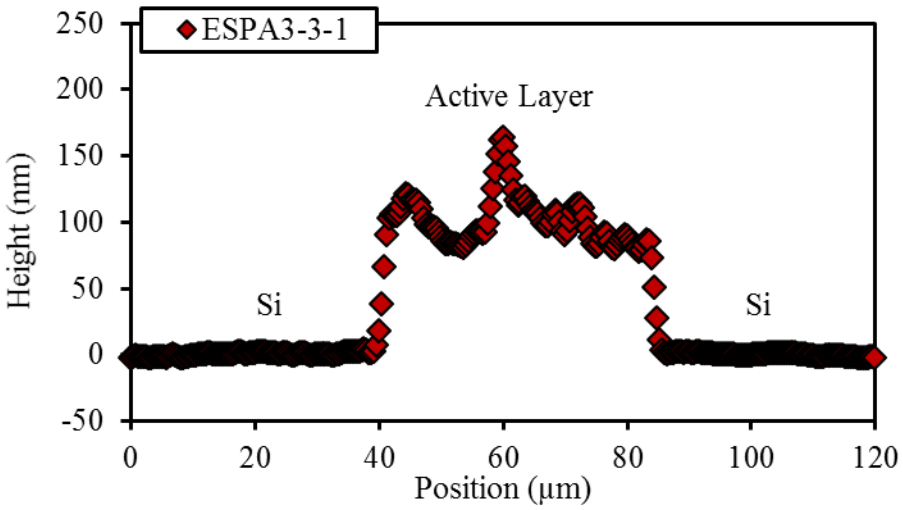
ESPA3-3-1
Active Layer
Si
Si
Height (nm)
Position (μm)
250
200
150
100
50
0
-50
0
20
40
60
80
100
120

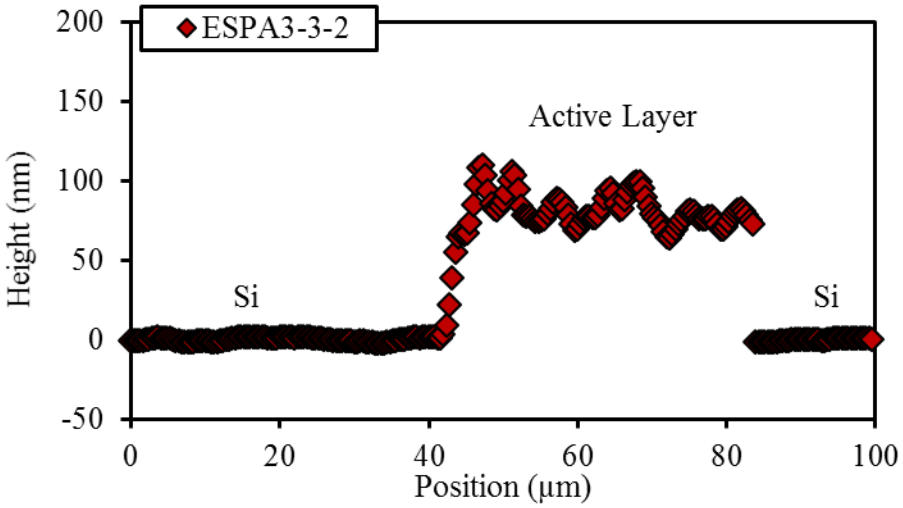
ESPA3-3-2
Active Layer
Si
Si
Height (nm)
Position (μm)
200
150
100
50
0
-50
0
20
40
60
80
100

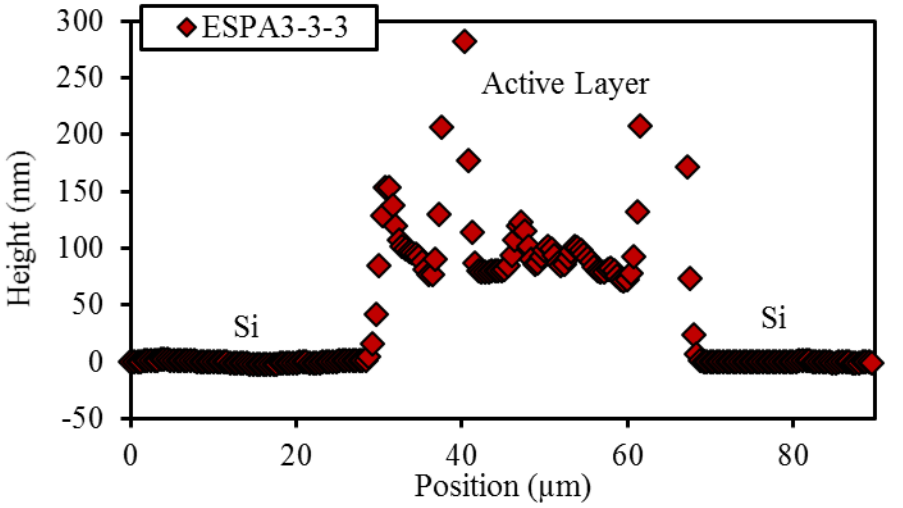
ESPA3-3-3
Active Layer
Si
Si
Height (nm)
Position (μm)
300
250
200
150
100
50
0
-50
0
20
40
60
80

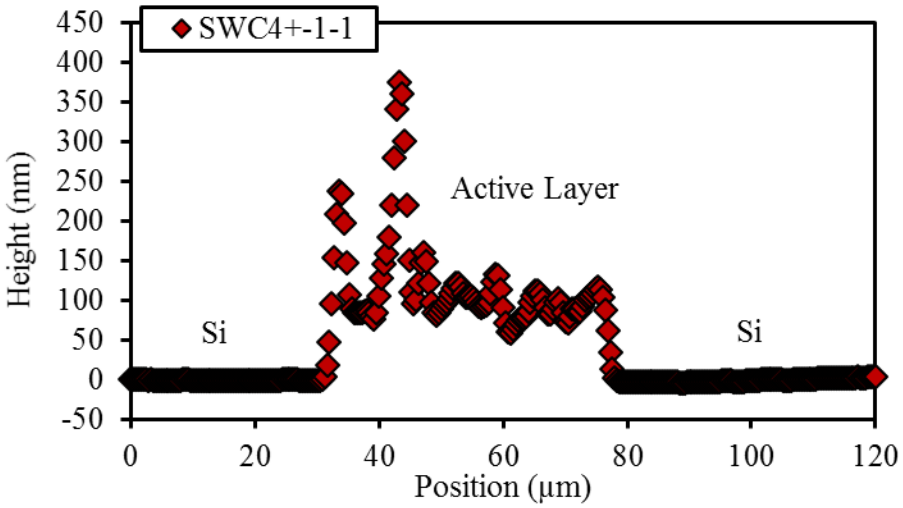
SWC4+-1-1
Height (nm)
Position (µm)
Active Layer
Si
Si
450
400
350
300
250
200
150
100
50
0
-50
0
20
40
60
80
100
120

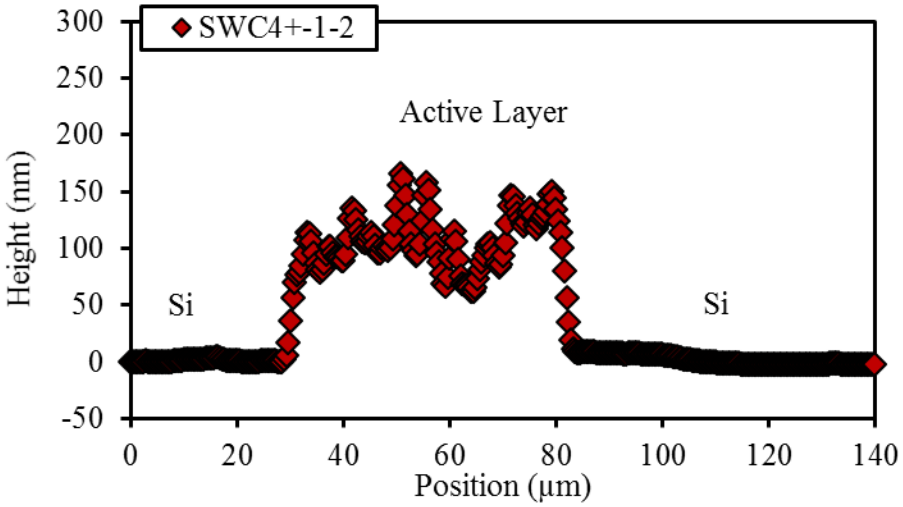
SWC4+-1-2
Height (nm)
Position (µm)
Active Layer
Si
Si
300
250
200
150
100
50
0
-50
0
20
40
60
80
100
120
140

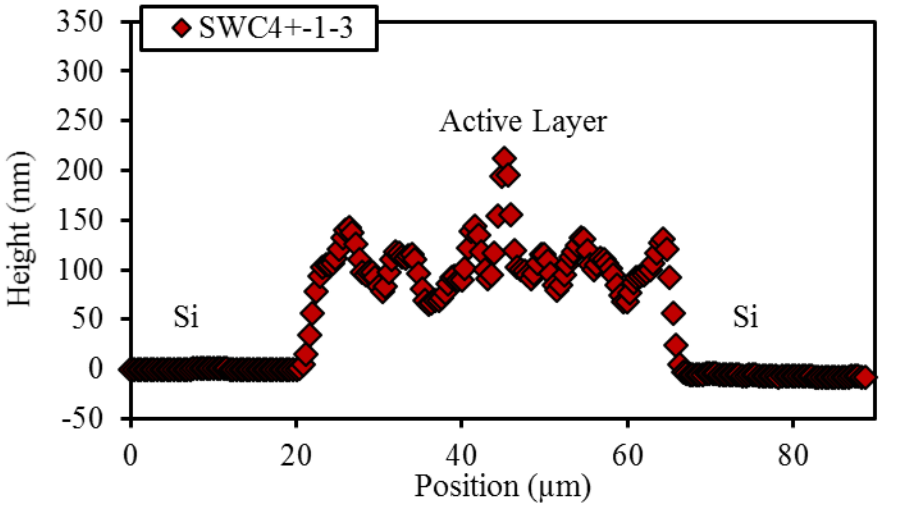
SWC4+-1-3
Height (nm)
Position (µm)
Active Layer
Si
Si
350
300
250
200
150
100
50
0
-50
0
20
40
60
80

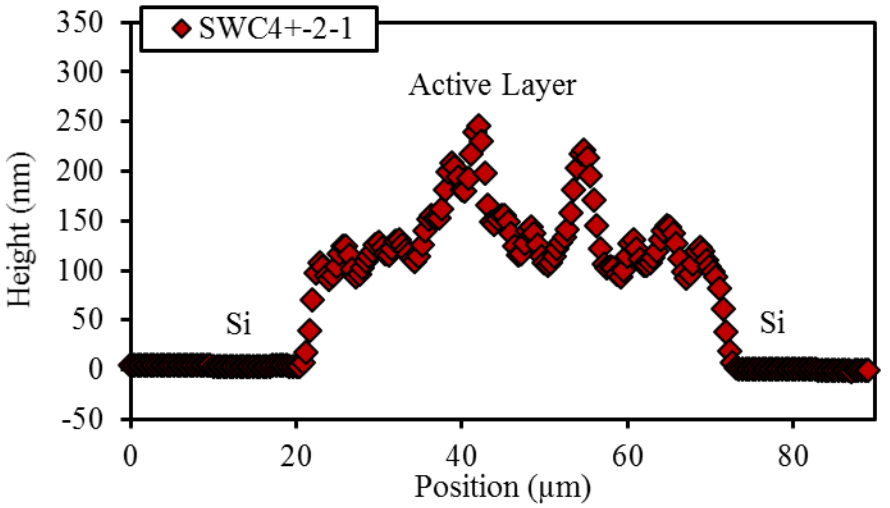
SWC4+-2-1
Active Layer
Si
Si
Height (nm)
Position (µm)
350
300
250
200
150
100
50
0
-50
0
20
40
60
80

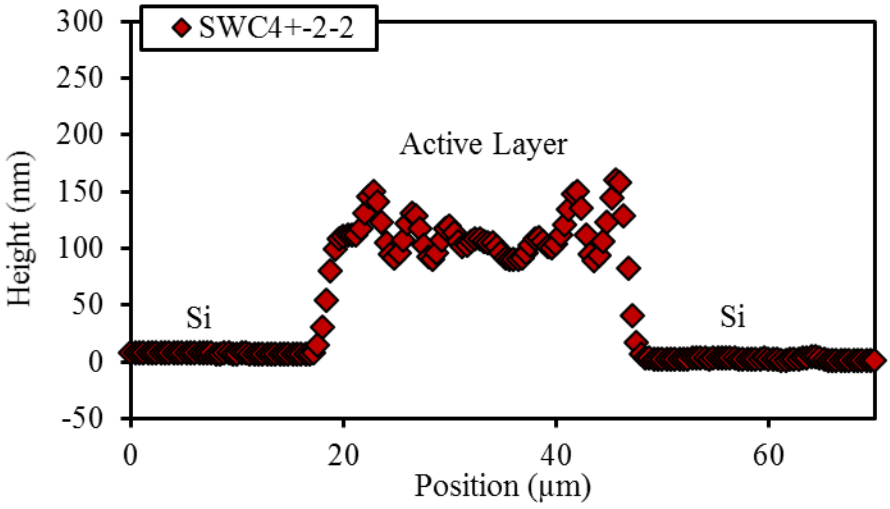
SWC4+-2-2
Active Layer
Si
Si
Height (nm)
Position (µm)
300
250
200
150
100
50
0
-50
0
20
40
60

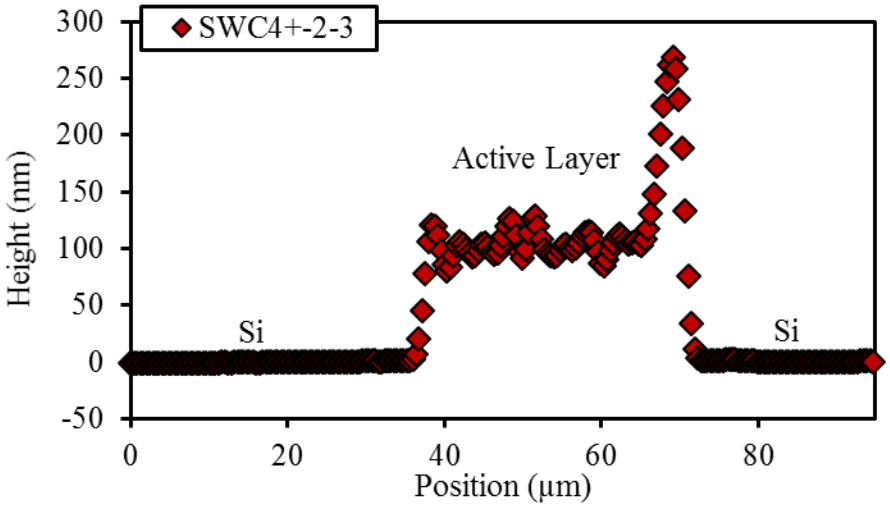
SWC4+-2-3
Active Layer
Si
Si
Height (nm)
Position (µm)
300
250
200
150
100
50
0
-50
0
20
40
60
80

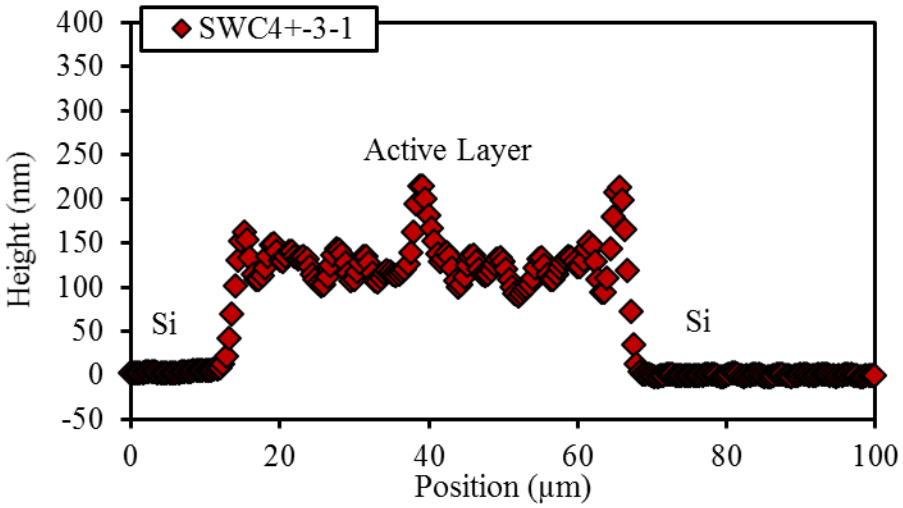
SWC4+-3-1
Active Layer
Si
Si
Height (nm)
Position (µm)
400
350
300
250
200
150
100
50
0
-50
0
20
40
60
80
100

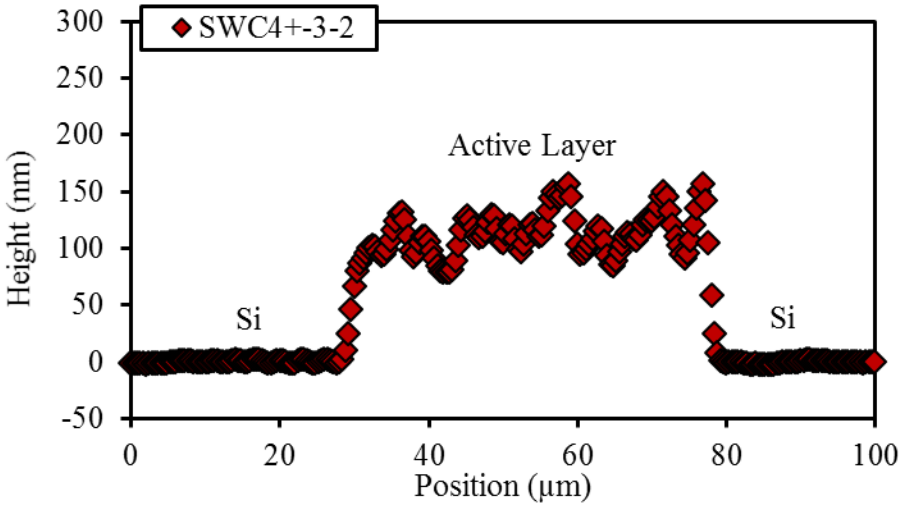
SWC4+-3-2
Active Layer
Si
Si
Height (nm)
Position (µm)
300
250
200
150
100
50
0
-50
0
20
40
60
80
100

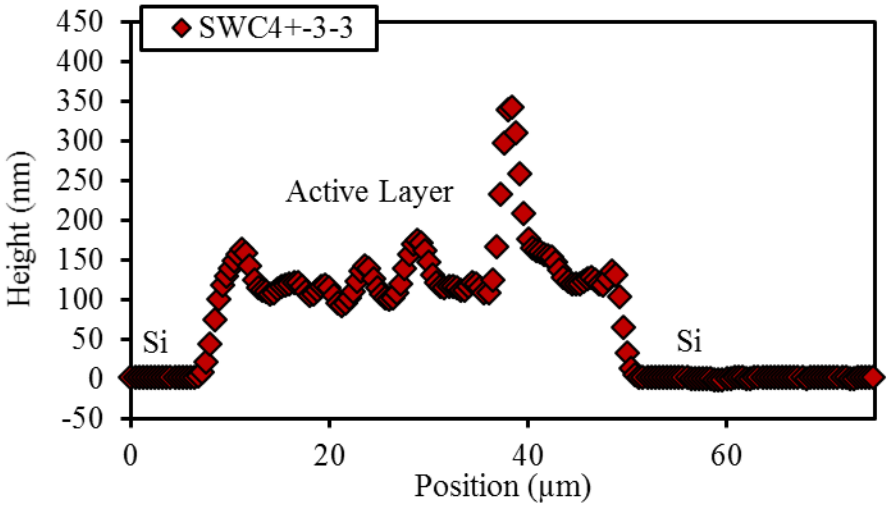
SWC4+-3-3
Active Layer
Si
Si
Height (nm)
Position (µm)
450
400
350
300
250
200
150
100
50
0
-50
0
20
40
60

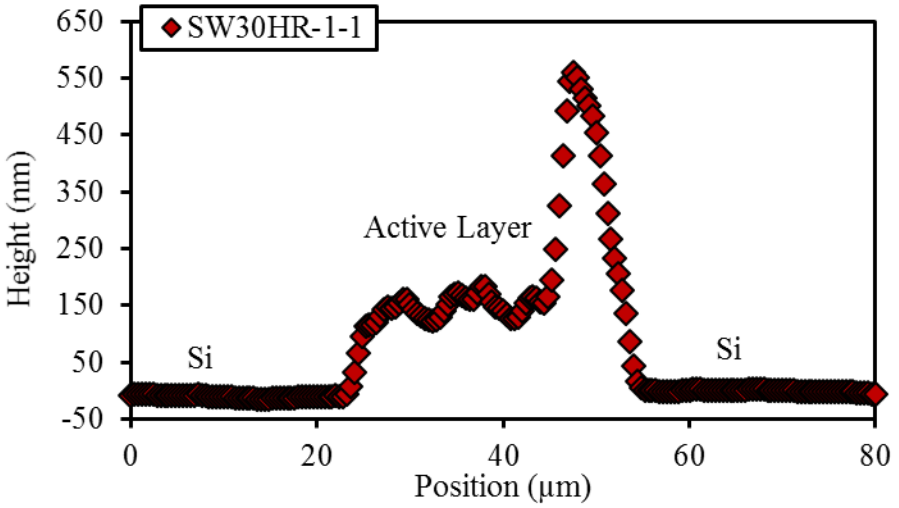
SW30HR-1-1
Height (nm)
650
550
450
350
250
150
50
-50
Active Layer
Si
Si
0
20
40
60
80
Position (μm)

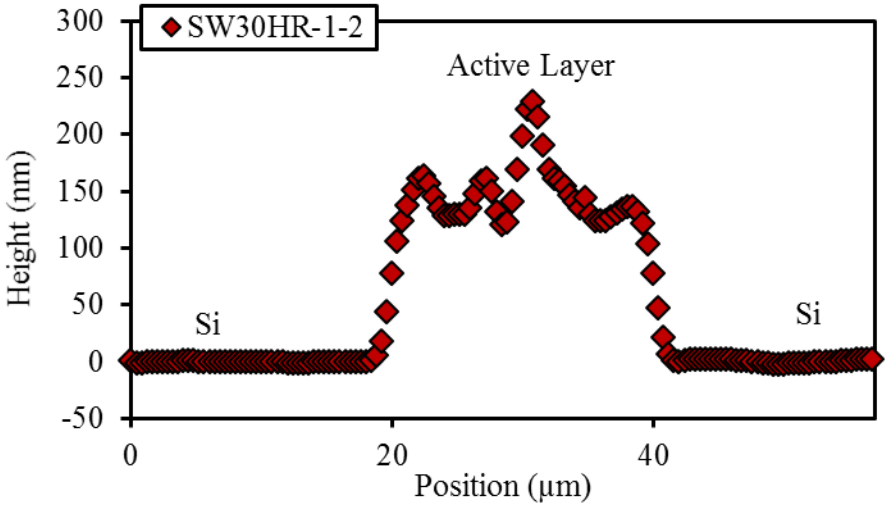
SW30HR-1-2
Height (nm)
300
250
200
150
100
50
0
-50
Active Layer
Si
Si
0
20
40
Position (μm)

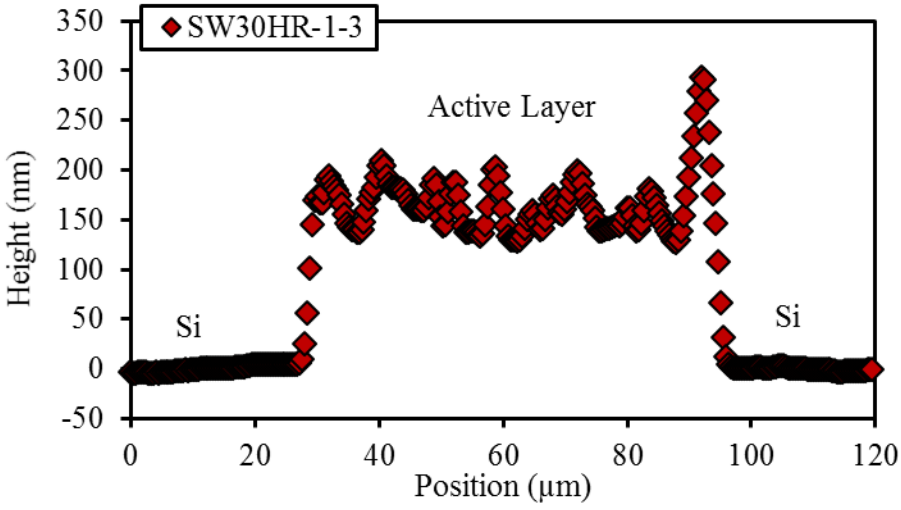
SW30HR-1-3
Height (nm)
350
300
250
200
150
100
50
0
-50
Active Layer
Si
Si
0
20
40
60
80
100
120
Position (μm)

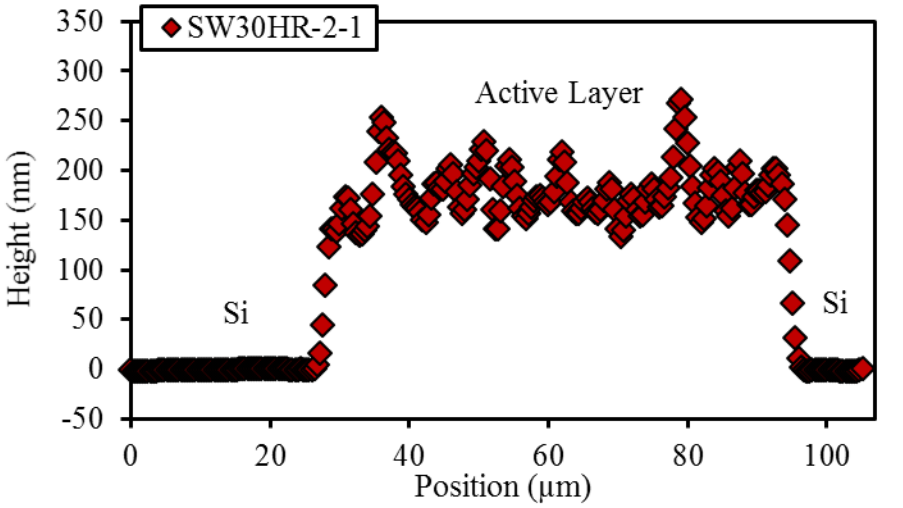
SW30HR-2-1
Active Layer
Si
Si
Height (nm)
Position (μm)
350
300
250
200
150
100
50
0
-50
0
20
40
60
80
100

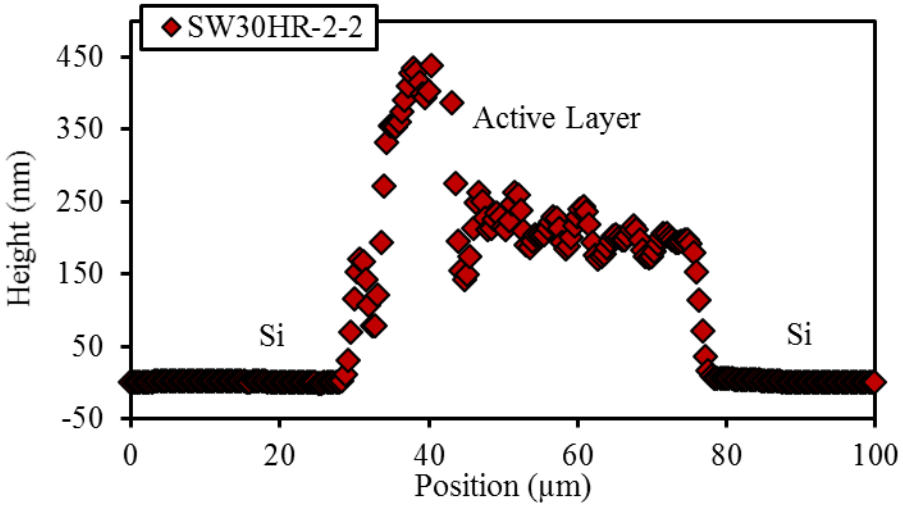
SW30HR-2-2
Active Layer
Si
Si
Height (nm)
Position (μm)
450
350
250
150
50
-50
0
20
40
60
80
100

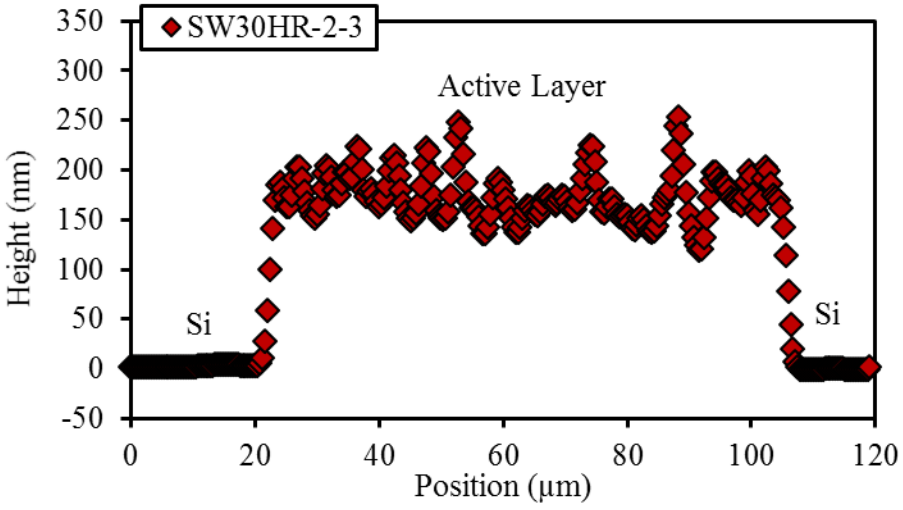
SW30HR-2-3
Active Layer
Si
Si
Height (nm)
Position (μm)
350
300
250
200
150
100
50
0
-50
0
20
40
60
80
100
120

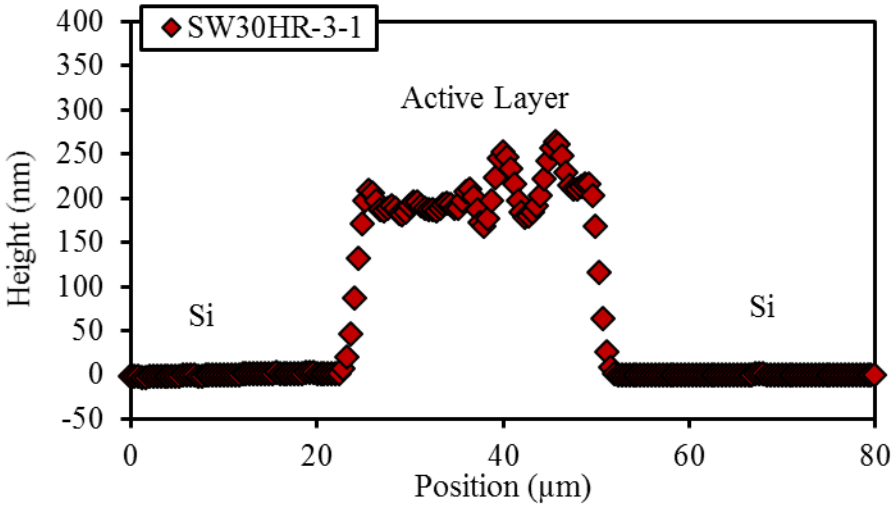
SW30HR-3-1
Active Layer
Si
Si
Height (nm)
Position (μm)
400
350
300
250
200
150
100
50
0
-50
0
20
40
60
80

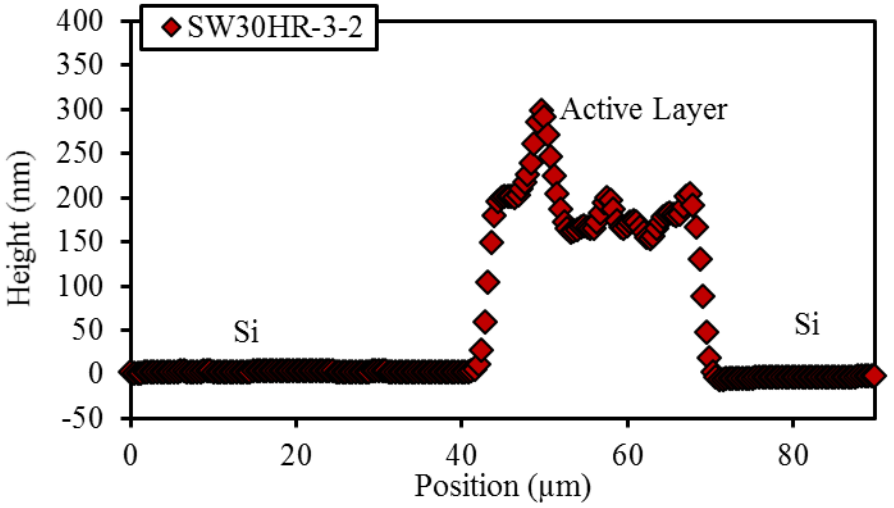
SW30HR-3-2
Active Layer
Si
Si
Height (nm)
Position (μm)
400
350
300
250
200
150
100
50
0
-50
0
20
40
60
80

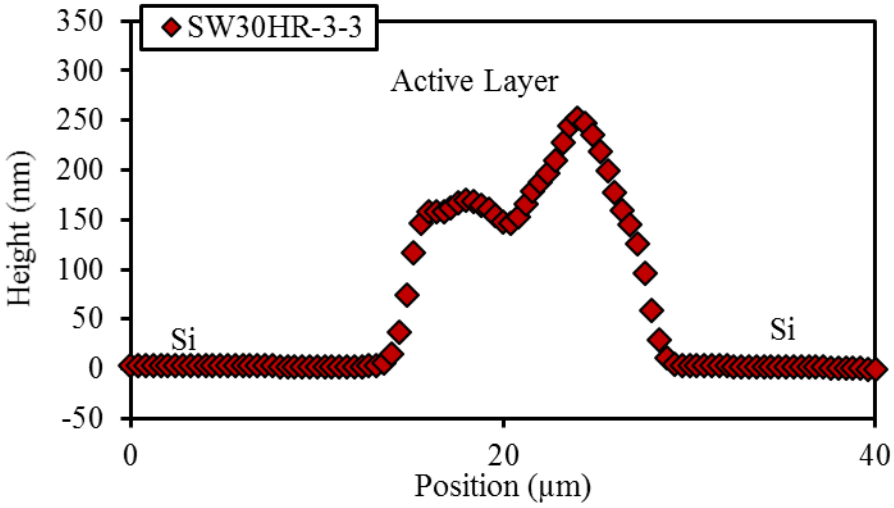
SW30HR-3-3
Active Layer
Si
Si
Height (nm)
Position (μm)
350
300
250
200
150
100
50
0
-50
0
20
40

APPENDIX 7: RESULTS OF ELLIPSOMETRY ANALYSES OF ACTIVE LAYER THICKNESS

Membrane	Sample Number	Location Number	MSE[a]	Thickness	A[b]	B[b]	C[b]	α[b]	β[b]
NF270	1	1	0.9	21.4	1.25	0.0	0.0	0.0	0.3
		2	1.2	22.1	1.24	0.0	0.0	0.0	0.3
		3	0.8	21.2	1.28	0.0	0.0	0.0	0.3
	2	1	0.9	22.1	1.26	0.0	0.0	0.0	0.3
		2	1.3	22.4	1.25	0.0	0.0	0.0	0.3
		4	0.9	22.4	1.26	0.0	0.0	0.0	0.3
	3	1	1.0	21.1	1.24	0.0	0.0	0.0	0.3
		2	1.0	21.1	1.23	0.0	0.0	0.0	0.3
		3	1.2	21.7	1.23	0.0	0.0	0.0	0.3
NF90	1	1	11.0	118.7	1.58	0.0	0.0	0.2	0.3
		2	10.6	123.1	1.57	0.0	0.0	0.2	0.2
		3	10.7	120.4	1.58	0.0	0.0	0.2	0.2
	2	1	11.1	143.1	1.54	0.0	0.0	0.2	0.1
		2	9.3	147.2	1.51	0.0	0.0	0.2	0.0
		3	9.5	148.9	1.52	0.0	0.0	0.2	0.0
	3	1	10.4	126.9	1.58	0.0	0.0	0.2	0.2
		2	10.2	127.1	1.56	0.0	0.0	0.2	0.2
		3	11.5	126.6	1.57	0.0	0.0	0.2	0.2
XLE	1	1	11.8	136.0	1.49	0.0	0.0	0.2	0.2
		2	15.3	134.9	1.45	0.0	0.0	0.2	0.3
		3	12.6	134.9	1.47	0.0	0.0	0.2	0.3
	2	1	11.9	132.8	1.46	0.0	0.0	0.2	0.3
		2	12.4	129.8	1.48	0.0	0.0	0.2	0.3
		3	12.3	132.5	1.48	0.0	0.0	0.2	0.3
	3	1	12.7	138.5	1.49	0.0	0.0	0.2	0.3
		2	16.1	142.5	1.49	0.0	0.0	0.2	0.2
		3	12.0	137.2	1.51	0.0	0.0	0.2	0.3
ESPA3	1	1	3.4	92.3	1.47	0.0	0.0	0.1	0.2
		2	3.0	93.0	1.44	0.0	0.0	0.1	0.2
		3	3.7	92.5	1.46	0.0	0.0	0.1	0.2
	2	1	2.6	91.7	1.41	0.0	0.0	0.1	0.4
		2	2.9	86.1	1.42	0.0	0.0	0.1	0.3
		3	2.5	91.7	1.46	0.0	0.0	0.1	0.2
	3	1	3.4	88.4	1.39	0.0	0.0	0.1	0.5
		2	3.9	88.8	1.44	0.0	0.0	0.1	0.4
		3	3.0	87.6	1.39	0.0	0.0	0.1	0.5

Membrane	Sample Number	Location Number	MSE[1]	Thickness	A[2]	B[2]	C[2]	α [2]	β [2]
SWC4+	1	1	4.4	99.4	1.38	0.0	0.0	0.2	0.6
		2	4.8	94.6	1.39	0.0	0.0	0.2	0.6
		3	6.5	106.1	1.39	0.0	0.0	0.2	0.6
	2	1	9.1	127.3	1.39	0.0	0.0	0.2	0.4
		2	6.9	137.1	1.35	0.0	0.0	0.2	0.3
		3	7.9	142.3	1.34	0.0	0.0	0.2	0.3
	3	1	10.0	115.4	1.42	0.0	0.0	0.1	0.5
		2	8.3	111.6	1.39	0.0	0.0	0.2	0.5
		3	7.5	106.6	1.39	0.0	0.0	0.2	0.5
SW30HR	1	1	10.3	160.7	1.43	0.0	0.0	0.1	0.3
		2	12.4	155.1	1.44	0.0	0.0	0.2	0.4
		3	9.3	168.3	1.41	0.0	0.0	0.1	0.3
	2	1	14.7	155.3	1.55	0.0	0.0	0.2	1.0
		2	15.0	154.3	1.53	0.0	0.0	0.2	0.8
		3	19.0	162.2	1.52	0.0	0.0	0.2	0.5
	3	2	15.7	153.5	1.50	0.0	0.0	0.2	0.8
		3	11.6	153.3	1.48	0.0	0.0	0.2	0.6
		4	17.1	151.9	1.51	0.0	0.0	0.2	0.7

[a] Mean square error

[b] Fitting parameters in the Cauchy model

APPENDIX 8: SUPPORTING INFORMATION FOR CHAPTER 3

Summary of contents:

- 21 pages
- Section S1. Materials and methods (extended version)
- Section S2. Thermodynamics of water partitioning into active layers exposed to liquid water and humidified nitrogen gas
- Section S3. Mass density of dry and humidified nitrogen gas
- References cited in the Supporting Information

Section S1. Materials and methods (Extended version)

Target membranes and sample preparation.

Five polyamide TFC membranes were studied: NF90, XLE and SW30HR were received as flat sheets in dry state from Dow Filmtec (Minneapolis, MN), and ESPA3 and SWC4+ were received as flat sheets in wet state from Hydranautics (Oceanside, CA). The membranes tested cover a wide performance range, with NF90 being a nanofiltration (NF) membrane, XLE and ESPA3 being brackish water RO membranes, and SW30HR and SWC4+ being seawater RO membranes. Attenuated total reflectance Fourier transform infrared spectroscopy (ATR-FTIR) analyses indicated that the five membranes used have fully-aromatic polyamide active layers (see Figure S1.1).[1,2] The ATR-FTIR analyses also indicated that the active layer of the SW30HR membrane has a coating, which is likely polyvinyl alcohol.[2] Membrane samples were initially prepared as 2.5×5.0 cm^2 coupons which were thoroughly rinsed with and stored in ultrapure water (>18 MΩ·cm). Before further sample preparation for TEM, QCM, ellipsometry and atomic force microscopy (AFM) analyses, the coupons were blot dried by placing them between two filter paper circles (qualitative grade circles No.1, 9 cm in diameter, Whatman) and applying fingertip pressure.[3,4] Pressure exerted in this manner is orders of magnitude lower than the pressure that RO/NF membranes experience during membrane operation in treatment plants (~100-1,200 psi). The coupons were then air dried overnight.

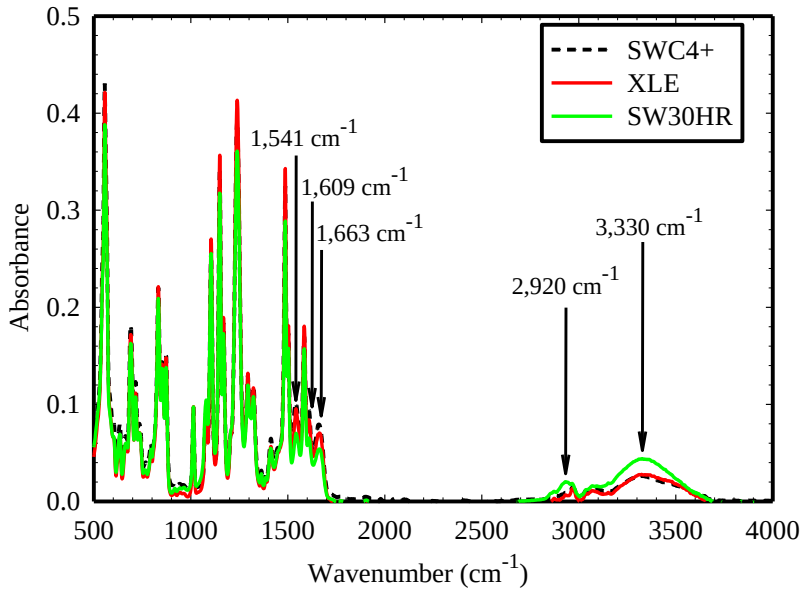

Figure S1.1. ATR-FTIR absorption spectra of XLE, SWC4+ and SW30HR membranes. The peaks around 1,663 cm^{-1} (amide I band, C=O stretching, C-N stretching and C-C-N deformation vibration), 1,609 cm^{-1} (aromatic amide, N-N deformation vibration or C=C ring stretching vibration) and 1,541 cm^{-1} (amide II band, N-H in-plane bending and N-C stretching vibration) are characteristic of fully aromatic polyamide.[2] The increased intensity of the peaks around 3,330 cm^{-1} (O-H stretching) and 2,920 cm^{-1} (C-H stretching) for the SW30HR membrane is consistent with the existence of a coating layer, likely of polyvinyl alcohol.[2,5] NF90 and ESPA membrane samples were also analyzed with ATR-FTIR in a previous publication[1] and their spectra indicate that both have uncoated fully aromatic polyamide active layers.

TEM analyses.

For TEM analyses, we used a membrane sample preparation procedure similar to that described by Tang *et al.*[5] In brief, membrane samples were dehydrated with 100% ethanol (Fisher Scientific, Pittsburgh, PA) three times, 15 min each time. The dehydrated samples were infiltrated and embedded with LR White resin (London Resin Co., Reading, UK) diluted in ethanol as follows: 50%v/v (1 h), 67%v/v (2 h), 100%v/v (3 h) and again 100%v/v (2 h). The resin was then cured at 48 ℃ for 3 days. Next, the samples were cut into thin slices approximately 90-100 nm thick with a Sorvall MT 6000 Ultramicrotome (RMC Co., Tucson, AR). Then TEM imaging of membrane cross-sections was performed with a JEOL 100CX II TEM (JEOL USA, Peabody, MA) at an acceleration voltage of 80 kV. Three images were taken for each membrane studied at magnifications of 29,000× or 72,000× depending on the thickness of the active layers.

While most of our samples for TEM analyses were air dried and then dehydrated with ethanol, we obtained control TEM images for samples of the SWC4+ RO membrane (Hydranautics) dried using supercritical CO_2 drying which confirmed that air/ethanol drying did not affect the active layer structure (see Figure S1.2). As observed in the figure, the sample dried using supercritical drying exhibits voids of similar shape and size ranges to those observed in samples that were air/ethanol dried. A Welch's t-test at a 95% confidence level between the void fraction (28.3±2.3%) calculated for triplicate SWC4+ samples that were air/ethanol dried and the void fraction (26.5±1.5%) calculated for triplicate SWC4+ samples that were dried using supercritical drying indicates that the drying procedure did not affect void fraction results. Also importantly, air drying should not significantly affect the polyamide active layer structure, as Xie *et al.* [6] examined different membrane curing techniques at the end of the polyamide membrane

fabrication process and showed that curing the membrane in an oven at 80 °C in air (i.e., drying the membrane) had no effect on membrane performance compared to curing the membrane in hot water (i.e., not drying the membrane). Curing the membranes in air in an oven is common practice in the peer-reviewed literature in the fabrication of polyamide membranes.[7–12] Finally, it should be noted that Dow Filmtec ships their flat sheet membranes dry.

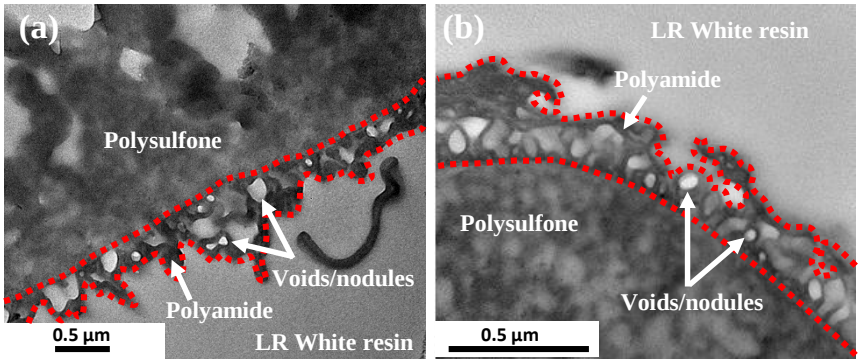

Figure S1.2. Cross-sectional TEM images of the active layer of SWC4+ RO membrane samples that were (a) air dried and dehydrated with ethanol, and (b) dried using supercritical CO_2 drying. The perimeter of the active layers is outlined in red.

Scanning transmission electron microscopy-energy dispersive X-ray spectroscopy (STEM-EDS) and electron energy loss spectroscopy (STEM-EELS) analyses.

Membrane sample preparation and sectioning for STEM-EDS and STEM-EELS analyses were performed in the same manner as for TEM analyses (see above). The STEM-EDS and STEM-EELS analyses of SWC4+ membrane samples were performed with an aberration corrected scanning transmission electron microscope (STEM) FEI Titan (FEI, Houston, TX) at an acceleration voltage of 200 kV and magnification of 80,000×. The Titan was equipped with a SuperX EDS system with four Bruker silicon drift detectors (Bruker AXS, Madison, WI) and a Gatan Enfinium spectrometer with high-speed spectrum imaging (Gatan Inc., Pleasanton, CA). Multiple locations on SWC4+ sample cross-sections were analyzed.

SEM analyses.

Membrane coupons were taken out from the ultrapure water and gently shaken twice to remove excess water on the surface. Next, the samples were immersed in liquid nitrogen for 30 seconds, taken out and cracked in air. Secondary electron SEM imaging of membrane cross-sections was performed with a FEI Helios 600 Nanolab Dual Beam System after the samples were coated with a thin film (<5 nm) of Au (60%):Pd (40%) (Ted Pella, Redding, CA) using a Cressington 108 Auto Sputter Coater (Cressington Scientific Instruments, Watford, UK). Triplicate images were taken for each membrane studied at magnifications of 40,000×, 60,000× or 80,000× depending on the thickness of the active layers.

Active layer isolation.

Membrane active layers were isolated onto gold-coated QCM sensors and silicon wafers for ellipsometry and AFM analyses. The active layer isolation procedure was similar to that described in our previous study,[13] is based on a protocol previously reported by Freger,[14] has been successfully used by various research groups,[15–17] and has been shown not to affect

physico-chemical and transport properties of the active layer.[13,18] Briefly, the membrane polyester backing was peeled off by hand leaving behind a composite of the polyamide active layer and polysulfone support layer which was placed on a clean sensor/wafer, with the active layer facing the sensor/wafer and the sensor/wafer resting on top of a customized stainless steel support. A matching customized stainless steel frame with an open window in the center was used to secure the composite and sensor/wafer to the metal support. Then, dimethylformamide (DMF) (Fisher Scientific, Pittsburgh, PA) was added in a dropwise manner through the metal frame window to dissolve the polysulfone layer and the DMF-polysulfone solution was discarded after 1 min. This process was repeated 15 times, after which the assembly was air dried. Next, the sensor/wafer with the active layer already isolated onto it was removed from the metal assembly and the isolated active layer was left in air overnight for further drying. In order to remove any polysulfone remaining on the sample, the sensor/wafer coated with the active layer was dipped in fresh DMF for 4 h and air dried overnight. The sample was finally rinsed with ultrapure water and gently dried with ultrapure nitrogen gas. Any potential gaps created between the isolated active layers and sensor/wafer surfaces caused by roughness of the membrane surface were shown not to affect the active layer void fractions estimated from QCM and ellipsometry analyses (see Section S5 below).

QCM analyses.

A Q-Sense E4 QCM (Biolin Scientific, Lithicum Heights, MD) was used to measure the areal mass ($ng \cdot cm^{-2}$) of active layer polymer isolated on QCM sensors and the areal mass of water absorbed by active layers. For each membrane, we tested two samples, each with an area of 1.54 cm^2, and for each sample we conducted duplicate measurements of water sorption in each liquid and vapor environments. The mass of active layer isolated on a sensor (m_{AL}) was

obtained as described in our previous study[13] from the difference in QCM response between the uncoated sensor and the sensor coated with the active layer. Water uptake in liquid environment (m_l) was obtained from the difference in QCM response to the coated sensor exposed to dry nitrogen (<0.02% relative humidity-RH) and to ultrapure water. Similarly, water sorption in vapor environment (m_v) was obtained from the difference in QCM response to the coated sensor exposed to dry nitrogen and to humidified nitrogen gas at 96% RH. In all cases, an uncoated control sensor was exposed to the same liquids or gases as the coated sensors to account for the changes in the response of the QCM caused by variations in the viscosity and density of the fluid to which the sensor was exposed.[13,19,20] All experiments were performed at a temperature of 22 ±0.02 ℃. Humidified nitrogen gas at 96% RH was used to prevent water condensation during experiments (i.e., at 96% RH, dew point is 21ºC).

Water sorption measurements in water vapor were obtained with the coated sensors placed in Q-Sense humidity modules (Biolin Scientific, Lithicum Heights, MD). The humidity modules had two chambers separated by a GORE™ membrane (W. L. Gore & Associates, Newark, DE). While the dry and humidified nitrogen streams flowed through the 'outer' chamber (<0.1 psi), the sensor surface was in contact with the 'inner' chamber. Each of the dry and 96% RH nitrogen streams were allowed to flow through the outer chamber until the outer chamber-inner chamber- active layer system reached equilibrium, as indicated by a change of areal mass lower than 3.6 ng·cm^{-2}·min^{-1}. The 96% RH level in the nitrogen stream was achieved by flowing dry nitrogen through cylinders filled with water and verifying the relative humidity of the exit stream with a humidity meter.

Water sorption measurements in ultrapure water were obtained with the coated sensors placed in Q-Sense flow modules (Biolin Scientific, Lithicum Heights, MD). In the flow

modules, the surface of the sensors was in direct contact with the liquid water. The water flow rate (0.1 $mL \cdot min^{-1}$) was adjusted to ensure laminar conditions and negligible disturbance of the sensor.

Ellipsometry analyses.

The refractive indices of the membrane active layers were obtained using spectroscopic ellipsometry. Samples for analysis consisted of active layers isolated on silicon wafers. Triplicate samples were analyzed for each membrane, and three locations (0.3 cm^2 each) were analyzed in each sample using a J. A. Woollam variable angle spectroscopic ellipsometer (J.A. Woollam Co., Lincoln, NE). Data acquisition was performed at incidence angles of 65 °, 70 ° and 75 ° and wavelength range of 380-1000 nm using the Autoretarder feature. Data analysis was performed using the software WVASE® (J.A. Woollam Co.) modelling the overall sample structure as a thin polymer layer on a 2-nm thick silicon dioxide layer[21] supported by an infinite silicon substrate. Cauchy dispersion formulae[22] were used to describe the optical properties of the polymer layer by selecting the appropriate option in the WVASE® software whose database also contains the well-known optical constants for silicon and silicon dioxide. The refractive index and thickness of the active layers were obtained with the WVASE® software by fitting the data to the model until a minimized mean squared error of less than 20 was reached.

The specific details for the ellipsometry analyses are provided as follows. In the spectroscopic modality, the relative amplitude and phase changes between two orthogonal polarizations of a light beam reflected off the sample under study are measured as a function of light wavelength and incidence angle. This information is then fitted to an electromagnetic model of the sample leaving the unknown properties or geometrical features (in this case the active layer refractive index and thickness) as adjustable parameters. The particular way in

which the refractive index is a function of the light wavelength is referred to as “dispersion formulae”. “Cauchy” formulae is the simplest dispersion used since 1836, and it is particularly suitable to describe the optical properties of weakly absorbing materials[22] such as various transparent polymers.[23–25] Therefore, our complete model used to fit the ellipsometric data consisted of a 3-layer structure having a Cauchy layer at the surface representing the active layer, an intermediate 2-nm silicon dioxide layer, and silicon as the substrate. We used the Cauchy formulae to describe the active layer optical behavior by selecting the appropriate option in the software used to analyze the data (WVASE®, J.A. Woollam Co. Inc., Lincoln, NE). Silicon and silicon dioxide are standard materials with well-known optical constants in the database of the WVASE® software and can be selected from the WVASE® menu. The refractive index and thickness of the active layers were obtained with the WVASE® software by fitting the data to the model until a minimized mean squared error of less than 20 was reached. The Cauchy formulae were found to describe well our data as depicted by the illustrative fitted data in Figure S1.3.

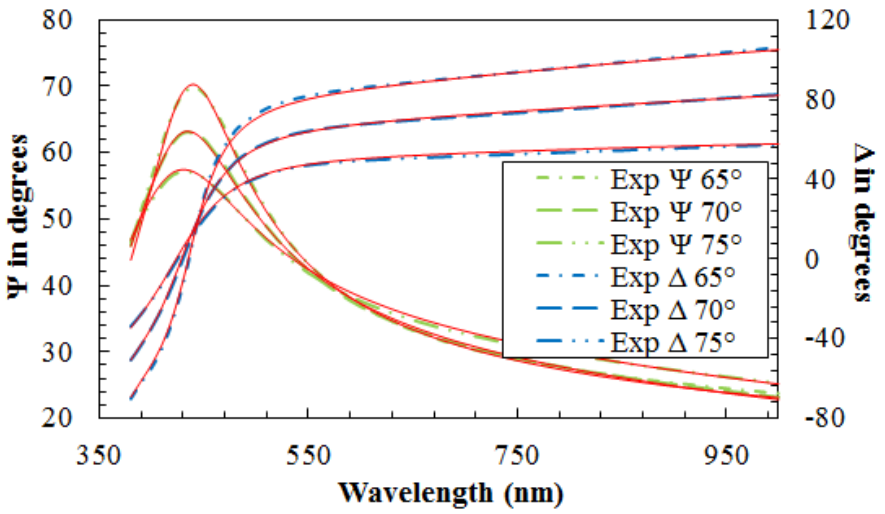

Figure S1.3. Representative experimental (interrupted lines) and fitted (continuous lines) ellipsometry spectra of isolated polyamide active layers on silicon wafers. Ψ and Δ correspond to the amplitude component and the phase difference, respectively, of the measured complex reflectance ratio. The data in the figure was obtained with the isolated active layer of an ESPA3 RO membrane sample. The refractive index at 589 nm and thickness of the sample analyzed in the figure were 1.47±0.01 and 92.3±1.33 nm, respectively, with a mean squared error of the fitting of 3.39.

AFM analyses.

Membrane surface roughness and active layer thickness were characterized using AFM analyses. For surface roughness measurements, we used 2.5×5.0 cm^2 membrane coupons rinsed and dried as described above, and an Asylum Research MFP-3D AFM (Santa Barbara, CA) equipped with Tap300Al tips (BudgetSensors, Sofia, Bulgaria). For each membrane sample, the membrane surface topography was obtained by scanning the AFM tip in tapping mode over the membrane sample surface, covering areas of 10×10 μm^2. Surface roughness was reported as root-mean-square roughness and was calculated from the surface topography profiles as described by Kwak *et al.*[26] For active layer thickness measurements, we used a procedure similar to that described by Freger.[14] Briefly, active layers isolated on silicon wafers were gently scratched with a sharp razor to expose the surface of the wafer and obtain multiple polyamide thin strips. Then AFM analysis was used to obtain topography profiles covering areas approximately 30×30 μm^2 in size of the thin strips. The topography profiles allowed the determination of the average thickness of the isolated polyamide film from the difference of the average height of the polyamide surface and the average height of the silicon wafer surface. While we did not detect any polyamide rolling up or separation from the substrate, to avoid any potential confounding edge effects, we did not use in the calculations the data from ≈6-μm wide bands of polymer and substrate next to either edge of the film strips (see Figure S1.4). Triplicate samples of each membrane were analyzed for each surface roughness and active layer thickness measurements.

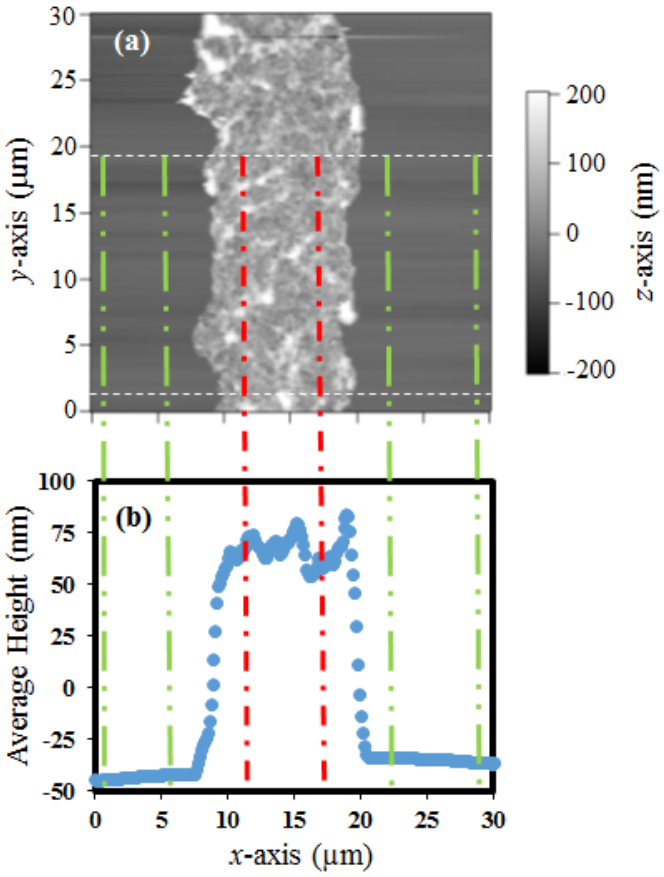

Figure S1.4. (a) An AFM image of a thin strip of NF90 membrane active layer isolated on a silicon wafer, and (b) its corresponding height profile obtained by analyzing the region between the two horizontal dashed white lines in (a). The Average Height in (b) at a specific *x*-axis location corresponds to the average *z*-axis value in (a) along the corresponding *x*-axis location. The average thickness of the active layer was calculated as the difference between the average heights of the active layer between the two (red) dash-dot lines and the average height of the silicon substrate between the two (green) dash-dot-dot lines on the left and on the right. The ≈6-µm wide bands between the (red) dash-dot lines and (green) dash-dot-dot lines were not used in the calculations to avoid any potential confounding edge effects. For the sample shown in the figure, the average thickness of the active layer was 107.3±9.2 nm.

Water permeation tests.

Permeation experiments were performed in duplicate for each membrane using a Sterlitech^{TM} (Kent, WA) HP4750 dead-end stirred filtration system (14.6 cm^2 effective membrane area) operated with ultrapure water at 20±2^{o}C and at a transmembrane pressure (ΔP) of 0.67 MPa. Permeate volume was measured using an electronic balance and filtration time using a stopwatch until a stabilized water flux (J_v, $m \cdot s^{-1}$) was reached. Under the framework of solution-diffusion theory,[27] the water permeability of the active layers was quantified by the water permeability coefficient (A, $m \cdot s^{-1} \cdot Pa^{-1}$) as calculated from

$$J_v = A(\Delta P - \Delta \pi), \quad \text{(S1.1)}$$

where $\Delta \pi$ (Pa) is the transmembrane osmotic pressure which in our experiments was zero.

Section S2. Thermodynamics of water partitioning into active layers exposed to liquid water and humidified nitrogen gas

The underlying fundamentals to our statements are of a thermodynamic nature. The key insight from the thermodynamic analysis of the test in which the active layer is exposed to a bulk phase[27–29] such as liquid water or humidified nitrogen gas is that as long as polyamide is permeable to a given species "*i*" (e.g., water, nitrogen) present in that bulk phase, then, at equilibrium, species *i* will also be present in the polyamide phase and the "void" phase. While it is known that polyamide is permeable to water, we could not find reports in the literature confirming the permeability of interfacially-polymerized polyamide to nitrogen gas; however, the diameter of molecular nitrogen (0.35 nm)[30] is similar to that of water (0.28 nm)[31], and therefore it is reasonable to assume that polyamide is permeable to nitrogen to some degree. Even assuming a conservatively low diffusion coefficient of nitrogen in the active layer six orders of magnitude lower than that of water (i.e., nitrogen's permeability has been reported to be about four orders of magnitude lower than that of water in Nylon 6[32]), the time scale of nitrogen diffusion in the active layer would be under half a minute (i.e., $t = L^2/(4D_{N2}) = 25$ s with L=100 nm and $D_{N2} = 1\times10^{-16}$ $m^2\cdot s^{-1}$ given that $D_{H2O} \approx 1\times10^{-10}$ $m^2\cdot s^{-1}$ in crosslinked polyamide[33]) which is much lower than the time to which the samples are exposed to nitrogen during the tests (>60 min). We ensured that our measurements were taken at equilibrium by verifying that the mass change per unit time was no larger than 3.6 $ng\cdot cm^{-2}\cdot min^{-1}$, which is a negligible value compared to the range of mass changes measured in our tests (i.e., 1,682-11,377 $ng\cdot cm^{-2}$).

From irreversible thermodynamics, at equilibrium, the chemical potential of any given species "*i*" (μ_i) will be the same in the three phases as expressed by[27–29]

$$\mu_{i,B} = \mu_{i,PA} = \mu_{i,V}. \quad \text{(S3.1)}$$

where the subscript B refers to the bulk water or humidified nitrogen gas phases, and the subscripts PA, V and *i* refer to the polyamide phase, void phase and the species of interests (water, W, or nitrogen, N), respectively. Since in our experiments there is no pressure difference across the phases, Equation S3.1 can be rewritten in terms of the activity of species *i* (a_i) as[27,29]

$$a_{\mathrm{i,B}} = a_{\mathrm{i,PA}} = a_{\mathrm{i,V}} . \quad \text{(S3.2)}$$

In turn, the activity of species *i* in each phase is given by

$$a_{\mathrm{i}} = \gamma_{\mathrm{i}} c_{\mathrm{i}} \ , \quad \text{(S3.3)}$$

where γ_i and c_i represent the activity coefficient and concentration (e.g., molar fraction) of species *i*, respectively. The activity coefficient accounts for non-idealities in the system such as non-negligible interactions with other species (e.g., ions in bulk water or polymer in polyamide). Because Equation S3.2 must hold true (if polyamide is permeable to species *i*), then c_i must be non-zero in each phase. Equations S3.1-S3.3 therefore indicate that when we expose our samples to liquid water, once equilibrium is reached, water is present in both polyamide and voids. Similarly, when we expose our samples to humidified nitrogen gas, once equilibrium is reached, water and nitrogen are present in polyamide and voids. Under the assumption that the voids are polymer-less regions, there is no difference in the nature of the voids and the outside of the active layer, and accordingly Equations S3.1-S3.3 indicate that the voids are filled up with the bulk phase to which the active layer is exposed (i.e., liquid water or humidified nitrogen gas). The assumption that the voids are polymer-less regions is supported by TEM imaging (i.e., sharp visual contrast between voids and polyamide), STEM-EELS/EDS imaging (i.e., significantly lower nitrogen signal from the voids compared to from the surrounding polymer), water uptake tests by QCM (i.e., significantly larger water uptake by active layers when exposed to liquid

water than when exposed to humidified nitrogen), and spectroscopic ellipsometry analyses (i.e., lower refractive index of active layers than of polyamide).

Section S4. Mass density of dry and humidified nitrogen gas

Mass density of a gas

The ideal gas law for any species *i* in a gas mixture can be written as

$$p_i \cdot V = n_i \cdot R \cdot T, \quad \text{(S4.1)}$$

where R is the ideal gas constant and p_i, V, n_i and T are the partial pressure, volume occupied, moles and temperature of the gas, respectively. Multiplying both sides of Equation S4.1 by the molecular weight of species *i* (MW_i), we obtain

$$p_i \cdot V \cdot MW_i = m_i \cdot R \cdot T, \quad \text{(S4.2)}$$

where m_i corresponds to the mass of species *i*. Reorganizing Equation S4.2 to solve for the mass density of species *i*, (ρ_i), we obtain

$$\rho_i = m_i/V = p_i \cdot MW_i/(RT). \quad \text{(S4.3)}$$

Mass density of dry nitrogen gas

For our experiments with dry nitrogen gas, the partial pressure in Equation S4.3 is approximately equal to atmospheric pressure (101,325 Pa) since nitrogen gas is the only species in the gas mixture and we performed our tests at negligible applied pressure. Replacing values in Equation S4.3 (p_{N2} = 101,325 Pa, MW_{N2} = 28.02 $g \cdot mol^{-1}$, R= 8.314 $m^3 \cdot Pa \cdot K^{-1} \cdot mol^{-1}$, T = 295.15 K), we obtain ρ_{N2} = 1.157 $Kg \cdot m^{-3}$.

Mass density of humidified nitrogen gas

The mass density of humidified nitrogen gas ($\rho_{N2,h}$) is given by

$$\rho_{N2,h} = (m_{N2} + m_{H2O})/V, \quad \text{(S4.4)}$$

where m_{N2} and m_{H2O} are the masses of nitrogen and water, respectively, in the humidified nitrogen gas mixture. Replacing Equation S4.3 in S4.4 for each nitrogen and water, we obtain

$$\rho = (p_{N2} \cdot MW_{N2} + p_{H2O} \cdot MW_{H2O})/(RT). \quad \text{(S4.5)}$$

Given that the experiments were performed at 96% RH (close to saturation), we can use the vapor pressure of liquid water at 22ºC (2,645 Pa)[34] as the partial pressure of water in the humidified nitrogen gas mixture. Replacing values in Equation S4.5 (p_{H2O} = 2,645 Pa, p_{N2} = 101,325 Pa – 2,645 Pa = 98,680 Pa, MW_{H2O} = 18.016 g/mol, MW_{N2} = 28.02 $g \cdot mol^{-1}$, R= 8.314 $m^3 \cdot Pa \cdot K^{-1} \cdot mol^{-1}$, T = 295.15 K), we obtain ρ = 1.146 $Kg \cdot m^{-3}$.

Thus, there is less than 1% difference between the mass densities of dry nitrogen (1.157 $Kg \cdot m^{-3}$) and humidified nitrogen (1.146 $Kg/\cdot m^{-3}$).

Notice that even if the voids were initially empty and then filled up with humidified nitrogen gas, the mass increment due to humidified nitrogen gas uptake would still be negligible (i.e., on the order of a few $ng \cdot cm^{-2}$) because the mass density of these gases is very low (about three orders of magnitude lower than the mass density of water).

REFERENCES

(FOR APPENDIX 8: SUPPORTING INFORMATION FOR CHAPTER 3)

(1) Coronell, O.; González, M. I.; Mariñas, B. J.; Cahill, D. G. Ionization behavior, stoichiometry of association, and accessibility of functional groups in the active layers of reverse osmosis and nanofiltration membranes. *Environ. Sci. Technol.* **2010**, *44*, 6808–6814.

(2) Tang, C. Y.; Kwon, Y.-N.; Leckie, J. O. Effect of membrane chemistry and coating layer on physiochemical properties of thin film composite polyamide RO and NF membranes I. FTIR and XPS characterization of polyamide and coating layer chemistry. *Desalination* **2009**, *242*, 149–167.

(3) Zhang, X.; Cahill, D. G.; Coronell, O.; Mariñas, B. J. Partitioning of salt ions in FT30 reverse osmosis membranes. *Appl. Phys. Lett.* **2007**, *91*, 181904.

(4) Coronell, O.; Mariñas, B. I.; Cahill, D. G. Accessibility and ion exchange stoichiometry of ionized carboxylic groups in the active layer of FT30 reverse osmosis membrane. *Environ. Sci. Technol.* **2009**, *43*, 5042–5048.

(5) Tang, C. Y.; Kwon, Y.-N.; Leckie, J. O. Probing the nano- and micro-scales of reverse osmosis membranes—A comprehensive characterization of physiochemical properties of uncoated and coated membranes by XPS, TEM, ATR-FTIR, and streaming potential measurements. *J. Membr. Sci.* **2007**, *287*, 146–156.

(6) Xie, W.; Geise, G. M.; Freeman, B. D.; Lee, H.-S.; Byun, G.; McGrath, J. E. Polyamide interfacial composite membranes prepared from m-phenylene diamine, trimesoyl chloride and a new disulfonated diamine. *J. Membr. Sci.* **2012**, *403-404*, 152–161.

(7) Chen, G.; Li, S.; Zhang, X.; Zhang, S. Novel thin-film composite membranes with improved water flux from sulfonated cardo poly(arylene ether sulfone) bearing pendant amino groups. *J. Membr. Sci.* **2008**, *310*, 102–109.

(8) Rao, A. P.; Joshi, S. V; Trivedi, J. J.; Devmurari, C. V; Shah, V. J. Structure–performance correlation of polyamide thin film composite membranes : effect of coating conditions on film formation. *J. Membr. Sci.* **2003**, *211*, 13–24.

(9) Rana, D.; Kim, Y.; Matsuura, T.; Arafat, H. A. Development of antifouling thin-film-composite membranes for seawater desalination. *J. Membr. Sci.* **2011**, *367*, 110–118.

(10) Li, L.; Zhang, S.; Zhang, X.; Zheng, G. Polyamide thin film composite membranes prepared from isomeric biphenyl tetraacyl chloride and m-phenylenediamine. *J. Membr. Sci.* **2008**, *315*, 20–27.

(11) Song, Y.; Sun, P.; Henry, L. L.; Sun, B. Mechanisms of structure and performance controlled thin film composite membrane formation via interfacial polymerization process. *J. Membr. Sci.* **2005**, *251*, 67–79.

(12) Ghosh, A. K.; Jeong, B.-H.; Huang, X.; Hoek, E. M. V. Impacts of reaction and curing conditions on polyamide composite reverse osmosis membrane properties. *J. Membr. Sci.* **2008**, *311*, 34–45.

(13) Perry, L. A.; Coronell, O. Reliable, bench-top measurements of charge density in the active layers of thin-film composite and nanocomposite membranes using quartz crystal microbalance technology. *J. Membr. Sci.* **2013**, *429*, 23–33.

(14) Freger, V. Swelling and morphology of the skin layer of polyamide composite membranes: an atomic force microscopy study. *Environ. Sci. Technol.* **2004**, *38*, 3168–3175.

(15) Pacheco, F. A.; Pinnau, I.; Reinhard, M.; Leckie, J. O. Characterization of isolated polyamide thin films of RO and NF membranes using novel TEM techniques. *J. Membr. Sci.* **2010**, *358*, 51–59.

(16) Yan, H.; Miao, X.; Xu, J.; Pan, G.; Zhang, Y.; Shi, Y.; Guo, M.; Liu, Y. The porous structure of the fully-aromatic polyamide film in reverse osmosis membranes. *J. Membr. Sci.* **2015**, *475*, 504–510.

(17) Lee, J.; Doherty, C. M.; Hill, A. J.; Kentish, S. E. Water vapor sorption and free volume in the aromatic polyamide layer of reverse osmosis membranes. *J. Membr. Sci.* **2013**, *425-426*, 217–226.

(18) Bason, S.; Oren, Y.; Freger, V. Ion transport in the polyamide layer of RO membranes: Composite membranes and free-standing films. *J. Membr. Sci.* **2011**, *367*, 119–126.

(19) Marx, K. A. Quartz crystal microbalance: a useful tool for studying thin polymer films and complex biomolecular systems at the solution-surface interface. *Biomacromolecules* **2003**, *4*, 1099–1120.

(20) O'Sullivan, C. K.; Guilbault, G. G. Commercial quartz crystal microbalances—Theory and applications. *Biosens. Bioelectron.* **1999**, *14*, 663–670.

(21) Huang, Y.; Paul, D. R. Physical aging of thin glassy polymer films monitored by gas permeability. *Polymer.* **2004**, *45*, 8377–8393.

(22) Irene, E. A. A brief history and state of the art of ellipsometry. In *Ellipsometry at the Nanoscale*; Losurdo, M.; Hingerl, K., Eds.; Springer-Verlag Berlin Heidelberg, 2013; pp. 1–30.

(23) Ogieglo, W.; van der Werf, H.; Tempelman, K.; Wormeester, H.; Wessling, M.; Nijmeijer, A.; Benes, N. E. n-Hexane induced swelling of thin PDMS films under non-equilibrium nanofiltration permeation conditions , resolved by spectroscopic ellipsometry. *J. Membr. Sci.* **2013**, *431*, 233–243.

(24) Kahle, O.; Wielsch, U.; Metzner, H.; Bauer, J.; Uhlig, C.; Zawatzki, C. Glass transition temperature and thermal expansion behaviour of polymer films investigated by variable temperature spectroscopic ellipsometry. *Thin Solid Films* **1998**, *313-314*, 803–807.

(25) Ogieglo, W.; Wormeester, H.; Wessling, M.; Benes, N. E. Spectroscopic Ellipsometry Analysis of a Thin Film Composite Membrane Consisting of Polysulfone on a Porous α-Alumina Support. *Appl. Mater. Interfaces* **2012**, *4*, 935–943.

(26) Kwak, S.-Y.; Jung, S. G.; Yoon, Y. S.; Ihm, D. W. Details of surface features in aromatic polyamide reverse osmosis membranes characterized by scanning electron and atomic force microscopy. *J. Polym. Sci. Part B Polym. Phys.* **1999**, *37*, 1429–1440.

(27) Wijmans, J. G.; Baker, R. W. The solution-diffusion model: a review. *J. Membr. Sci.* **1995**, *107*, 1–21.

(28) Turner, L. A. Zeroth Law of Thermodynamics. *Am. J. Phys.* **1961**, *29*, 71–76.

(29) Paul, D. R. Reformulation of the solution-diffusion theory of reverse osmosis. *J. Membr. Sci.* **2004**, *241*, 371–386.

(30) Yang, K.; Zhu, L.; Xing, B. Adsorption of Polycyclic Aromatic Hydrocarbons by Carbon Nanomaterials. *Environ. Sci. Technol.* **2006**, *40*, 1855–1861.

(31) Lo, S. Anomalous State of Ice. *Mod. Phys.* **1996**, *10*, 909–919.

(32) Metz, S. J.; van de Ven, W. J. C.; Potreck, J.; Mulder, M. H. V; Wessling, M. Transport of water vapor and inert gas mixtures through highly selective and highly permeable polymer membranes. *J. Membr. Sci.* **2005**, *251*, 29–41.

(33) Kotelyanskii, M. J.; Wagner, N. J.; Paulaitis, M. E. Atomistic simulation of water and salt transport in the reverse osmosis membrane FT-30. *J. Membr. Sci.* **1998**, *139*, 1–16.

(34) *MWH Water treatment: Principles and design*; Crittenden, J. C.; Trussell, R. R.; Hand, D. W.; Howe, K. J.; Tchobanoglous, G., Eds.; John Wiley & Sons: Hoboken, NY, USA, 2012; p. 1870.

APPENDIX 9: RESULTS OF TRANSMISSION ELECTRON MICROSCOPY (TEM) ANALYSES OF ACTIVE LAYER NODULE FRACTION

Membrane	Void Fraction				
	Sample 1	Sample 2	Sample 3	Average	Standard Deviation
NF90	21%	34%	26%	27%	7%
XLE	37%	29%	30%	32%	4%
ESPA3	23%	34%	29%	29%	6%
SWC4+	31%	26%	28%	28%	2%
SW30HR	31%	36%	23%	30%	7%

APPENDIX 10: RESULTS OF QUARTZ CRYSTAL MICROBALANCE (QCM) ANALYSES OF ACTIVE LAYER VOID FRACTION

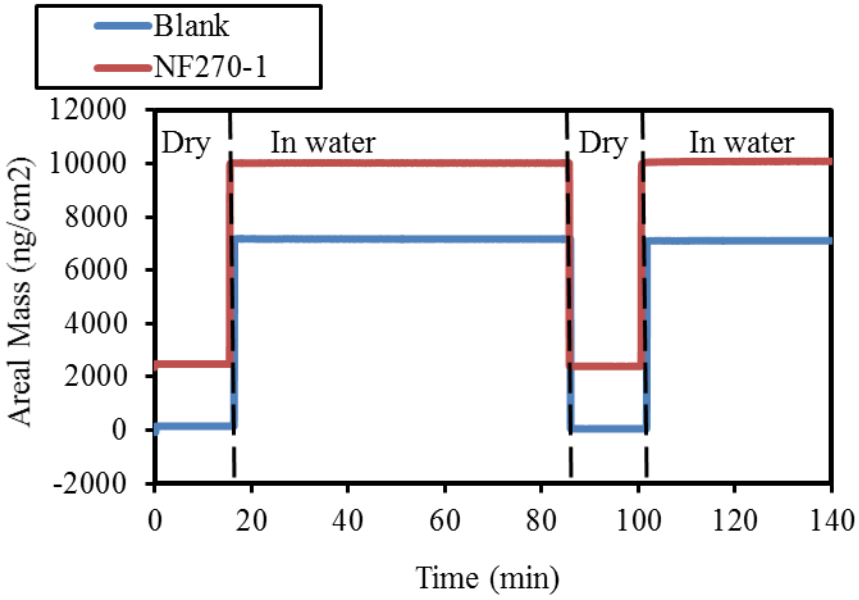

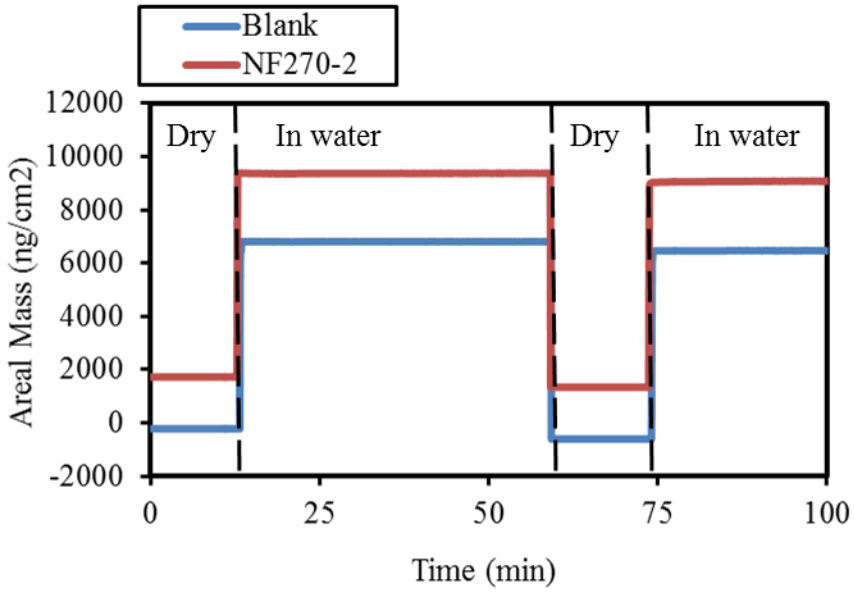

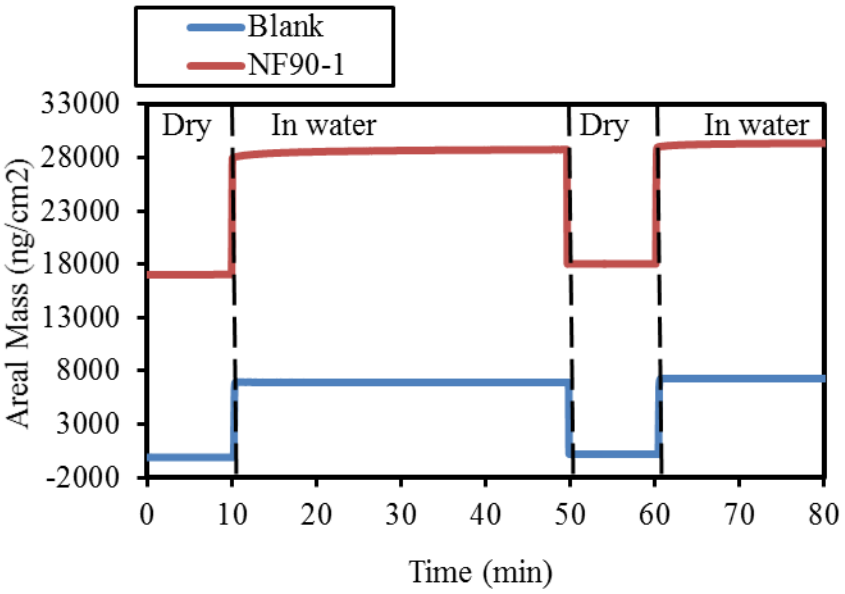
Blank
NF90-1
Dry
In water
Dry
In water
Areal Mass (ng/cm2)
33000
28000
23000
18000
13000
8000
3000
-2000
0
10
20
30
40
50
60
70
80
Time (min)

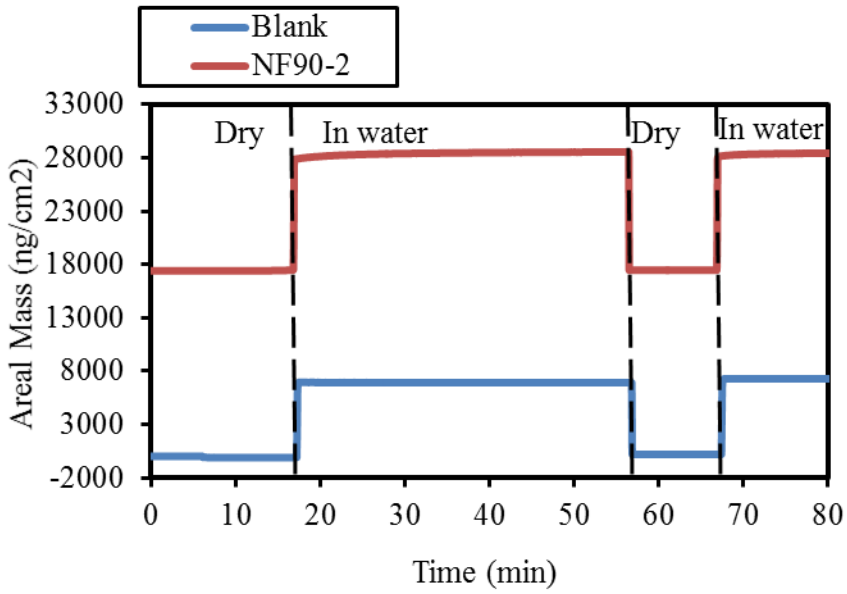
Blank
NF90-2
Dry
In water
Dry
In water
Areal Mass (ng/cm2)
33000
28000
23000
18000
13000
8000
3000
-2000
0
10
20
30
40
50
60
70
80
Time (min)

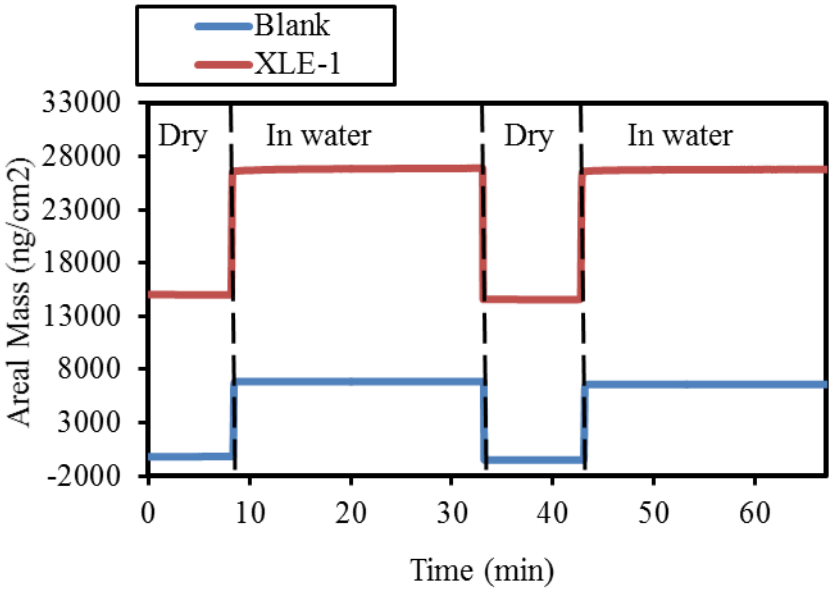
Blank
XLE-1
Dry
In water
Dry
In water
Areal Mass (ng/cm2)
33000
28000
23000
18000
13000
8000
3000
-2000
0
10
20
30
40
50
60
Time (min)

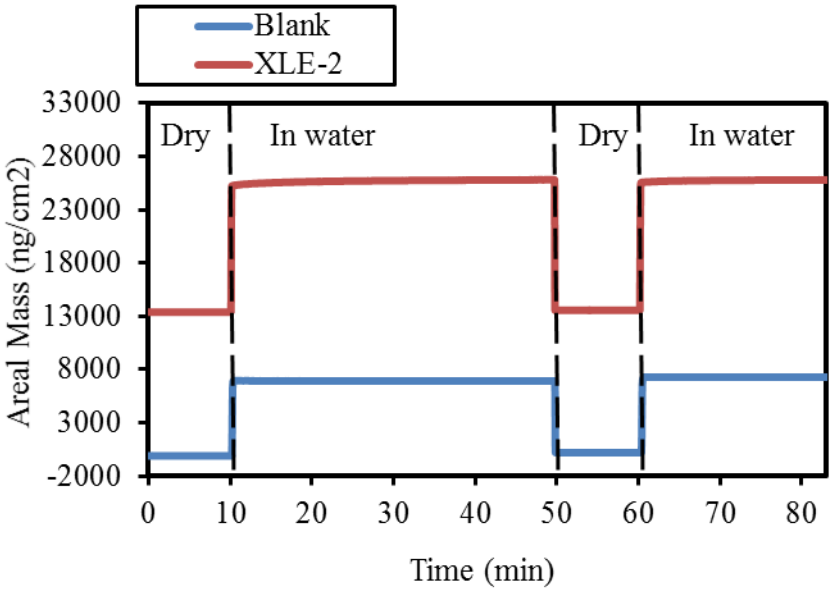
Blank
XLE-2
Dry
In water
Dry
In water
Areal Mass (ng/cm2)
33000
28000
23000
18000
13000
8000
3000
-2000
0
10
20
30
40
50
60
70
80
Time (min)

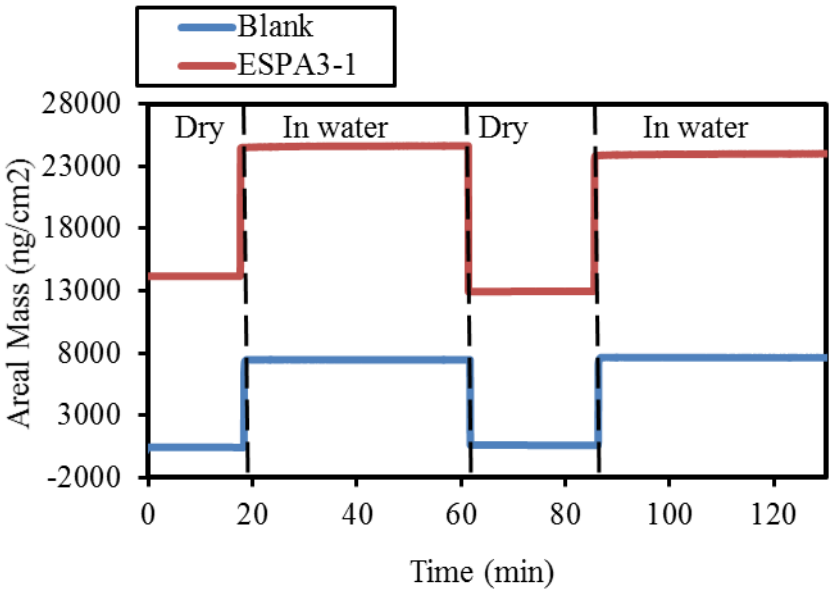
Blank
ESPA3-1
Dry
In water
Dry
In water
Areal Mass (ng/cm2)
28000
23000
18000
13000
8000
3000
-2000
0
20
40
60
80
100
120
Time (min)

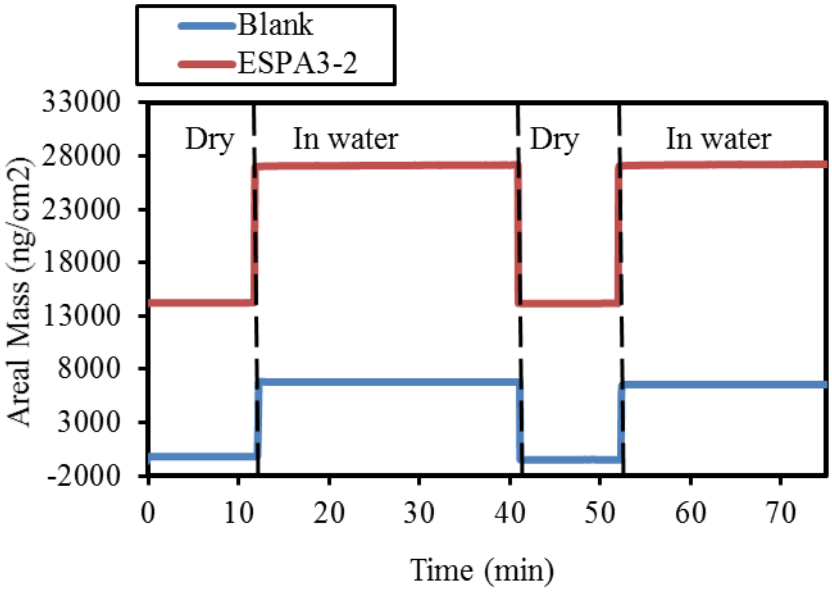
Blank
ESPA3-2
Dry
In water
Dry
In water
Areal Mass (ng/cm2)
33000
28000
23000
18000
13000
8000
3000
-2000
0
10
20
30
40
50
60
70
Time (min)

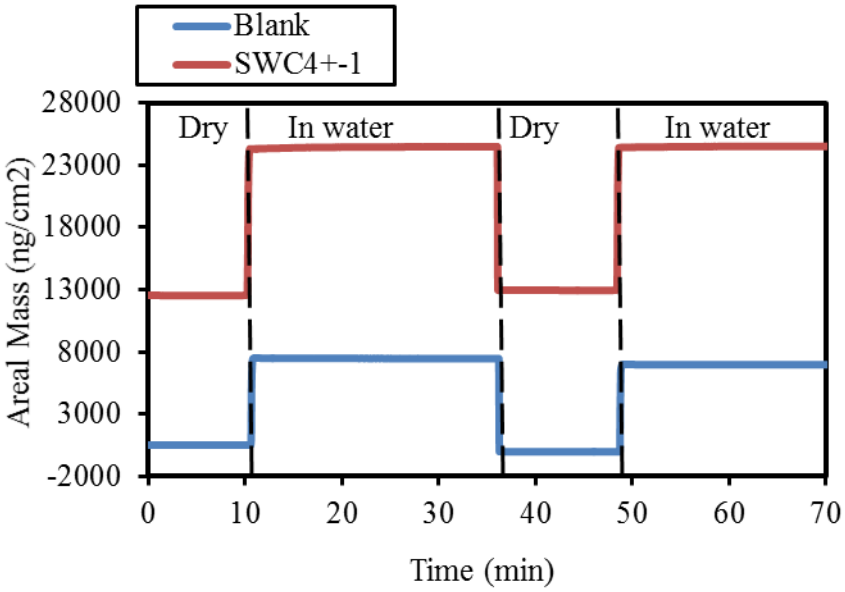
Blank
SWC4+-1
Dry
In water
Dry
In water
Areal Mass (ng/cm2)
28000
23000
18000
13000
8000
3000
-2000
0
10
20
30
40
50
60
70
Time (min)

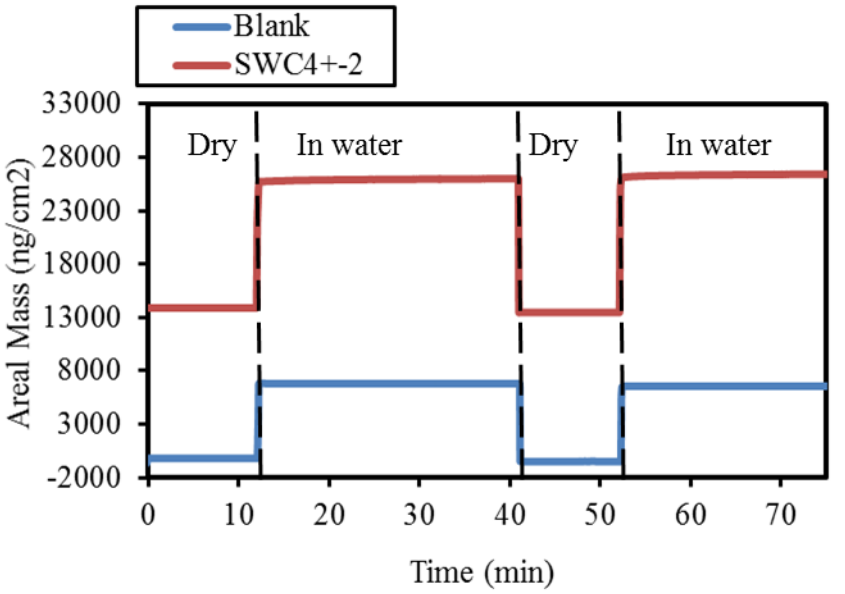
Blank
SWC4+-2
Dry
In water
Dry
In water
Areal Mass (ng/cm2)
33000
28000
23000
18000
13000
8000
3000
-2000
0
10
20
30
40
50
60
70
Time (min)

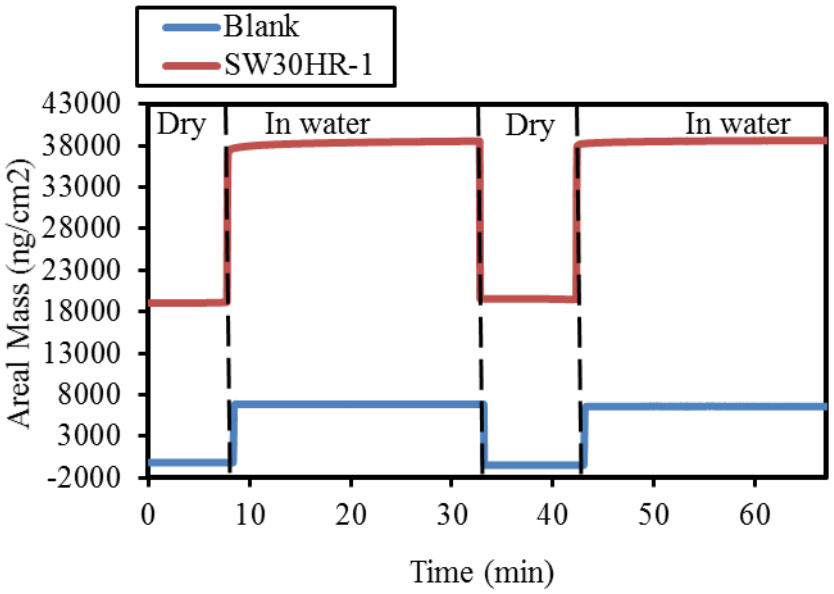
Blank
SW30HR-1
Dry
In water
Dry
In water
Areal Mass (ng/cm2)
43000
38000
33000
28000
23000
18000
13000
8000
3000
-2000
0
10
20
30
40
50
60
Time (min)

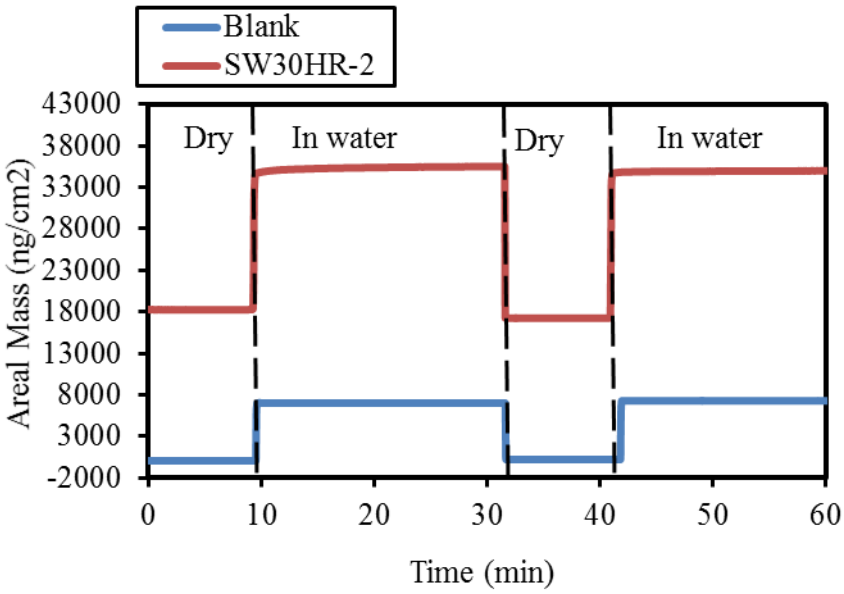
Blank
SW30HR-2
Dry
In water
Dry
In water
Areal Mass (ng/cm2)
43000
38000
33000
28000
23000
18000
13000
8000
3000
-2000
0
10
20
30
40
50
60
Time (min)

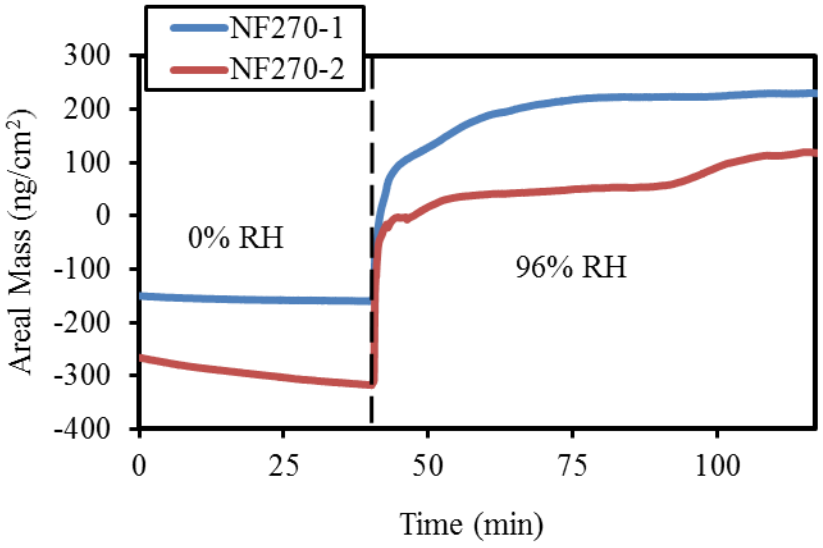
NF270-1
NF270-2
300
200
100
0
-100
-200
-300
-400
Areal Mass (ng/cm²)
0% RH
96% RH
0
25
50
75
100
Time (min)

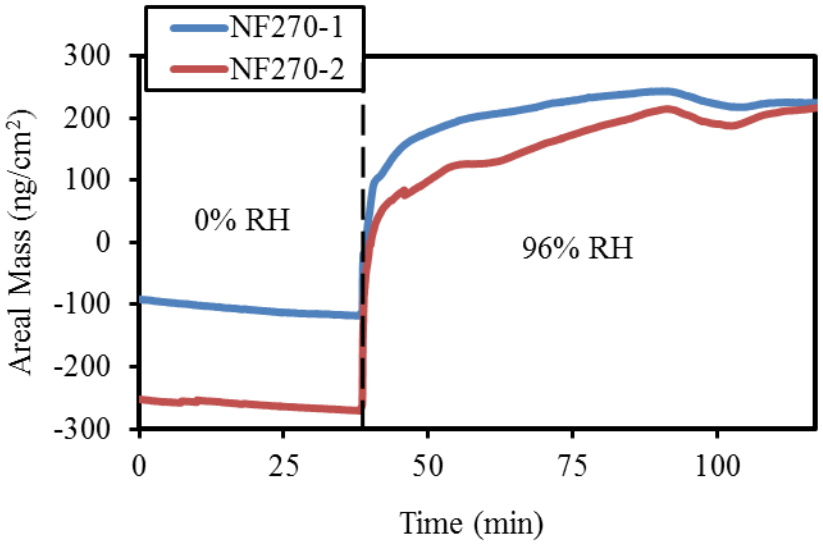
NF270-1
NF270-2
300
200
100
0
-100
-200
-300
Areal Mass (ng/cm²)
0% RH
96% RH
0
25
50
75
100
Time (min)

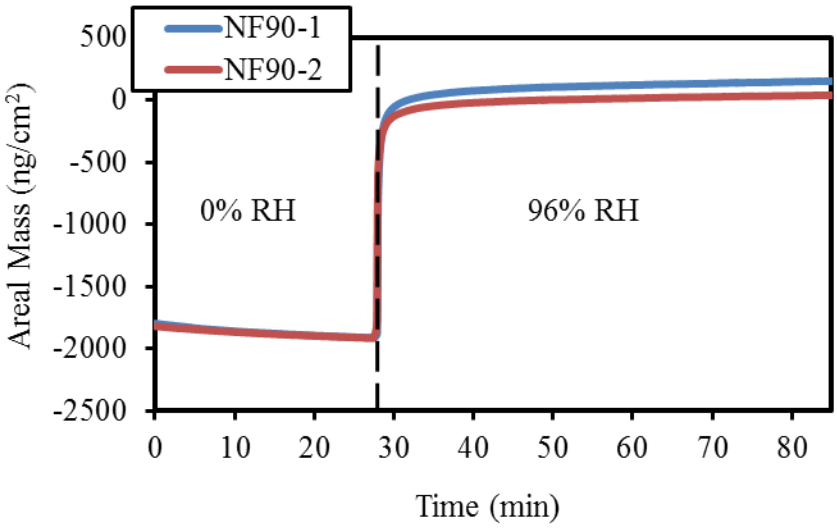
NF90-1
NF90-2
500
0
-500
-1000
-1500
-2000
-2500
Areal Mass (ng/cm²)
0% RH
96% RH
0
10
20
30
40
50
60
70
80
Time (min)

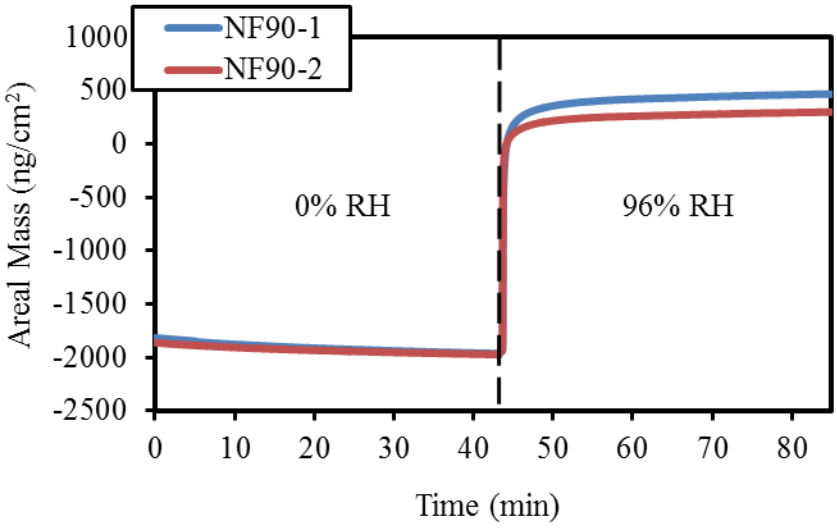
NF90-1
NF90-2
1000
500
0
-500
-1000
-1500
-2000
-2500
Areal Mass (ng/cm²)
0% RH
96% RH
0
10
20
30
40
50
60
70
80
Time (min)

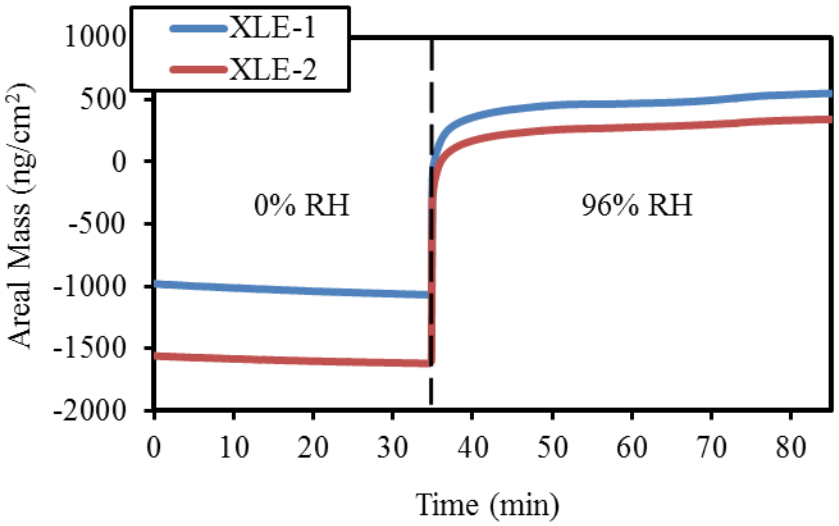
XLE-1
XLE-2
1000
500
0
-500
-1000
-1500
-2000
Areal Mass (ng/cm²)
0% RH
96% RH
0
10
20
30
40
50
60
70
80
Time (min)

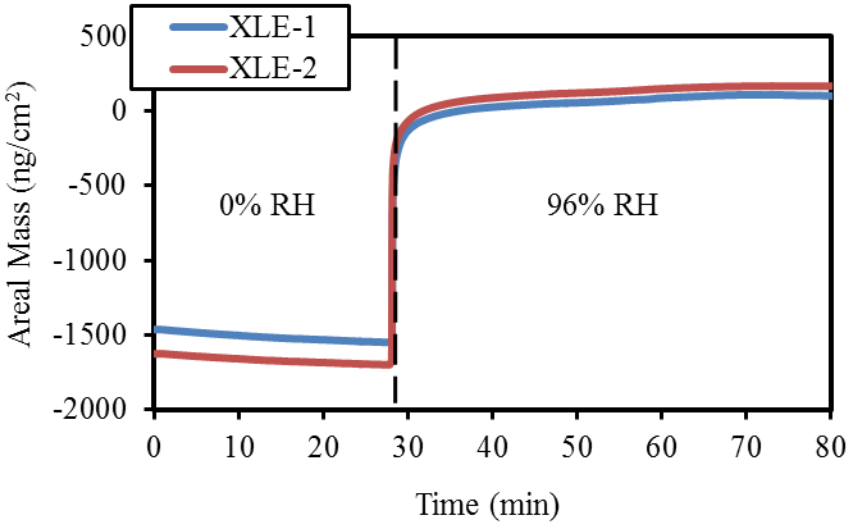
XLE-1
XLE-2
500
0
-500
-1000
-1500
-2000
Areal Mass (ng/cm²)
0% RH
96% RH
0
10
20
30
40
50
60
70
80
Time (min)

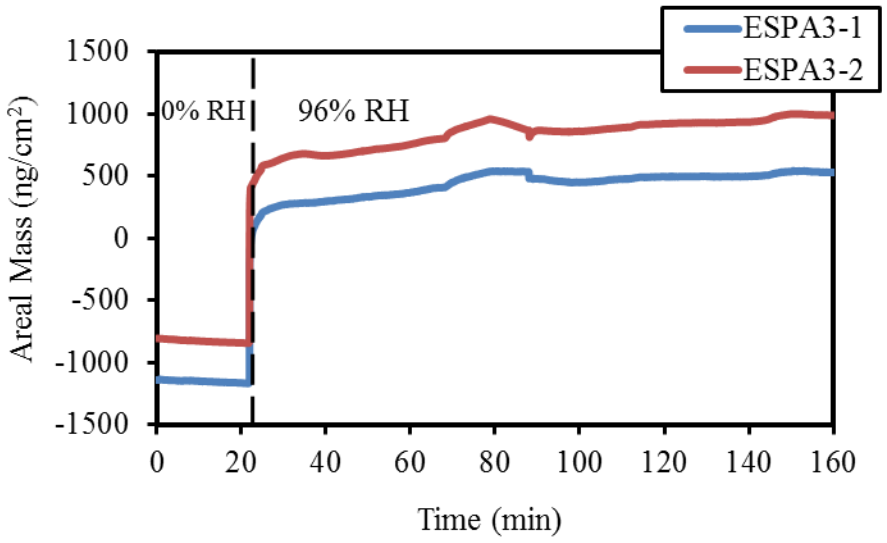
ESPA3-1
ESPA3-2
0% RH
96% RH
Areal Mass (ng/cm²)
Time (min)

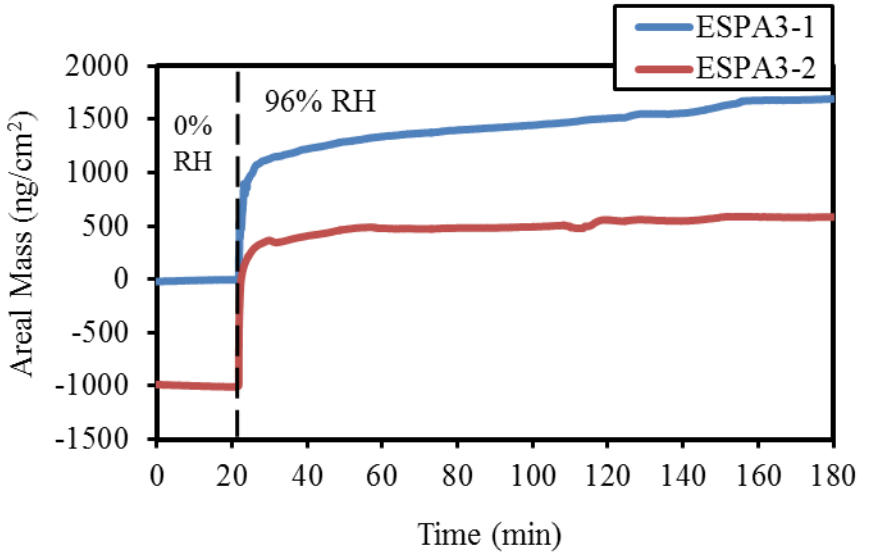
ESPA3-1
ESPA3-2
0% RH
96% RH
Areal Mass (ng/cm²)
Time (min)

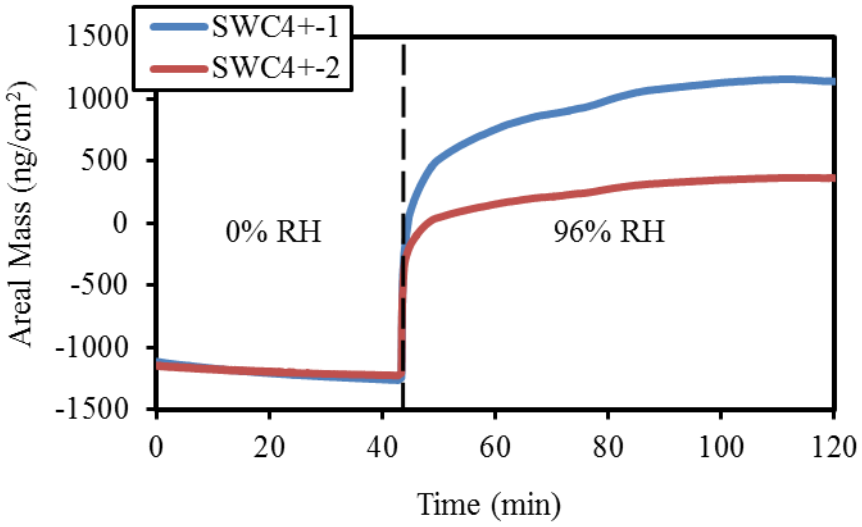
SWC4+-1
SWC4+-2
1500
1000
500
0
-500
-1000
-1500
Areal Mass (ng/cm²)
0% RH
96% RH
0
20
40
60
80
100
120
Time (min)

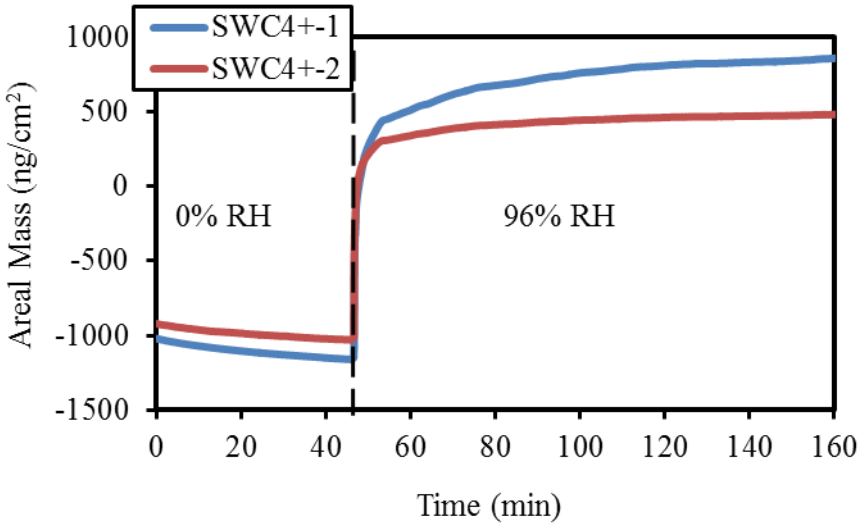
SWC4+-1
SWC4+-2
1000
500
0
-500
-1000
-1500
Areal Mass (ng/cm²)
0% RH
96% RH
0
20
40
60
80
100
120
140
160
Time (min)

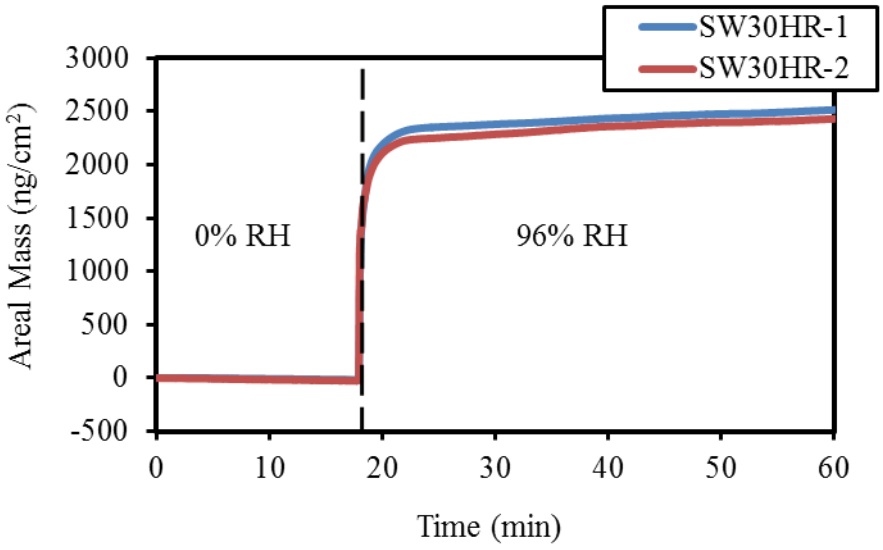
SW30HR-1
SW30HR-2
Areal Mass (ng/cm²)
3000
2500
2000
1500
1000
500
0
-500
0% RH
96% RH
0
10
20
30
40
50
60
Time (min)

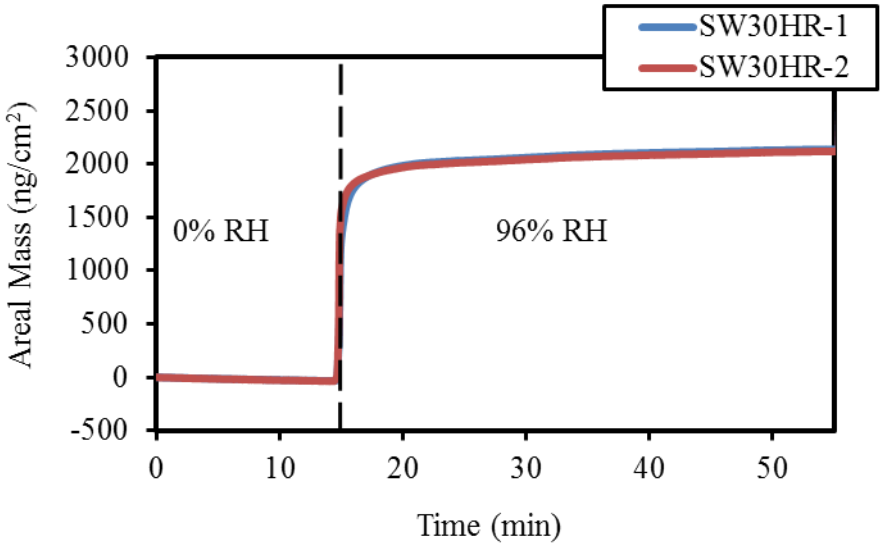
SW30HR-1
SW30HR-2
Areal Mass (ng/cm²)
3000
2500
2000
1500
1000
500
0
-500
0% RH
96% RH
0
10
20
30
40
50
Time (min)

APPENDIX 11: RESULTS OF ELLIPSOMETRY ANALYSES OF ACTIVE LAYER VOID FRACTION

Membrane	Sample Number	Location Number	Refractive Index
NF90	1	1	1.5832
		2	1.5704
		3	1.5827
	2	1	1.5359
		2	1.5091
		3	1.5181
	3	1	1.5785
		2	1.5565
		3	1.5742
XLE	1	1	1.4893
		2	1.4492
		3	1.4656
	2	1	1.4646
		2	1.482
		3	1.4821
	3	1	1.4898
		2	1.4852
		3	1.5094
ESPA3	1	1	1.4661
		2	1.4387
		3	1.4585
	2	1	1.4116
		2	1.4163
		3	1.4567
	3	1	1.3887
		2	1.4382
		3	1.3918

Membrane	Sample Number	Location Number	Refractive index
SWC4+	1	1	1.3819
		2	1.3923
		3	1.3865
	2	1	1.3869
		2	1.3511
		3	1.3436
	3	1	1.4161
		2	1.3917
		3	1.3935
SW30HR	1	1	1.428
		2	1.4431
		3	1.4084
	2	1	1.5516
		2	1.5307
		3	1.5181
	3	1	1.499
		2	1.4828
		3	1.5093

APPENDIX 12: WATER PERMEATION TEST RESULTS

Membrane	Sample Number	Time (hour)	Water Collection Time (s)	Mass of Water Collected (g)
NF270	1	0	240	10.83
		0.5	180	7.89
		1	180	7.79
		1.5	180	7.46
		1.5	180	7.47
		2	180	7.43
		3	180	7.32
		3	180	7.37
		4.5	180	7.16
		4.5	180	7.31
		6	180	7.23
	2	0	180	7.55
		0.5	180	7.40
		1	180	7.36
		1.5	180	7.15
		1.5	180	7.33
		2	180	7.37
		3	180	7.14
		3	180	7.37
		4.5	180	7.15
		4.5	180	7.34
		6	180	7.27

Membrane	Sample Number	Time (hour)	Water Collection Time (s)	Mass of Water Collected (g)
NF90	1	0	180	4.22
		0.5	180	4.13
		1	180	4.03
		1.5	182	4.13
		2	179	3.89
		2.5	180	3.91
		2.5	182	3.88
		3	180	3.79
		4	180	3.99
		5	180	3.79
		5	180	3.88
		6	180	3.82
		7	180	3.78
	2	0	180	4.62
		0.5	180	4.58
		1	180	4.52
		1.5	180	4.53
		2	180	4.36
		2.75	180	4.23
		2.75	180	4.40
		3.25	180	4.31
		4	180	4.10
		5	180	4.04
		5	180	4.15
		6	180	3.92
		7.5	180	3.94

Membrane	Sample Number	Time (hour)	Water Collection Time (s)	Mass of Water Collected (g)
XLE	1	0	180	3.21
		0.5	180	3.22
		1	180	3.22
		1.5	180	3.17
		2	180	3.17
		3	180	3.10
		3	180	3.06
		4	180	3.07
		6	180	3.00
	2	0	180	3.90
		0.5	360	7.79
		1	360	7.71
		2	360	7.67
		3	360	7.28
		3	360	7.33
		4	360	7.18
		6	360	6.94

Membrane	Sample Number	Time (hour)	Water Collection Time (s)	Mass of Water Collected (g)
ESPA3	1	0	180	2.74
		0.5	181	2.74
		1	180	2.77
		1.5	182	2.82
		2	183	2.80
		3	180	2.81
		4	183	2.71
		4	180	2.60
		4.5	177	2.59
		5.5	180	2.59
		7	180	2.50
	2	0	180	2.6501
		0.5	180	2.6441
		1	180	2.6447
		2	180	2.6402
		3	180	2.6511
		4	180	2.6093
		4	180	2.423
		5	180	2.6043
		7	180	2.5325

Membrane	Sample Number	Time (hour)	Water Collection Time (s)	Mass of Water Collected (g)
SWC4+	1	0	300	0.53
		0.5	300	0.77
		1	300	0.73
		2	300	0.75
		4	300	0.78
		6	300	0.79
		8	300	0.79
		9	300	0.72
	2	0	180	0.53
		0.5	180	0.54
		1	180	0.54
		2	180	0.54
		3	180	0.54
		4	180	0.48
		5	180	0.51
		6	180	0.55

Membrane	Sample Number	Time (hour)	Water Collection Time (s)	Mass of Water Collected (g)
SW30HR	1	0.5	1800	2.00
		1	1800	1.90
		2	1800	1.76
		3	1800	1.77
		5	1800	1.72
		7	1800	1.70
	2	0.5	1800	3.19
		1	1800	2.91
		2	1800	2.70
		3	1800	2.55
		5	1800	2.43
		7	1800	2.31